



Molecular Simulation of Protein Adhesion for Rational Design of Antimicrobial Surfaces

A thesis submitted in fulfilment of the requirements for the degree of Doctor of
Philosophy

Kamron James Ley

BSci (Applied Sciences) (Hons. 1st class), RMIT University, 2012

B. Sc. (Nano.) , RMIT University, 2011

B. Sc. (App. Sc.), RMIT University, 2011

School of Engineering

College of Science, Engineering and Health

RMIT University

January 2018

Declaration of Candidature

I certify that except where due acknowledgement has been made, the work is that of the author alone; the work has not been submitted previously, in whole or in part, to qualify for any other academic award; the content of the thesis is the result of work which has been carried out since the official commencement date of the approved research program; any editorial work, paid or unpaid, carried out by a third party is acknowledged; and, ethics procedures and guidelines have been followed.

I acknowledge the support I have received for my research through the provision of an Australian Government Research Training Program Scholarship.

Kamron James Ley

January 16, 2018

Acknowledgements

This work would not have been made possible without the support, guidance, and collaboration of many people who deserve to be acknowledged.

First and foremost, I wish to thank my supervisor, Prof. Irene Yarovsky for the opportunity to work on this project. Your patience, support, and mentorship, have been invaluable, and without which this project would not have been possible. You have been critical in my professional development, and I will never be able to thank you enough for offering the opportunity to join the Molecular Modelling and Simulations Group in my undergraduate years.

I would also like to say a special thank you to Prof. Dave Winkler, for your continued mentoring, advice and assistance. The wealth of knowledge you have provided to this project, and being able to provide a fresh outside perspective have been pinnacle to this work.

Thank you to my supervisory team over the years, Dr. Matthew Penna, Dr. Andrew Christofferson, and Dr. George Yiapanis. You have provided several helpful comments and suggestions over the years that has helped make this thesis a better piece of work, and the whole experience enjoyable. I also thank Dr. Timothy Trudgian, for accepting to read and proof this thesis.

I would like to thank Shane Maclaughlin, from BlueScope Steel, for being one of the driving forces behind this project. Your ideas and suggestions have greatly improved this project, and I will always be appreciative of your hospitality in Wollongong.

I would like to thank CSIRO for providing financial support for this project, and acknowledge the National Computing Infrastructure (NCI), Victorian Life Sciences

Computation Initiative (VLSCI) and the Victorian Partnership for Advanced Computing (VPAC) for providing computational facilities.

On a personal note, thank you to all my family, for your support, and assistance over the past few years. To my Greg and Tash, a very special thank you for being a massive support in my life, you have always been there for me when I needed you, and I can never thank you enough.

To all my friends, I thank you for your tolerance and encouragements over the years, and especially for all the coffee, drinks, and cheap and cheerful dinners to provide a much-needed distraction. I am blessed to have such wonderful people in my life, and will never be able to thank you all enough.

Publication List

- [1] **Ley, K. J.**, Shaw, L. A., Yiapanis, G., Maclaughlin, S., & Yarovsky, I. (2015). Effect of Substrate on the Responsive Behaviour of Functionalised Surfaces: Insights from Molecular Simulation. *Molecular Simulation*, 1-10.
- [2] **Ley, K.**, Christofferson, A., Penna, M., Winkler, D., Maclaughlin, S., & Yarovsky, I. (2015). Surface-Water Interface Induces Conformational Changes Critical for Protein Adsorption: Implications for Monolayer Formation of EAS Hydrophobin. *Front Mol Biosci*, 2, 64.
- [3] Penna, M., **Ley, K.**, Maclaughlin, S., & Yarovsky, I. (2016). Surface Heterogeneity: a Friend or Foe of Protein Adsorption - Insights from Theoretical Simulations. *Faraday Discussions*, 191, 435-464.
- [4] **Ley, K.**, Penna, M., Winkler, D., Maclaughlin, S., & Yarovsky, I. (2018, Accepted/In Press), Molecular Mechanisms of Anti-Fouling Efficacy for Ligand Protected Surfaces.

Conference Presentations

- [1] **Kamron Ley**, George Yiapanis, Dave Winkler, Shane Maclaughlin, Evan Evans and Irene Yarovsky - 8th Annual International Electromaterials Science Symposium 2013 - ARC Centre of Excellence of Electromaterials Science, Wollongong University, NSW, Australia - *Molecular Simulation of Protein Interactions with PEG-Grafted Silica Surfaces*
- [2] **Kamron Ley**, George Yiapanis, Dave Winkler, Shane Maclaughlin, Evan Evans and Irene Yarovsky - 12th Melbourne Protein Group Student Symposium 2013 - La Trobe University, Melbourne, Australia - *On the Adsorption of Hydrophobin Protein on Functionalised Silica Surfaces*
- [3] **Kamron Ley**, George Yiapanis, Dave Winkler, Shane Maclaughlin, Evan Evans and Irene Yarovsky - 4th Asia-Pacific Symposium on Nanobionics 2013 - University of Melbourne Law School, Melbourne, VIC, Australia - *Investigating the Social Behaviour of EAS Hydrophobin with Static and Dynamic Surfaces*
- [4] **Kamron Ley**, George Yiapanis, Dave Winkler, Shane Maclaughlin, Evan Evans and Irene Yarovsky - The 37th Annual Conference of the Australian Society for Biophysics - RMIT University, Melbourne, VIC, Australia - *Implications of Surface Mobility on Anti-Microbial Behaviour*
- [5] **Kamron Ley**, George Yiapanis, Dave Winkler, Shane Maclaughlin, Evan Evans and Irene Yarovsky - RACI PhysChem 2013 - Hobart Waterfront, TAS, Australia - *Flexible or Rigid? Investigating the Effect of Surface Hardness on Anti-Fouling Performance*
- [6] **Kamron Ley**, George Yiapanis, Dave Winkler, Shane Maclaughlin, Evan Evans and Irene Yarovsky - 12th International Conference on Frontiers of Polymers and Advanced Materials 2013 - University of Auckland, New Zealand - *Investigating the Behaviour of Fungal Proteins on PEG-Modified Surfaces*
- [7] **Kamron Ley**, George Yiapanis, Dave Winkler, Shane Maclaughlin, Evan Evans and Irene Yarovsky - International Conference on Nanoscience and Nanotechnology 2014 - Adelaide Convention Centre, South Australia, Australia - *A Computational Study of Protein Adhesion on Anti-Fouling Surfaces*
- [8] **Kamron Ley**, Andrew Christofferson, Dave Winkler, Shane Maclaughlin, Evan Evans and Irene Yarovsky - Molecular Modelling 2014: From biomolecules to materials - Lamington National Park, Queensland, Australia - *Elucidating Mechanisms and Limitations of Anti-Fouling Surfaces*
- [9] **Kamron Ley**, Andrew Christofferson, Dave Winkler, Shane Maclaughlin, Evan Evans and Irene Yarovsky - 3rd Biennial Conference of the Combined Australian Materials Societies 2014 - Charles Perkins Centre, University of Sydney, NSW, Australia - *Anti-Fouling Effectiveness of PEG-Modified Surfaces: A Molecular Dynamics Study*

[10] **Kamron Ley**, Matthew Penna, Dave Winkler, Shane Maclaughlin and Irene Yarovsky –
10th World Biomaterials Congress 2016 – Charles Perkins Centre, Montréal, Québec,
Canada - *PEG vs POX: A Molecular Dynamics Comparison of Anti-Fouling Effectiveness*

Contents

Molecular Simulation of Protein Adhesion for Rational Design of Antimicrobial Surfaces.....	i
Declaration of Candidature	ii
Acknowledgements.....	iii
Publication List	v
Conference Presentations.....	vi
Contents	viii
List of Tables	xiv
List of Figures	xv
Abstract.....	xxii
Chapter 1.....	1
1. Introduction/Literature Review:.....	1
1.1. Overview	1
1.2. Background and Motivation.....	2
1.3. Biofouling Process	4
1.3.1. Initial and Irreversible Attachment	4
1.3.2. Initial Growth	5
1.3.3. Final Growth and Dispersion	6
1.4. EAS Hydrophobin	6

1.5. Combating Biofilm formation	9
1.6. Strategies for anti-fouling coating design	10
1.6.1. Surface Chemistry effects	10
1.6.2. Topographical/Surface Roughness effects	11
1.6.3. Surface Heterogeneity	13
1.7. Interactions and involvement of water	14
1.8. Current theories on Anti-fouling coatings.....	16
1.8.1. Steric repulsion theories	16
1.8.2. Hydration theories	18
1.9. Surface Functionality and Roughness Topography	19
1.9.1. Linear systems.....	20
1.9.1.1. Grafted Systems	20
1.9.1.2. Self-Assembled Monolayers	24
1.9.2. Branched/Comb-like chains	26
1.9.3. Poly-Zwitterionic chains	29
1.10. Project Aims.....	31
Chapter 2.....	32
2. Computational Techniques for Modelling Anti-Fouling Systems	32
2.1. Overview	32
2.2. Introduction to Molecular Modelling.....	33
2.3. Molecular Mechanics and Force-Fields	36

2.4.	Potential Energy Expression – Class 1 FF	36
2.5.	Force-Field Parameterisation	39
2.6.	Energy Minimisation.....	41
2.7.	Molecular Dynamics	42
2.8.	Periodic Boundary Conditions	44
2.9.	Non-Bonded interactions.....	46
2.10.	Thermodynamics Ensembles.....	46
2.11.	Temperature Coupling.....	47
2.12.	Bond Constraint Algorithms	48
2.13.	Enhanced Sampling Techniques	49
Chapter 3.....		51
3.	Protein and Surface Models	51
3.1.	Overview	51
3.2.	Modelling Anti-fouling:	52
3.3.	Substrates	53
3.3.1.	Polyester	53
3.3.2.	Silica/oxide.....	55
3.4.	Modelling Protein-Inorganic Surface Interactions.....	56
3.5.	Computational Models	58
3.5.1.	Polyester Surface Model	58
3.5.2.	Silica Surface Model	59

3.5.3. Surface functionalisation.....	59
Chapter 4.....	60
4. Effect of Substrate Behaviour on Tethered Surfaces	60
4.1. Overview	60
4.2. Introduction	61
4.3. Method	62
4.3.1. Models of PEG grafted silica and polyester substrates.....	62
4.3.2. Computational details.....	64
4.3.3. Simulating the hydration induced response of PEG grafts	64
4.4. Results	66
4.4.1. De-swelling of PEGylated surfaces upon drying	66
4.4.2. Swelling of PEGylated surfaces.....	70
4.4.3. Effects of surface hardness and roughness.....	74
4.5. Conclusion.....	75
Chapter 5.....	77
5. Elucidating molecular mechanisms of PEG and POX anti-fouling coating efficacy	77
5.1. Overview	77
5.2. Introduction	78
5.3. Methods.....	79
5.4. Results and Discussion.....	81
5.4.1. Average Chain Structure	85

5.4.2. Hydrophobicity.....	93
5.4.3. Chain Dynamics	95
5.4.4. Hydration behaviour.....	99
5.5. Conclusion.....	105
Chapter 6.....	107
6. Binding Motifs and Behaviour of EAS Hydrophobin at the Silica Surface- Water Interface.....	107
6.1. Overview	107
6.2. Introduction	108
6.3. Methodology	110
6.3.1. Protein-solvent system	110
6.3.2. Surface-protein system.....	111
6.3.3. Simulation settings	112
6.4. Results	112
6.4.1. Protein binding at the surface-water interface.....	113
6.4.2. Specific interactions	116
6.4.3. Behaviour of the Cys7-Cys8 and Cys3-Cys4 loops	118
6.4.4. The role of structure and dynamics of interfacial water in hydrophobin adsorption	121
6.5. Conclusion.....	129
Chapter 7.....	131
7. Modelling Anti-Fouling Systems	131

7.1. Overview	131
7.2. Introduction	131
7.3. Method	133
7.4. Results and discussion.....	134
7.4.1. Initial adsorption process	136
7.4.2. Adsorbed state analysis	139
7.4.3. Chain dynamics	140
7.4.4. Protein behaviour	143
7.5. Conclusions	145
Conclusions and Future Work	147
8. Conclusions	147
9. Future Work	149
Appendices.....	151
References.....	157

List of Tables

Table 4.1 Summary of substrate models.....	63
Table 5.1 Quantitative description of surfaces.	81
Table 5.2 PEG chain conformations based on a twin height difference cut-off between the oxygen before PEG repeat units (O(0)), of the third repeat unit (O(3)) and the terminal unit (O(T)).....	87
Table 5.3 Conformational Distribution – Shows the percentage breakdown for all transitions occurring during the simulations.....	91
Table 5.4 Detailed Hydrogen bond information for all systems. Hydrogen bond cut-offs used a distance of 3.5 Å and angle 20°.	100
Table 6.1 Average loss of contacts with water for residues in the region Gln20-Ile50 for systems that adsorbed at the air-water and surface-water interface (Binding Motif 1), compared to the bulk environment, over the last 10 ns of simulation. A contact was defined as a water atom coming within 3 Å of the amino acid group type defined by Livingstone and Barton [393]. A detailed plot can be found in Appendices Figure A6.5.	126
Table 7.2 Simulated system data summary: R = Total number of runs performed; NIR = non interacting runs; AR = adsorbed runs; AA = high contact area ARs used for adsorbed state analysis, DE = Number of disruption events. Low (L) and Medium (M) refer to the chain coverage density used (1.4 and 2.2 chains/nm ²).	136

List of Figures

Figure 1.1 Overview of the anti-fouling process. Only the initial attachment stage of biofouling is a reversible procedure [45].	4
Figure 1.2 An overview of the structure, function and applications of hydrophobins [72].	7
Figure 1.3 SEM images of engineered topographies on a PDMS _e surface. (A) 2 mm ribs of lengths 4, 8, 12, and 16 mm combined to create the Sharklet AFTM; (B) 10 mm equilateral triangles combined with 2 mm diameter circular pillars; (C) hexagonally packed 2 mm diameter circular pillars; (D) 2 mm wide ridges separated by 2 mm wide channels. From reference [102].	12
Figure 1.4 Example of a grafted polymer system, showing formation via both “grafting-to” to and “grafting-from” methods [175].	20
Figure 1.5 Illustration showing PEG chains in mushroom and brush configurations [186] where D = distance, R_F = Flory radius (radius of gyration).	22
Figure 1.6 Example of a self-assembled monolayer coating. Reprinted with permission from [197].	24
Figure 1.7 Example of a branched polymer coating [211].	26
Figure 1.8 Example of poly-zwitterionic Coating for anti-fouling. Adapted with permission from [234]. Copyright (2012) American Chemical Society.	29
Figure 2.1 The approximate time and length scales involved in different classes of molecular simulations: Quantum Mechanical (QM), Atomistic, Coarse-Grained (CG), and Continuum models. [243]	34
Figure 2.2 An example of Martini mapping (large blue circles represent martini bead) for selected molecules: (A) Standard water particle representing four water molecules. (B) Polarizable water molecule with embedded charges. (C) DMPC lipid. (D) Polysaccharide	

fragment. (E) Peptide. (F) DNA fragment. (G) Polystyrene fragment. (H) Fullerene molecule. In all cases Martini CG beads are shown as cyan transparent beads overlaying the atomistic structure [244]......35

Figure 2.3 Potential energy expressions, showing both bonded and non-bonded interactions and equations. Reprinted from *Advanced Drug Delivery Reviews*, 65(2), Rebecca Notman, Jamshed Anwar, “Insights from molecular simulation of model membranes”, 237-250, Copyright (2013), with permission from Elsevier.....37

Figure 2.4 A two-dimensional illustration of periodic boundary conditions. Sourced from <<http://isaacs.sourceforge.net/phys/psc.html>> on 11/01/201845

Figure 2.5 Example of a free-energy landscape for a system. There are several local minima states (1-6), before the system is finally in the global energy minimum (7).50

Figure 3.1 Schematic representation of the interfacial force field (IFF) method applied to a peptide adsorption simulation. The solution and solid surface phases are modelled by force fields that accurately represent their respective intra-phase interactions while interactions between atoms of the solution phase with the solid phase are represented by an interfacial force field parameter set that is tuned to accurately represent peptide adsorption free energy [273]......52

Figure 3.2 generic peptide adsorption mechanism proposed by Penna and Biggs [118]. This mechanism is composed of three phases: (1) biased diffusion of the peptide from the bulk phase toward the surface; (2) anchoring of the peptide to the water/solid interface via interaction of a hydrophilic group with the water adjacent to the surface or a strongly interacting hydrophobic group with the surface; and (3) lockdown of the peptide on the surface via a slow, stepwise and largely sequential adsorption of its residues. WL = water layer.....57

Figure 4.1 Typical model setup highlighting dehydration (W(a)→V(b) transition) and hydration (V(b) →W(c) transition) of PEGylated substrates. Colour codes: white-hydrogen, grey-carbon, red-oxygen and yellow-silicon.	65
Figure 4.2 Change in PEG height (Δh) during de-swelling as a function of coverage density for PEG5 grafted substrates simulated at 298 K. Error bars represent the standard deviation.....	67
Figure 4.3 Radius of gyration profiles for PEG in the lateral (x-y) plane as a function of (z) for PEGylated silica in water (a) and vacuum (b) and PEGylated polyester in water (c) and vacuum (d). Simulations were at 298 K for low, intermediate and high coverage densities.....	68
Figure 4.4 Change in PEG height (Δh) during the W→V transition as a function of coverage density for (a) SiOH- σ PEG5 and (b) SiOH- σ PEG8 systems simulated at 298 K and 370 K. Error bars represent the standard deviation.....	69
Figure 4.5 Radius of gyration profiles for PEG in the lateral (x-y) plane as a function of (z) for PEGylated silica during de-swelling at (a) 370 K and (b) 298 K for low, intermediate and high coverage densities.	69
Figure 4.6 Average number of inter-molecular H-bonds per PEG between available donor-acceptor pairs in PEG and water as a function of coverage density for SiOH- σ PEG8 systems simulated at 298 K and 370 K.	70
Figure 4.7 Change in PEG height (Δh) during swelling as a function of coverage density for PEG5 grafted substrates simulated at 298 K. Error bars represent the standard deviation.....	71
Figure 4.8 Atomic density profiles of $\sigma = 0.40$ pentamer PEGylated silica systems at 298K (a) before and (b) after dehydration.	71

Figure 4.9 Average number of intermolecular hydrogen bonds between PEG and water before and after dehydration of pentamer silica systems.72

Figure 4.10 Snapshots of the three types of hydrogen bonding networks formed. (a) intra-molecular hydrogen bonding between PEG repeat units (b) intra-molecular hydrogen bonding of water to PEG, encouraging the trans-trans-gauche conformational adoption as suggested by Gaub *et al.* [346]. (c) inter-molecular hydrogen bonding of water.72

Figure 4.11 Atomic density profiles of PEGylated silica (a-c) and polyester (d-f) at low (a and d), intermediate (b and e) and high (c and f) coverage densities. PEGylated with PEG5 chains and simulated in vacuum at 298 K.75

Figure 5.1 Schematic of PEG and water molecules for density plots in Figure 5.2. Colours: Silica (orange), PEG primer (black) and sweeping (grey) layers, surface-bound water (green), bulk water (dark blue). Water within 3.5 Å of the polymer layer is separated into H-bond donor (yellow), acceptor (red) or no H-bond (light blue).83

Figure 5.2 Z (left) and X-Y (right) profile of (A) Low PMeOx, (B) High PMeOx, (C) Low PEG, (D) High PEG. For Z profiles, density is normalised such that a value of 1 is the heavy atom density of bulk water. Colours represent silica (orange), polymer (grey), surface-bound water (green), bulk water (dark blue). Water within 3.5 Å of the polymer layer is separated into H-bond donor (yellow), acceptor (red) or no H-bond (light blue). For PEG systems, the polymer layer is broken into primer (black) and sweeping (grey) layers. For X-Y profiles, blue = hydrophobic segments of chains (CH₂, CH₃), red = hydrophilic segments (O, N, OH, NH) and gold = the exposed substrate.84

Figure 5.3 Chain z-length distribution plots for all systems at (A) Low, (B) Medium and (C) High grafting densities. Colours: PEG (black), PMeOx (green), PEtOx (blue) and PPrOx (red).86

Figure 5.4 Distribution of PEG conformations for low (black), medium (red) and high (blue) grafting densities.	90
Figure 5.5 Average RMSD of chains: PEG (black), PMeOx (green), PEtOx (blue) and PPrOx (red) at low (solid) medium (dotted) and high (dash) coverage densities.....	97
Figure 5.6 RMSD of PEG chains separated into sweeping (solid) and primer (dotted) layers at low (black), medium (red) and high (blue) grafting densities.....	98
Figure 5.7 Average dipole moment of water calculated with respect to the Z-axis (001 plane). The dipole angle for water in the first water layer is shown for low (black) medium (blue) and high (red) grafting densities, as well as bulk water (grey) for PEG (A), PMeOX (B), PEtOX (C), and PPrOX (D) systems.....	102
Figure 5.8 MSD (a) and decay profile (b) of water molecules in the first water layer for PMeOx (green) and PEG (black) at low (solid) and medium (dashed) grafting densities.	104
Figure 6.1 Snapshots of the four different initial orientations (A,B,C,D) of EAS hydrophobin with respect to the silica surface. The protein is positioned approximately 9 Å from the surface.	112
Figure 6.2 Distance between the centre of mass of residues and the average height of the surface hydroxyl groups for systems that adsorbed (A) through the Cys3-Cys4 loop (Residues 19 to 45, Binding Motif 1) and (B) with the Cys3-Cys4 loop in bulk water (Binding Motif 2). (C) Distance between the centre of mass of residues and the average profile of the air-water interface. Different colours represent the initial protein orientation as shown in Figure 6.1. In Binding Motif 1, black and green colours were from orientation (A), red from orientation (D). In Binding Motif 2, red was from orientation (D) again, and black was from orientation (C).....	114

Figure 6.3 Average number of contacts with the surface for EAS over the last 10 ns of simulation in binding motif (A) 1 and (B) 2. Colours are matched to the residue-surface distance plots in Figure 6.2 and represent different simulation runs. Heavy atoms of a given residue are considered in contact with the surface if they fall within 4.5 Å of any surface atom.....117

Figure 6.4 Snapshots of EAS hydrophobin conformations (A) in bulk water, (B) at the surface-water interface when adsorbed through the Cys3-Cys4 loop (Binding Motif 1) and (C) at the surface-water interface with the Cys3-Cys4 loop in bulk (Binding Motif 2). Yellow arrows represent β -sheet structuring. The amyloidogenic region (F72-I75) is shown in purple and the Cys3-Cys4 loop shown in green.....118

Figure 6.5 Snapshots of EAS hydrophobin conformations highlighting hydrogen bonding between (A) residues Asn79 and Lys62, Ala77 and Ala41, resulting in a helical formation, (B) histogram showing the separation distance of residues Ala77 and Ala41 in system where Cys7-8 loop remains folded and (C) residues Asn79 and Lys62, Asn76 and Lys62, encouraging the formation of the β -hairpin (D) histogram showing the separation distance of residues Ala77 and Ala41 in the system where Cys7-8 loop unfolds over time. 120

Figure 6.6 Histograms showing the distribution of water dipoles around the surface with no protein (red) and with protein (blue) for water trapped between the surface and residues (A) Gln20 and (B) Asp38123

Figure 6.7 Snapshots of hydrophobicity for EAS in (A) Binding Motif 1 and (B) Binding Motif 2, as seen by the silica surface and (C) at the air-water interface from top view and (D) side view showing the interface boundary (air layer is above water molecules, water molecules below have been hidden for clarity). Blue and red colors represent hydrophobic and hydrophilic regions respectively.125

Figure 6.8 Mean squared displacement (MSD) plots of: (A) water molecules at the, air-water, bulk water and surface-water interface; both with and without the presence of EAS hydrophobin. (B) lateral MSD of the protein at the air-water interface, in bulk solution, and in both binding motifs at the surface-water interface.	128
Figure 7.9 Exemplar temporal behaviour of the protein above low PEG chains (black); height of minimum of the protein (blue); and maximum (red).	138
Figure 7.10 Average contact area of EAS at the solid/liquid interfaces of the adsorbed runs. The errors associated with the averages are the standard deviations across all such runs and do not consider fluctuations within individual runs.	139
Figure 7.11 RMSD of chains for adsorbed runs for chains in contact (within 5Å) with EAS. Colours: PMeOx (green), PEtOx (blue) and PEG (black), and the RMSD of chains in a solvent environment: PMeOx (dark green), PEtOx (dark blue) and PEG (grey) at low (solid) and medium (dotted) grafting densities.	142
Figure 7.12 Probability for residues of EAS coming in contact with PEG/POX surfaces.	145

Abstract

This thesis employs atomistic level modelling to investigate behaviour of surfaces protected through functionalisation with short organic ligands, and their interaction with protein contaminants. A detailed description of the motivation for this project, a detailed literature review on the biofouling process, strategies to prevent biofouling and anti-fouling theory are presented in Chapter 1.

Classical Molecular Dynamics (MD) techniques are employed to describe the behaviour of our functionalised surfaces in aqueous environments, and the physical interactions with our protein contaminant, EAS hydrophobin. A detailed description of these computational techniques is included in Chapter 2.

In Chapter 3, we outline the challenges and limitations of molecular modelling techniques, followed by a detailed background in the development and validation of silica and polyester substrates that have been used in this study. We have also included a detailed description of the computational surface models and surface functionalisation process.

In order to tailor surfaces for specific applications, the underlying molecular mechanism that enables a functionalised surface to change properties in response to an external trigger must be understood. In Chapter 4 we investigate de-swelling and swelling of some of the most commonly used responsive materials, poly(ethylene glycol) (PEG) functionalised silica and polymer surfaces, as a function of hydration and temperature. We also investigate the difference between the hard (silica) and soft (polyester) substrates, and PEG grafting density on responsive behaviour. We show that enhancement of the surface hardness must be considered when designing responsive surfaces for solution based applications, such as antimicrobial coatings for interchangeable wet/dry environments and biomedicine.

In Chapter 5, we compare the hydration and chain dynamics of PEG and poly(2-oxazoline) (POX) modified silica surfaces as a function of heterogeneity. We assess how chemistry and surface density of commonly used anti-fouling surface ligands affect the interfacial properties relevant to biofouling. We show how existing theories that attempt to explain underlying molecular mechanisms of biofilm formation and its attenuation are not consistent with experiments, and detail findings that can be exploited in the rational design of biofouling resistant surfaces for industrial and biomedical applications.

To better understand our protein contaminant, EAS hydrophobin, we study the initial stages of monomeric EAS hydrophobin's spontaneous adsorption on fully hydroxylated silica. Presented in Chapter 6, a series of MD simulations are undertaken with EAS in solvent only, and also positioned above the silica surface, enabling us to gain a better understanding of EAS' behaviour in solvent phase, and at interfaces. This allows us to explore the anti-fouling efficacy of PEG and POX surface coatings.

Combining the detailed knowledge of our surfaces, and the protein, in Chapter 7 we look to elucidate whether entropic barriers associated with surface mobility or those from interfacial water have greater contributions to anti-fouling efficacy. To do this, we simulate the initial stages of the spontaneous adsorption of monomeric EAS hydrophobin on PEG and POX functionalised silica surfaces. From the knowledge gained, we have developed several updated design principles and an updated understanding of anti-fouling surfaces, which we summarise in Chapter 8. Several ideas for continuation of research in anti-fouling surfaces is then presented in the Future Work section.

Chapter 1

1. Introduction/Literature Review:

1.1. Overview

In this Chapter, we present a detailed overview of the current understanding of biofouling, and highlight the need for further research in the field of self-cleaning coatings. First we outline the background and motivation for the work included in this thesis, followed by a detailed literature review on the biofouling process, focusing on the initial and irreversible protein attachment stages. We then detail the importance and current understanding of EAS Hydrophobin, the protein contaminant studied in this thesis.

In section 1.6 we discuss the theories pertaining to the repellence of foulants, including the effects of surface morphology, chemistry and heterogeneity, and how they can be tailored to prevent microbial fouling. Following this, the current theories of what makes effective anti-fouling coatings are described, followed by a detailed review in the experimental and computational studies on currently used anti-fouling coatings.

1.2. Background and Motivation

Nonspecific adsorption of proteins and other foulants is a very problematic and expensive issue, with governments and industry spending billions of dollars annually combating the effects of biofouling. Surfaces that have the potential to maintain their clean state by resisting the non-specific binding of proteins and other foulants are sought after in many applications, ranging from biomedical and bionic devices [1-3] to large-scale industrial coatings [4, 5] where significant efforts have been targeted towards solving issues of surface discolouration and degradation; some of the major complications affecting the life-span of the coatings. Despite experimental studies dating back to the 1960s [6] there is not yet a detailed understanding of the mechanisms through which proteins adsorb or are repelled at a various solid/liquid interface [7, 8].

For the past few decades, silicates and other oxides have been used as mineral binding agents for industrial paint coatings. Combined with the prominence of significant advances in prosthetics and biomedical technologies, understanding and improving the potentially toxic or anti-fouling behaviour of these materials and their environment is crucial. It is important to note that there are significant studies on aluminium oxide [9-14], titanium oxide [15-20] and clay surfaces [21-29], however, this study will focus on the more industrially relevant silica. In this section, we will give a brief outline of the silica surface model development and applications for anti-fouling studies. For more detail on silica, an excellent review was published by Rimola *et al.* [30].

Mineral paints containing colloidal silica came into existence in the 19th century, as the paints are able to permanently bond to the substrate material, resulting in a highly durable connection between paint and substrate. These coatings are naturally porous, promoting significant water adsorption, aiding the functionality and durability in cool climates.

However, in tropical environments these coatings have been seen to undergo significant discolouration and degradation due to fouling. To understand this phenomenon at the molecular level, many studies have implemented MD and other computational techniques to understand what is happening with these surfaces at the atomistic scale.

Whilst several techniques like X-ray diffraction and nuclear magnetic resonance can be used to study proteins in solution, the resolution of these techniques is insufficient to detail the structure and dynamics of proteins at interfaces [31]. In addition, there is significant neglect in current publications on the surface density of grafted chains [32], a critical property in prominent anti-fouling theories [33-35]. This lack of understanding limits the capacity to design and produce sophisticated coatings which can control protein adsorption [4]. Although the list of experimental techniques is ever growing, there is still a significant deficiency in the resolution that cannot be addressed through experimental techniques. With significant advances in the performance of computational hardware, computational methods are becoming significantly more popular and viable as an insight into the atomistic scale processes [36].

1.3. Biofouling Process

Fouling of surfaces through both organic and inorganic contaminants has been a major issue for millennia. Throughout history, as our understanding of the fouling process grew, so too did the complexity of coatings, as we progress from waxes and tars to metals, paints and a combination of materials [37]. However, even today, fouling of surfaces presents a significant challenge to a variety of industries from biomedical [38-40] to industrial [41, 42] and marine [43, 44] applications. Long-term exposure of surfaces to extreme climatic and polluting conditions allows not only discolouring and degradation of the top-most surface layer, but also subjects the surface to bacteria and fungi suspended in the atmosphere that are deposited on the surface by wind and rain. These microbes attach, grow and reproduce in a self-reproducing process known as biofouling. Herein we detail the interactions and stages of biofouling, as outlined in Figure 1.1.

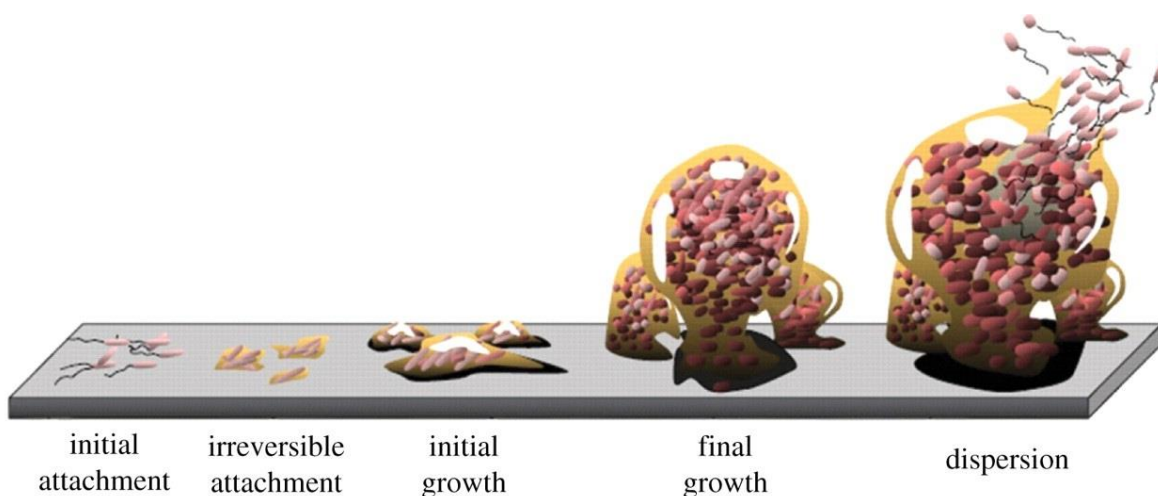


Figure 1.1 Overview of the anti-fouling process. Only the initial attachment stage of biofouling is a reversible procedure [45].

1.3.1. Initial and Irreversible Attachment

Surfaces exposed to the atmosphere will generally undergo direct interactions with nearby water, resulting in a layer of structured water orientated a particular way depending on the surface chemistry and charge [46]. This sub-nanosecond orientation process results in

structured water layers above the surface [47], called the interfacial water layer. The interfacial layer is known to have significant effects on a contaminant, which is detailed later in this thesis (Section 1.6).

In the atmosphere, bacteria and fungi exist in highly resistant, dormant structures with little metabolic activity called spores. Whilst most spores are non-toxic, they can survive in low-nutrient environments, and are resistant to most anti-biotics and disinfectants [48] rendering them hard to eliminate, and able to survive in extreme climatic conditions. When spores are deposited on a nutrient rich surface, a transformation occurs, beginning the biofouling process [49]. These spores release small organic molecules like proteins with the purpose of conditioning the outer layer such that it supports further microbial growth.

These proteins are usually secreted as monomers (particularly fungal species), and adsorb in a conformation strongly influenced by both the physical and chemical properties of the surface [50], and the interfacial water structure [51]. As more proteins adsorb to the surface, they begin to cluster and consequently undergo some type of unfolding or changes in protein secondary structure which allows the interaction and formation of a layer of proteins [52, 53], significantly altering the surface chemistry and reducing surface tension [54].

1.3.2. Initial Growth

This conditioned layer now presents a surface ideal for larger microbes, including bacteria or fungal spores, which adsorb on the surface in a matter of hours. The adsorbed microbes then undergo a series of phenotypic changes, one of which results in the excretion of an extracellular polysaccharide (EPS) coating [55]. This coating connects the various types of bacteria or spores to the surface in a layer called a biofilm. Once formed, this layer is not easily removed, needing significant toxic chemicals/acids or mechanical treatment to remove. This creates a significant problem for many industries, as the biofilms are often only in the

order of tens to hundreds of micrometres thick, and therefore not easily visible to the naked eye. This is a significant issue to marine industries in particular, as the penalty of these coatings result in as much as a 15% increased fuel consumption [56], due to hydrodynamic drag, not to mention the difficulties and costs involved in removing a vessel from the water to clean.

1.3.3. Final Growth and Dispersion

If the biofilm layer is left untreated, this will allow for even further fouling, in which a macroscopic layer can be formed where algae, barnacles, and other large organisms attach. Although many of these are more of an aesthetic and economic nuisance, there are added environmental and health implications particularly associated with algae. As large densities of algae around marine structures and vessels begin to decompose, they consume significant amounts of dissolved oxygen, can produce potent toxins or can contain physical attributes which can damage fish gills [57]. Furthermore, for industrial paint coatings, this fouling process significantly reduces the life-span of coatings. Macroscopic colonies are then able to release new spores and other microbes in the atmosphere, which then colonize new sites and present as health risks when inhaled, as they often go unnoticed by the immune system until they change from a dormant to active state [49].

1.4. EAS Hydrophobin

In this thesis, we have studied the protein EAS hydrophobin, which is known to be involved in the fungal biofouling process. Unique to filamentous fungi, hydrophobins are a family of small proteins that fulfil a broad spectrum of functions in fungal growth and development. As summarised in Figure 1.2, some of these include: (i) Protective roles, forming monolayers on the outside of spores and hyphae, protecting them and allowing them to grow in otherwise unsuitable conditions [58-61]; (ii) Immunogenic stealth properties,

where a hydrophobin rodlet monolayer covers the spore surface, imparts immunological inertness to the spores, thus preventing the activation of host immune system, inflammation, and tissue damage [62-65]; and most relevant to this thesis, (iii) dual functionality in both protecting, and facilitating the adhesion of fungi to surfaces [66]. Hydrophobins are secreted by fungi in monomeric form, and possess the ability to spontaneously adsorb into stable amphipathic monolayers upon reaching an interface. These monolayers significantly alter the surface environment, reducing surface tension [67] and altering the wettability [68] of both hydrophobic and hydrophilic surfaces, conditioning them for further fungal adhesion including the production of hyphae [69-71].

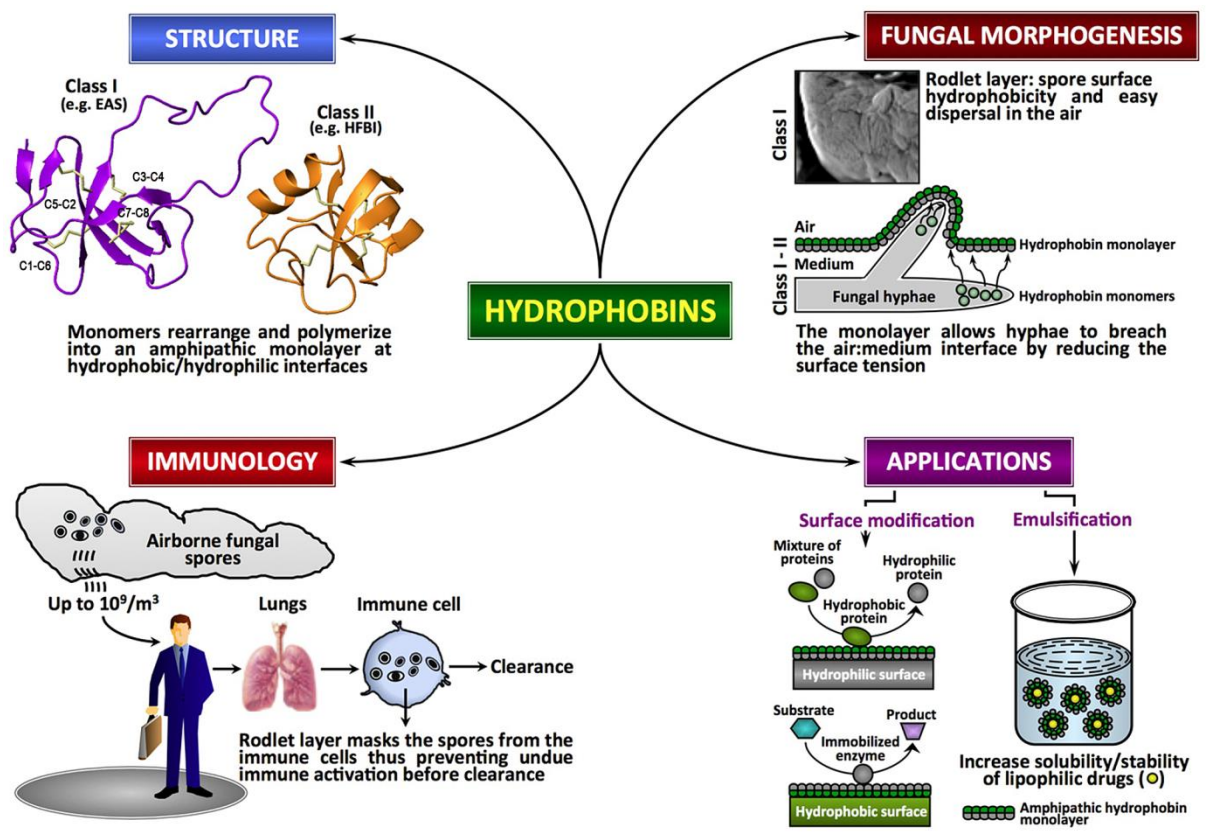


Figure 1.2 An overview of the structure, function and applications of hydrophobins [72].

There are two classes of hydrophobins based on the aggregates they form. Class I hydrophobins assemble into ordered rodlets with an amyloid-like structure that is incredibly

robust, requiring strong acids to dissolve [51]. Class II hydrophobins are significantly less robust, dissolving in detergent and alcohol solutions, and lack well-defined rodlet morphology [54, 73, 74].

Although the self-assembly of hydrophobins is still being studied for greater clarity, it is well established that adsorption at interfaces is accompanied by conformational changes in the protein secondary structure. At the water-air interface, class I hydrophobins attain more β -sheet structure (called the β -sheet state), while at the interface between water and a hydrophobic solid, a form with increased α -helix is observed (the α -helical state) [75]. The α -helical state seems to be an intermediate of self-assembly, whereas the β -sheet state is the stable end-form.

Because of their greater difficulty in removal, current focus in literature, and relevance to fungal biofouling, the focus of this thesis is the Class I hydrophobin EAS, found in the fungus *Neurospora Crassa* [76]. Like all class I hydrophobins, EAS has a β -core region, comprising three sets of anti-parallel β -sheets, with the overall structure maintained through four disulfide bonds [76] and four flexible and unstructured loops that make up the protein surface. The largest of the loops, Cys3-Cys4, while largely hydrophobic, shows highly amphipathic regions with alternating hydrophobic and hydrophilic residues. The Cys7-Cys8 loop contains a large number of polar residues, with a large hydrophobic section between F72-N79. Recent studies have identified several key regions for EAS. The flexible, intrinsically disordered Cys3-Cys4 loop is believed to prevent the protein aggregation in bulk solution [77, 78]. Although not required for monolayer formation [79], at the air-water interface the Cys3-Cys4 loop was theoretically shown to stabilize into surfactant-like conformations. Also of interest is the Cys7-Cys8 loop, specifically residues F72-I75, believed to be the amyloidogenic region responsible for rodlet formation [80].

1.5. Combating Biofilm formation

Methods to combat biofouling through the design of protective surface coatings can be found as early as 700BC [11] when Phoenicians and Carthaginians used waxes, tars and other materials to extend the life of vessels. Millennia later, thanks to a greater understanding of the biofouling process, the efficacy and versatility of coatings has increased significantly [37, 81]. These coatings largely fall into two categories: bio-active coatings, which aim to kill contaminants either on contact or through biocide release; and bio-passive coatings, which look to prevent protein attachment, rather than having toxic effects on contaminants. Details on these coatings can be found in a recent review [5].

In recent years there has been a large push towards biopassive coatings, mostly due to the environmental impact of some bioactive coatings. Perhaps the most significant example of this is the marine industry, where it was shown that low concentrations of tributyltin (TBT), used in anti-fouling coatings estimated to cover about 70% of the present world's fleets [82], caused defective shell growth in the oyster *Crassostrea gigas* and imposex in the dog-whelk *Nucella sp.* at concentrations as low as 1-20ng/l [83, 84]. Following an International Convention held on 5 October 2001, a significant ban was made to the application of tributyltin (TBT) [82].

Although current biopassive coatings are still not 100% effective, significant research has been undertaken to understand the interaction of microbes with surfaces, and how best to combat the initial attachment of proteins so that biofilm formation can be avoided. There now exist several design strategies for anti-fouling coatings, detailed below.

1.6. Strategies for anti-fouling coating design

To date, several strategies have been employed to combat surface fouling. Like many technologies, the inspiration for these modifications comes from natural sources. To prevent the undesired protein adsorption in both biomedical and industrial contexts, there is a large focus on the various avenues of achieving surface heterogeneity. These surfaces can be separated into 3 themes: surfaces with altered chemistry which possess both hydrophobic and hydrophilic domains; surface topography, where surfaces feature random geometries of different length and size scales; and heterogeneous surfaces, that combine the effects of both surfaces.

1.6.1. Surface Chemistry effects

It is well known that both morphology and chemistry [85, 86] have significant influences on the adsorption of proteins on surfaces, both of which can be manipulated through functionalisation of either extended surfaces or nanoparticles. As highlighted earlier, due to the vast differences in environments and industries in which biofouling is present; there are several examples of technologically relevant substrates that have been used for such applications, including metals, [87, 88] polymers [89, 90] and oxides like silica [91, 92]. Proteins are generally believed to interact stronger with hydrophobic surfaces [7, 93], however this should not necessarily be used as a metric to adsorbed proteins, as it has been shown that hydrophilic surfaces only allow limited surface-induced conformational changes, typically resulting in weaker adherence [94], and hence generally have a lower interaction energy.

Significant limitations in these coating technologies arise due to our limited understanding of the interactions and behaviour of microbes at interfaces. Experimental research has shown that the hydrophobicity of surfaces has significant effects on adhesion,

with hydrophobic substrates generally incurring increased amounts of microbial adhesion in terms of increased numbers of attached cells, rates of attachment and binding strengths [89, 95, 96]. Conversely, hydrophilic surfaces that are highly hydrated have been shown to be more resistant to adhesion [95, 97]. This has been attributed to their ability to adsorb more water, which must be displaced before adhesion can occur [86, 98], as well as limiting the amount of conformational rearrangement a protein will undergo [94].

1.6.2. Topographical/Surface Roughness effects

The influence of engineered topographies and surface roughness has been summarised experimentally in several review articles [42, 98-101]. In these works, several methods of creating textured surfaces are noted, with prominent methods being etching, electron-beam lithography, and self-assembly/grafting of tethered ligands (Section 1.9.1). Regardless of the method, these techniques aim to design highly reproducible nanoscale features, with unique and coherent structures over large areas, called nanopatterning. Such an example exists in a study by Schumacher *et al.* [102] where PDMS surfaces were patterned using photolithographic techniques into a variety of shapes and domain sizes (Figure 1.3).

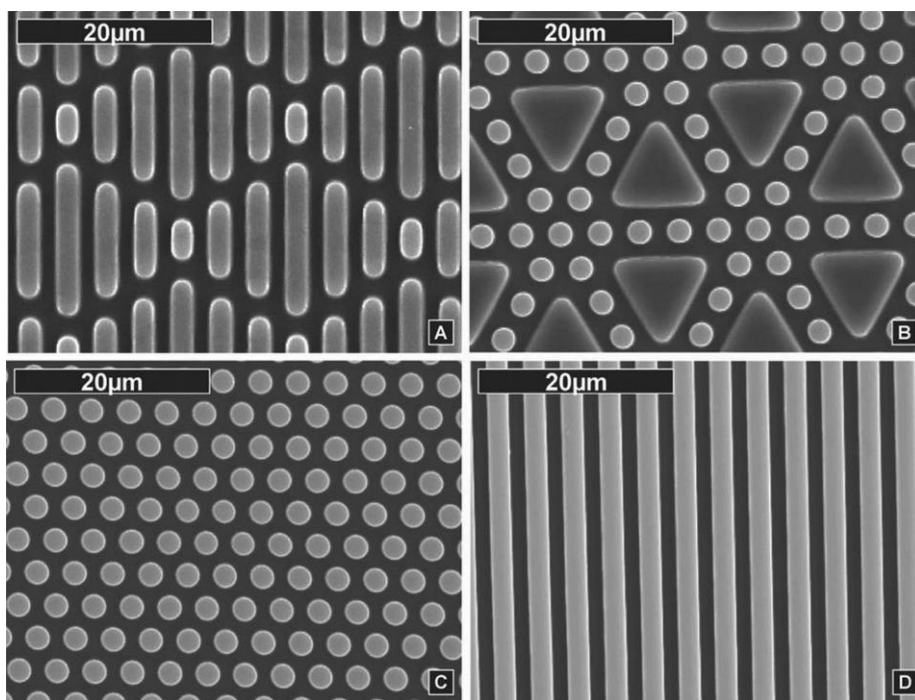


Figure 1.3 SEM images of engineered topographies on a PDMS surface. (A) 2 mm ribs of lengths 4, 8, 12, and 16 mm combined to create the Sharklet AFTM; (B) 10 mm equilateral triangles combined with 2 mm diameter circular pillars; (C) hexagonally packed 2 mm diameter circular pillars; (D) 2 mm wide ridges separated by 2 mm wide channels. From reference [102].

With constant surface chemistry across all surfaces, this paper examined the effect of various nanopatterns, and developed a quantifier for comparing surfaces with engineered topography; termed the engineered roughness index (ERI). By factoring in the tortuosity of surfaces, it is believed this ERI factor gives a better description of a surface's ability to resist contaminant settlement, with a larger ERI corresponding to more effective/resistant surfaces.

It should be noted that in this study, and others [41, 101, 103], the effect of feature size and spacing are noted to have significant effect on particle spacing. Generally speaking, these works follow the principle that: feature spacing should suffice to prevent contaminants from settling between features; feature size should not be larger than the contaminant, to prevent stabilisation on a single feature; finally, the number of attachment points should be minimised, by preventing contact with the channel between features.

1.6.3. Surface Heterogeneity

Nanostructured surfaces with alternating hydrophobic/hydrophilic characteristics has recently been shown to be able either to promote or to inhibit protein adsorption [104]. The phenomenon can potentially be exploited to design surfaces resistant to biofouling. In recent years with emergence of nanotechnology, an alternative approach to altering surface resistance to protein adsorption was proposed, including the manipulation of the nanoscale morphology of chemically identical materials [105, 106]. Nanopatterned surfaces of increasing morphological sophistication have been employed to study and exploit the interactions between nanostructured materials and biological systems [107]. More recently, research in controlling surface chemistry and topography has been achieved through the tethering of various polymers to surfaces. To date, several types of methods have been used, starting from grafting polymers with known anti-fouling properties like poly(ethylene glycol) (PEG), through to self-assembled monolayers (SAM's), lipid bi-layers, and more recently, poly-zwitterionic surfaces. These coatings will be discussed in detail in Chapter 3, detailed strategies for these techniques can be found in several reviews [5, 108-110].

An example of such protein resistant materials are monolayer protected nanostructured surfaces [106]. Two component ligand mixtures form monolayers of striped domains on the surface of nanoparticles through entropy driven self-assembly [111, 112] with the length scales of the domains being 1-2 nm. These nanoparticle surfaces exhibit low protein binding despite having a substantial hydrophobic component [106, 113] and, counter intuitively, show increased protein adsorption with increased fraction of the hydrophilic functional chains [104]. While the mechanism of this uncorrelated binding affinity remains unclear the adsorption behaviour of proteins has been shown to be significantly influenced by the nano-scale patterning [104, 114]. Amphipathic amino acid residues on the protein surface have been shown to drive the adsorption on domain separated nanoparticles due to their

inherent ability to interact with both the hydrophobic and hydrophilic domains but most importantly, with the domain boundaries [104]. It has been proposed that surfaces can be functionalised to create a functional and morphological heterogeneity (nano-pattern) that will either facilitate or prevent protein adsorption by matching or mismatching the protein surface functionality [114].

1.7. Interactions and involvement of water

In recent years, there has been significant research into the behaviour of interfacial water, and the critical role it plays in protein adhesion [95, 115]. At the surface-water interface, water has been seen to form two distinct "shells" which have significantly different properties to that of bulk water. The first shell is highly ordered and tightly bound, as water molecules form hydrogen bonds with the surface. A second layer is subsequently formed through hydrogen bonding with neighbouring water molecules, resulting in a weakly-ordered region. However, in areas with significant spacing between hydroxyl groups or high surface roughness, this interfacial layer often creates areas void of water, encouraging the adsorption of hydrophobic molecules [116, 117]. It has been observed that the specific ordering of these shells plays a pivotal role in the promotion or retardation for the adsorption of proteins and other contaminants. Specifically, as a protein approaches the surface, interfacial water layer undergoes structural changes which will help repel or promote adsorption of the protein [9, 118]. These hydration forces have mainly been attributed to the surface heterogeneity, orientation and local density of interfacial water [119]. This has inspired significant research into the behaviour of interfacial water as a protein comes toward a surface, and strategies that can be adopted to prevent protein adsorption [114, 120-122].

Some of the prominent work in this field is based on work by Argyris on the characterisation of interfacial water around oxide and graphite surfaces [10, 123-126]. These

studies noted the effect of surface hydroxylation, and how tailoring the surface orientation, or density of hydroxyls could be used to dictate amount of water molecules in the first interfacial layer, as well as the distance between the first adsorbed layer and the substrate [126]. Furthermore, when considering more realistic solvents with ions in solution, it was noted that negatively charged chloride ions adsorb to the surface, whilst positively charged sodium ions would adsorb to 2nd water layer and heavy metal ions like caesium remain in bulk solution [125, 127]. The repulsive force attributed to these interfacial water layers was then measured using MD simulations. In this proof-of-concept study, a carbon nanotube model was used to probe interfacial water, with the repulsive force as a function of distance from the surface being measured [9]. It was noted that the nature of this repulsion is due to the structure and orientation of the water, and changes in surface termination had significant effects on this force. However, perhaps more importantly, the paper explains the need for combined experimental works, showing how AFM studies could be used to facilitate modellers in understanding the effect of surface heterogeneity and functionalisation.

Water behaviour at the hydrophobic/hydrophilic interface proposed by Granick *et al.* [128-131] suggests that the interplay of water at a hydrophobic/hydrophilic interface will result in the formation of a flickering vapour phase where water molecules are unable to structure in accordance to either surface. These water molecules are believed to diffuse through several favourable metastable energy states, with varied stability time and frequency of contact with the surface. Due to the size and instability of these water layers, there is little to no ability for water molecules to form ordered hydration shells around a homogeneous surface.

1.8. Current theories on Anti-fouling coatings

Over the last decade, significant research efforts have focused on finding anti-fouling surface coatings with good efficacy, novelty, and design simplicity. However, the ability to design more effective anti-fouling coatings is limited by the paucity of fundamental knowledge on how these surfaces behave at a molecular level. Existing theories that attempt to explain anti-fouling coating efficacy are dated (late 90s and early 2000s) and are often conflicting. This has arisen because of the difficulty of studying these three phase systems at the molecular level using experimental techniques [31], hampering rational design and development of more effective coatings [4], and vital experimental validation of molecular level theories and simulations.

The “gold standard” archetypal material for preventing surface fouling is grafted poly (ethylene glycol) (PEG) chains. PEG displays a valuable ability to change conformation in response to various stimuli [132] assisting in excluding foreign materials such as proteins from a surface [133, 134]. The efficacy of PEG coatings has been linked to its relative biological inertness and compatibility with water. To date, no theory adequately explains how PEG coatings resist protein attachment in terms of the chain length and grafting densities that have been employed in recent experimental studies [135]. The existing theories suggest two types of molecular interactions being responsible for anti-fouling properties of polymer coatings, namely steric repulsion and hydration theories, described below.

1.8.1. Steric repulsion theories

Some of the earliest and enduring theories on PEG’s anti-fouling properties were reported by Andrade’s group [136-139]. They suggested that the anti-fouling ability of PEG was due to steric repulsion of the chains, while that of polyethylene oxide (PEO) was due to a combination of mobility and excluded volume effects that also generated steric repulsion.

This theory treated solvated PEO chains as random coils having a high mobility and excluded volume, while proteins were described by hard spheres. As a protein or other contaminant adsorbs to a surface, the polymer chains are compressed to a thermodynamically unfavourable state, resulting in the exclusion of water molecules hydrogen-bonded to the layer, and a strong van der Waals repulsive force. This theory suggests that the anti-fouling efficacy of surfaces should increase with the chain length and grafting density of the PEG chains. While several experimental studies have supported the theory [140-143], a number of other studies have shown anti-fouling efficacy in low molecular weight PEG coatings [144-147] in conflict with the theoretical predictions. Szleifer *et al.* utilized single-chain mean-field (SCMF) theory [33-35] to reconcile the anti-fouling behaviour of short PEG chains and self-assembled monolayers (SAMs). The polymer-protein-solvent system is taken to be inhomogeneous perpendicular to the grafting surface, and potentials of mean force of the protein with the surface can be calculated relative to grafting density and degree of protein adsorption. The protein is modelled as spherical, and the protein-polymer, protein-solvent, and polymer-solvent attractive interactions are all assumed to be equal. Interactions determining the structure of the system are purely repulsive. This theory rationalizes the anti-fouling ability of hydroxy terminated SAMs, and suggests that grafting density rather than chain length is more important for anti-fouling efficacy.

Grunze *et al.* described the conformational behaviour of PEG systems and its contribution to anti-fouling efficacy [148-150]. In particular, they investigated the conformational behaviour of PEO/PEG SAMs on gold and silver surfaces [148]. On silver, the polymer layer adopted a densely packed all-trans conformation, resulting in enhanced protein adsorption. In contrast, on gold surfaces, PEG adopted helical conformations with reduced protein adsorption. Subsequent Monte-Carlo studies [151, 152] suggested that lower protein attachment was due to the helical chain interacting with larger amounts of water.

Similar conclusions were reported more recently by Unsworth *et al.* [153-155], who focused on the effect of grafting density, chain length, and end-group hydrophobicity on fouling. They concluded that, regardless of chain length, maximum anti-fouling effectiveness occurred at a grafting density of 0.5 chains/nm², corresponding to chains in a brush-like regime [153]. At higher grafting densities protein resistance begins to decrease, which Unsworth *et al.* attributed to a combination of loss of layer mobility and the formation of hydrophobic patches on the surface [155]. By studying methyl and hydroxy terminated PEO polymers they identified a third important factor, rearrangement of water molecules around the terminal groups, particularly at high grafting densities.

1.8.2. Hydration theories

Other hydration theories also incorporated the effect of interfacial water on protein resistance. Besseling [156] suggested that the interaction between two surfaces causes changes in the orientation of water molecules relative to disordered bulk water, with repulsion occurring when a hydrogen bond donor-acceptor mismatch occurs. Whitesides *et al.* [157, 158] elaborated this idea by investigating SAM surfaces with approximately 50 different functional groups. This study identified four important properties for nonfouling surface coatings: (i) not hydrophobic, (ii) contain hydrogen bond acceptors (iii) do not contain hydrogen bond donors and (iv) electrically neutral. It should be noted that several studies contradict the claim for universality of these criteria. For example, hydroxyl terminated oligo ethylene glycol (OEG) SAM surfaces [122, 159] and polysaccharides [160, 161] such as dextran [162, 163] have been shown to prevent protein adsorption despite containing hydrogen bond donors. More recently, Kitano *et al.* [164-167] investigated the structuring of water around poly-zwitterionic (PZI) surfaces. They argued that the well-documented anti-fouling properties of PZI are not due to the material itself, but result from PZI's effect on water structuring. Specifically, they proposed that surfaces which are able to

form strong interactions with interfacial water, whilst maintaining a disordered, bulk-like water layer, would provide limited entropic benefits for an approaching protein.

1.9. Surface Functionality and Roughness Topography

The effects of surface roughness and cavities have recently become major focus points in literature [99, 100, 104, 114, 117, 168]. In a recent experimental study by Scopelliti [169] it was noted that up to 90% reduction in protein binding affinity could be achieved by increasing nanoscale roughness from 15 to 30nm. In some cases, like those of the cicada wings, nanoscale roughness can in fact cause biocidal behaviour [170-173] to incoming bacterial contaminants. It has been observed that nanoscale surface roughness, combined with the significant spacing between hydroxyl groups on amorphous silica, form areas void of water in the interfacial layer, encouraging the adsorption of hydrophobic molecules [116, 117]. This has significant implications on the local density of interfacial water [119], and combined with hydration forces attributed to the surface heterogeneity and orientation, has a pivotal role in the adsorption of a protein as it approaches the surface. Studies have shown that the interfacial water layer undergoes structural changes which will help repel or promote adsorption of the protein [9, 118]. This has inspired significant research into the behaviour of interfacial water as a protein comes toward a surface, and strategies that can be adopted to prevent protein adsorption by tuning the surface roughness [98, 101, 104, 114, 174] or adding improved hydration properties through tethered moieties [95].

In sections 1.6 and 1.8 we outlined the strategies for anti-fouling designs, and how modern coatings have controlled surface chemistry and topography through the tethering of various polymers to surfaces. To date, several types of methods have been used, starting from grafting polymers with known anti-fouling properties like poly(ethylene glycol) (PEG), through to self-assembled monolayers (SAM's), lipid bi-layers, branched polymers like

poly(2-oxazoline) (POX) and more recently, poly-zwitterionic surfaces. These coatings will be discussed below, more information including other commonly used anti-fouling polymers and the formulation of these coatings can be found in some recent reviews [5, 108-110].

1.9.1. Linear systems

1.9.1.1. Grafted Systems

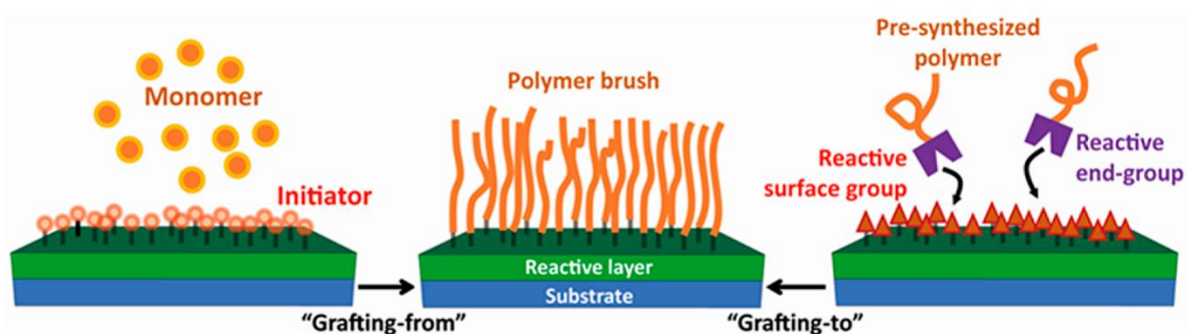


Figure 1.4 Example of a grafted polymer system, showing formation via both “grafting-to” and “grafting-from” methods [175].

Two strategies, the “graft-from” and “graft-to” methods (Figure 1.4), are generally used to covalently immobilize protein-resistant polymers. The “graft-from” approach, in which the polymer is synthesized in situ by polymerizing monomers from the surfaces, can be used to prepare high-density polymer brushes that often give better anti-fouling properties [176]. In the “graft-to” approach, the polymer is directly immobilized on the substrate by a surface coupling reaction. Typically, the polymer is derivatized with a functional group that can subsequently react with the substrate. Several antimicrobial polymers have been investigated for anti-fouling influence, as highlighted by several reviews [46, 177-180]. Due to the prevalence of PEG and poly(ethylene oxide) (PEO) in modelling work, a summary of relevant experimental studies on these polymers is detailed below.

For many years the gold standard of preventing surface biocontamination or other undesirable adhesion has been achieved through grafting of PEG chains. PEG displays a

unique ability to change conformation in response to various triggers [132] which in turn can assist in excluding foreign materials such as organic contaminants including proteins, from its proximity [133, 134]. Experimental work by Sheparovych *et al.* examined composite PEO - polydimethylsiloxane (PDMS) surfaces using AFM in both air and water environments to calculate adhesion between samples surface and AFM tip [181, 182]. The authors developed responsive mixed brush films with low adhesive properties in different media, where the mixed brushes display layer segregation in air and water. Major findings showed that in water PEO dominates the outer layer while in air PDMS dominates. Furthermore, the low interfacial energies of PEO in water and PDMS in air combine to generate a low adhesive property of the mixed PEO-PDMS brush in both media by the spontaneous rearrangement of polymer chains. Studies have shown that PEG molecules grafted onto metal substrates using surface-initiated polymerization reduce cell adhesion [183, 184]. This surface-initiated polymerization technique has the advantage of attaining a high grafting density and film thickness, factors which are considered important in controlling undesirable adhesion. Silanated PEG molecules have also been grafted onto glass substrates using solution-based techniques, again resulting in reduced cell adhesion [185]. These examples illustrate that PEG's unique ability to reject proteins and other contaminants combined with its non-toxic and anti-genetic properties is a justification of its extensive use as a surface protector for biomedical and industrial applications. Despite this, an understanding of its fundamental behaviour at the atomic level is still lacking.

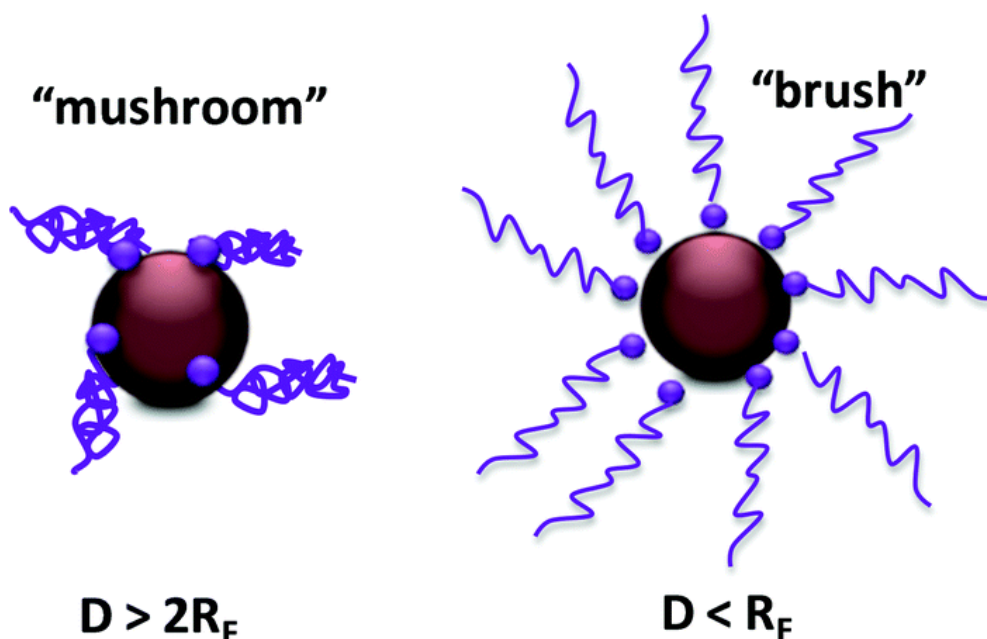


Figure 1.5 Illustration showing PEG chains in mushroom and brush configurations [186] where D = distance, R_F = Flory radius (radius of gyration).

It has been well documented that one of the key characteristics associated with PEG’s ability to reduce protein adhesion is its ability to adopt specific conformations in water (Figure 1.5). Importantly, it was identified that a flat or ‘pancake’ orientation of the PEG chains would likely result in an attractive PEG-Protein interaction, whereas mushroom-brush conformations were likely to provide repelling interactions [187, 188]. This was strongly related to the fact that compression of PEG chains was likely to increase the accessible surface area of the non-polar PEG segments, which encouraged hydrophobic interactions promoting protein adsorption [189]. This finding is strongly supported by other works which looked at the ability of PEGylated films to prevent microbial adsorption, where hydrophobic microbes had been shown to exhibit higher adherence than their hydrophilic counterparts [190].

At low grafting density, the end-to-end distances of PEGs are even smaller than the distances between the grafting points, thus the thickness of the PEG layer matches the size of mushroom. However, when the end-to-end distances of PEGs become larger than the

distances between the grafting points, PEG chains are crowded and thus extend like a brush, yielding the increased thickness of the PEG layer beyond the mushroom regime, which agrees with the Alexander–de Gennes theory [191]. However, it should be noted that the chain lengths and spacing between grafting points are such that the length of chains is larger than the chain separation distance. The relationship between the inter-chain separation distance and chain conformation has been reported previously, notably in work by Benková [192-194] where they noted a critical grafting density exists at 2.185 chains per nm², at chain lengths of 18-30 monomers, below which chains displayed strong interactions with the silica surface. In more recent work, described in this thesis, Ley *et al.* [195] investigated a range of grafting densities and chain lengths on both polyester and silica substrates to further describe this process. In this work, it was noted that at chain lengths sufficiently lower than the separation distance, chain-surface interactions were too strong to allow mushroom/brush conformations. These studies deduce two design concepts to allow mushroom/brush surfaces, increasing the coverage density of short chains or increasing the chain length, such that the length of the chains is longer than the separation distance of the chains. Unfortunately, with both approaches there are significant limitations for surfaces to be considered for anti-fouling applications.

Oelmeier *et al.* [196] applied MD simulations to investigate the hydration of single PEG molecules of variable length in explicitly simulated water. They note that as the chain length increases, the chain is more likely to adopt an increased helical structure, thereby reducing the solvent accessible surface area (SASA) of the chains. Unfortunately, the loss in hydrophilic SASA is much higher than the hydrophobic counterpart, correlating to a reduction in the amount of H-bonds per sub-unit and hence increased surface hydrophobicity of the chain. This becomes problematic for anti-fouling surfaces, as hydrophobic exposure of PEG has been shown to promote protein adsorption [189].

1.9.1.2. Self-Assembled Monolayers

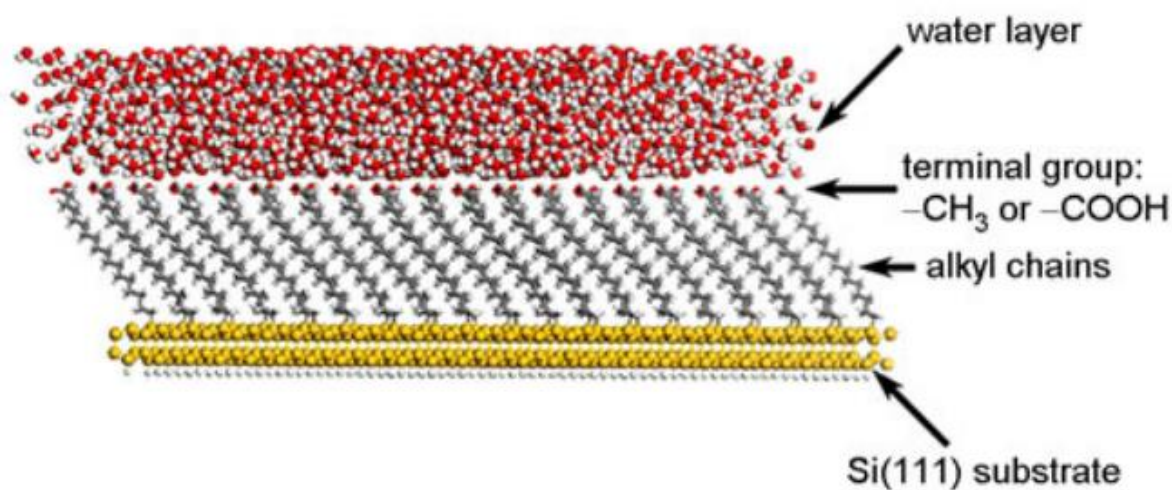


Figure 1.6 Example of a self-assembled monolayer coating. Reprinted with permission from [197].

Similar to grafted surfaces, many of the self-assembled monolayers (SAM's) have typically used polymers with known anti-fouling properties like PEG [147, 159, 198-201], however they are typically used at coverage densities significantly higher than grafted approaches (>5 chains/nm²), as shown in Figure 1.6. Due to the high density of molecules, the degree of the freedom for PEG SAM's is low. Therefore, the protein resistance cannot be explained by the idea of steric repulsion alone. This has led to strong research in the contributions of wettability and the effect of head-group chemistry on resistance to contaminants [147, 159, 202, 203].

Although the added functionality usually improves resistance to protein attachment, considerations of the underlying substrate are still important. One such example exists where gold and silver surfaces were modified with short oligo (ethylene glycol) SAM's [148, 204, 205]. In these works, it was noticed that both surfaces had similar wettability (water contact angle $\sim 65^\circ$), however surfaces with gold substrates were noticed to reduce interaction with the protein, whilst silver substrates enhanced interactions. The main difference between these

coatings was noted to be the packing density of chains on the surface. Using Fourier Transform Infrared Reflection-absorption (FTIR) spectroscopy, Harder *et al.* [148] noted a dominant helical structure of the chains on gold surfaces, while on silver chains were in an all-trans conformation. Pertsin *et al.* then performed Monte-Carlo simulations to explore the behaviour of water on these SAM's, and showed that water molecules were able to penetrate the polymer layer and hydrate the chains, whereas on the silver surface this was not possible [151, 152]. Further to this, these computational studies also noted that both hydrophobic end-terminal groups, and chains with a more hydrophobic interior structure (oligo(propylene glycol)), resulted in reduced ability to resist proteins. This suggests that the ability for water to penetrate into the polymer layer is a prerequisite for protein resistance.

There have been several studies involving “mixed” SAM's, which either incorporate mixed/alternating head-group chemistry [206], or alternating chains with different charge, hydrophobicity or length [106, 112, 113, 207, 208] to create heterogeneous surfaces. Similar to SAM's, biological membranes and lipid bi-layers have also been applied in marine and medical applications, with well-documented hydration behaviour [209, 210]. In particular, Frequency Modulation Atomic Force Microscopy (FM-AFM) studies confirm the presence of 2 hydration layers on the lipid bilayer surface [209, 210].

1.9.2. Branched/Comb-like chains

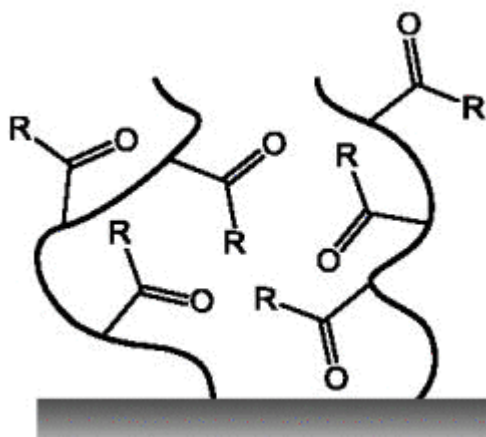


Figure 1.7 Example of a branched polymer coating [211].

Branch/comb-like polymers (Figure 1.7) have recently gained significant attention for anti-fouling applications. These polymers, like POX, contain a linear backbone with side-chains that can be easily tuned to suit desired properties. POX recently attracted significant attention for applications to biomaterials, specifically as a contender to PEG polymers [212-214]. Recent work revealing low biofouling properties [214, 215] and good biocompatibility [216-218] has gained interest in POX, especially for biomaterials [219], coatings [109, 219, 220], and biomedical applications of POX [221, 222]. However, despite the exponential growth in applications and patents, particularly in the biomedical field [221], POX polymers are not approved by the FDA for medical purposes, limiting the development of POX based biomaterials. It should be noted that, to the best of our knowledge, there have been no MD/computational studies on brush like polymers or POX systems, particularly in a grafted/non-fouling coating context.

Until recently, many POX studies focused on suspensions in solution. Now, with increasing demand for use as PEG alternatives, several methods of surface attachment are being investigated. Methods comprising spin coating [223] grafting from/to [212, 224], photo-polymerization [176] and electrostatic interactions [225] and plasma deposition [226, 227] have been utilised. However, it should be noted that all the above studies use chain

lengths significantly longer than those implemented in this study. Furthermore, plasma deposition can be used to allow partial retention of the oxazoline ring, which would allow biomolecules to retain bioactivity, which allows application for bio-sensing and diagnostic purposes [226].

Generally speaking, the nature of the monomer, and in turn the wettability of the coatings, tends to control the anti-fouling efficacy of POX. Both PMeOx and PEtOx have been shown to suppress protein adsorption [176, 212, 219, 220, 225, 228] while PPrOx promote cell adhesion and growth [226, 228]. This is largely believed to be due to the increased length and hydrophobic content in the side-chain of PPrOx coating allowing significant hydrophobic contact. Perhaps more relevant to the application for industrial paint surfaces, PMeOx coatings have been used for marine and bacterial fouling prevention on surfaces [220]. Remarkably, these coatings were stable in sea water for 1 month without significant loss in film thickness. Furthermore, the authors note that settlement of *Barnacles* and *Amphora* on PMeOx coated surfaces was significantly reduced, and the surfaces were also able to prevent *S. aureus* and *E. coli* adhesion.

However, it should be noted there are several inconsistencies across studies using the same monomers. For example in a study by Chang *et al.* [223] 380,000 molecular weight (MW) PEtOx is seen to stabilise cell adsorption [223], however a study by Wang *et al.* [176] examines PEtOx surfaces from 5,000-500,000 MW showed significantly reduced adsorption of BSA on all surfaces, with increased efficacy as MW increased. It should be noted that there are high separation distances between PEtOx chains in this study. This allows exposure of the underlying substrate, the effects of which can be seen where there is increased BSA adsorption on gold surfaces compared to silica. Furthermore, the effect of large spacing of grafted chains has been well reported to have a significant effect on anti-fouling ability [140, 195] so it is little surprise that longer chains perform better at the large separation distances

between grafted chains in this study. Furthermore, Cavallaro *et al.* compared plasma deposited PEtOx and PMeOx films at varying deposition conditions, noting that PEtOx films were sufficiently more effective at resisting adsorption of *S. epidermidis*.

Currently, there are several experimental studies comparing the anti-fouling efficacy of PEG and POX coatings [212, 213, 229, 230]. Whilst it is clear that both polymers show remarkable properties including stealth ability for drug-delivery and protein resistance for anti-fouling surfaces, the general trends show POX coatings outperforming PEG for a number of reasons. Firstly, in oxidative environments, POX coatings are shown to be much more stable than PEG [212]. If both coatings break down either through cleavage or oxidation, PEG chains decompose into toxic components like peroxides [213], whilst POX is both more stable in oxidative conditions [212] and remains non-toxic [212, 213]. Furthermore, whilst some studies have shown that PEG can retain anti-fouling efficacy whilst the coating degrades [231], generally this decomposition leads to a rapid decline in protein resistance [212, 232, 233].

1.9.3. Poly-Zwitterionic chains

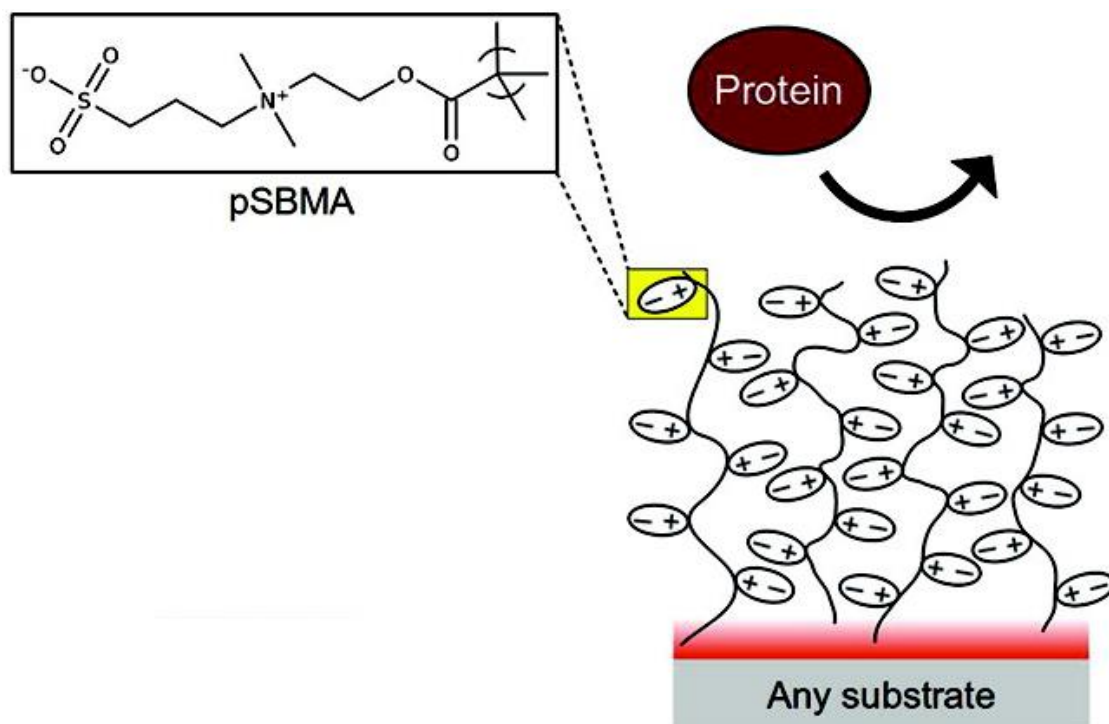


Figure 1.8 Example of poly-zwitterionic Coating for anti-fouling. Adapted with permission from [234]. Copyright (2012) American Chemical Society.

Poly-zwitterionic (PZI) molecules are the most recent focus-group for anti-fouling surfaces, as they combine strong interactions with water, as well as a heterogeneous distribution of charges whilst still maintaining an overall neutral charge. An example of a PZI coating is shown in Figure 1.8, and a detailed explanation of the anti-fouling performance of PZI's can be found in a recent review by Schlenoff [235]. To date, the major theory of PZI surface anti-fouling ability has been attributed to water structuring and solvation effects. Several studies have been conducted to investigate the effects of the charged groups in PZI ligands on the water hydrogen-bonding network, specifically the association of water hydrating zwitterion charges, and how they then interact with the water molecules around them. Where PEG coatings are believed to have approximately a 1:1 ratio of tightly bound water per EG monomer, some PZI coatings like poly(sulfobetaine methacrylate) have been noticed to have up to 8 tightly bound water molecules per monomer unit [236]. It should be

noted this is not an isolated case, as several other PZI coatings have been reported to have similar hydration levels [237, 238].

This behaviour has also been studied computationally by Shao *et al.* [239] where a combination of DFT, molecular dynamics and free-energy perturbation was used to investigate the hydration behaviour around carboxybetaine and sulfobetaine charged groups. In this study, results showed that positively charged groups are surrounded by more water molecules than negatively charged groups, however the water molecules around the negatively charged groups are more ordered. Furthermore, the hydration free energy of both chains was 2-3 times lower than studied OEG₄ segments, suggesting they would have a greater potential to resist protein adsorption. Further to this, experiments using Raman [164, 166] and FTIR [165] spectroscopy by Kitano *et al.* analysed the effect of PZI's on the water H-bonding network. Specifically, they noted no disruption to the water network, including associated water, by zwitterionic polyelectrolytes. In contrast, regular polyelectrolytes induced a net loss of hydrogen bonds. More recently, Kitano has also investigated the effect of charge-balance on zwitterionic surfaces, where it was noted that zwitterionic distributions enabled water to behave in a bulk-like manner, whilst lop-sided distributions of charges led to structuring according to the charge distribution on surfaces, a behaviour that could lead to enhanced protein adsorption [167].

Current modelling work on PZI is quite limited, particularly for anti-fouling applications. There have been studies using MD [240] and coarse-grained modelling [241] which have been used to reproduce experimental/material properties of coatings, however, to get an accurate description of these surfaces studies quantum simulations like QM/MM or DFT are needed to treat atomic charges and charge effects. Due to the computational power required to simulate the quantum region, simulations would be severely limited in the overall system size. Although QM/MM should allow a small surface to be modelled, we believe the

current computational power is not sufficient to accommodate simulations including the surface, protein and explicit water.

1.10. Project Aims

The aim of this project is to apply atomistic modelling techniques to examine the mechanism by which soft protein contaminants like EAS hydrophobin adsorb to surfaces and develop strategies to reduce the surface contamination. Specifically, this project aims to:

- Investigate the influence of substrate chemistry and hardness on the responsive behaviour of tethered surfaces.
- Investigate and understand the interaction of EAS with unmodified surfaces.
- Examine adsorption method and determine if there are any specific interactions critical to EAS adsorption.
- Investigate the difference in responsive behaviour between PEG and POX.
- Investigate and understand the interaction of EAS with PEG/POX modified surfaces.
- Examine key interactions and potential anti-fouling properties of PEG/POX surfaces.
- Determine if there is a relationship between PEG/POX responsive behaviour and anti-fouling efficacy.
- Provide molecular level insight into anti-fouling theories (steric repulsion and hydration theory).

Chapter 2

2. Computational Techniques for Modelling Anti-Fouling Systems

2.1. Overview

In the previous chapter we determined the need for advanced computational techniques in order to better understand the atomic scale events of fouling, and design more advanced and effective anti-fouling coatings. Therefore, for this project, we have implemented molecular modelling and force-field mechanics in order to gain an atomic level understanding. This chapter presents an overview of some of the more frequently used procedures for investigating protein function and dynamics under various conditions.

Firstly, we introduce the field of molecular modelling and types of atomistic modelling. We then explore the potential energy expression, and how force-fields are used to describe atom types. Following this, we discuss the importance and process of relaxing a system using energy minimisation, before detailing how molecular dynamics can be used to simulate the time-based evolution of a system. The procedures and techniques utilised to maintain temperature and pressure are discussed. Finally, we briefly discuss the advanced sampling techniques that can be used to explore the free-energy landscape of molecular systems under investigation.

2.2. Introduction to Molecular Modelling

Molecular modelling is a general term that describes the theoretical and computational techniques applied to model and simulate the atomistic behaviour of molecules. These models apply the fundamental laws of physics and chemistry to atomistically determine the structure, energy and dynamics of a system. Whilst often used to complement experimental data, there is a significant advantage with computational simulations in addressing the systematic changes at an atomic level, an impossible task to achieve with experimental resolution. One such example is presented in studying the anti-fouling surfaces, where it is possible to simulate the conformational changes during the single protein adsorption to surfaces. By keeping other conditions constant, it is then possible to investigate the effect of surface modification on protein adsorption, and the specific interactions that may prove critical in this process.

As shown in Figure 2.1 [243], molecular modelling can be separated into several categories, based on the system size and timescale ranges. The most accurate of these simulations are based on Quantum Mechanics (QM), and can be separated into wave function (*ab-initio*) and Density Functional Theory (DFT) methods. These methods provide detailed information about the electronic structure of material and are typically used to investigate bond breaking and forming processes, and electronic effects such as polarisation and force-field parameterisation. At present the QM methods are limited to several picoseconds and Ångstroms in time and length scales respectively. Due to the large size scales required to study anti-fouling systems, these techniques are not suitable for this project, however, it is worth noting that these techniques have been used extensively to develop accurate silica surface models and force-field parameters for atomistic models of organic-inorganic interfaces [242], which are relevant to this project.

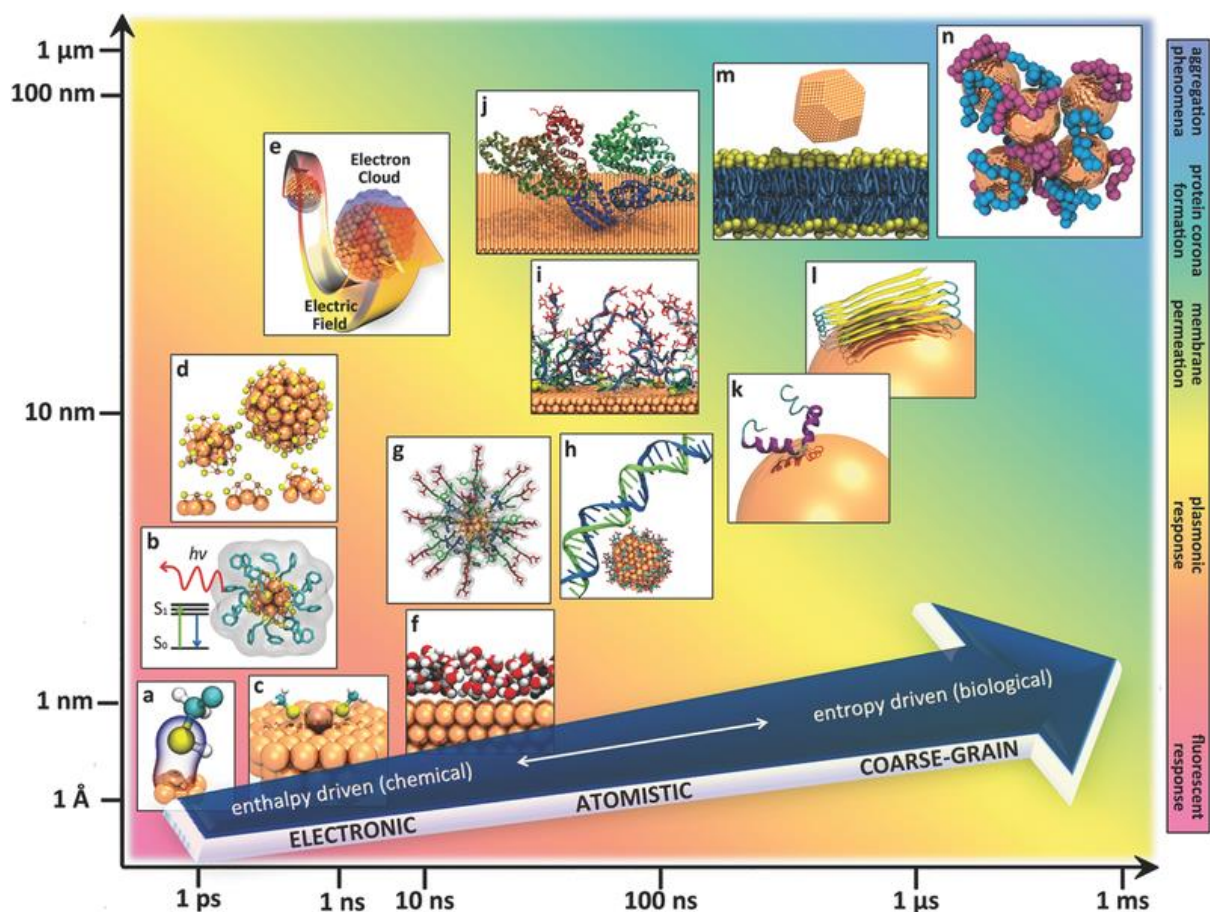


Figure 2.1 The approximate time and length scales involved in different classes of molecular simulations: Quantum Mechanical (QM), Atomistic, Coarse-Grained (CG), and Continuum models. [243]

All-atom simulations allow the investigation of longer time and length scales, enabling simulations in the order of nano to microseconds and nanometres respectively. To do this, a number of approximations are made based on the Born-Oppenheimer approximation, which allows the separation of electronic movement from the Hamiltonian of the system, leaving only variables pertaining to the nucleus of an atom. In this classical approach, the energy of the system is evaluated using a combination of potentials describing the bonded and non-bonded interactions that occur between atoms and molecules in the system, which will be explained in detail in Section 2.4. This approach is significantly less computationally expensive than QM approaches, as it ignores electronic characteristics, therefore not allowing bond breaking or forming during the simulation, however it is able to

describe physical interactions within the system, and reproduces structural, conformational, thermodynamic and vibrational properties with reasonable accuracy.

To investigate even larger system sizes, Coarse-grained (CG) methods may be used. These methods further simplify the atomic model by grouping atoms together into a single “bead” based on a range of conditions, called mapping. An example for mapping using the CG force-field (Martini) [244] is shown in Figure 2.2. This simplification significantly reduces the number of interacting particles, allowing much larger and longer simulations. There are however several limitations presented through this simplification, including the protein secondary structure being fixed, and the inability to properly describe interfacial water.

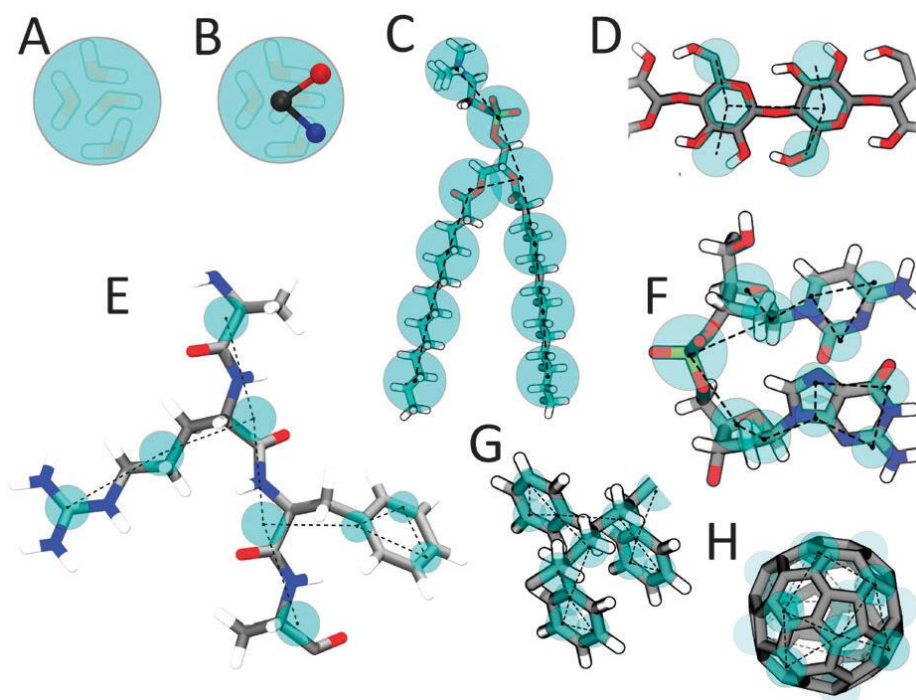


Figure 2.2 An example of Martini mapping (large blue circles represent martini bead) for selected molecules: (A) Standard water particle representing four water molecules. (B) Polarizable water molecule with embedded charges. (C) DMPC lipid. (D) Polysaccharide fragment. (E) Peptide. (F) DNA fragment. (G) Polystyrene fragment. (H) Fullerene molecule. In all cases Martini CG beads are shown as cyan transparent beads overlaying the atomistic structure [244].

All the calculations in this thesis have utilised atomistic simulations, allowing the exploration of protein dynamics and structure, as well as a detailed structure of the surface

and dynamic behaviour of tethered ligands, without the significant loss in functionality and degrees of freedom presented through CG methods.

2.3. Molecular Mechanics and Force-Fields

Within atomistic simulation framework, there exist several force-fields that have been parameterised to reproduce experimental behaviour observed for a particular system. These can be separated into two classes, Class 1, which have been primarily parameterised to study biomolecular systems, and Class 2 force-fields, which provide additional cross-term energy functions and parameters, making them more rigorous but computationally expensive. In this project both classes have been used, however as it is imperative to understand and observe protein physico-chemical behaviour, class 1 force-fields were mostly used. Therefore, the majority of this section will be highlighting the Class 1 FF methods, however in Section 2.5 we will give a brief overview of the Class 2 methods and theory.

2.4. Potential Energy Expression – Class 1 FF

The force-field potential is used to evaluate the potential energy (U) of a system, and is expressed as a function of the nuclear coordinates using mechanical equations. These potentials contain energy terms pertaining to forces that govern the atomic motions, derived from pairwise atom-atom interactions. These terms describe the bonded (E_{bonded}) and non-bonded ($E_{non-bonded}$) interactions between the atoms of a system; these are then split in accordance with Figure 2.3. The $E_{non-bonded}$ terms describe interactions between non-bonded parts of the system, or bonded segments separated by two or more intervening atoms. These include van der Waals (A) and electrostatic interactions (B). E_{bonded} terms refer to valence terms and account for changes to the internal coordinates of the system, such as bond length (C), bond angle (D), torsion angle (E) and improper torsion angle (F).

$$\begin{aligned}
U &= \sum_{i < j}^{(A)} \sum 4\epsilon_{ij} \left[\left(\frac{\sigma_{ij}}{r_{ij}} \right)^{12} - \left(\frac{\sigma_{ij}}{r_{ij}} \right)^6 \right] \\
&+ \sum_{i < j}^{(B)} \sum \frac{q_i q_j}{4\pi\epsilon_0 r_{ij}} \\
&+ \sum_{bonds}^{(C)} \frac{1}{2} k_b (r - r_0)^2 \\
&+ \sum_{angles}^{(D)} \frac{1}{2} k_a (\theta - \theta_0)^2 \\
&+ \sum_{torsions}^{(E)} k_\phi [1 + \cos(n\phi - \delta)] \\
&+ \sum_{impropers}^{(F)} k_d (1 + \cos(n_d \omega - \omega_d))
\end{aligned}$$

Figure 2.3 Potential energy expressions, showing both bonded and non-bonded interactions and equations. Reprinted from *Advanced Drug Delivery Reviews*, 65(2), Rebecca Notman, Jamshed Anwar, “Insights from molecular simulation of model membranes”, 237-250, Copyright (2013), with permission from Elsevier.

Non-bonded terms, as mentioned above, represent the intermolecular forces acting on two atoms separated by at least two atoms. The van der Waals (vdW) force (A) takes the form of a Lennard-Jones equation, and describes dispersion and repulsive forces, according to the separation distance (r) as shown. At very large separation distances, the vdW potential can be seen to approach 0. As the atoms come closer together, the energy decreases, passing through a minimum (ϵ). With further reduction in the separation distance, the attractive dispersion force rapidly decreases, and a minimum separation distance (σ) is reached. At separation distances below this point a repulsive force is applied to the atoms. It should be noted that $\left(\frac{\sigma_{ij}}{r_{ij}}\right)^6$ is the attractive part and $\left(\frac{\sigma_{ij}}{r_{ij}}\right)^{12}$ is the repulsive part of term A.

The electrostatic interactions (B) are modelled using Coulomb’s law. In this equation, the partial charge (q_i and q_j) between particles i and j , at a separation distance (r_{ij}) is seen to have a large attractive force the closer together these atoms are. The charge is restricted to the

centre of each atom and reproduces the electrostatic properties of the molecule/atomic environment, where the sum of a charge within a molecule must equal the molecule's formal charge. The sum of all energy terms then allows the total potential energy for the system to be calculated, in accordance with Equation 2.1.

$$U = E_{bonded} + E_{non-bonded} + E_{other} \quad (2.1)$$

Lastly, energy changes due to bond stretching (C), are calculated in a quadratic form, equivalent to Hooke's Law where k_b is the spring constant, account for deviations in bond length (r) from the experimental reference value (r_0). The angle-bending term (D) describes the bending of the angle between three atoms (θ). k_a and θ_0 are experimental reference values for stiffness and the equilibrium angle respectively. These two terms are often described as 'hard' degrees of freedom, as substantial energy is required to cause changes in bond length or valence angles. A far greater contribution to the relative energy of the system is achieved through deviation of the torsion angle (E). In a chain of atoms 1-2-3-4, the torsion angle (φ) is the angle between the plane containing atoms 123 and the plane containing 234. Here k_φ corresponds to the height of the torsional barrier and gives an indication of the energy required for the rotation around the corresponding bond, compared to the experimental reference angle (δ). The final bonded term, the improper or out-of-plane torsion angle (ω) describes the energy required to achieve correct geometrical alignment of atoms. This ensures that during equilibrium the correct alignment is achieved for the angle between the plane of the molecule and the out-of-plane bond (ω). A value of 0° corresponds to the atom being in plane.

It should be noted that some force-fields, especially Class 2 force-fields, may have additional energy components calculated that attribute to the final term, (E_{other}). Some Class 2 examples of this will be mentioned in Section 2.5.

2.5. Force-Field Parameterisation

The energy functions above are subjected to a set of parameters that describe the energetic and geometric properties of the interacting particles, depending on the chemistry of an atom/molecule, defined by various atom types. The optimisation of force field parameters involves adjusting values to reproduce experimental data or data computed using QM methods. Typical examples of experimental data used for parameterisation of a force field or the consequent refinement are: vibrational spectra, densities, solvation free-energies, electron, or X-ray diffraction structures, and relative conformational energies and barrier heights. Generally, each force-field is based on a different type of experimental data, although there is some overlap, parameters are not transferable between force fields. As mentioned earlier, there are two classes of force-fields, their examples are given below.

Examples of Class 1 Force-Fields:

There are four most commonly used empirical force-fields, AMBER [245], CHARMM [246], OPLS-AA [247] and GROMOS [248]. The parameters for these force fields were extensively optimised with particular emphasis on the treatment of proteins. For the CHARMM force-field, primarily employed in this study, partial atomic charges were based on QM calculations (Hartree-Fock/6-31G* supramolecular data [246]). Due to the differences between parameterisation of force-fields, a slight bias towards a particular type of protein secondary structure often exists, for example, as discovered by Mu *et al.* [249] and Hu *et al.* [250], the CHARMM22 force field has a strong preference for α -helical conformations for di- and tri-peptides [249-251], whereas 2D-IR and NMR measurements

consecutively show that these peptides adopt primarily polyproline II (PPII) conformations [249]. To fix this, a CMAP correction was added to the potential energy function (implemented in CHARMM29 and CHARMM36 forcefields), which assigns Φ and Ψ cross-terms, realised from grid based energy correction maps. Unfortunately, until recently a CMAP implementation was not possible in LAMMPS [252], the simulation package used in this project. However, as shown in Chapter 5, lack of CMAP correction had negligible effects on protein dynamics as the protein under investigation is globular, and experimentally is shown to display high levels of disorder in solution.

Examples of Class 2 Force-Fields:

For Class 2 force-fields there are two prominent force-fields, the COMPASS force-field [253], used in this thesis, and the polymer consistent force-field (PCFF), which was a precursor to COMPASS. Parameterisation of the COMPASS force-field, was undertaken by Sun [253] and involved a two stage hybrid procedure. In the first stage, atomic partial charges were derived based on *ab initio* calculation of electrostatic potential energy, the potential arising from the force acting on a unit of positive charge. Valence parameters (e.g. bond length, spring constants) were determined from *ab initio* energies including first and second derivative of the total energies. The vdW parameters were initially fixed to a set of initial values taken from PCFF. In the second stage, parameters were refined to yield good agreement with experimental data using empirical optimisation. In this optimisation, valence parameters were adjusted using molecular structures, dipole moments, vibrational frequencies and conformational energies taken from isolated molecules in gas phase systems. The vdW parameters were also adjusted based on density and cohesive energy of liquid molecules in their condensed phase.

These force-fields have been developed to accurately model complex organic-inorganic interfacial systems and contain additional cross-term parameters; bond-bond, bond-

angle, middle-bond-torsion end-bond-torsion, angle-torsion, angle-angle-torsion, bond-bond-13-torsion and angle-angle parameters. Whilst this does allow the accurate modelling of more detailed and cross-linked polymer surfaces, the additional calculations involved for cross-terms significantly increase the computational cost. Furthermore, these force-fields were not parameterised to accurately describe large protein dynamics, including folding and secondary structure and thus cannot be reliably applied to protein/surface systems.

Due to these restrictions, the Class 1 CHARMM22 [246] force-field has been used for the majority of this thesis as it contains parameters that allow accurate description of the protein behaviour, as well as having parameters for silica [254], PEG, and POX [255]. The Class 2 COMPASS force-field was required for studies comparing the effect of polyester and silica substrates on responsive behaviour of PEG (Chapter 5), as Class 1 force-fields do not contain parameters required to provide an accurate description of crosslinked polyester surfaces.

2.6. Energy Minimisation

Before a Molecular Dynamics simulation can be initiated, the molecular model must be optimised in order to remove overlapping atoms, and reset the position of atoms as close to equilibrium positions as possible. For a large system of N number of atoms, the energy surface can be rather complex, as the potential will be a function of $3N$ cartesian coordinates. One of the most interesting aspects of the energy surface is the minimum energy points, as these correspond to stable and meta-stable states of the system. There may be a very large number of minima on the energy surface, with the purpose of energy minimisation being to attain a configuration that corresponds as close to the global energy minimum as possible. Energy minimisation algorithms [256, 257] use numerical methods to gradually change the coordinates of an atom, lowering the energy until a minimum is reached. Derivative

algorithm methods are able to provide information about the shape and size of the energy surface, and enhance the efficiency at which the minimum can be found.

The derivative of the energy function with respect to the atomic coordinates, termed the energy gradient, provides important information useful in the energy minimisation process. The direction of the gradient indicates where a minimum is located, whilst the magnitude indicates how far away from the minimum the current coordinates are. The energy of the system is then reduced by stepping in the direction of the net force until the energy converges to a minimum when the first derivative is zero and the second derivative is positive.

In this study, the Polak-Ribiere version of the conjugate method [258] has been used. In these methods, steps are taken in the negative direction of the energy gradient, to locate an energy point that is lower in potential than the previous point. Once the point of energy is located, the next direction in the algorithm is determined by taking the conjugate gradient of the previous direction. The local energy minimum is eventually attained when the user-defined convergence criterion is met.

2.7. Molecular Dynamics

To simulate the motion of atoms in a system and investigate its structural evolution, the molecular dynamics approach is employed. In molecular dynamics (MD), the system is allowed to evolve at a finite temperature according to the Newton's second law of motion:

$$\mathbf{F} = -\frac{dU}{d\mathbf{R}} = \mathbf{m} \frac{d^2\mathbf{R}}{dt^2} = \mathbf{ma} \quad (2.2)$$

Here U is the potential energy determined by the force-field energy expression, example given by Equation 2.1, \mathbf{R} is the vector that contains x , y and z coordinates of the

particles, and \mathbf{F} and \mathbf{a} are the force and acceleration vectors respectively. To begin a dynamics simulation, we require a set of initial atomic coordinates, velocities and the interaction potential. For a short period of time, known as a time-step, the interaction within the system may be considered constant. During each time-step, the interactions between atoms are computed and combined with the current positions and velocities to generate new atomic positions and velocities. The atoms are then moved to their new position, and a set of updated positions and velocities are determined. By undertaking a large number of time-steps, a molecular dynamic trajectory is generated, and the time behaviour of a system is obtained.

MD allows for a larger portion of the energy surface to be explored and also allows for time dependent properties to be determined, since atomic movement is generated according to Newton's second law of motion, using numerical integration. In this study, the velocity-Verlet *al.gorithm* [259] (a variant of the Verlet method [260]) is used to determine new positions and velocities. In the velocity-Verlet *al.gorithm* the position (\mathbf{R}) and velocity (\mathbf{V}) vectors after time step Δt are defined as follows:

$$\mathbf{R}_{(t+\Delta t)} = \mathbf{R}_{(t)} + \mathbf{V}_{(t)}(\Delta t) + \frac{1}{2}\mathbf{a}_{(t)}(\Delta t)^2 \quad (2.3)$$

$$\mathbf{V}_{(t+\Delta t)} = \mathbf{V}_{(t)} + \frac{1}{2}\Delta t(\mathbf{a}_{(t)} + \mathbf{a}_{(t+\Delta t)}) \quad (2.4)$$

The velocity-Verlet method is implemented as a three-stage process. First, the new position vector ($\mathbf{R}_{(t+\Delta t)}$) is calculated (Equation 2.3) where initial velocities ($\mathbf{V}_{(t)}$) are randomly assigned using a uniform Maxwell-Boltzmann distribution for a given temperature, and acceleration ($\mathbf{a}_{(t)}$) is calculated from the derivative of the interaction potential (Equation 2.2).

Next, the atomic coordinates are updated, and the new values of the acceleration are determined ($\mathbf{a}_{(t+\Delta t)}$) using the interaction potential (Equation 2.2). In the third step, values of $\mathbf{a}_{(t)}$ and $\mathbf{a}_{(t+\Delta t)}$ are used to determine the new velocity vector $\mathbf{V}_{(t+\Delta t)}$ (Equation 2.4). It should be

noted that the velocity-Verlet *al.gorithm* assumes that acceleration is dependent on the position of the particles and not on their velocities.

2.8. Periodic Boundary Conditions

A system's size is required to be large enough so that the macroscopic properties calculated from simulation match those of experiment. Periodic boundary conditions [256, 257] in theory allow for a system of "infinite" size to be modelled. Firstly, particles are enclosed in a box known as a unit cell. This unit cell therefore contains all "unique" atoms of the system. This cell is then replicated by rigid translation in all three Cartesian directions (x, y, and z) forming an infinite sized system. For example, consider Figure 2.4 which shows a two-dimensional illustration of periodic boundary conditions. In the centre of the image we see our origin cell, containing our "unique" atoms, surrounded by 8 unit cells containing our image atoms. As can be seen, a blue atom has just exited the right of our origin cell, and has moved into the image cell. In our origin cell, the atom from our image cell has entered the origin cell, thus maintaining a constant number of atoms in the origin cell.

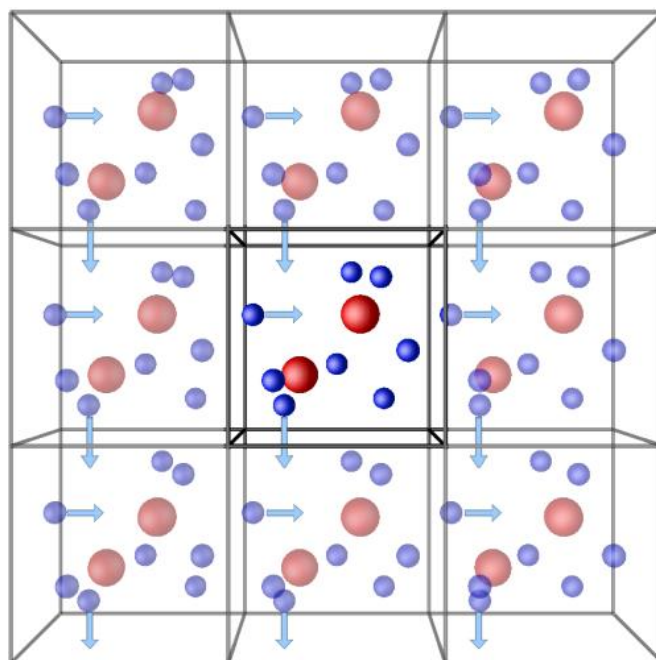


Figure 2.4 A two-dimensional illustration of periodic boundary conditions. Sourced from <http://isaacs.sourceforge.net/phys/pbc.html> on 11/01/2018

The use of such periodic boundary conditions also eliminates surface effects near boundaries which can lead to erroneous results. Depending on the system to be examined, there are several space-filling type boxes that may be more computationally efficient for running molecular dynamics calculations. In this project, we have implemented the most commonly used triclinic unit cell.

It should also be noted that periodic boundary conditions have been implemented in this thesis to create an “infinite surface” for simulations. To allow this, a unit-cell is created whereby opposite surface edges are bonded together, eliminating the possibility of edge and other erroneous surface effects. This also allows scaling up of a surface to suit the size of contaminant models, where the surface model can be extended as a factor of the lateral dimensions.

2.9. Non-Bonded interactions

The most time-consuming part of a molecular dynamics simulation is the calculation of the non-bonded energies and forces, namely long-range electrostatic and Lennard-Jones interactions. In this thesis, a potential truncation method has been implemented to deal with non-bonded interactions. The potential truncation method introduces a small perturbation to the potential and force calculations, rendering it not accurate enough for calculations of long-range electrostatic interactions, and becomes computationally expensive as the system size increases. To lessen the computational burden, various truncation schemes have been developed whereby non-bonded interactions beyond a cut-off distance are ignored, and a smoothing function like the Ewald summation technique [261] is typically applied. This alleviates such effects by dampening interactions between atoms separated by a distance larger than the cut-off criteria, attempting to correctly connect the vdW and electrostatic interaction energy to zero.

In this thesis, the more computationally efficient Particle-Particle Particle-Mesh (PPPM) [262] method has been used. This style invokes a particle-particle particle-mesh solver which maps atom charges to a 3D mesh, uses 3d Fourier transforms to solve Poisson's equation on the mesh and then interpolates electric fields on the mesh which point back to the atoms. This allows for rigorous treatment of long-range electrostatics in a computationally efficient manner [263].

2.10. Thermodynamics Ensembles

In this thesis, a canonical ensemble is applied whereby the thermodynamic state of the system of interest is described by a fixed volume V , fixed number of molecules N , and fixed temperature T . Therefore, during molecular dynamics in the canonical ensemble (NVT), the system under periodic boundary conditions is evolved at constant volume and temperature.

Other simulations are often done in the isothermal-isobaric (NPT) ensemble, as many experimental measurements are made in environments of constant temperature and pressure. However, in this study we employ a fixed and “infinite” surface benchmarked to experimental results, meaning an NPT ensemble would be unsuitable as a change in volume will result in the surface being stretched/shrunk to fit the periodic cell, and as such the density and other properties of the surface will be affected.

2.11. Temperature Coupling

Temperature (T) is an important parameter in MD simulations. It specifies the thermodynamic state of the system, but perhaps more importantly, the control of it helps mitigate several sources of error including solute drift during equilibration, drift as a result of force truncation and integration errors or heating due to external and frictional forces. In a molecular dynamics simulation, the initial velocities are generated to produce a Maxwell-Boltzmann distribution at a user-defined temperature. However, as the simulation progresses the temperature does not remain constant as kinetic and potential energy are exchanged. To maintain a constant temperature, the velocities need to be adjusted accordingly, using a temperature coupling scheme.

A method which gives the correct description for canonical ensemble simulations is the extended-ensemble approach first proposed by Nosé [264] and later modified by Hoover [265], now known as the *Nosé-Hoover* temperature coupling algorithm. In this method, the system Hamiltonian is extended by introducing a thermal reservoir and a friction term in the equations of motion. The friction force is proportional to the product of each particle’s velocity and friction parameter ξ . This friction parameter, or ‘heat-bath’ variable, is an independent dynamics quantity with its own equation of motion, where the time derivative (Equation 2.2) is calculated from the difference between the current kinetic energy and the

reference temperature. In Hoover's formulation, the particles' equations of motion (Equation 2.2) are replaced by:

$$\frac{d^2 \mathbf{R}_i}{dt^2} = \frac{\mathbf{F}_i}{m_i} - \xi \frac{d\mathbf{R}_i}{dt} \quad (2.5)$$

$$\frac{d\xi}{dt} = \frac{1}{Q} (T - T_0) \quad (2.6)$$

Where the equation of motion for the heat bath parameter ξ is given by Equation 2.6, where T_0 denotes the reference temperature, T is the current instantaneous temperature of the system, Q determines the strength of the coupling, \mathbf{R} is the vector that contains x , y and z coordinates of the particle, \mathbf{F} is the force vector, m_i is the mass of the particle and t is the timestep.

We have also used the Andersen [266] temperature control method for simulations with the polyester surface; an alternative method to velocity scaling that generates rigorous canonical ensembles. This method is based on stochastic collisions between particles, whereby particle's velocities are adjusted to produce a predefined collision frequency. Effectively, a series of constant energy states are generated whose distribution of energies match a Gaussian function.

2.12. Bond Constraint Algorithms

As previously discussed, one of the most demanding aspects of simulation is the computation of non-bonded interactions, as large systems require millions of pairs to be evaluated at each time-step. One way to enhance computational efficiency is by extending the time step used for each calculation. However, this will introduce systematic errors, as the shortest timescale in biological simulations are the hydrogen bond vibrations at 1 fs. Fortunately, in most simulations the hydrogen bond vibrations are not of significant interest,

and can be removed entirely by introducing bond constraint algorithms such as SHAKE [267] to make it possible to extend time-steps to 2 fs.

In the SHAKE algorithm, bonds and angles are set to prescribed values by moving the bonded particles parallel to the previous bond directions. This is an iterative method, where all the bonds are reset sequentially to the correct length. Because the bonds are coupled, this procedure has to be repeated until the desired accuracy is reached. SHAKE is simple and numerically stable since it resets all constraints within a prescribed tolerance; however, this method has the drawback that no solutions may be found when displacements are large. This is due to the coupled bonds being handled one by one, thus correcting one bond may tilt a coupled bond so far that the method does not converge.

2.13. Enhanced Sampling Techniques

Whilst molecular dynamics simulations present as a very useful and accurate method for simulating the time evolution of a system, one of the largest limitations is the ability to adequately sample the free energy landscape of a system. For large systems, the complexity and ruggedness of the free energy surface presents significant limitations in exploring conformational states, particularly for processes such as protein folding and in some cases protein aggregation. As shown in Figure 2.5, these complex processes present a series of favourable conformational states and local energy minima. The system can easily be trapped in one of the local minima and fail to sample the entire conformational space. To solve this problem, enhanced sampling algorithms have been developed that can accelerate configurational changes that involve the crossing of large free energy barriers.

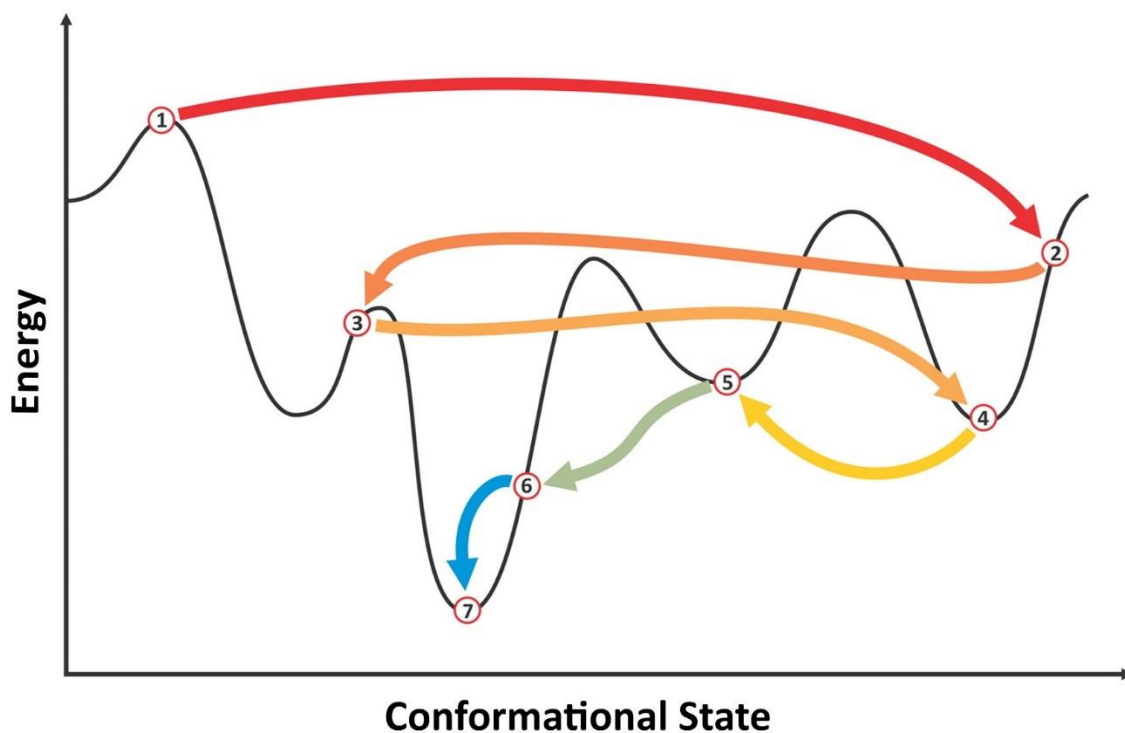


Figure 2.5 Example of a free-energy landscape for a system. There are several local minima states (1-6), before the system is finally in the global energy minimum (7).

There are several types of enhanced sampling techniques, such as Replica Exchange Solute Tempering (REST) [268], Replica Exchange Molecular Dynamics (REMD) [269] and Umbrella Sampling [270]. Detailed information on sampling techniques and their benefits can be found in a recent review by Bernardi *et al.* [271]. Unfortunately, for this study there are significant difficulties adopting these methodologies due to the system sizes studied in anti-fouling systems, particularly systems containing both proteins and surfaces with functional modifiers.

Chapter 3

3. Protein and Surface Models

3.1. Overview

There are several major challenges in using atomistic modelling to study anti-fouling systems. We begin this section by outlining the challenges and limitations of molecular modelling techniques. We then present a detailed background in the development and validation of silica and polyester substrates that have been used in this study, and how molecular modelling methods have previously been used to model protein-surface interactions. We then present the surface models used in this study, including functionalisation methods.

3.2. Modelling Anti-fouling:

In Chapter 1 we outlined how experimentalists have elucidated several molecular level phenomena contributing significantly to the adsorption of proteins and other foulants. The resolution of these experimental techniques alone is insufficient to detail the structure and dynamics of proteins at interfaces. Molecular modelling studies are a powerful tool to address this shortcoming in resolution, with many theoretical studies now being conducted in conjunction with, or compared against experimental studies. There are several recent reviews published on the molecular modelling of protein-surface interactions [8, 243, 272-279] all detailing approaches, methodologies and limitations in molecular dynamics simulations. Although these are significantly important considerations, these current reviews do not address how simulations can and have been used to further the understanding of anti-fouling systems.

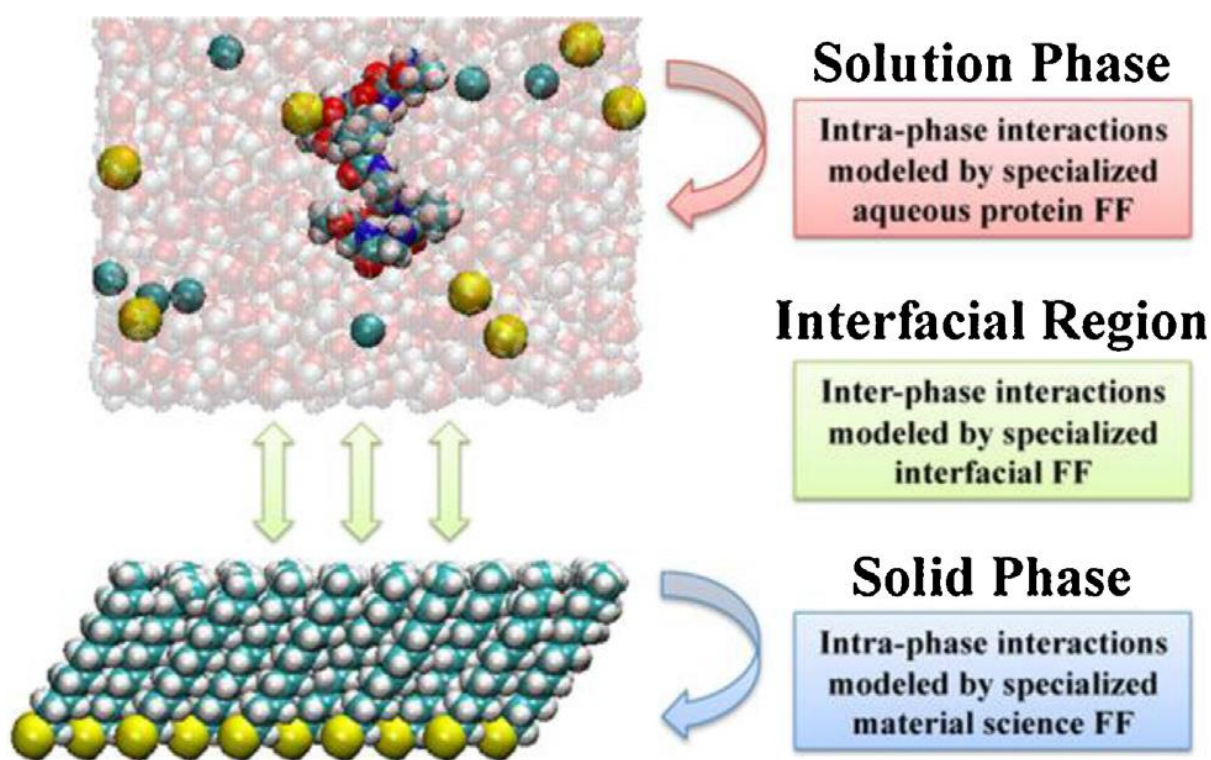


Figure 3.1 Schematic representation of the interfacial force field (IFF) method applied to a peptide adsorption simulation. The solution and solid surface phases are modelled by force fields that accurately represent their respective intra-phase interactions while interactions between atoms of the solution phase with the solid phase

are represented by an interfacial force field parameter set that is tuned to accurately represent peptide adsorption free energy [273].

As described in many of these reviews, modelling protein-surface interactions are widely done in a 3-phase process, summarised in Figure 3.1. Essentially, analysis of both the protein in solution (solution phase) and surface (solid phase) must be independently detailed to accurately describe conformational changes in the protein at the surface-water interface (interfacial region). With significant improvements in computational power, highly complex models with advanced functionality as mentioned above can now be accurately studied within a reasonable timeframe. The biggest hurdle facing anti-fouling modelling is brought about through complexities in modelling the interfacial region. Herein lies several complications, one being the limitations on system sizes and time-scales associated with current modelling techniques, as summarised in Figure 2.1. Another issue is the adequate sampling of the protein during adsorption. Although this has often been solved through enhanced sampling techniques (Section 2.13), there are difficulties adopting these methodologies due to the system sizes studied in anti-fouling systems. Finally, one of the largest hurdles is the deficiencies in parameters to accurately describe interactions between the highly complex surfaces currently being experimentally developed, and the protein contaminant model [273].

3.3. Substrates

The following sections focus on understanding anti-fouling materials and the development of computational models able to reproduce experimental results. We start with the history, development and challenges associated with substrate models of both polyester and silica, two of the prominent surfaces used for industrial and biomedical applications.

3.3.1. Polyester

Organic coatings including epoxy resins, polyester and similar paints have been used for decades in architectural coatings, however modelling work on their anti-fouling properties

only began in the mid-1990s, due to their failing caused by atmospheric contamination. Investigations in the interfacial structure and properties of organic coatings on aluminium and other metal oxide coatings [280] were used to identify methods of the coating's adhesion at the interface, degree of curing in polymers and permeability to water and oxygen. As research progressed, a computational method was developed to accurately predict the cross-linking of epoxy resins [281]. Similar methods have since been used, with results showing density and elastic constants very close to experimental values [282, 283], predictions of glass transition temperatures, linear thermal expansion coefficients and Young's modulus [284]. Furthermore, these detailed atomistic calculations come with the added benefit of knowing the molecular detail and structuring of the polymers. Coarse-grained simulations have also been implemented, allowing simulation of commercial grade polymers (i.e. polymers in the 2000+ monomer range), as well as meso-scale properties like hydrodynamic radius, radius of gyration [285] and glass-transition temperature [286] which have all been shown to be in good agreement with experimental results.

With detailed models now available for these materials, there have been significant studies on the anti-fouling behaviour of these surfaces. Due to business needs (atmospheric contamination with carbon), complex polymer surfaces have only investigated adhesion with soot like contaminants such as graphite, amorphous carbon and C60 [96, 287-292]. From these results, several insights on designing surfaces resisting adhesion were identified through surface modification, as hydroxylation, carboxylation and fluorination were all shown to reduce adhesion of graphite [96, 288, 289] and C60 [287, 291, 292]. Furthermore, it was identified that increasing atomic scale roughness also reduced adhesion [96, 291], however it is important to note that roughness should not be commensurate with the size of the contaminant, as "cavitation" or large surface roughness has been shown to significantly increase adsorption [293].

It has been shown that a significant limitation of relatively soft polyester surfaces arises due to “hydrophobic recovery” [292]. In this study, it was noted that in systems with high surface mobility and non-crosslinked polymer fragments (the introduced functional groups) were able to protrude into the surface, resulting in loss of functionality and strong adhesion with a fullerene molecule. Conversely, in stiffer, more rigid systems, this hydrophobic recovery was not possible, resulting in a less favourable adsorption, whilst still maintaining the core flexibility of the polymer bulk. This phenomenon has also been seen occurring in experimental studies [294].

Unfortunately, due to the complexity of these models outlined above, the ability to accurately model protein interactions with these organic coatings is very limited. There have been some studies which have used simplistic models of a basic polyethylene surface interacting with a protein [295, 296], but force-field parameters and other limitations [297] are still issues that need to be addressed.

3.3.2. Silica/oxide

As with polyester based surfaces, there were significant hurdles in the early stages of computational research to be addressed to model industry relevant surfaces. The first of these hurdles was developing an accurate starting structure representative of amorphous silica rather than quartz/crystalline silica. Methods to reduce topological and bonding defects presented in these surfaces were first addressed by Garofalini *et al.* [298, 299], who used empirical molecular dynamics to compare develop accurate vitreous silica models. Since this work, there have been several alternative models proposed [300], a detailed overview can also be found in Rimola’s review [30].

As pH increases above ~3, deprotonation of silanol terminal groups takes place, leading to negatively charged surfaces [301, 302]. Methods using *ab-initio* calculations to

describe these deprotonated states at pH 7 were first implemented by Hassanali *et al.* [303]. Due to the significantly higher than normal bulk silica charges in this method, a more recent parameter set by Buteneth *et al.* [242] has been proposed. These MD parameters are able to closely reproduce *ab-initio* and DFT results at the surface-water interface [242], however there is limited experimental data to compare with.

Complexity to the problem is also added when considering the water models to use, as the combination of force-field and water model has been shown to significantly affect the behaviour of proteins [304-306]. The quartz-water interactions using the Lopes [307], CHARMM water contact angle [254] and Clay force-field [26], have been compared with x-ray reflectivity and *ab initio* calculations [308]. In spite of these force-fields all having a very similar functional form, the Clay force-field was seen to best represent the structuring/dipole moment of interfacial water from these experiments, however the Clay force-field is not designed to describe bulk silica, as all bonding terms other than those for the surface hydroxyls are absent. The structural differences between quartz, amorphous silica and pH effects have significant implications on the behaviour of interfacial water and hydrophobicity of the surface. Specifically, the highly ordered surfaces of quartz have been seen both theoretically and experimentally to feature a dense distribution of geminated surface silanols, leading to ordered water layers [116, 309, 310]. Conversely, amorphous silica surface is characterised by isolated silanols [311, 312], resulting in disordered water layers [313-315].

3.4. Modelling Protein-Inorganic Surface Interactions

As elaborated earlier, there are several limitations in the modelling of protein-surface interactions. Whilst protein models have been significantly refined and applied for suitability in studying protein folding [316-318], protein-protein [319, 320] and protein-membrane [321, 322] interactions, there is limited literature for protein-surface interactions [272]. This is

slowly being addressed, with prominent force-fields including the Dual force-field [323] and Interfacial force-field [252, 324] by Latour *et al.* and the INTERFACE force-field [325] by Heinz *et al.* It should be noted, however, that although these force-fields are being developed to more accurately describe protein-surface interactions, we can still utilise traditional class 1 force-fields to gain insight into the adsorption process.

Another challenge that is slowly being bridged in protein-surface modelling is the trade-off that exists in system size/detail and simulation time. Whilst computational power is significantly increasing, allowing larger and longer simulations, there are several studies using peptides or small/rigid proteins that are of high relevance in the field of anti-fouling. For example, work by Schwierz used steered molecular dynamics to “push” a polyalanine peptide onto a polar surface, mimicking and comparing the behaviour to AFM [97]. These simulations revealed that the peptide adsorption resistance is caused by the strongly bound water hydration layer and characterized by the simultaneous gain of both total entropy in the system and total number of hydrogen bonds between water, peptide, and surface. Similarly, Penna has simulated peptide adsorption on surfaces [118, 326] to propose a generalized molecular level mechanism for peptide adsorption. These works noted that an incoming contaminant would undergo a multi-phase adsorption process, as summarised in Figure 3.2.

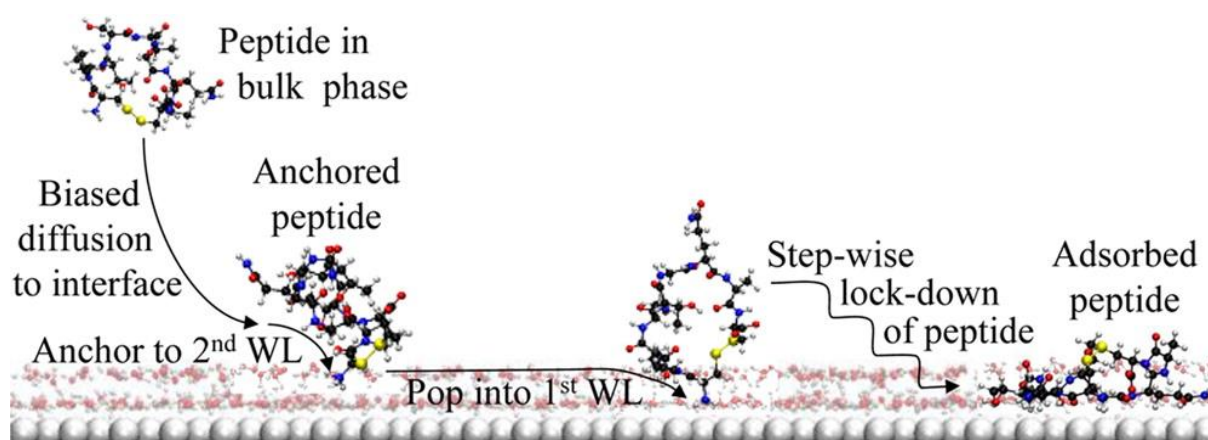


Figure 3.2 generic peptide adsorption mechanism proposed by Penna and Biggs [118]. This mechanism is composed of three phases: (1) biased diffusion of the peptide from the bulk phase toward the surface; (2) anchoring

of the peptide to the water/solid interface via interaction of a hydrophilic group with the water adjacent to the surface or a strongly interacting hydrophobic group with the surface; and (3) lockdown of the peptide on the surface via a slow, stepwise and largely sequential adsorption of its residues. WL = water layer.

It should be noted that there are several studies involving protein adsorption on surfaces [327-332], however, the direct relevance to anti-fouling is limited. These studies have provided some insight to protein adsorption, for example how the terminal group effects the folding and dynamics of proteins [332], or the effect of silica surface hydroxylation on protein adsorption orientation [333]. However, it should be noted that the majority of these studies use hard proteins, like lysozyme, as the contaminant model. These proteins are not relevant for biofouling, and are more sensitive to environmental influences like surface features [52, 320, 334].

In this thesis, we have studied the soft protein EAS hydrophobin, which is known to be involved in the fungal biofouling process. Whilst the Class 2 hydrophobin HFb1 has been simulated adsorbing on graphite [335] and PDMS [336], EAS has only been computationally studied in solution and at the air-water interface [77, 79].

3.5. Computational Models

Surface and protein models are presented below with a brief description outlining relevant details on construction or source of the model. Due to the variance in simulation detail and force-fields used, a brief description of the simulation procedure will be presented at the beginning of each results chapter (Chapters 4-7).

3.5.1. Polyester Surface Model

The polyester substrate model comprised polyester chains comprising 15 units of 2-butyl-2-ethyl-1,3-propanediol, 2 units of trimethylolpropane and 16 units of isophthalic acid. Tributoxymethyl-melamine crosslinks were reacted with the polyester chains to form the

crosslinked polyester film typical of common industrially used coatings. Details of the construction procedure can be found in work by Yarovsky and Evans [281]. The polyester surface has a density of 1.3 g per cm³, compatible with experiments, and an average film thickness of 15 Å, with lateral dimensions of 37 Å in the x and y directions.

3.5.2. Silica Surface Model

To allow for both experimental comparison and future surface modification we used a previously modelled silica surface [287, 337] described by Garofalini *et al.* [298]. This represents a realistic, highly hydrated amorphous silica surface with a surface silanol density of 4.7 OH groups per nm². The amorphous silica substrate displays a density of 2.6 g/cm³ (comparable to experiment), an average film thickness of 17 Å (in the z direction) and lateral dimensions of 27 Å (Chapter 4), and 81 Å (Chapters 5-7), in both x and y directions.

3.5.3. Surface functionalisation

To incorporate functionality to the polyester surface, the ‘grafting from’ and ‘grafting to’ approaches were considered. To simulate a ‘grafting from’ method, whereby PEG/POX chains are grown from all available functionalisation sites [338], PEG/POX molecules were attached to the polyester substrate, leaving no OH groups unreacted. In contrast, for the ‘grafting to’ method, fully grown chains typically react with only a portion of available functional sites [253], and therefore functional ligands were attached to randomly identified OH groups on the polyester surface, leaving a portion of unreacted OH groups. The ‘grafting to’ approach was also employed to generate functionalised silica models.

Chapter 4

4. Effect of Substrate Behaviour on Tethered Surfaces

4.1. Overview

This work finalises studies focusing on environmentally responsive coatings, under the Australian Research Council (ARC) Linkage Grant LP0990511 in partnership with BlueScope Steel. In this chapter, we present a molecular dynamics study investigating deswelling and swelling of some of the most commonly used responsive materials – PEG-functionalised silica and polymer surfaces – as a function of hydration and temperature.

We show that PEG chains grafted onto the hard silica substrates exhibit a dehydration induced collapse that is far more pronounced compared to chains grafted onto the soft polyester surface. The difference between the hard and soft substrates is particularly notable at low coverage densities where the chains are sufficiently separated from one another. We conclude that soft substrates may be detrimental for the efficient response of the functionalised surfaces to changes in hydration. Therefore, enhancement of the surface hardness must be considered when designing responsive surfaces for solution-based applications, such as antimicrobial coatings for interchangeable wet/dry environments and biomedicine.

In this chapter, simulations on silica surfaces performed by Lachlan Shaw are used for comparison with simulations of both polyester models, conducted by Kamron Ley, who also performed all the analyses. This work has been published in the peer-reviewed journal, *Journal of Molecular Simulation* [195].

4.2. Introduction

Surfaces that are able to resist the non-specific binding of proteins and other foulants are sought after in many applications, with the aim to not only deter but control biomolecule adhesion. In biomedicine, functionalised surfaces are used to manufacture prosthetic devices to replicate functions of human tissues and organs [339, 340], as well as to act as carriers in drug delivery systems [341-344]. In these applications, a solid surface is grafted with oligomers that display non-immunogenicity, non-antigenicity, hydrophilicity, and protein-rejection properties to target the issue of protein adhesion, rendering the material biocompatible.

In Section 1.9.1.1 we presented a detailed overview of PEG's unique ability to change conformation in response to various triggers [132] which in turn can assist in excluding foreign materials such as organic contaminants including proteins, from its proximity [133, 134]. These examples illustrate that PEG's unique ability to reject proteins and other contaminants combined with its non-toxic and anti-genetic properties is a justification of its extensive use as a surface protector for biomedical and industrial applications. Despite this, an understanding of its fundamental behaviour at the atomic level is still lacking.

The specific interactions of PEG with water molecules have long been shown to be responsible for the induced conformational changes. Atomic-force microscopy [345] and *ab-initio* calculations [346] have shown that the distance between adjacent oxygen units in a PEG oligomer was responsible for the type of hydrogen bonding formed, with shorter distances stabilising helical conformations. Another study using low-field NMR [149] discovered that the swelling response of PEG chains could be attributed to water. In this study, it was noticed that once a 1:1 ratio of tightly bound water per unit of ethylene glycol (EG) was achieved, additional water would induce swelling behaviour on the PEG chains.

Unfortunately limitations arise in the experimental characterisation of PEG's dynamic behaviour due to its relatively small length and extreme flexibility [347]. This is particularly prevalent in the case of low molecular weight PEG oligomers (e.g. pentamers), which are of particular interest for self-cleaning surface design. Limitations in experimental characterisation combined with the desire to understand the surface grafted behaviour of this 'popular' polymer have instigated the use of computational modelling and in particular classical force-field molecular dynamics [194, 348-351]. However, the majority of molecular dynamics studies have so far concentrated on the conformation, chain dimension and overall behaviour of isolated PEG chains in solution. To the best of our knowledge, there has been no fully-atomistic molecular dynamics study investigating the hydration induced conformational transitions of low molecular weight PEG chains grafted on different substrates.

In this thesis, we use force-field molecular dynamics to investigate the hydration induced response of PEGylated substrates at various temperatures. Substrates included inorganic and organic films in the form of silica and polyester respectively, with various PEG coverage densities examined. These interfaces are prominent in both biological and non-biological systems [352], as shown by some of the examples described above. Understanding the behaviour and interactions in these systems at the nanoscale [353-355] will facilitate design of responsive surfaces for applications in industry and medicine.

4.3. Method

4.3.1. Models of PEG grafted silica and polyester substrates

Silica and polyester models were constructed as detailed in sections 3.5.1 and 3.5.2. The silica model was a periodically replicated three-dimensional cell with a vacuum spacer in

the z direction and 3D periodic boundary conditions to mimic a 2D periodic silica film. For all subsequent simulations the surface, OH groups remained free to move, while the underlying SiO₂ atoms were kept fixed (constrained) at their initial x, y and z coordinates. Unlike silica, the polyester model lacks hydroxyl groups at the outer surface layer and therefore, attachment of hydroxyl residues onto polyester substrates was required [291, 292, 356] to enable subsequent covalent tethering of PEG derivatives [340].

PEGylation of both silica and polyester substrates was undertaken as described previously (Section 3.5.3). The PEGylated polyester and silica substrates with a finite number of OH groups unreacted (“grafting to” approach) are denoted PolyOH-σPEG_n and SiOH-σPEG_n respectively, while Poly-σPEG_n denotes PEGylated polyester surfaces with no OH groups unreacted, attained from the ‘grafting from’ method. The parameter σ represents the grafting density of PEG chains in units of PEG molecules per unit area, and the subscript (n) represents the degree of PEG oligomerization. PEG chains were tethered to polyester at a surface density ranging between 0.29-1.00 PEG/nm² and to silica at a density ranging between 0.13-0.94 PEG/nm². We considered PEG pentamers (n=5) and octamers (n=8) which display a free radius of gyration of ~4.8 Å and 6 Å respectively. A summary of all substrate models examined is presented in Table 4.1.

Table 4.1 Summary of substrate models

Substrate	Description	Residual silanol coverage density (OH groups per nm ²)	PEG coverage density (PEG per nm ²)	PEG chain length
Poly-σPEG ₅	PEGylated polyester without residual OH sites	n/a	0.29-1.00	5
Poly-σPEG ₈				8
PolyOH-σPEG ₅	PEGylated polyester with residual OH sites	4.36-5.07	0.29-1.00	5
PolyOH-σPEG ₈				8
SiOH-σPEG ₅	PEGylated silica with residual OH sites	3.23-4.04	0.13-0.94	5
SiOH-σPEG ₈				8

4.3.2. Computational details

The COMPASS force field [253], optimised for the simulation of condensed phase polymers and organic/inorganic interfaces was used to evaluate the inter- and intra-molecular interactions within the all-atom models. The COMPASS force field has been demonstrated to predict cohesive properties of an extensive number of polymers including polyethylene glycol oligomers [357]. Energy minimisation was performed to relieve any induced strain in the constructed models prior to molecular dynamics simulations. For energy minimisation, non-bonded interactions were calculated using the Ewald procedure with an accuracy of 0.01 kcal mol⁻¹ and an update width of 1.0 Å. The conjugate gradient algorithm was used for energy minimisation, with an energy convergence criterion of 0.01 kcal mol⁻¹ Å⁻¹. For MD procedures, non-bonded interactions were calculated using the atom-based summation method with a cutoff radius of 15.5 Å, a spline width of 5.0 Å and a buffer width of 2.0 Å. A long-range vdW tail correction was applied for non-bonded interactions larger than the cutoff radius. A 1.0 fs time step was used for the NVT dynamics, utilising the Andersen thermostat [266] to control the temperature with a collision ratio of 1.0. All systems were equilibrated by ensuring that no energy drifts occur during the data collection stage of MD. Analysis of properties for all substrates listed in Table 4.1 was undertaken over the final 1 ns of equilibrium MD that continued for the total time specified in the next section for each system.

4.3.3. Simulating the hydration induced response of PEG grafts

Having prepared the PEGylated substrates, we utilized a molecular dynamics (MD) procedure that emulates the wetting (hydration) and drying (dehydration) of the grafted films [338]. To represent a fully hydrated state we use a flexible simple point charge (SPC) water model [253] to explicitly solvate the systems and a vacuum environment to emulate a de-

hydrated state. PEG chains were initially extended in the direction normal to the surface plane prior to MD in explicit solvent (hydrated state), where a ~ 20 Å water layer was added to solvate the PEGylated substrates with water density of $1 \text{ g}\cdot\text{cm}^{-3}$, as shown in Figure 4.1a. The water layer extended over 30 Å from the terminal PEG unit and a ~ 30 Å vacuum spacer was also added above the water layer. MD simulation of these systems was then undertaken for 2 ns at temperatures of 298 K and 370 K. After simulations in the aqueous (W) environment, PEG chains were subjected to dehydration by removing water molecules and undertaking MD of the PEGylated films in a vacuum (V) environment. A schematic diagram of the setup is shown in Figure 4.1b. Simulation of the vacuum systems was again undertaken for 2 ns at a temperature of 298 K and 370 K. Once simulated in the vacuum environment, resultant systems were transitioned back to a fully hydrated environment (Figure 4.1c) by undertaking molecular dynamics in solvated systems for 2 ns at temperatures of 298 K and 370 K.

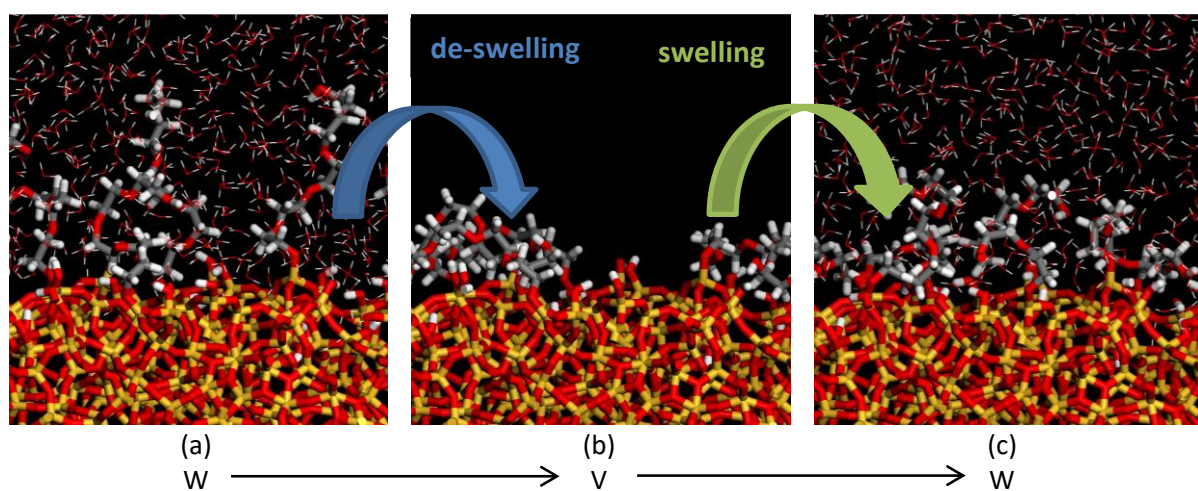


Figure 4.1 Typical model setup highlighting dehydration (W(a) \rightarrow V(b) transition) and hydration (V(b) \rightarrow W(c) transition) of PEGylated substrates. Colour codes: white-hydrogen, grey-carbon, red-oxygen and yellow-silicon.

We monitored the height of the grafted PEG chains in both dry and wet environments over the final 1 ns of equilibrium MD. This height was defined as the vertical distance from the anchor point (reacted O atoms) to the uppermost atom of the PEG. A change in chain

height (Δh) was then determined according to the following: $\Delta h = h_w - h_v$ where h_w and h_v represents the chain height in the water and vacuum states respectively. During dehydration (W \rightarrow V transition), a positive change in chain height (Δh) indicates a collapse of the grafted molecules, while the hydration induced transition (V \rightarrow W transition) is expected to result in swelling of the grafts. We also monitored the shape of the tethered PEG chains by calculating their radius of gyration in the xy plane as a function of distance from their individual anchor points in the direction normal to the surface (z axis). These profiles were then mirrored about the z -axis providing a visual representation of the chain-occupied volume.

4.4. Results

The majority of the results presented henceforth are focused on PEGylated pentamer surfaces. This has been undertaken to focus the discussion on qualitative trends common to pentamer and octamer systems. Any difference in behaviour will be highlighted.

4.4.1. De-swelling of PEGylated surfaces upon drying

When the hydrated PEG chains are subjected to dry conditions (W \rightarrow V transitions), they exhibit a collapse manifested by a change in chain height (Δh). Figure 4.2 shows that the extent of collapse is strongly dependent on the chemical nature of the substrate. PEG chains grafted onto silica demonstrate a significant collapse, particularly within the low coverage density range (σ) of 0.13 – 0.5 PEG per nm². PEG chains grafted onto polyester substrates also exhibit a dehydration induced collapse, but far less pronounced compared to silica. The difference between silica and polyester substrates is particularly notable at coverage densities below 0.5 PEG per nm² where the chains are adequately isolated from one another. This is in agreement with previous experimental studies which have suggested that in the low grafting density regime, the response of the grafted chains is strongly dependent on the nature of the substrate [358, 359]. The conformation of the chains is depicted in Figure 4.3, which displays

the radius of gyration of the chains in the xy plane, as a function of vertical distance from their anchor point. It can be seen from Figure 4.3a and b that the de-swelling of PEGylated silica can be characterised by two types of key conformational transitions during dehydration: an extended-to-mushroom transition at high grafting densities (0.94 PEG per nm²) and an extended-to-pancake transition at low grafting densities (0.13 PEG per nm²). In contrast, dehydration of PEGylated polyester (Figure 4.3c and d) is characterised by a slight compression of the chains in the lateral direction and limited de-swelling perpendicular to the surface. Overall, PEG chains tethered onto polyester display a globule-like conformation in both wet and dry environments, which explains the limited response observed for these systems. These qualitative trends detected for pentamer chains were also observed for octamers, although for the latter, the degree of collapse was greater due to the longer tethered segments.

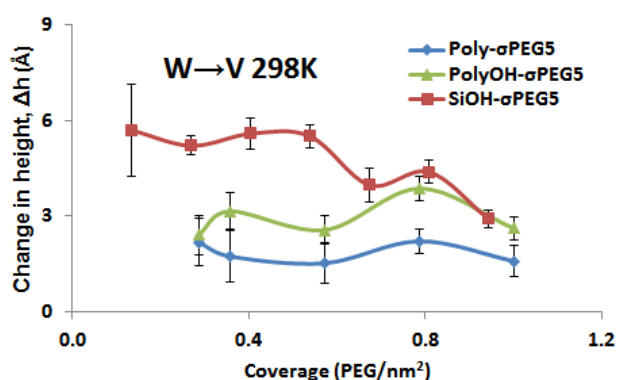


Figure 4.2 Change in PEG height (Δh) during de-swelling as a function of coverage density for PEG5 grafted substrates simulated at 298 K. Error bars represent the standard deviation.

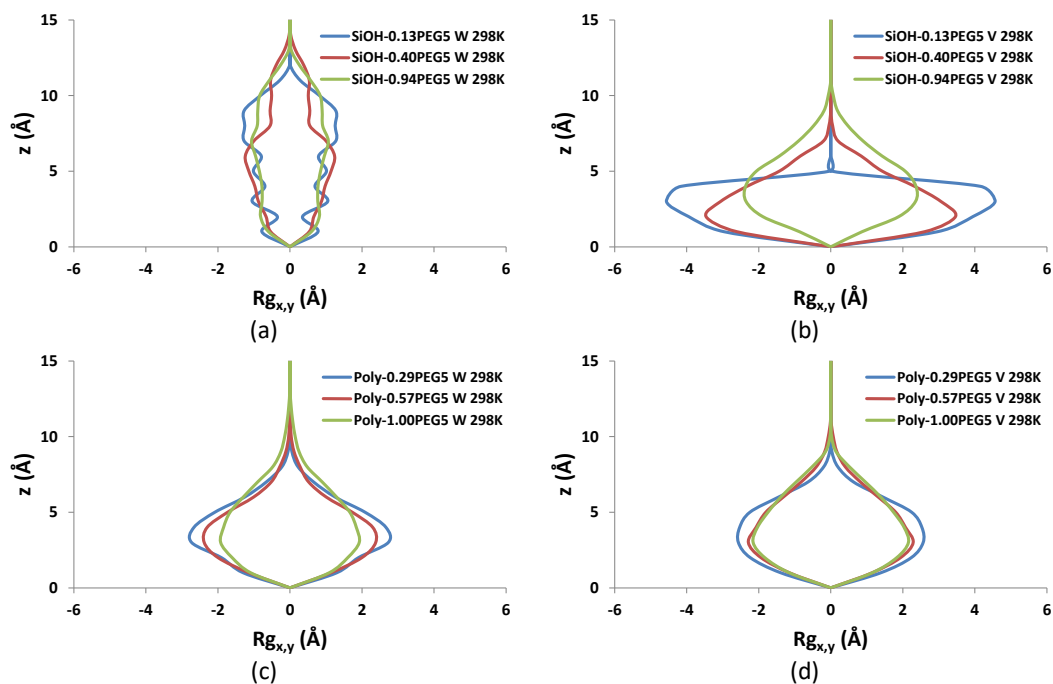


Figure 4.3 Radius of gyration profiles for PEG in the lateral (x-y) plane as a function of (z) for PEGylated silica in water (a) and vacuum (b) and PEGylated polyester in water (c) and vacuum (d). Simulations were at 298 K for low, intermediate and high coverage densities.

Our simulations indicate that the dehydration induced collapse of PEG octamers is strongly influenced by temperature. At 370 K the extent of collapse is reduced relative to the room temperature transition (Figure 4.4). This behaviour is observed for both silica and polyester grafted films and is associated with the conformation of the grafted chains in water. At 370 K, the octamer chains adopt a partially collapsed state in water (Figure 4.5a) while at 298 K, they display a much more extended chain conformation (Figure 4.5b). This temperature induced collapse is a result of expulsion of interfacial waters and the breaking of intermolecular hydrogen bonds between water and PEG segments. This is shown in Figure 4.6 where we observe an increase in the inter-molecular hydrogen bonding between water and PEG chains for systems simulated at 298 K in comparison to systems simulated at 370 K. Such temperature sensitive solubility usually originates from the existence of a lower critical solution temperature (LCST) beyond which the polymer becomes insoluble in water. PEG has indeed been shown to exhibit a low critical solution temperature of ~ 371 K [360].

Interestingly, the LCST has been shown to decrease with increasing molecular weight [360, 361], which may explain why the octamer tethered chains are more sensitive to this temperature induced transition compared to their pentamer counterparts.

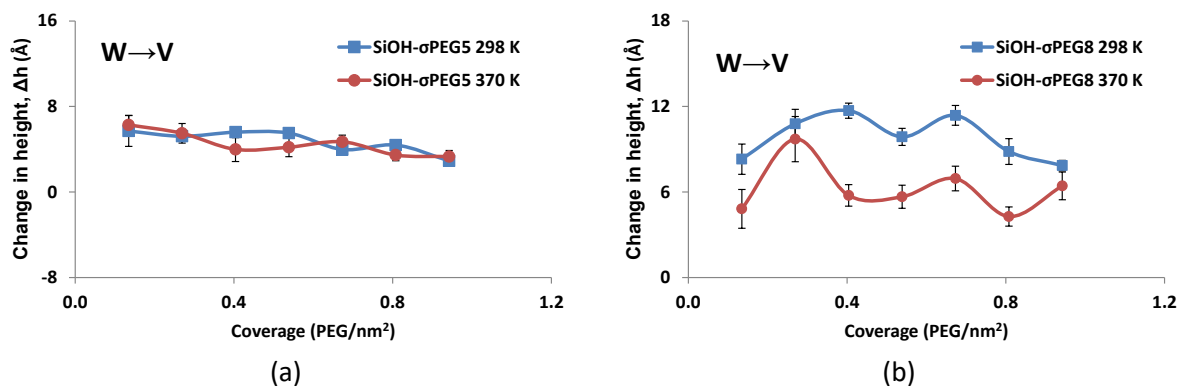


Figure 4.4 Change in PEG height (Δh) during the W→V transition as a function of coverage density for (a) SiOH-σPEG5 and (b) SiOH-σPEG8 systems simulated at 298 K and 370 K. Error bars represent the standard deviation.

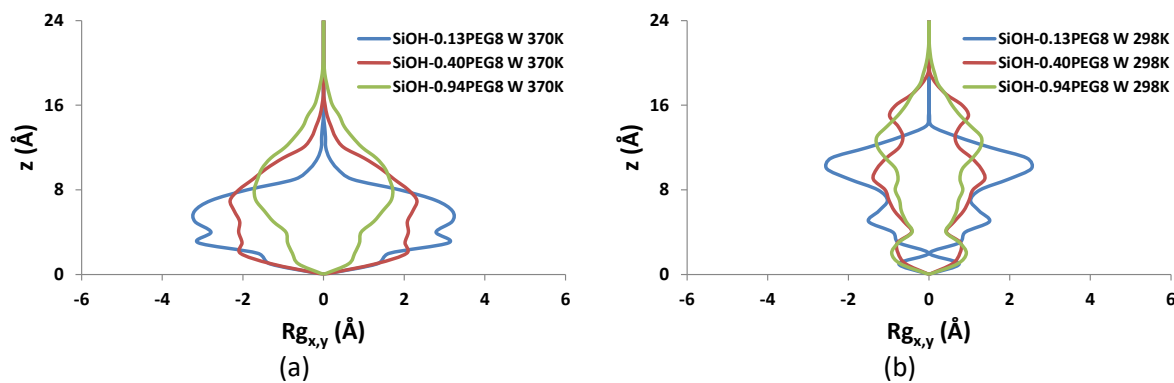


Figure 4.5 Radius of gyration profiles for PEG in the lateral (x-y) plane as a function of (z) for PEGylated silica during de-swelling at (a) 370 K and (b) 298 K for low, intermediate and high coverage densities.

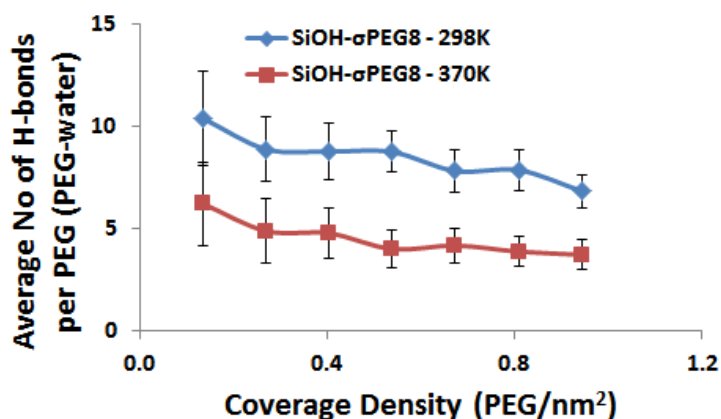


Figure 4.6 Average number of inter-molecular H-bonds per PEG between available donor-acceptor pairs in PEG and water as a function of coverage density for SiOH- σ PEG8 systems simulated at 298 K and 370 K.

4.4.2. Swelling of PEGylated surfaces

When the dried films were immersed in water they exhibited negligible swelling within the timeframe of our simulation (Figure 4.7), indicating a slow response to solvation after the chains have collapsed onto the surface in dry environments, the effect especially prominent for PEGylated polyesters. It appears that the energy requirements for a reversible wetting-dewetting response depend on the initial conformational state of the system. The simulations showed that the brushes fully extended in water exhibit a quick collapse when dehydrated. This collapsed layer forms a densely packed zone at the surface which slows down diffusion of water into the film, as seen in Figure 4.8, showing a reduction in the density of water near the PEG film boundary as a result of chain collapse during dehydration.

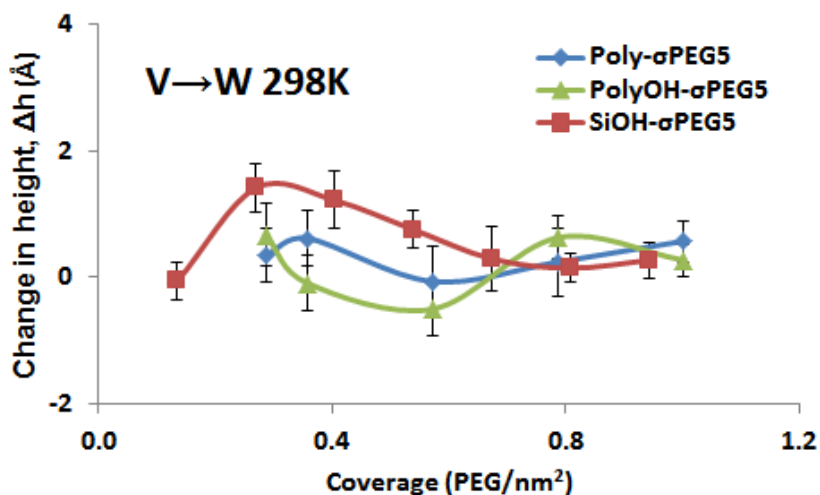


Figure 4.7 Change in PEG height (Δh) during swelling as a function of coverage density for PEG5 grafted substrates simulated at 298 K. Error bars represent the standard deviation.

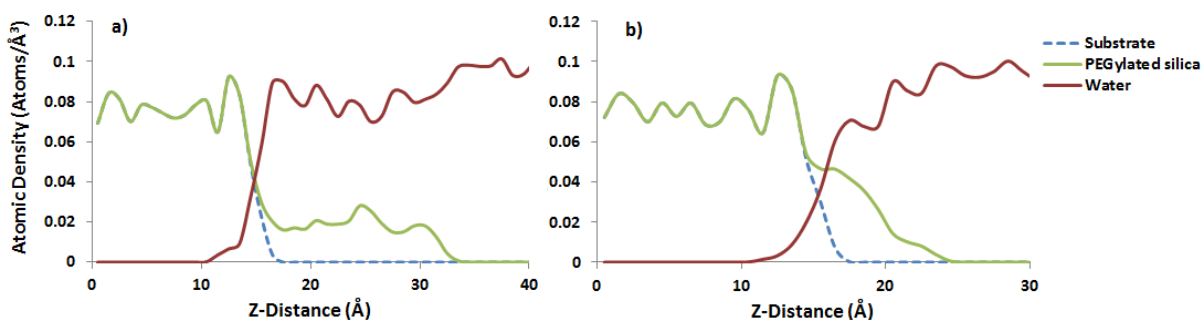
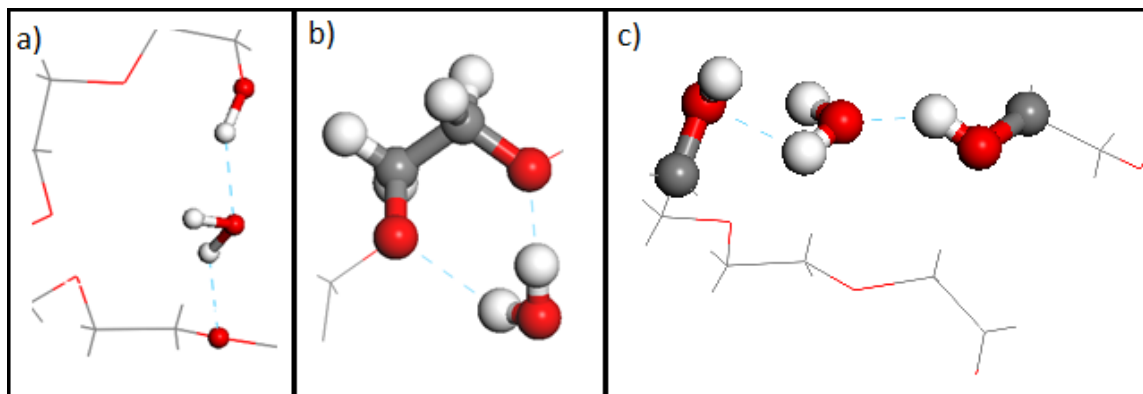


Figure 4.8 Atomic density profiles of $\sigma = 0.40$ pentamer PEGylated silica systems at 298K (a) before and (b) after dehydration.

Work by Chen [21] has suggested that limited swelling will occur until a ratio of 1:1 of tightly bound water per EG unit is achieved, at which point additional water will interact with the hydrated chains causing swelling of the chains. Figure 4.9



shows the average number of intermolecular hydrogen bonds between pentamer PEG systems

and water. Before dehydration, the PEG chains adopt an extended conformation in water, and there is generally more than 1 hydrogen bond per EG unit. Post-dehydration, the tethered segments maintain a collapsed state despite re-immersion into water. In this case there is less than 1 hydrogen bond per EG unit, re-affirming that 1:1 H-bonding ratio is needed for full hydration of the chains. It can then be assumed that the collapsed layer we observe in our simulations most likely does not correspond to an equilibrium structure but constitutes a kinetically trapped conformation of the layer.

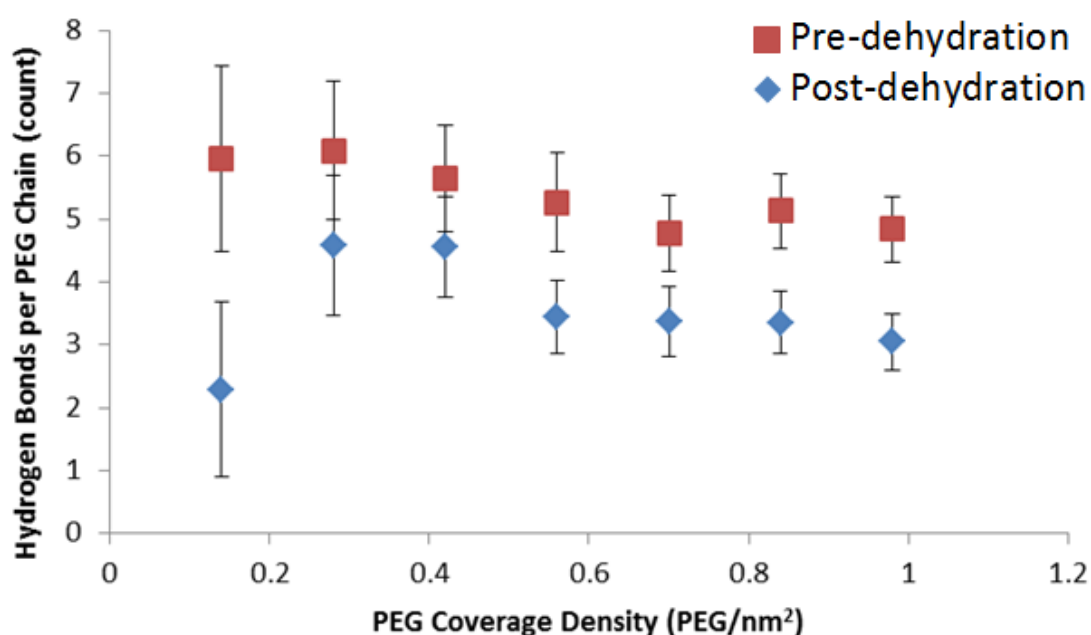


Figure 4.9 Average number of intermolecular hydrogen bonds between PEG and water before and after dehydration of pentamer silica systems.

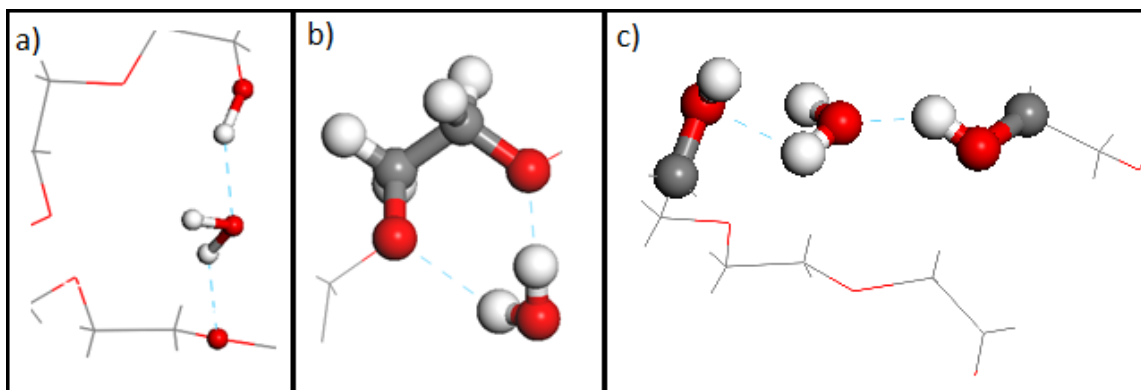


Figure 4.10 Snapshots of the three types of hydrogen bonding networks formed. (a) intra-molecular hydrogen bonding between PEG repeat units (b) intra-molecular hydrogen bonding of water to PEG, encouraging

the trans-trans-gauche conformational adoption as suggested by Gaub *et al.* [346]. (c) inter-molecular hydrogen bonding of water.

Investigation into the water structuring near the PEG layer revealed three key types of water interactions. At low hydration levels (1-3 H-bonds per chain), the involvement of water appears to assist in forming an extended (more than one EG unit apart) intra-molecular H-bonding network (Figure 4.10a) causing the tethered chain to ‘backfold’ and adopt globular states. As the chains became more hydrated (3-5 H-bonds per chain), water molecules are still involved in intra-molecular interactions; however, in this case, the water mediated H-bonding network is formed between neighbouring EG repeat units, which promote a trans-trans-gauche conformation of the chains (Figure 4.10b). At the highest levels of solvation (>5 H-bonds per chain) we begin to see the formation of inter-molecular H-bonds between adjacent PEG molecules, promoting an extended PEG chain conformation (Figure 4.10c).

Further to the involvement of water in swelling, there have been other studies [146, 147] which have inferred that these trapped waters interacting with the oligomer oxygen are critical to anti-fouling behaviour. These works have suggested that during protein adsorption, PEG chains are compressed, releasing the trapped water and resulting in a significant thermodynamic penalty on the incoming contaminant. With this in mind, it becomes apparent that the intermediate-high coverage densities studied may be more appropriate for an anti-fouling surface, due to their ability to trap greater amounts of water molecules, with 5-6 hydrogen bonds per chain still possible in the pre-hydration state. However, we believe further investigation of the dehydration mechanics is necessary, especially if the re-swelling of these chains is prohibited due to unfavourable configurations formed in a vacuum environment, or are we presented with a trade-off in the re-swelling vs trapping of water in dry environments.

4.4.3. Effects of surface hardness and roughness

During dehydration, we observe a decrease in surface roughness for silica based substrates, while for polyester we observe no notable change. The roughness of silica is consistently higher than polyester in both wet and dry environments and across all coverage densities despite the fact that the end-grafted chains on both silica and polyester can adopt globule-like conformations (Figure 4.3b and d). Previous studies [340, 362] have shown that polyester is far more flexible than silica and is richer in the atomic-scale surface irregularities. Moreover, the flexibility of the polyester substrate provides a means for the formation of surface cavities as previously discussed [121, 291, 363]. The natural flexibility of the polyester substrate allows for significant rearrangement of tethered chains, while asperities along the surface of the polyester provide ample volume for the tethered chains to sink into. As a result, PEG chains are able to adopt a more compacted, denser arrangement on polyester compared to silica, in both aqueous and non-aqueous environments. To confirm this finding, we present density profiles of PEGylated substrates in dry environments (Figure 4.11). The solid lines in the profiles depict the atomic density along the perpendicular axis of the grafted films and the perforated lines mark the substrate/PEG interface boundary. Along the solid line, the point at which the density begins to decrease marks the onset of the surface boundary, around ~ 15 Å for silica (Figure 4.11a) and ~ 18 Å for polyester (Figure 4.11d). For PEGylated polyesters, we observe that the tethered chains display a surface profile that overlaps the substrate boundary, indicating penetration of the polyester by the PEG chains. In contrast, the concentration profiles for PEGylated silicas are characterised by a distinct peak away from the substrate boundary (around ~ 19 Å), associated with the protruding tethered chains (Figure 4.11c). Furthermore, for the polyester surfaces, the concentration of atoms (atomic density) at the substrate-chains interface increases significantly, indicating a more

compacted, denser surface film (Figure 4.11b). These trends were also detected for octamer tethered chains.

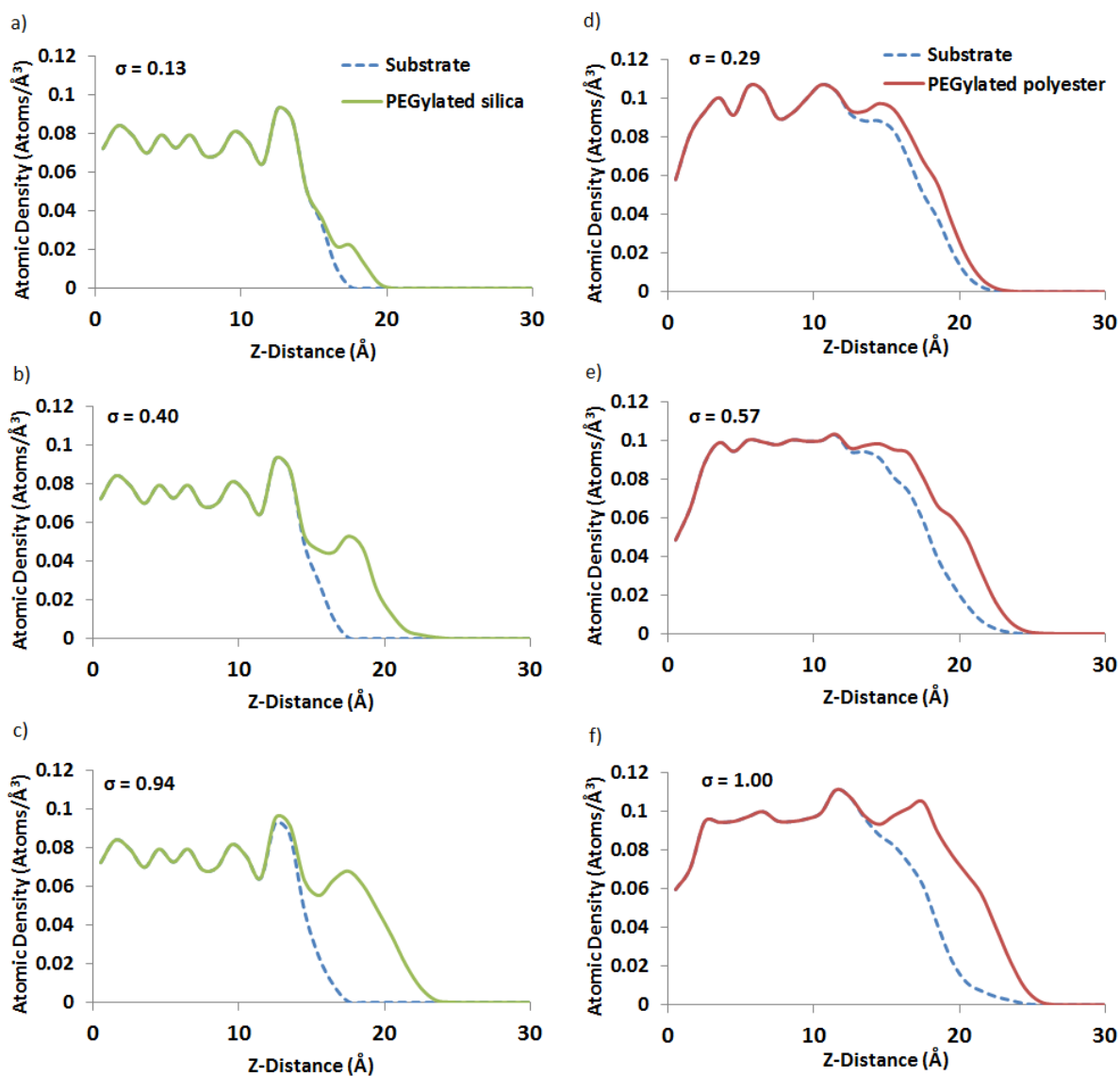


Figure 4.11 Atomic density profiles of PEGylated silica (a-c) and polyester (d-f) at low (a and d), intermediate (b and e) and high (c and f) coverage densities. PEGylated with PEG5 chains and simulated in vacuum at 298 K.

4.5. Conclusion

In this chapter we investigated the hydration-induced response of PEGylated substrates that include soft, organic polyester and hard, inorganic silica surfaces. PEG chains grafted onto silica exhibit significant de-swelling compared to chains grafted onto polyester.

The natural flexibility of the polyester substrate allows for significant rearrangement of tethered chains, with asperities along the polyester surface providing ample volume for the tethered chains to extend into and adopt a more compact and dense arrangement compared to silica, in both aqueous and non-aqueous environments. The difference between the substrates is particularly notable at low coverage densities where the chains are more spaced out.

The de-swelling of PEGylated silica can be characterised by an extended-to-mushroom transition at high grafting densities (0.94 PEG per nm²) and an extended-to-pancake transition at low grafting densities (0.13 PEG per nm²). In the extended conformation state, the PEG chains form more than 1 hydrogen bond per monomer unit with water. Below this ratio, the tethered PEG chains maintain a collapsed state despite the presence of water. We show that inter-molecular hydrogen bonding responsible for the conformational state of the tethered chain in water can be temperature controlled. At temperatures close to or higher than the low critical solution temperature of PEG, the extent of de-swelling can be reduced. This is attributed to the highly dynamic hydrogen bonds between PEG and water due to the thermally induced fluctuations.

Due to the significant loss in responsive behaviour observed for polyester surfaces, it was decided to investigate the effect of functionalised silica substrates for the remainder of this project.

Chapter 5

5. Elucidating molecular mechanisms of PEG and POX anti-fouling coating efficacy

5.1. Overview

In the previous chapter we assessed the effect of substrate hardness and chemistry on the responsive behaviour of functionalised surfaces, where it was concluded that silica surfaces significantly out-perform the soft polyester surfaces. In this chapter, we assess how chemistry and surface density of commonly used anti-fouling surface ligands affect the interfacial properties relevant to biofouling.

We compare the hydration, heterogeneity, and chain dynamics of poly(ethylene glycol) (PEG) and poly(2-oxazoline) (POX) modified silica surfaces. We show that PEG systems exhibit greater chain dynamics, whilst POX systems show superior hydrophobicity and hydration behaviour. Furthermore, the observed structure-property relations for the PEG and POX modified surfaces provide an improved molecular understanding of the effects of molecular features on anti-fouling properties, and highlight the importance of entropic barriers associated with surface ligand mobility and interfacial water structure and dynamics for anti-fouling efficacy.

5.2. Introduction

Over the last decade, significant research efforts have focused on discovering anti-fouling surface coatings with good efficacy, robustness, and design simplicity. However, the ability to design more effective anti-fouling coatings is limited by the paucity of fundamental knowledge on how these surfaces behave at a molecular level. Existing theories that attempt to explain anti-fouling coating efficacy are dated (late 90s and early 2000s) and are often conflicting. This has arisen because of the difficulty of studying these three phase systems at the molecular level using experimental techniques [31], hampering rational design and development of more effective coatings [4], and vital experimental validation of molecular level theories and simulations.

Computational simulations can provide a valuable adjunct to experiments in elucidating the important molecular interactions responsible for anti-fouling behaviour, and in supporting one or more of the anti-fouling theories summarised earlier in Section 1.8. POX has attracted significant attention as an alternative to PEG in biofouling applications [212-214]. Recent work elucidated its low biofouling properties [214, 215] and good biocompatibility [216-218], stimulating interest in POX as a valuable biomaterial [219] and anti-fouling coating [109, 219, 220] for biomedical applications [221, 222]. The hydrophobicity of the monomer, and resulting wettability of the coatings, are believed to control the anti-fouling efficacy of POX. The methyl and ethyl substituted analogues (PMeOx and PEtOx) have been shown to suppress protein adsorption [176, 212, 219, 220, 225, 228] while the propyl analogue (PPrOx) promotes cell adhesion and growth [226, 228]. It has been proposed that this behaviour is due to the increased length of the hydrophobic propyl side chain of the PPrOx coating providing larger hydrophobic contact. There are several experimental studies comparing the anti-fouling efficacy of PEG and POX coatings [212, 213, 229, 230]. Whilst it is clear that both polymers show remarkable properties, such

as imparting stealth abilities (avoiding immune response) for drug-delivery and protein resistance for anti-fouling surfaces, POX coatings generally outperform PEG coatings in most cases. This is due to several valuable properties of POX. In oxidative environments POX coatings are more stable than PEG coatings [212], the degradation products of PEG chains (e.g. peroxides) are toxic [213] whilst those of the more stable POX remain non-toxic [212, 213], and, whilst degraded PEG coatings may retain some anti-fouling properties [231], protein resistance usually declines rapidly [212, 232, 233].

Recent simulation studies have considered the behaviour of short PEG chains tethered to silica surface in the aqueous environment [121, 146, 194, 195, 292, 362, 364]. Despite the publication of a large number of detailed experimental studies on anti-fouling coatings, a molecular level understanding of POX surfaces is still far from complete. Here we use all-atom molecular dynamics (MD) simulations to systematically compare the properties of PEG and POX surfaces. Our results also allow the existing theories of anti-fouling surfaces to be examined for consistency with these molecular interactions.

5.3. Methods

A short propyl spacer separates PEG hexamers and POX tetramers from the silica surface (constructed as per Section 3.5.2), with methyl (PMeOx), ethyl (PEtOx) and propyl (PPrOx) as shown in the schematics (Table 5.1). Both PEG and POX Systems were grafted in a manner compatible with grafting to and grafting from methods [365] at coverage densities of 1.4, 2.2 and 3.0 chains/nm², corresponding to $\alpha = 0.32, 0.52, 0.71$, where α is the ratio of grafted chains to free silica surface hydroxyl groups.

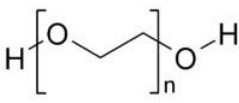
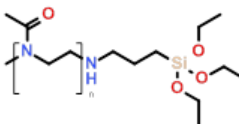
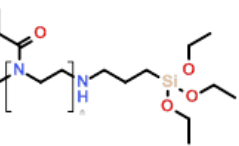
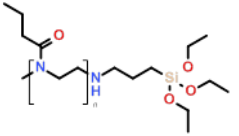
Systems were solvated using an explicit water layer of 80 Å thickness, with a 20 Å vacuum space above the water box added to create a pseudo air-water interface. Five replicas

were simulated using MD for 30 ns to accumulate statistics for the chain surface water and bulk water behaviour.

Simulation details

Simulations were performed using the LAMMPS [366] software with the CGENFF36 force-field used for the surface functionalization, and the CHARMM-compatible Cruz-Chu [254] silica parameters. The TIP3P [367] water model was applied, with the SHAKE [267] algorithm employed to constrain water bond length and angle. For the evaluation of non-bonded interactions, a twin-range cutoff of 0.8 and 1 nm were used for van der Waals interactions, with a 1 nm cutoff for electrostatics and the PPPM solver used to calculate the long-range damping effect. The energy minimizations were carried out using the conjugate gradient method with a convergence criterion of 10^{-4} kcal/mol energy tolerance and 10^{-6} kcal/mol.Å force tolerance. MD was performed in the NVT ensemble using a timestep of 1 fs and a temperature of 298 K was maintained by a Nosé-Hoover thermostat [264] with a 0.1 ps coupling time. Systems were simulated for 30 ns, and results averaged over the last 10 ns of simulation for 5 replicas, unless stated otherwise.

Table 5.1 Quantitative description of surfaces.

		Grafting Density (Chains/nm ²)			
		Low (1.37)	Medium (2.19)	High (3.01)	
Chain Type	<p>PEG</p> 	Surface Coverage (%)	92.0 ± 1.7	93.7 ± 1.8	96.2 ± 1.8
	Average thickness (Å)	22 ± 3	25 ± 4	28 ± 4	
	Hydrophobicity ratio	0.32 ± 0.01	0.33 ± 0.01	0.33 ± 0.01	
	D _{C-O} (Å)	-0.13 ± 0.01	0.34 ± 0.01	0.47 ± 0.01	
<p>PMeOx</p> 	Surface Coverage (%)	77.0 ± 3.3	80.9 ± 1.4	92.2 ± 1.4	
Average thickness (Å)	24 ± 4	27 ± 4	30 ± 4		
Hydrophobicity ratio	0.56 ± 0.01	0.59 ± 0.01	0.62 ± 0.01		
D _{C-O} (Å)	0.10 ± 0.01	0.54 ± 0.01	0.40 ± 0.01		
D _{O-N} (Å)	0.51 ± 0.01	1.31 ± 0.01	1.42 ± 0.01		
<p>PEtOx</p> 	Surface Coverage (%)	78.5 ± 2.8	83.5 ± 3.1	92.9 ± 2.1	
Average thickness (Å)	25 ± 4	29 ± 4	32 ± 4		
Hydrophobicity ratio	0.51 ± 0.01	0.55 ± 0.01	0.54 ± 0.01		
D _{C-O} (Å)	0.78 ± 0.01	1.05 ± 0.01	1.19 ± 0.01		
D _{O-N} (Å)	0.48 ± 0.01	1.14 ± 0.01	1.52 ± 0.01		
<p>PPrOx</p> 	Surface Coverage (%)	74.2 ± 4.3	87.4 ± 2.1	95.4 ± 1.7	
Average thickness (Å)	27 ± 4	30 ± 4	34 ± 4		
Hydrophobicity ratio	0.48 ± 0.01	0.50 ± 0.01	0.45 ± 0.01		
D _{C-O} (Å)	1.16 ± 0.01	1.58 ± 0.01	2.19 ± 0.01		
D _{O-N} (Å)	0.71 ± 0.01	1.35 ± 0.01	1.66 ± 0.01		

5.4. Results and Discussion

We employed molecular dynamics simulation to identify relationships between chain chemistry, grafting density, and interfacial properties. The two prevailing anti-fouling

theories, hydration theory and steric repulsion, drove a focus in this section on chain behaviour and interfacial hydration. The molecular level insight gained here can also aid interpretation of experimentally observed phenomena, and may allow identifications of functional groups with enhanced anti-fouling capacity.

Figure 5.2 shows the average atomistic composition of the interface in the direction perpendicular to the bulk surface for the low and high MPOX and PEG systems. The schematic in Figure 5.1 shows representations of the various components shown in Figure 5.2. The results presented below describe the relationship between average structure and dynamic behaviour of various components featured in Figure 5.1 with respect to chain chemistry and grafting density. Discussion of the grafted chain behaviour is presented first then the role of the interfacial water is discussed. The discussion is framed and informed by traditional anti-fouling theories, as well as previously identified factors which influence molecular adsorption on surfaces such as the atomic surface roughness, surface rigidity [121, 268, 287, 291, 292, 362, 364, 368] and dynamics [368].

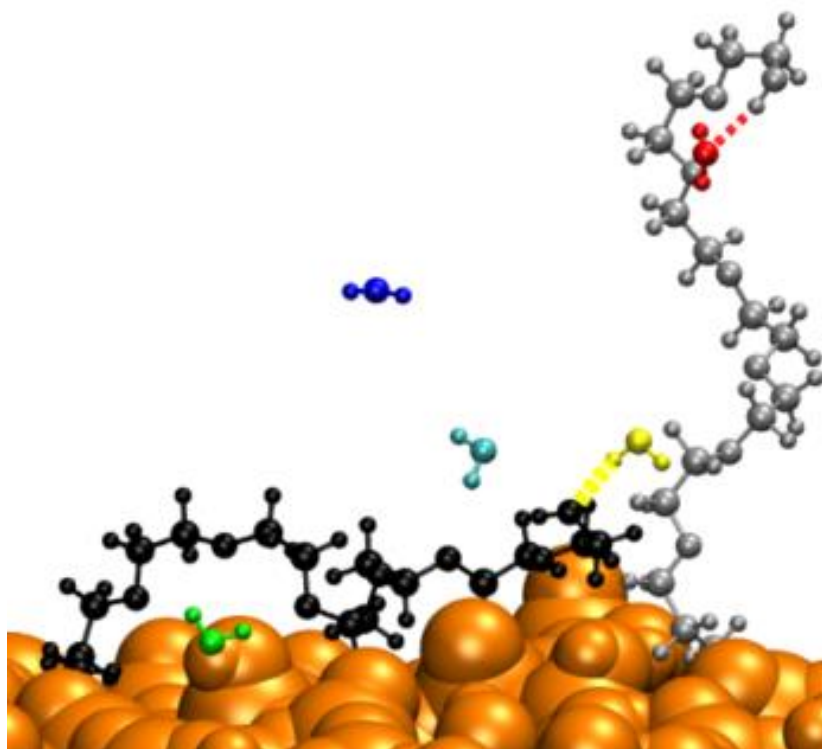


Figure 5.1 Schematic of PEG and water molecules for density plots in Figure 5.2. Colours: Silica (orange), PEG primer (black) and sweeping (grey) layers, surface-bound water (green), bulk water (dark blue). Water within 3.5 Å of the polymer layer is separated into H-bond donor (yellow), acceptor (red) or no H-bond (light blue).

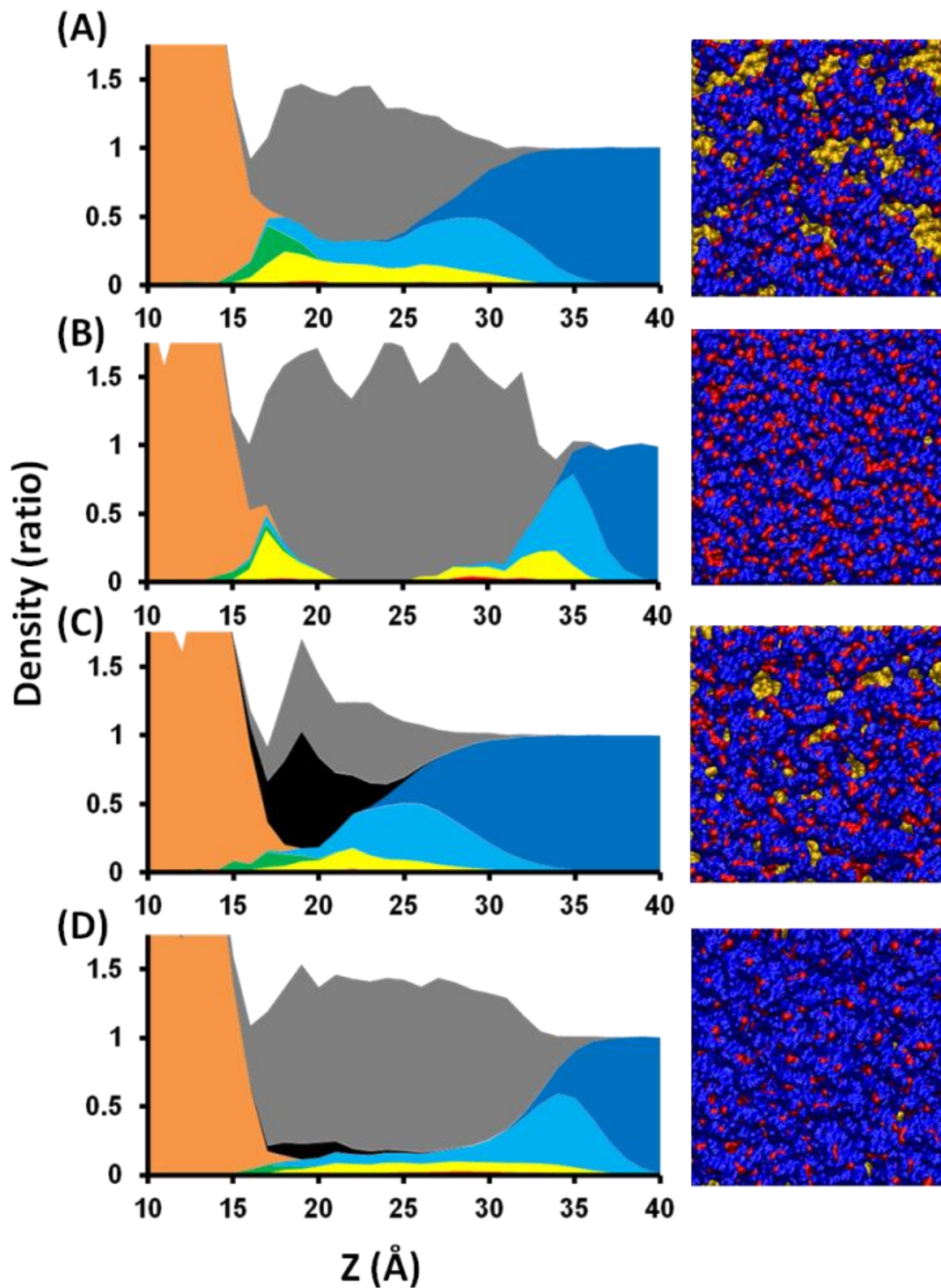


Figure 5.2 Z (left) and X-Y (right) profile of (A) Low PMeOx, (B) High PMeOx, (C) Low PEG, (D) High PEG. For Z profiles, density is normalised such that a value of 1 is the heavy atom density of bulk water. Colours represent silica (orange), polymer (grey), surface-bound water (green), bulk water (dark blue). Water within 3.5 Å of the polymer layer is separated into H-bond donor (yellow), acceptor (red) or no H-bond (light blue). For PEG systems, the polymer layer is broken into primer (black) and sweeping (grey) layers. For X-Y profiles, blue = hydrophobic segments of chains (CH₂, CH₃), red = hydrophilic segments (O, N, OH, NH) and gold = the exposed substrate.

5.4.1. Average Chain Structure

Chain z-length (normal to the surface) distributions for all systems are shown in Figure 5.3. Regardless of grafting density the distributions of POX systems become tighter around the mean with increasing side chain length. Similarly, for all three POX systems, the length distribution becomes more uniform with increasing grafting density. The average chain z-length correlates positively with side chain length. As discussed below, increased uniformity of the length distribution with side chain length does not influence the chain dynamics, however, the decrease in chain length variability will decrease interfacial roughness. Larger interfacial surface roughness increases the surface area, and allows a larger number of water molecules are in the interfacial region. This is reflected in the narrowing of the interfacial water bands from low to high grafting density as seen in Figure 5.2. Previous work has indicated that atomic scale roughness plays a role in enhancing anti-fouling efficacy [291]. Our results suggest that, regardless of side chain chemistry, well-ordered, uniform chains at the highest grafting density provide the least roughness and hence are likely to have lower anti-fouling efficacy.

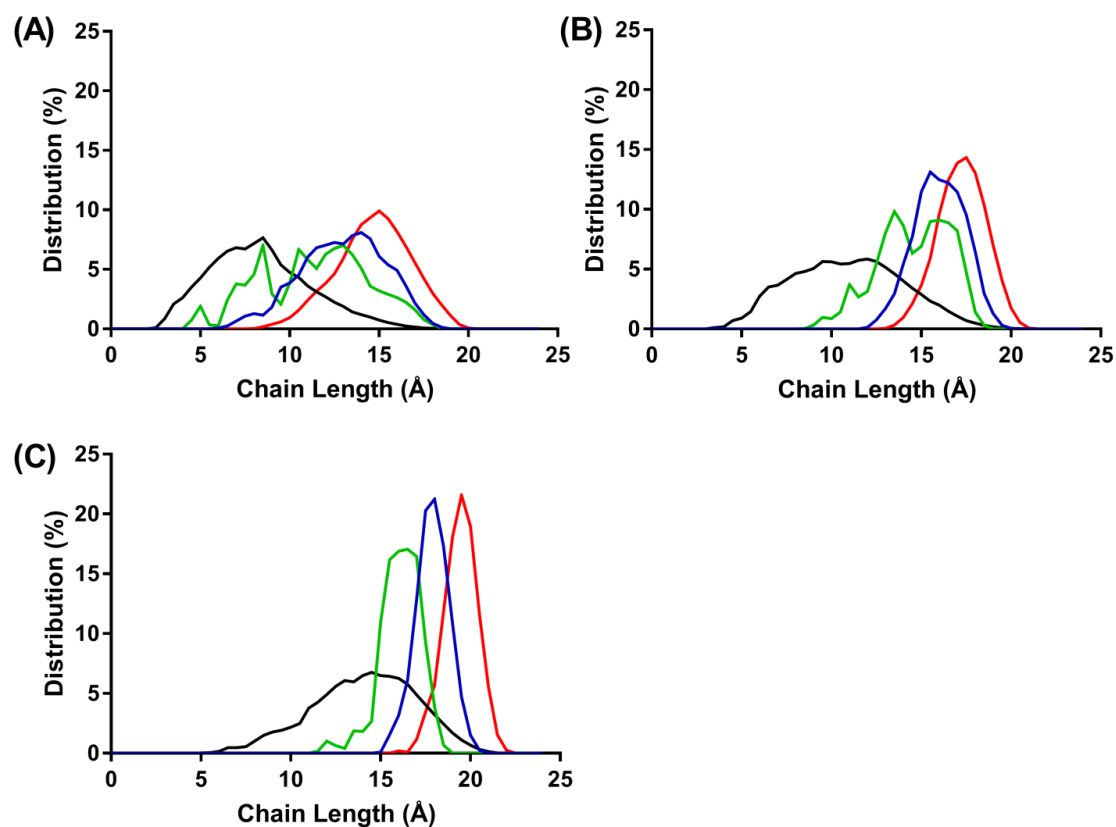


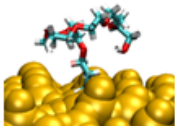
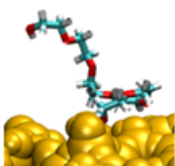
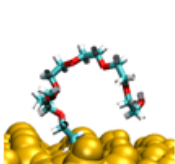
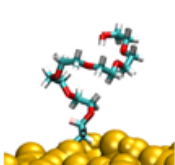
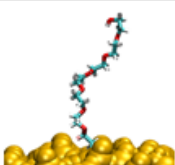
Figure 5.3 Chain z-length distribution plots for all systems at (A) Low, (B) Medium and (C) High grafting densities. Colours: PEG (black), PMeOx (green), PEtOx (blue) and PPrOx (red).

Surface coverage, characterised as the percentage of the silica substrate covered by functional chains and not exposed to the solvent, is summarised in Table 5.1. For POX films the presence of side chains, regardless of length, impedes collapse of the chains onto the surface. At low grafting density the chains do not collapse onto the surface, resulting in 74.2-78.5% surface coverage (Table 5.1). The space between chains is filled with water molecules and the water content does not drop below 40% of the bulk water density in the interfacial region. At medium grafting density there is an increase in the density of the polymer layers, and slightly less water permeation for all systems. Interestingly, medium PMeOx and PEtOx systems show similar amounts of hydrogen-bonded water to low grafting density systems (discussed later in the chapter), despite having lower water content. At high grafting densities

the POX layers are densely packed, with all systems showing 90-95% surface coverage and very little water permeation in the interfacial region.

Chain length distributions for the linear PEG chains are significantly different from those of the POX systems (Figure 5.3). The distributions are broader and centred about smaller values, despite PEG having a longer monomer length than its POX counterparts. The broader distributions indicate a higher degree of conformational flexibility, reflected in the dynamic behaviour discussed below. In comparison to the POX systems the length distributions do not increase uniformly with increasing grafting density suggesting a different mechanism than that discussed above.

Table 5.2 PEG chain conformations based on a twin height difference cut-off between the oxygen before PEG repeat units (O(0)), of the third repeat unit (O(3)) and the terminal unit (O(T)).

Conformation	O(0) - O(3) Distance (Å)	O(0) -O(T) Distance (Å)	Image
Pancake	$Z < 4$	$Z < 4$	
Hook	$Z < 4$	$4 < Z < 10$	
Arch	$Z > 4$	$Z < 4$	
Mushroom	$Z > 4$	$4 < Z < 10$	
Brush	$Z > 4$	$Z > 10$	

It has been well documented that one of the key characteristics associated with PEG's ability to reduce protein adhesion is its ability to adopt specific conformations in water. Importantly, it was identified that a flat or 'pancake' orientation of the PEG chains would likely result in an attractive PEG-protein interaction, whereas mushroom-brush conformations were likely to provide repulsive interactions [187, 188]. This is strongly related to the fact that compression of PEG chains is likely to increase the accessible surface area of the non-polar PEG segments, which encourage hydrophobic interactions that promote protein adsorption [189]. To investigate this, we studied five conformational states for PEG, based on distance cut-offs, as shown in Surface coverage, characterised as the percentage of the silica substrate covered by functional chains and not exposed to the solvent, is summarised in Table 5.1. For POX films the presence of side chains, regardless of length, impedes collapse of the chains onto the surface. At low grafting density the chains do not collapse onto the surface, resulting in 74.2-78.5% surface coverage (Table 5.1). The space between chains is filled with water molecules and the water content does not drop below 40% of the bulk water density in the interfacial region. At medium grafting density there is an increase in the density of the polymer layers, and slightly less water permeation for all systems. Interestingly, medium PMeOx and PEtOx systems show similar amounts of hydrogen-bonded water to low grafting density systems (discussed later in the chapter), despite having lower water content. At high grafting densities the POX layers are densely packed, with all systems showing 90-95% surface coverage and very little water permeation in the interfacial region.

Chain length distributions for the linear PEG chains are significantly different from those of the POX systems (Figure 5.3). The distributions are broader and centred about smaller values, despite PEG having a longer monomer length than its POX counterparts. The broader distributions indicate a higher degree of conformational flexibility, reflected in the

dynamic behaviour discussed below. In comparison to the POX systems the length distributions do not increase uniformly with increasing grafting density suggesting a different mechanism than that discussed above.

Table 5.2.

The surface coverage, characterised as the percentage of the silica substrate covered by functional chains and not exposed to the solvent, is summarised in Table 5.1. For POX films the presence of side chains, regardless of length, impedes collapse of the chains onto the surface. At low grafting density the chains do not collapse onto the surface, resulting in ~75% surface coverage. The space between chains is filled with water molecules and the water content does not drop below 40% of the bulk water density in the interfacial region. At medium grafting density there is an increase in the density of the polymer layers, and slightly less water permeation for all systems. Interestingly, medium PMeOx and PEtOx systems show similar amounts of hydrogen-bonded water to low grafting density systems (Table 5.4), despite having lower water content. At high grafting densities the POX layers are densely packed, with all systems showing 90-95% surface coverage and very little water permeation in the interfacial region. We examined the average conformational distributions of PEG chains (Figure 5.4) and transition behaviour (Table 5.3) with respect to these states.

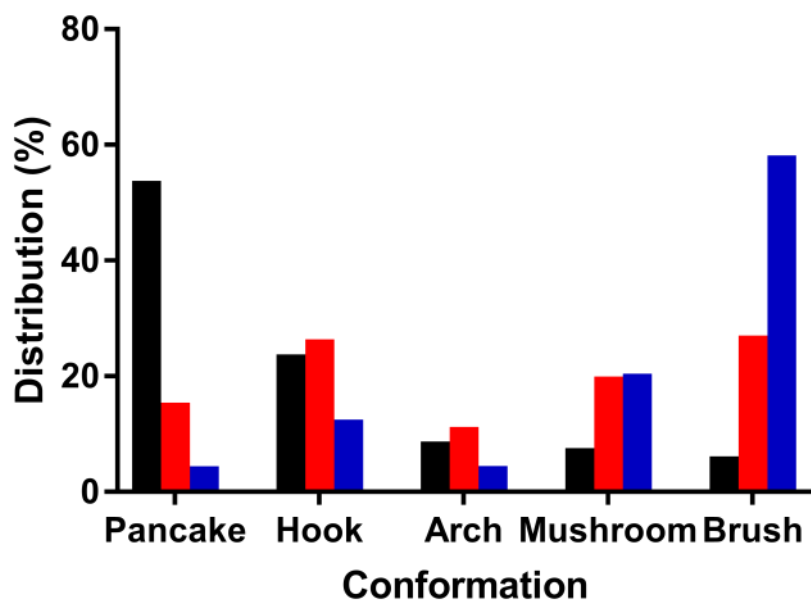


Figure 5.4 Distribution of PEG conformations for low (black), medium (red) and high (blue) grafting densities.

Table 5.3 Conformational Distribution – Shows the percentage breakdown for all transitions occurring during the simulations.

			Transfer To:				
			pancake	hook	arch	mushroom	brush
Transfer From:	Low	pancake	-	15	7	2	2
		hook	27	-	3	4	5
		arch	6	2	-	2	1
		mushroom	2	6	2	-	4
		brush	2	6	1	2	-
	Medium	pancake	-	5	7	2	2
		hook	7	-	1	7	7
		arch	7	2	-	5	2
		mushroom	2	5	5	-	13
		brush	1	7	1	12	-
	High	pancake	-	2	2	0	0
		hook	2	-	1	4	5
		arch	3	0	-	3	0
		mushroom	1	4	5	-	28
		brush	0	6	2	30	-

The relationship between the inter-chain separation distance and chain conformation has been reported previously [195], notably by Benková [192-194]. They noted a critical grafting density exists at 2.185 chains per nm², below which chains displayed strong interactions with the silica surface. At and above this value the chains adopted more extended/brush-like conformations. The results of our simulations are consistent with these observations, with more than 60% of the chains adopting pancake/arch regimes at low grafting densities, see Figure 5.4. When combined with the high percentage of PEG chains in the hook conformation (25%), it is evident that PEG-silica interactions are more favourable than PEG-water interactions. This strong interaction with the surface leads to high PEG surface coverage of ~92%, even at low grafting density, compared to 74-79% for the POX counterparts.

PEG chain behaviour can be categorised in terms of mobility and conformation. The chains are either behaving dynamically and undergoing frequent conformational transitions, or they are trapped in quasi-stable, relatively long-lasting (>1ns) conformations due to strong and persistent surface interactions. These chain categories have been named the sweeping and primer layers respectively (Figure 5.2(c,d and e)). It is the primer layer which leads to the increased surface coverage and results in very little water permeation in the interfacial region. At low surface coverage the percentage of chains in the primer layer is 43%, likely making the surface prone to fouling. An analysis of chain transitions (Table 5.3) provides an indication of how the primer layer is formed. Around 30% of all transitions lead to the hook conformation. From this hook state 27% of all transitions result in pancake conformation. This behaviour suggests that the hook state is an intermediate transitional state that fosters stepwise contact formation of the primer layer from the grafting point to the chain end.

At medium coverage densities there is a slight increase in surface coverage to 94%, and there is more even distribution of conformations. Approximately 25% of chains are still in the transition hook conformation, but the percentage in the pancake conformation has dropped from 53% to 15%. A substantial decrease in the number of transitions from the hook to pancake conformation is also observed. We conclude that the increased grafting density limits the ability of the chains to make stepwise contacts to form the pancake conformation due to volume exclusion effects of other grafted chains on the surface. The broad range of conformations this grafting density permits suggests it would be ideal if the anti-fouling ability of PEG coatings were due to spring-like compression/extension behaviour. We see a high population of transitions into both hook and arch conformations. However, at increased grafting density we see these chains preferring transitions into the higher energy mushroom and brush conformations.

At high grafting densities we approach the packing density of SAM surfaces and, unsurprisingly, we see a dominance of brush and mushroom conformations. Whilst some of these drop into a lower energy hook conformation, they quickly transition back into a brush/mushroom state. It is clear these chains are experiencing the lateral restrictions described by Benková, and are likely to result in increased PEG-protein interactions. It should be noted that the PEG chains in this study are significantly shorter than those used in Benková's work, with 66-80% lower molecular weight. This may explain why the medium grafting density systems show limited lateral repulsion compared to those in Benková's work.

We conclude that surface coverage is largely independent of POX side chain chemistry and that grafting density will determine the exposure of the substrate to biofouling material, with the increase in order at high grafting densities seeing decreased surface roughness. Conversely, the linear PEG chains collapse into a primer layer at low surface coverage and it is at higher surface coverages where the brush conformations exist that are known to promote anti-fouling efficacy. Due to the presence of the primer layer, surface exposure is largely independent of grafting density for PEG, in contrast to the POX systems.

5.4.2. Hydrophobicity

Recently, there has been significant research focusing on the effect of nanopatterned and heterogeneous surfaces to modulate the interplay between materials, the solvent environment and biological systems [107, 110, 369]. Since Ostuni [370] developed a simple model for examining hydrophobic patches, experimentalists have tailored heterogeneous interfaces with the patch length scales varying from microscale [371] to nanoscale [104, 106, 113, 114, 370, 372]. Using MD, Penna [368, 373] observed that nanoscale channels with domain sizes larger than a single chain width were too large and they facilitated hydrophobic

association. Whilst it is well known that atomic scale zwitterionic heterogeneity provides anti-fouling effects that can be achieved with homogenous coatings [235, 374, 375], to our knowledge there has been only limited investigation into the effect of the amphipathic character of polymers like PEG and POX on the anti-fouling performance of these chains (outside of limited discussion of hydrophobic/non-polar and hydrophilic patches [189]).

To examine this, we have plotted surface hydrophobicity (Figure 5.2 XY profiles) and calculated the hydrophobicity ratio (Table 5.1) of exposed heavy atoms to the solvent environment (carbon and oxygen/nitrogen atoms within 3.5 Å of interfacial water molecules), where a ratio of 1 = fully hydrophilic surfaces, and 0 = fully hydrophobic surfaces. Whilst POX chains show reasonable changes in hydrophobicity with grafting density, because of the flexibility of PEG chains we see a constant hydrophobicity ratio around 0.33, unsurprisingly the ratio of oxygen to carbon atoms in the repeating unit of PEG. The XY profiles (Figure 5.2) appear to show an increased hydrophilicity for PEG systems as the grafting density increases, however as seen in Table 5.1 the hydrophobicity ratio actually sees a very minor increase. This is due to the inherent flexibility of the PEG chains, described by the terminal C-O height in Table 5.1 (D_{C-O}) (z-distance from terminal carbon to oxygen, positive and negative value indicates the oxygen is above or below the carbon respectively). We see a slight increase from -0.13 Å at low grafting density, to 0.47 Å at high grafting density, suggesting that when a terminal carbon atom is most exposed to the solvent environment, the oxygen atom is still accessible.

Within the POX systems there is a significant relationship between side-chain length and hydrophobicity, with a shorter side-chain resulting in increased hydrophilicity for all grafting densities. For PMeOx systems, the hydrophilicity increases with grafting density. While PEtOx and PPrOx systems see a similar increase in hydrophilicity from low to medium grafting density, an increase in hydrophobicity is seen at high grafting densities that we again

attribute to the D_{C-O} length. For PMeOx systems we see very minor differences in D_{C-O} , fluctuating between 0.10-0.54 Å, with a consequential increase of 0.06 in the hydrophobicity ratio. For PEtOx systems we see a slight increase in D_{C-O} , from 0.78 Å at low grafting densities, to 1.05 Å at medium grafting densities, seeing an increase to the ratio (0.51-0.55). The slight increase in D_{C-O} to 1.19 Å at high grafting densities results in a decreased hydrophobicity ratio to 0.54. For PPrOx systems the grafting density appears important, as the ratio decreases from 0.50 to 0.45 when going from medium to high grafting density, and the D_{C-O} increases from 1.58-2.19 Å. Interestingly, there appears to be no correlation between D_{O-N} and the hydrophobicity ratio, with all systems showing an increased D_{O-N} as the grafting density increases.

5.4.3. Chain Dynamics

The sweeping mechanism proposed for long chains suggest that the dynamics of the chains at the interface can disrupt protein adsorption [136]. It was recently reported that increased dynamic behaviour of chains of varying length disrupts favourable short range interactions (hydrogen bonds etc.) and improves in anti-fouling efficacy [372]. Furthermore, a reduction in the chain mobility on contact with the protein suggests an entropic penalty working against protein adsorption [372].

Figure 5.5 shows the root mean squared displacement (RMSD) of the tethered chains for all systems. In Figure 5.5 it can be seen that the behaviour of POX systems at each grafting density is similar, indicating that increasing the length of side chain does not substantially restrict the chain dynamics. At low and medium grafting densities the PMeOx RMSDs have higher variance than the longer sidechain systems. This can be explained by the roughness of the chain length distributions (Figure 5.2) which show a noisy profile and multiple peaks, unlike the other POX systems. The grafting density has a significant impact

on the chain dynamics for the POX systems. At the highest grafting density, 3.0 chains per nm^2 , the RMSD values stabilize around 1 Å, suggesting that the tethered chains are in a very tightly packed configuration. There are substantial increases, approximately 100% averaged across the three systems, in the RMSD values of the chains when the grafting density is decreased from 2.2 to 1.4 chains per nm^2 . This absence of lateral crowding, along with limited chain collapse at the interface for the POX systems and increased interfacial hydration at the low grafting density, explains this increase in chain dynamics. The entropy penalty associated with protein adsorption arises from a loss of chain flexibility [372], rather than chain dynamics *per se*. The larger increase in RMSD from medium to low grafting density suggests that lower grafting density will be optimal for anti-fouling efficacy. However, as the total entropy penalty relates to not only the change in dynamics but also to the number of chains affected, both low and medium grafting densities should be investigated.

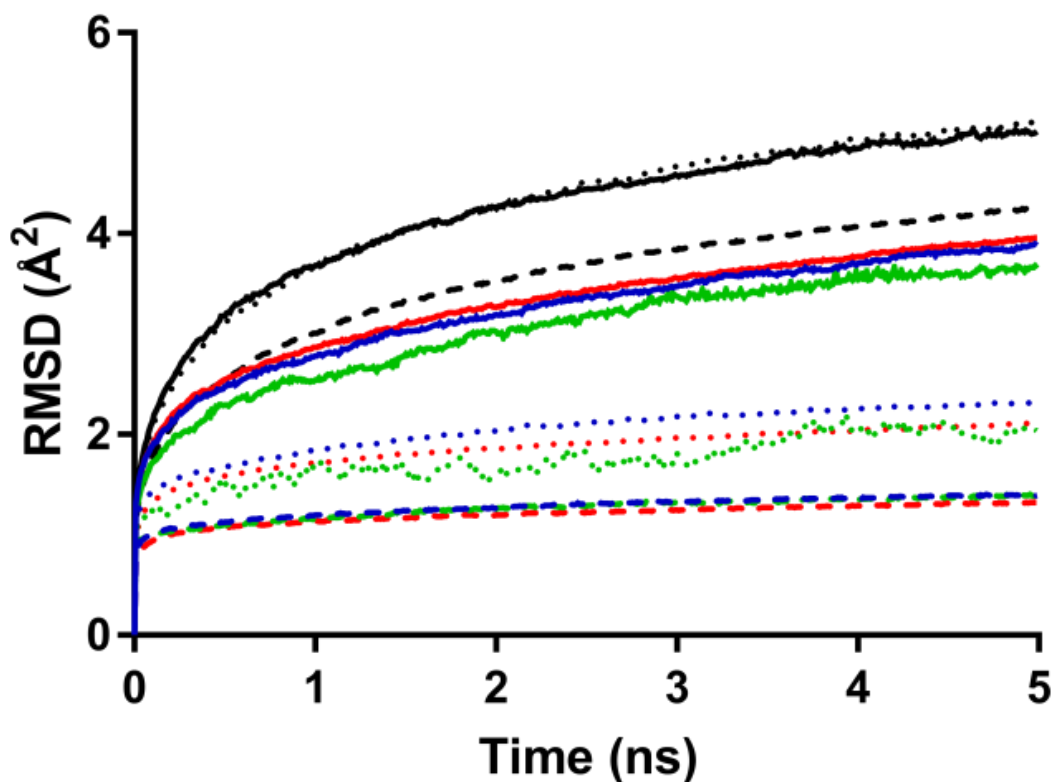


Figure 5.5 Average RMSD of chains: PEG (black), PMeOx (green), PEtOx (blue) and PPrOx (red) at low (solid) medium (dotted) and high (dash) coverage densities.

The dynamics of the PEG systems do not follow the same pattern as the POX. Linear PEG chains are more mobile than those in POX coatings, with all 3 grafting densities showing higher RMSDs than even the lowest grafting density of POX coatings. There is not the same increase in chain dynamics with decreasing grafting density for the PEG systems, with the profiles of 1.4 and 2.2 chains per nm^2 being very similar. We distinguish two categories of PEG conformations, primer and brush, and separating the RMSDs profiles of chains into these categories explains this phenomenon. Figure 5.6 shows that separating the PEG into the two types of conformations produces similar trends to those in POX systems, with the lower grafting density PEG, in both the primer and brush conformations, having higher RMSDs. This implies that the only way to increase chain dynamics for PEG systems is to increase the chain length rather than further decrease grafting density. We conclude that,

for the chain length investigated here, there exists some optimal grafting density for PEG between 1.4 and 2.2 chains per nm^2 , where we believe the contribution to the RMSD from the primer layer would be minimized, an increase in grafting density would not inhibit the lateral motion of the chains, and the entropic penalty for protein adsorption on the PEG chains would be highest.

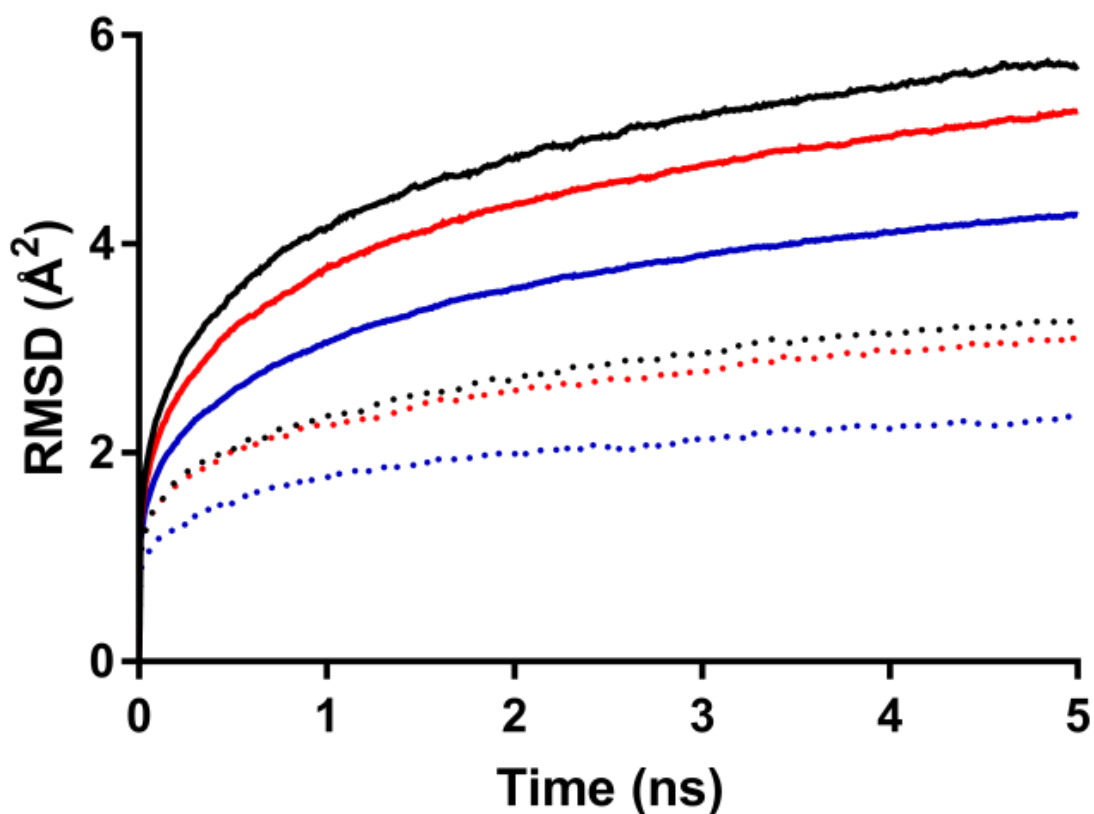


Figure 5.6 RMSD of PEG chains separated into sweeping (solid) and primer (dotted) layers at low (black), medium (red) and high (blue) grafting densities.

Clearly, the entropy cost associated with loss of flexibility of chains on protein adsorption requires further computational investigation. The grafting densities for the PEG and POX systems that we predict to have highest anti-fouling efficacy differ due to the different chemistry of the chains. PEG chains need an optimal density, whereas lower grafting density of POX chains increase the entropic penalty per chain. For POX, identifying

the optimal balance of the penalty per chain and the total number of chains impacted will result in the greatest anti-fouling efficacy.

5.4.4. Hydration behaviour

The relationship between polymer density and water penetration can be seen in the Z density plots (Figure 5.2). A comparison of polymer and water densities for all systems shows POX coatings have increased hydration within the polymer layer relative to PEG systems. We propose this is due to greater porosity and the absence of the primer layer in POX layers. For PMeOx surfaces we see a tethered layer that is less condensed than PEG, allowing significant hydration of the POX chains, particularly at low grafting densities. Furthermore, due to the side-chain on POX, we see small pockets of water being trapped between the chains and the surface at $\sim 15\text{-}20 \text{ \AA}$, the majority of which form hydrogen bonds to the POX chains. At high grafting densities it is clear the polymer layer is too dense to allow water permeation into the layer. However, in Table 5.4 we see a significant peak in water atoms acting as hydrogen-bond donors, likely due to exposure to the amide terminal group mentioned earlier. For PEG systems, the collapsed primer layer prevents the penetration of water molecules into the polymer layer, with water permeation being limited to small cavities that exist within the polymer layer. Work by Sheikh *et al.* [146, 147] has linked the anti-fouling performance of surfaces to the ability of water to permeate through the polymer layer. Their studies suggest that surfaces that allow greater hydration of the polymer layer should see increased anti-fouling efficacy. According to this theory we should see POX systems outperform PEG systems at both low and intermediate grafting densities, due to the significantly higher levels of surface hydration. However, between medium and high grafting density the brush PEG conformation start to dominate, and there is increased hydration of the

interface. Detailed hydrogen bonding data can also be seen in Table 5.4. At both low and medium grafting densities the additional hydrogen bonding sites presented in POX surfaces allow higher hydration than PEG chains. At both low and medium grafting densities there is little difference in the number of hydrogen bonds per chain for the POX systems. However, compared to PEG at these grafting densities, ~3 additional hydrogen bonds per chain are present. At high grafting densities the number of hydrogen bonds per chain levels out due to overcrowding within the polymer layer preventing hydration within the polymer. Around 40% of hydrogen bonds at high grafting densities originate from the terminal group in all systems. The extra 0.4-0.8 hydrogen bonds per chain at high grafting density for PMeOx and PEtOx systems demonstrates the advantage of extra hydrogen bonding groups and shorter hydrophobic side-chain length on POX chains.

Table 5.4 Detailed Hydrogen bond information for all systems. Hydrogen bond cut-offs used a distance of 3.5 Å and angle 20°.

		H-Bonds per Chain	Terminal Contribution (%)	Acceptor:Donor ratio
PMeOx	1.37	5.8 ± 0.3	25	0.87
	2.19	4.9 ± 0.2	29	0.86
	3.01	2.7 ± 0.1	39	0.87
PEtOx	1.37	5.6 ± 0.4	26	0.88
	2.19	4.4 ± 0.2	30	0.87
	3.01	2.3 ± 0.1	40	0.91
PPrOx	1.37	5.5 ± 0.3	26	0.88
	2.19	3.5 ± 0.2	33	0.87
	3.01	1.6 ± 0.1	40	0.92
PEG	1.37	3.1 ± 0.5	40	0.86
	2.19	2.3 ± 0.4	47	0.83
	3.01	1.9 ± 0.3	55	0.80

Whiteside's theories [157, 158] predict that hydrophilic chains should be hydrogen bond acceptors rather than donors. In our simulations, as grafting density increases, we see clearly that a higher percentage of POX chains accept hydrogen bonds while PEG systems

adopt a hydrogen bond donor role. Whiteside's theory predicts that we should see similar anti-fouling performance from all surfaces at low grafting densities; however, as the grafting density increases we would expect POX systems to outperform PEG based on hydration. This can be understood from consideration of the chain topography and terminal group chemistry. As the grafting density increases, we see predominantly hydrogen bonds with water by the terminal groups of PEG. Furthermore, as noted in Figure 5.4, PEG chains tend towards brush and mushroom configurations as the grafting density increases. This results in the terminal hydroxyl group being exposed to the surface, allowing an increase in hydrogen bond donor interactions. For POX systems, as the grafting density increases, the side-chains begin to extend outwards from the surface. This results in shielding/reduced exposure of the NH terminus, whilst still maintaining good exposure of the carbonyl group. This is reflected by the D_{O-N} values shown in Table 5.1, where an increase in grafting density sees increased D_{O-N} values, showing that the terminal side chain is extending above the terminal nitrogen. These values show a clear trend, where an increase in side-chain length corresponds to a higher D_{O-N} value and less fluctuation, for all grafting densities.

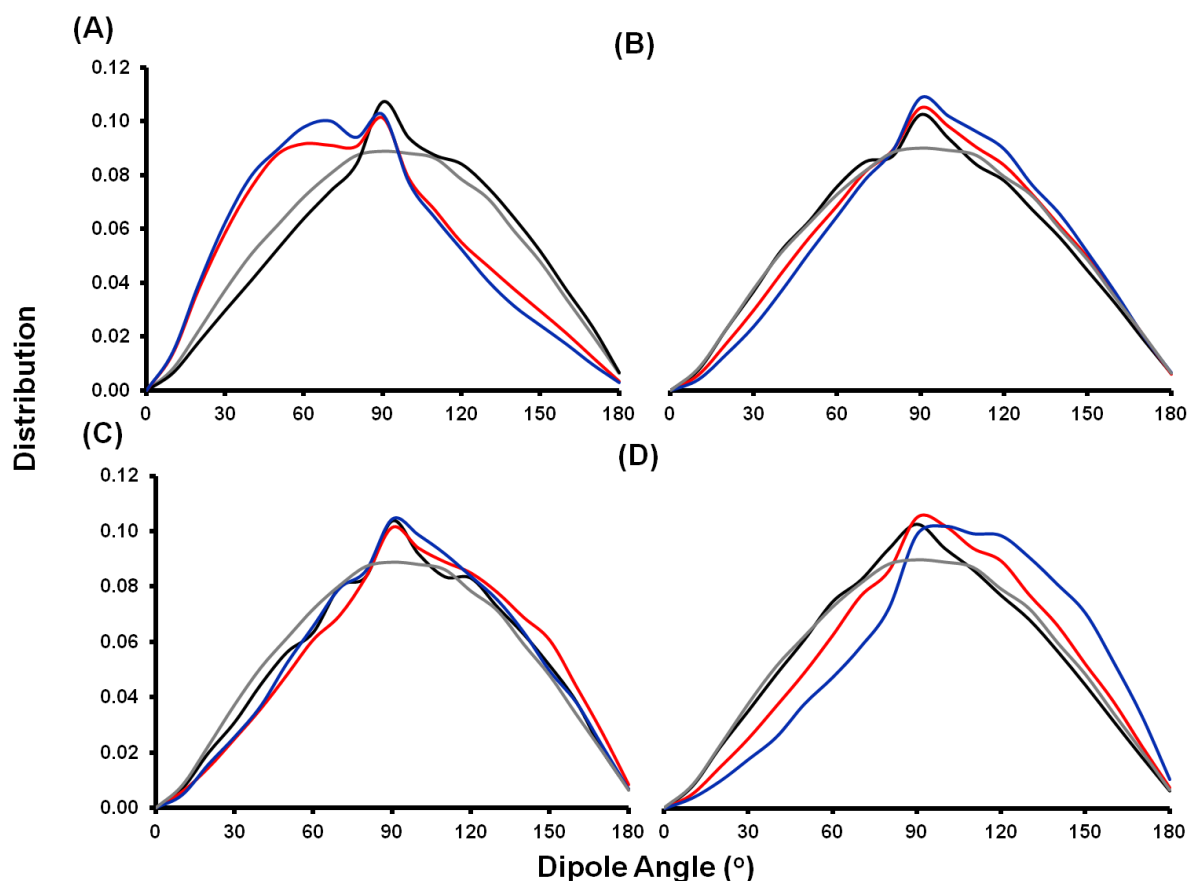


Figure 5.7 Average dipole moment of water calculated with respect to the Z-axis (001 plane). The dipole angle for water in the first water layer is shown for low (black) medium (blue) and high (red) grafting densities, as well as bulk water (grey) for PEG (A), PMeOX (B), PEtOX (C), and PPrOX (D) systems.

To characterise the structural orientation of water, the dipole moment of water molecules have been calculated (Figure 5.7). It can be seen that the hydration of polymer layers and heterogenic hydrophobicity of the surfaces (Table 5.1) has a significant impact on the dipole moment of water. In all systems, a noticeable peak is presented at 90° for the first and second water layer, reflective of the strong hydrogen bond acceptor ability for both surfaces. For PEG systems, these peaks show a subtle decrease in peak intensity as the grafting density is increased, due to the decrease in the percentage of hydrogen bond acceptors (Table 5.4). Furthermore, there is a very clear shift towards 60° in the dipole moment for the medium and high density PEG systems, due to water molecules orienting their oxygen towards the surface. The opposite is noticed for the PPrOX system, where a shift towards 120° intensifies with increasing grafting density, resulting in increased hydrogen

bond acceptor interactions. Although our surfaces are not zwitterionic, we believe the heterogeneous domain spacing between polar groups and hydrophobic groups on PMeOx and PEtOx systems may recapitulate the disordered water behaviour described by Kitano, and allow an even distribution of dipole orientations. For PMeOx, and to a lesser degree PEtOx systems, other than the consistent 90° peak, we observe small shifts in the dipole orientation of water molecules in the first water layer compared to those in bulk water, suggesting these surfaces would display the best protein repelling ability under Kitano's theories.

The MSD and density decay profile of water molecules in the first water layer (Figure 5.8) show trends which also suggest that POX systems should display higher anti-fouling efficacy than PEG systems. Specifically, the low PMeOx system show a highly mobile water layer, likely to be caused by the low surface coverage of the polymer. As seen in the density plots (Figure 5.2) the majority of water within the first layer does not form hydrogen bonds with the polymer layer. At low grafting densities, the additional surface coverage presented by the PEG primer layer appears to compensate for the reduced hydrogen bonding and contributes to the lower mobility.

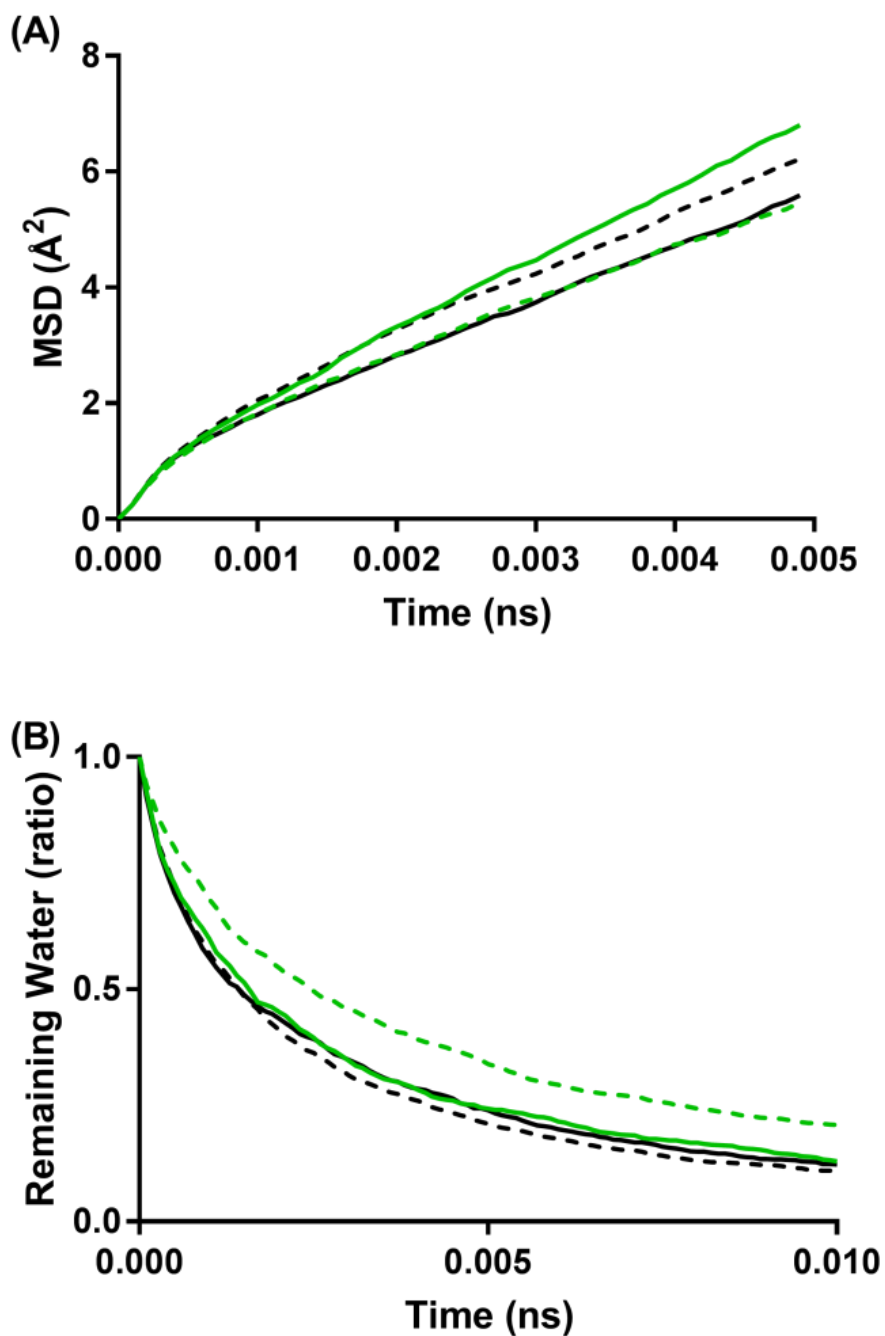


Figure 5.8 MSD (a) and decay profile (b) of water molecules in the first water layer for PMeOx (green) and PEG (black) at low (solid) and medium (dashed) grafting densities.

At medium grafting densities the PMeOx surface displays significantly lower mobility than the low grafting density systems, as more water in this layer forms hydrogen bonds with the polymer chains. This has a significant effect on the decay profile of the water layer (Figure 5.8b) where we see water density decaying at almost half the rate of the PEG and low

PMeOx. We suggest that this is due to the POX carbonyl groups allowing stronger interactions with the water molecules than those formed with the PEG ether/terminal group. Furthermore, the increase in exposed hydrophilic surface area for PMeOx surfaces, particularly at medium grafting densities (Table 5.1) is likely to contribute to this behaviour. Although these results suggest medium PMeOx systems present almost a two-fold increase in water affinity, it is unclear whether this will lead to reduced protein-surface, and further theoretical and experimental studies are needed.

5.5. Conclusion

We have used molecular dynamics simulations to study the typical behaviour of common ligand protected anti-fouling surfaces, the molecular details of chain dynamics, and the contributions of ligand hydrophobicity and hydration. We have identified the presence of a PEG primer layer, that allows high surface coverage even at low PEG grafting densities. Furthermore, we identified quasi-stable conformational states for PEG chains, and how these interact with neighbouring chains/surface molecules, allowing the extension or collapse into other conformations.

We believe the medium grafting density PMeOx and PEtOx systems studied here are leading candidates for high anti-fouling efficacy, as they combine atomic scale heterogeneity, and a hydration layer with almost twice the surface binding affinity to that of PEG. We propose that the hydrophobic exposure of PEG systems, particularly at medium and high grafting densities, is likely to lead to the enhancement of protein adsorption, whilst low grafting density POX systems do not provide sufficient surface coverage. However further investigation of protein adsorption on these surfaces is needed to confirm these hypotheses. In Chapter 7 we look to address this area.

Our results suggest that current anti-fouling theories do not fully account for some of the more complicated atomistic detail of the traditional and novel chain functionalisation now being developed. Synergy between experimental characterisation and theoretical calculations will help design more effective anti-fouling coating strategies and technologies.

Chapter 6

6. Binding Motifs and Behaviour of EAS Hydrophobin at the Silica Surface-Water Interface

6.1. Overview

In the previous two chapters we established a strong understanding of the interfacial behaviour of anti-fouling surfaces in water. Before we explore the anti-fouling efficacy of these surface coatings, it is important to understand the behaviour of our model contaminant, EAS hydrophobin, both in solvent phase, and at interfaces. To do this, we have employed all-atom molecular dynamics to study initial stages of the spontaneous adsorption of monomeric EAS hydrophobin on fully hydroxylated silica. Particular interest has been paid to the Cys3-Cys4 loop, which has been shown to exhibit disruptive behaviour in solution, and the Cys7-Cys8 loop, which is believed to be involved in the aggregation of EAS hydrophobin at interfaces. Specific and water mediated interactions with the surface were also analysed.

We have identified two possible binding motifs, one which allows unfolding of the Cys7-Cys8 loop due to the surfactant-like behaviour of the Cys3-Cys4 loop, and another which has limited unfolding due to the Cys3-Cys4 loop remaining disordered in solution. We have also identified intermittent interactions with water which mediate the protein adsorption to the surface, as well as longer lasting interactions which control the diffusion of water around the adsorption site. These results have shown that EAS behaves in a similar way at the air-water and surface-water interfaces, and have also highlighted the need for hydrophilic ligand functionalisation of the silica surface in order to prevent the adsorption of EAS hydrophobin.

This work has been published in the peer-reviewed journal, *Frontiers in Molecular Biosciences* [376].

6.2. Introduction

Although the technologies to remove biofilms are improving considerably, there are significant limitations in reactive treatments due to the small length scales where biofilms are problematic. Examples of this are particularly evident in marine environments, where 25-50 μm biofilms on a ship hull increase hydrodynamic drag by 8-22% respectively [56, 377], as well as health industries, where it is estimated that 20% of fatalities world-wide are due to infectious diseases, of which 80% are associated with biofilm formation [378]. With these factors considered, it is not surprising that the focus of anti-fouling technologies has shifted to the design of surfaces that have the potential to maintain their clean state by resisting the non-specific binding of proteins and other foulants. However, significant limitations in these coating technologies arise due to our limited understanding of the interactions and behaviour of microbes at interfaces.

Nanostructured surfaces with alternating hydrophobic/hydrophilic characteristics have recently been shown to be able to either promote or inhibit protein adsorption [104], the phenomenon can potentially be exploited to design surfaces resistant to biofouling. These phenomena were further detailed in Section 1.6. More recently there has been significant research into the behaviour of interfacial water, and the critical role it plays in protein adhesion. A detailed summary of this research was presented in Section 1.7.

The focus of this study is on Class I hydrophobins, specifically, the Class I hydrophobin EAS, found in the fungus *Neurospora Crassa* [76]. Detailed background and information on hydrophobin can be found in Section 1.4. To date there has been significant research on the behaviour of EAS hydrophobin in bulk water solution and at the air-water

interface which has shown several important properties, including the inability for EAS to aggregate in aqueous solution [78, 80] which has largely been attributed to the flexible, intrinsically disordered Cys3-Cys4 loop [77]. Although it has been previously shown that the Cys3-Cys4 loop is not required for monolayer formation [79], at the air-water interface the Cys3-Cys4 loop was theoretically shown to stabilize into surfactant-like conformations, with hydrophobic residues being directed to the air, and hydrophilic residues to the water.

Despite the high interest and some significant research on hydrophobin at the air-water interface, both experimental and theoretical, to the best of our knowledge there have been no studies investigating the behaviour of EAS hydrophobin with atomistic detail at the surface-water interface. Therefore, although some advances have shown significant value for anti-fouling technologies, many fundamental aspects of microbial adhesion have not yet been described. For example, certain microbes have a higher preference for hydrophilic surfaces rather than hydrophobic [379] while hydrophobins are able to adsorb strongly on surfaces regardless of hydrophobicity. To combat some of these deficiencies in understanding, MD simulations and other modelling techniques have become increasingly popular [380, 381]. Thanks largely to advances in computational performance [382] the value of all-atom and coarse-grained models in MD has significantly increased as researchers are now able to simulate experimentally relevant system sizes and timescales. This allows the investigation of proteins and peptides at surfaces, however newer issues arise with the limitations in parameters available that accurately describe the interactions of both organic and synthetic surfaces, and issues in adequate conformational sampling [383, 384] that restrict the simulations of relatively large protein-surface systems.

In this study, we implement MD to get insights into the initial stages of monomeric adsorption of EAS hydrophobin on highly hydrated silica surfaces, in order to gain some understanding of the possible conformational changes that may be responsible for monolayer

formation. Specific attention is paid to the behaviour of both the Cys3-Cys4 and Cys7-Cys8 loops, due to their previously described behaviour at the air-water interface [76, 77, 79]. We also examine the behaviour of water at the protein-silica interface, specifically the role of water bridged interactions that promote protein adhesion to the surface. These interfaces are prominent in both biomedical and industrial environments [203, 385, 386] and understanding the behaviour and interactions in these systems at the nanoscale [93, 362, 387] will be critical for the rational design of anti-fouling surfaces.

6.3. Methodology

6.3.1. Protein-solvent system

The NMR solution structure of the class I hydrophobin EAS, determined by Kwan *et al.*, was obtained from the PDB structure 2FMC [76]. The protein was protonated in zwitterionic form and simulated in a periodic box of $70 \times 70 \times 70$ Å filled with explicit water and 2 counter-ions to maintain system neutrality. The system was simulated for 30 ns with five replicas using the CHARMM22 [246] force-field, and another five replicas using the CHARMM27 [388] force-field with CMAP corrections to refine the NMR structure as a benchmark for comparison between the solution and the surface-water interface behaviour. In solution, the CHARMM22 protein models were seen to better maintain the β -core structure from the NMR data than the CHARMM27, as shown by the root mean square deviations (RMSD) of key areas (Appendices Figure A6.1). For the β -core and Cys7-Cys8 loop, which are expected to be reasonably stable in solution, the CHARMM22 force-field simulations exhibited significantly lower RMSD than those for the CHARMM27 force-field. Conversely, for the highly mobile and flexible Cys3-Cys4 loop, the CHARMM22 force-field simulations exhibited a higher RMSD than CHARMM27.

On evaluation of secondary structure behaviour over time (Appendices Figure A6.2), it was noted that the CHARMM22 simulation led to a slight diminishing in the anti-parallel β -sheets of the core region, however the Cys7-Cys8 structuring was maintained. The CHARMM27 force-field maintains the core region, however due to the unfolding of the Cys7-Cys8 loop in solution, the β -structuring in these regions was completely lost. For these reasons, we have chosen to use the CHARMM22 force-field, as it gives a more experimentally consistent representation of the protein structure and behaviour in solution.

6.3.2. Surface-protein system

The protein initially equilibrated in bulk solvent as described above was placed approximately 9 Å from the surface, in four different initial orientations rotated 90° about the y-axis (as shown in Figure 6.1), to allow the investigation of binding orientations in spontaneous adsorption. The system was solvated using an explicit water layer of 80 Å thickness, with a 20 Å vacuum space above the water box added to create an air-water interface, and two counter-ions added to maintain system neutrality. Systems were first energy minimised using the conjugate gradient method. Following this, the water molecules were allowed to relax around the protein and surface by applying a short (2 ns) MD with the protein and surface constrained. Constraints were then removed and MD applied to the entire system for 50 ns to investigate the spontaneous initial adsorption events of the protein onto the silica surface. Simulations were repeated for each starting protein orientation with different initial velocities and equilibration was monitored by assessing the total energy trend. Whenever the protein adsorbed to the surface it happened spontaneously within the first 10 ns of the simulations. Data for analyses were collected from the equilibrated 20 ns of the simulation trajectory unless otherwise specified.

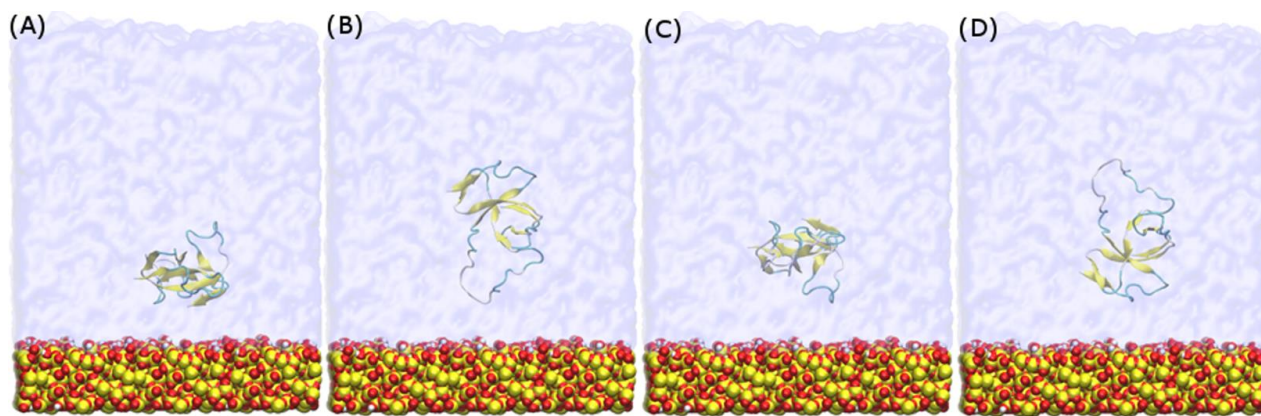


Figure 6.1 Snapshots of the four different initial orientations (A,B,C,D) of EAS hydrophobin with respect to the silica surface. The protein is positioned approximately 9 Å from the surface.

6.3.3. Simulation settings

Simulations were performed using the LAMMPS [366] software with the CHARMM22 [246] force-field used for the protein, and the CHARMM-compatible Cruz-Chu [254] silica parameters. The TIP3P [367] water model was applied, with the SHAKE [267] algorithm employed to constrain water bond length and angle. For the evaluation of non-bonded interactions, a twin-range cutoff of 0.8 and 1 nm were used for van der Waals interactions, with a 1 nm cutoff for electrostatics and the PPPM solver used to calculate the long-range damping effect. The energy minimisations were carried out using the conjugate gradient method with a convergence criterion of 10^{-4} kcal/mol energy tolerance and 10^{-6} kcal/mol.Å force tolerance. MD was performed in the NVT ensemble using a time-step of 1 fs and a temperature of 298 K was maintained by a Nosé-Hoover thermostat [264] with a 0.1 ps coupling time.

6.4. Results

Five of the eight simulated systems adsorbed at the surface-water interface, whilst the other three adsorbed at the air-water interface. Our analyses will primarily focus on the systems that adsorbed at the surface-water interface, with particular emphasis on the behaviour of the Cys3-Cys4 loop, Cys7-Cys8 loop and the role of interfacial water in the

adsorption of EAS hydrophobin. This behaviour will be compared to behaviour in bulk and at the air-water interface to determine whether the physicochemical properties or water behaviour are maintained, and validated against the existing and already detailed studies of EAS hydrophobin at the air-water interface [77, 79].

6.4.1. Protein binding at the surface-water interface

Hydrophobin adsorption at the surface-water interface occurred spontaneously and we were able to identify two possible binding motifs at the interface, one in which adsorption occurs through the Cys3-Cys4 loop (Binding Motif 1, Figure 6.2A and B), and another which has the Cys3-Cys4 loop away from the surface (Binding Motif 2, Figure 6.2B and Figure 6.4C). Interestingly, the initial protein orientation had minimal impact on the binding motif at the surface-water interface, as most systems experienced a slight reorientation in bulk water prior to adsorbing. The exception to this is the system that initially had the Cys3-Cys4 loop closest to the surface (Figure 6.1B), where the protein segregated to the air-water interface. This is most likely due to the Cys3-Cys4 loop initially contracting towards the β -core of the protein, resulting in increased distance between the protein and surface and therefore minimising the attractive long-range interactions between them.

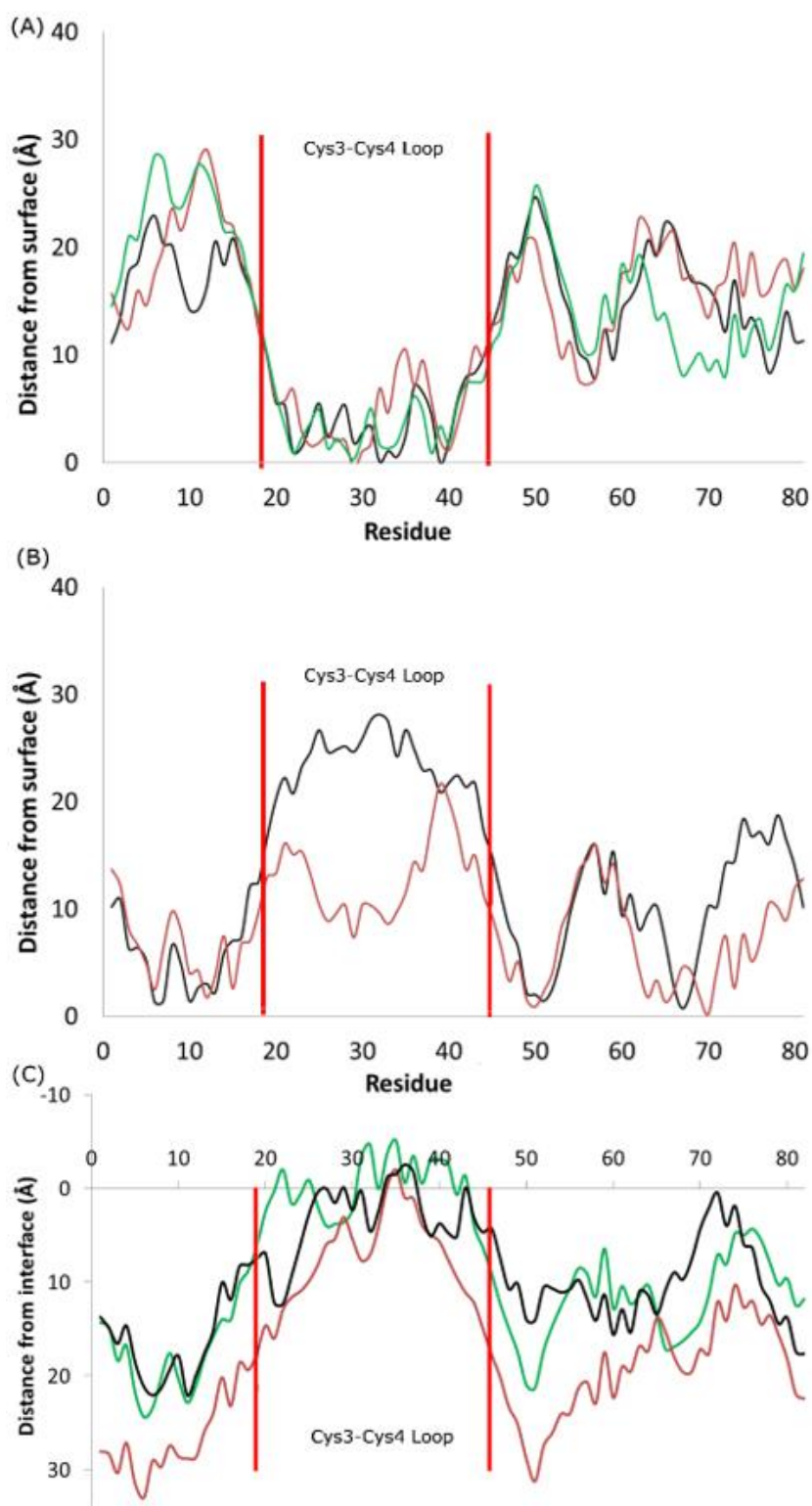


Figure 6.2 Distance between the centre of mass of residues and the average height of the surface hydroxyl groups for systems that adsorbed (A) through the Cys3-Cys4 loop (Residues 19 to 45, Binding Motif 1) and (B) with the Cys3-Cys4 loop in bulk water (Binding Motif 2). (C) Distance between the centre of mass of residues and the average profile of the air-water interface. Different colours represent the initial protein orientation as shown in Figure 6.1. In Binding Motif 1, black and green colours were from orientation (A), red from orientation (D). In Binding Motif 2, red was from orientation (D) again, and black was from orientation (C).

As expected, the interactions involved in both binding motifs are dominated by the surface-protein hydrogen bonding, due to the highly hydrophilic nature of the surface. There are, however, subtle differences in the specific nature of these hydrophilic interactions. In Binding Motif 1 (Figure 6.2A), the adsorption is largely due to the direct or water-mediated anchoring of residues 20-24 (QSMSG) and 38-40 (DLS) (detailed in figures 6.3 and 6.6), which are found at the beginning and end of the Cys3-Cys4 loop (residues 19 to 45). Within these groups, there are significant interactions between the surface hydroxyl groups and the hydrophilic side-chains of serine and aspartic acid, which encourage a tighter initial binding to the surface and subsequent interactions between the protein backbone and surface hydroxyls. Work by Sunde *et al.* [79] has shown that removal of these residues inhibits surface activity and rodlet formation, however this only coincided with the mutated proteins EAS Δ 17 and EAS Δ 19 (EAS mutations with residues 24-40 and 23-41 removed respectively). It would be interesting to see if there was correlation between the mutation of residues 20-24 and 38-42 to glycine and a delay/inhibition of rodlet formation.

In Binding Motif 2 (Figure 6.2B), persistent interactions with the surface occur in regions 6-7 (PN), 10-13 (SIDD), 50-52 (IGS) and 65-68 (VTNT) (detailed in figures 6.3 and 6.6). Unlike Binding Motif 1, these regions are dominated by backbone interactions, with very few side chain interactions having a significant occupancy over the simulation. Interestingly, this binding motif is almost identical to the binding of the EAS Δ 15 (EAS mutation with residues 25-39 removed) monomer at the air-water interface [79]. From our results, it appears that the presence of the Cys3-Cys4 loop can inhibit the unlocking of the Cys7-Cys8 loop and thus monolayer formation, which will be discussed further below. It should be noted that due to the high flexibility, mobility and disordered behaviour of the Cys3-Cys4 loop in bulk water, a broad distribution of distances from the surface can be seen

in Binding Motif 2 (Figure 6.2B). This behaviour has also been shown to occur at the air-water interface. [79]

6.4.2. Specific interactions

To date there have been several studies by Walsh *et al.* on how the spacing of hydroxyl groups on silica surfaces affects the behaviour of interfacial water, and how that influences the binding of hydrophobic and hydrophilic molecules and peptides [116, 389]. Importantly, these works highlighted that larger spacing of hydroxyl groups on the surface would result in areas void of water. Free energy calculations have shown that it was energetically favourable for small hydrophobic moieties like methane to penetrate these voids, where they would then be shielded by the surface interfacial water. This phenomenon was further explored on amorphous silica models with atomistic roughness, similar to those used in this study, by Schneider and Ciacchi [117]. In this study, it was noted that these hydrophobic voids were present in larger volumes due to surface cavities, which allowed penetration of hydrophobic side chains. On peptides which had alternating hydrophilic and hydrophobic residues, similar to those on EAS hydrophobin, it was noticed that adsorption was significantly enhanced as the hydrophobicity of the interfacial water and voids could be matched, as well as allowing increased electrostatic interactions with the surface. In our simulations of EAS with the atomistically rough amorphous silica surface, we do indeed notice this phenomenon occurring. The average number of contacts for residues in contact with the surface during the last 20ns of simulations for both binding motifs is presented in Figure 6.3.

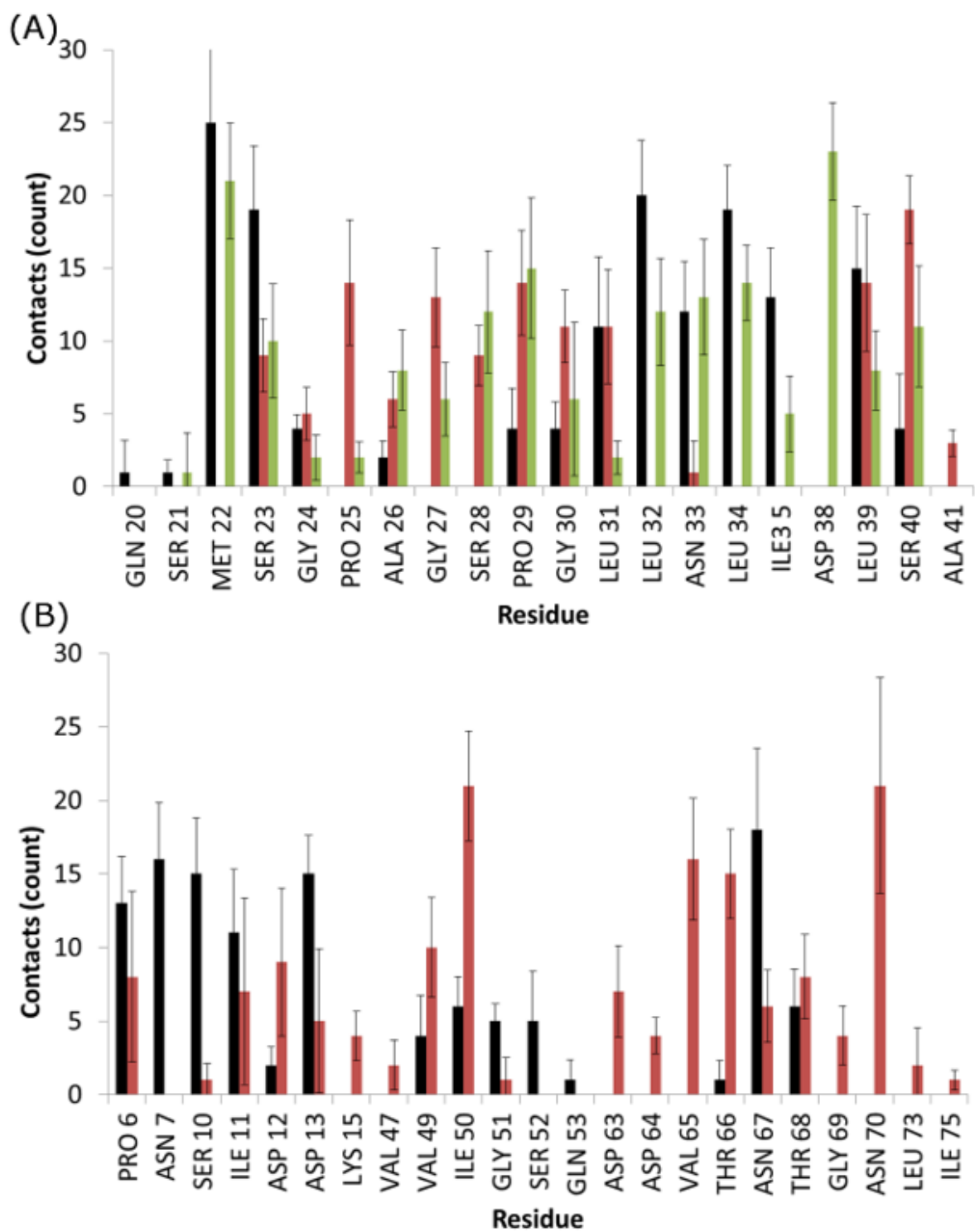


Figure 6.3 Average number of contacts with the surface for EAS over the last 10 ns of simulation in binding motif (A) 1 and (B) 2. Colours are matched to the residue-surface distance plots in Figure 6.2 and represent different simulation runs. Heavy atoms of a given residue are considered in contact with the surface if they fall within 4.5 Å of any surface atom.

As can be seen, significant contacts occur in hydrophobic residues such as Met22 in Binding Motif 1 and Ile50 in Binding Motif 2, as the hydrophobic sidechain penetrates the

surface cavities. As with the aforementioned studies, these residues become shielded by surrounding interfacial water, which holds the residue sidechains in these voids, and allows further electrostatic interactions to occur as backbone atoms and shorter residues like glycine, proline and alanine come in contact with the surface hydroxyl groups, as well as charged and polar residues like serine, aspartic acid and asparagine, which form direct interactions with the surface and surrounding water.

6.4.3. Behaviour of the Cys7-Cys8 and Cys3-Cys4 loops

The comparison of EAS hydrophobin features in bulk water and at the surface-water interface revealed several key differences. In bulk water, the amyloidogenic region (F72-I75) of the Cys7-Cys8 loop [80] interacts with the hydrophobic core of the protein, forming anti-parallel β -sheets in all five protein simulations in solution (Figure 6.4A). Interestingly, in two of the systems where the protein adsorbed through the Cys3-Cys4 loop to the surface-water interface (Binding Motif 1), we see significant interactions between adjacent strands in the Cys7-Cys8 loop, encouraging the formation of an exposed β -hairpin (Figure 6.4B). This intermediate state is consistent with the proposed model for EAS aggregation into monolayers at an interface [80].

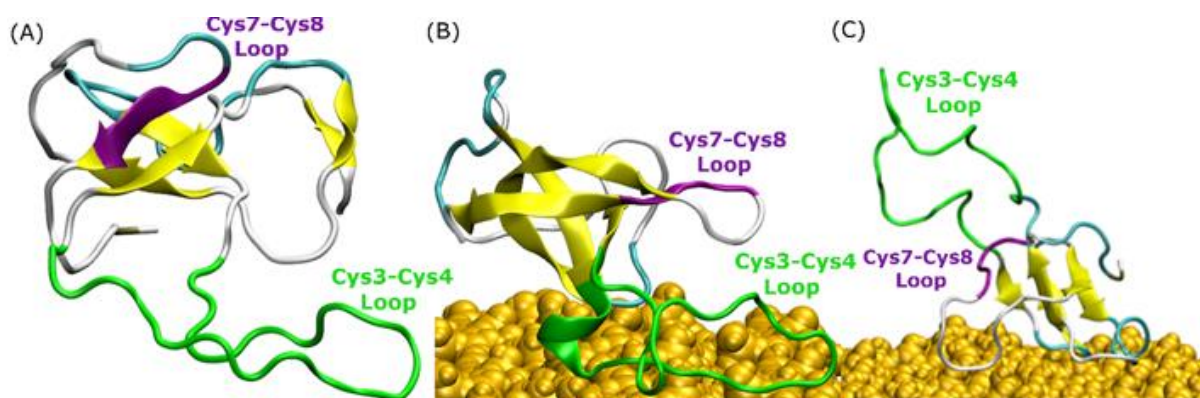


Figure 6.4 Snapshots of EAS hydrophobin conformations (A) in bulk water, (B) at the surface-water interface when adsorbed through the Cys3-Cys4 loop (Binding Motif 1) and (C) at the surface-water interface with

the Cys3-Cys4 loop in bulk (Binding Motif 2). Yellow arrows represent β -sheet structuring. The amyloidogenic region (F72-I75) is shown in purple and the Cys3-Cys4 loop shown in green.

In one of the systems that adsorbed through the Cys3-Cys4 loop (Binding Motif 1) a partial unlocking of the amyloidogenic region was observed, however interactions with the Cys3-Cys4 loop prevented the development of a β -hairpin structure. As can be seen in Figure 6.5, hydrogen bonding of residues near the C-terminus of EAS encourages the formation of either an alpha-helical structure (Figure 6.5A) which promotes the folded conformation of the Cys7-Cys8 loop seen in all bulk water simulations, or a β -sheet (Figure 6.5B), which encourages the unfolding of the Cys7-Cys8 loop. Upon conformational rearrangement at the surface-water interface, two of the three systems that adsorbed through the Cys3-Cys4 loop (Binding Motif 1) were able to overcome the energy barrier needed to break a critical hydrogen bond between residues Ala41 of the Cys3-Cys4 loop and Ala77 of the Cys7-Cys8 loop. Interestingly, there is a strong positive correlation between the degree of β -sheet formation for the Cys7-Cys8 loop and the number of contacts between the Ser40 (adjacent to the key Ala41 residue) sidechain and the surface (Figure 6.3A black, green, and red bars, and Appendices Figure A6.3 B, C, and D, respectively). This interaction between Ser40 and the surface may be the first step in the process of unlocking the amyloidogenic region and subsequent hydrophobin monolayer formation. *In silico* mutation of the Ser40 to glycine could provide some insight into this relationship but is outside the scope of this thesis.

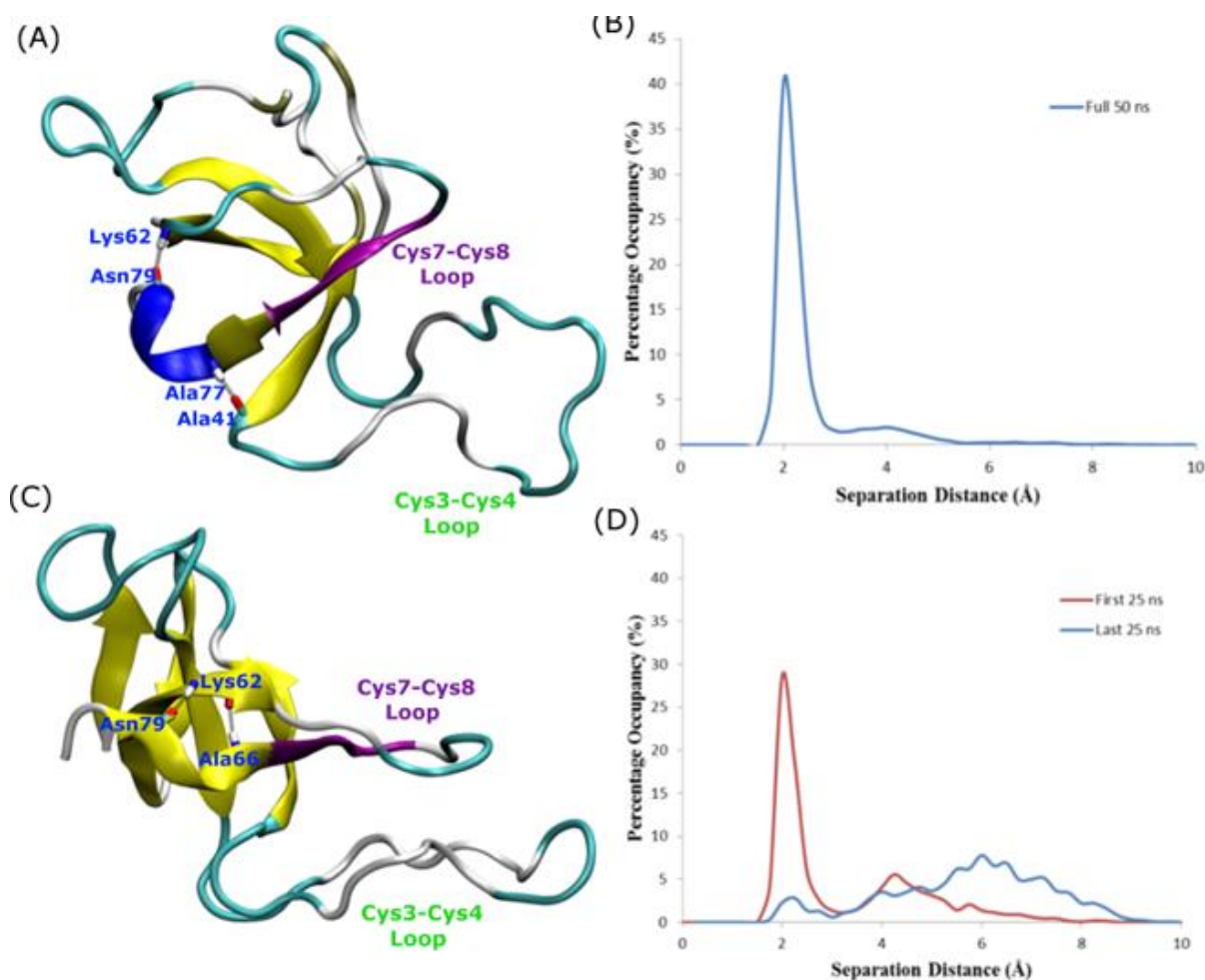


Figure 6.5 Snapshots of EAS hydrophobin conformations highlighting hydrogen bonding between (A) residues Asn79 and Lys62, Ala77 and Ala41, resulting in a helical formation, (B) histogram showing the separation distance of residues Ala77 and Ala41 in system where Cys7-8 loop remains folded and (C) residues Asn79 and Lys62, Asn76 and Lys62, encouraging the formation of the β -hairpin (D) histogram showing the separation distance of residues Ala77 and Ala41 in the system where Cys7-8 loop unfolds over time.

In systems which did not adsorb through the Cys3-Cys4 loop (Binding Motif 2) partial unfolding of the Cys7-Cys8 region was observed, however due to the aforementioned hydrogen bond (Ala41 to Ala77) persisting, there was no formation of a β -hairpin. This is likely to be due to the Cys3-Cys4 loop remaining in bulk solution, which enables it to retain the mobility and flexibility that is highly disruptive for the monolayer formation. As mentioned previously, this binding motif is consistent with the experimental observations by Sunde *et al.* [79] of the binding of EAS Δ 15 at the air-water interface. Our finding also supports a more recent study by de Simone *et al.* [77] which suggested that the primary role of the Cys3-Cys4 loop is to prevent the aggregation of hydrophobin in bulk water. Combined

with the knowledge that these EAS Δ 15 proteins form rodlets that are almost indistinguishable from the native EAS [79], we hypothesize that formation of an exposed β -hairpin is extremely likely in the event of the Cys3-Cys4 loop (A) being removed or (B) unfolding and interacting with the interface.

Changes in secondary structure on adsorption to the surface-water interface (Appendices Figure A6.3) further show the disruptive influence the Cys3-Cys4 loop has on the protein conformation. In systems adsorbing through Binding Motif 2 (Appendices Figure A6.3A), we see no structuring in the Cys7-Cys8 region due to disruptive interactions with the Cys3-Cys4 loop. This disruptive influence on the secondary structure is significantly reduced for systems interacting with the surface through Binding Motif 1. However, we also see how significant the Ala41-Ala77 interaction is. When this interaction is persistent (Appendices Figure A6.3B) we see a stable 3_{10} -helix in residues 76-79. Other than a temporary isolated β -sheet formation in residues 68-69 we see no significant changes in secondary structure. When this interaction is broken (Appendices Figure A6.3C), we begin to see the significant enhancement in β -sheet formation, particularly in residues 73-81. On the system with no Ala41-Ala77 interaction (Appendices Figure A6.3D) we see a very early and persistent β -hairpin formed.

6.4.4. The role of structure and dynamics of interfacial water in hydrophobin adsorption

It has been well documented that highly hydroxylated silica surfaces, similar to those in this study, form significant hydrogen bonding with water molecules that enable them to retain an ordered interfacial water layer [390]. Furthermore, with studies showing the importance of water-mediated interactions for bio-fouling [9, 114, 118-122], we have investigated the specific involvement of water in the mechanisms of hydrophobin adsorption

observed in our simulations. Studies have shown that proteins initially anchor to the surface-bound first hydration layer, resulting in significant restructuring of the interfacial water [118]. It is then believed that intermittent interactions between these water molecules and protein residues encourage protein adsorption to the surface, which results in the displacement of these water molecules. Indeed, in our simulations, such dynamics have been observed as polar and charged amino acid residues experience transient interactions with the interfacial water molecules, encouraging rotation of the residues to maximize the contact surface area with the silica surface. As a result, due to the preferential interactions of the protein residues with the surface hydroxyl groups, the number of hydrogen bond sites available to water molecules is significantly reduced, leading to the observed displacement of water. In all three of the air-water simulations a partial unlocking of the Cys7-Cys8 loop occurred. However, this was perturbed by the formation of anti-parallel β -sheets between Ile75 of the Cys7-Cys8 loop and Leu43 from the Cys3-Cys4 loop, suggesting that although this intermediate transition is seen at both interfaces, the effects of multiple proteins at the interface must be investigated to confirm whether this physicochemical transition is critical for the formation of monolayers.

In our simulations, the protein adsorption displaces water molecules as it adsorbs to the surface, resulting in surface areas significantly void of water, and a high level of occupancy around the protein. This displacement results in concentrated areas of high water occupancy around the protein adsorption site, as it is highly likely that the water molecules in this region are still forming “cushioned” interactions. Due to steric hindrances, the sections of the protein around these areas of high occupancy cannot move closer to the surface, and instead form long lasting interactions with water, which results in slower water diffusion. To clarify this phenomenon, we have monitored the change in dipole moment orientation of water from interfacial regions around the surface, in a similar method to Hung *et al.* [114].

We have first computed the average water dipole moment at the water-surface interface without the influence of the protein. Water molecules within 3 Å of the surface hydroxyls have been considered, with an average distribution taken from the last 0.2 ns of simulation. As can be seen in Figure 6.6, the average dipole moment shows a broad symmetric distribution peaking at 90°. This distribution can be attributed to the high levels of surface hydroxylation, combined with a relatively smooth and rigid surface.

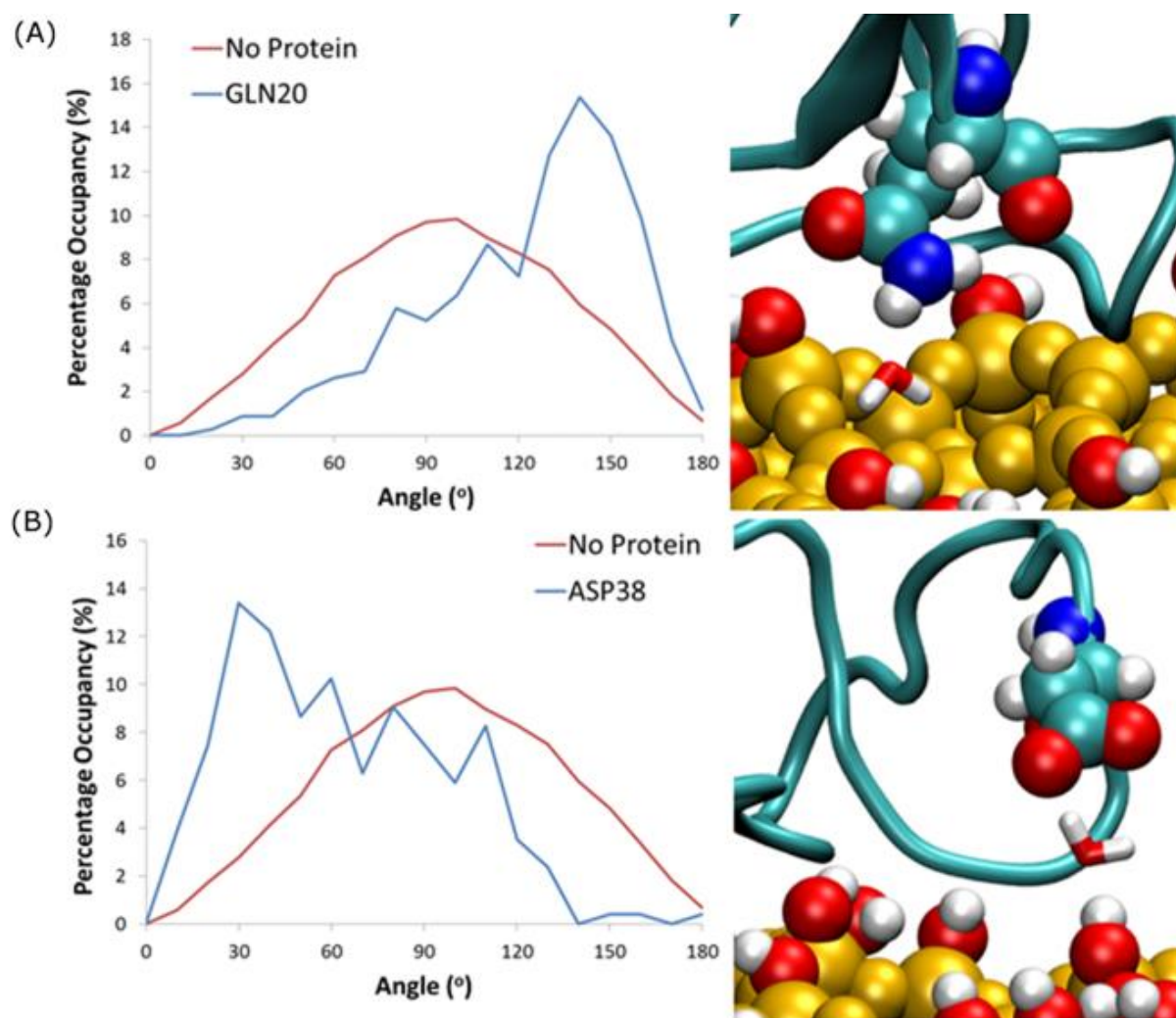


Figure 6.6 Histograms showing the distribution of water dipoles around the surface with no protein (red) and with protein (blue) for water trapped between the surface and residues (A) Gln20 and (B) Asp38

When comparing to systems with the protein at the surface-water interface, we consider cushioned water to be those that are within 3 Å of both the silica surface and a protein residue. All water molecules over the last 20 ns that fit this criterion have been

considered, and the average dipole moment has been shown as a probability with an angle bin size of 10° . Results have shown that for these bridging interactions it is largely the side chain of charged and polar amino acid residues that have been involved in the formation of these long-lasting hydrogen bonds, enabling the water mediated protein-surface interactions. Specifically, for water trapped between polar residues such as Gln20 (Figure 6.6A) there is a significant shift in water dipole orientation towards 150° , which shows that the water molecule acts as hydrogen bond acceptor, resulting in its hydrogens pointing towards the surface. Conversely for negatively charged residues like Asp38 (Figure 6.6B) water acts as a hydrogen bond donor, resulting in a shift towards 30° , and hydrogen atoms pointing away from the surface. Residues that were more than 5 \AA away from the surface are seen to have no effect on the dipole moment of cushioned waters. This is likely because the distance between the protein and surface does not allow for water molecules to form bridging bonds with both the protein and surface, and suggests that these water molecules still have a greater binding affinity to the protein rather than the surface.

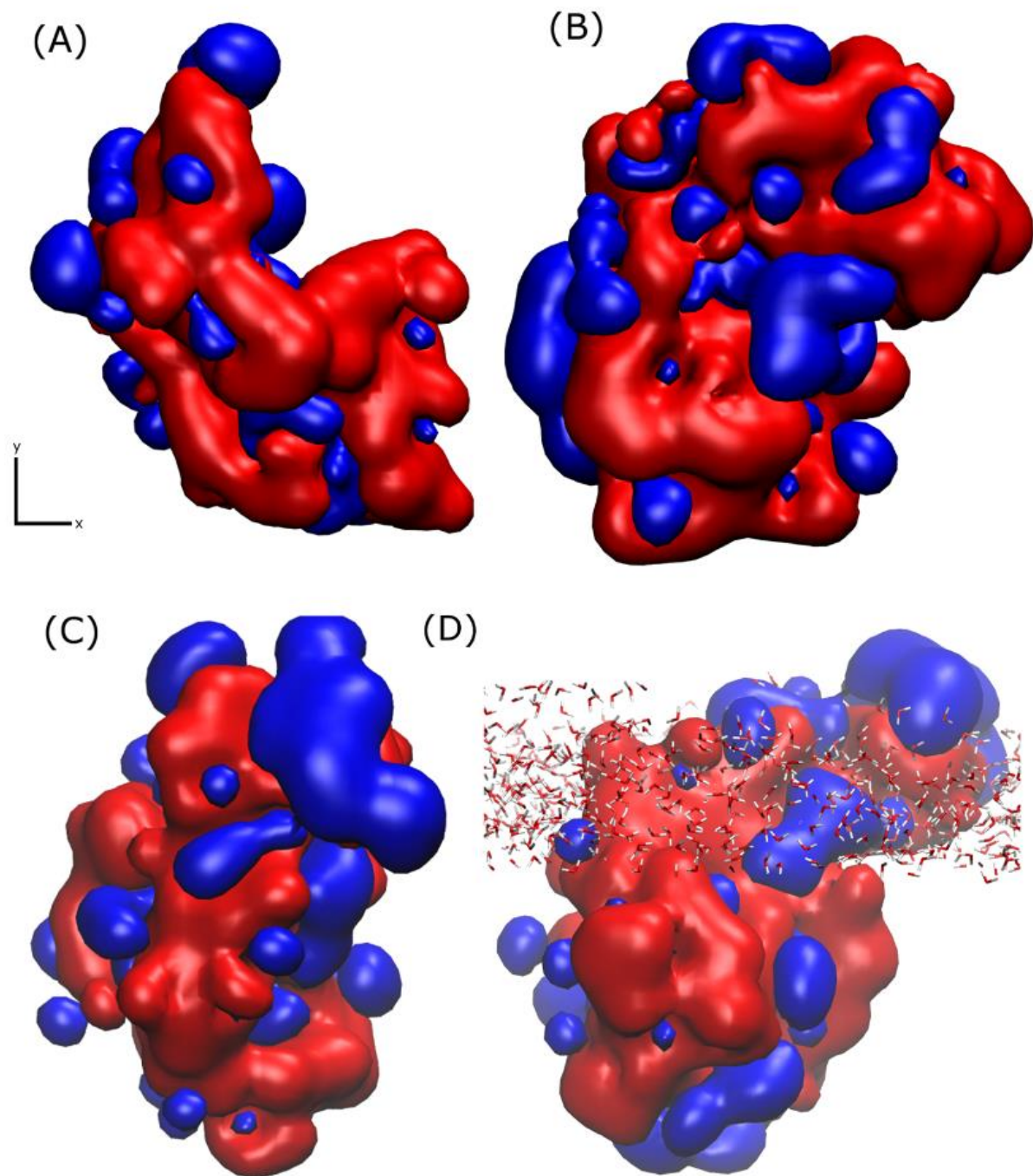


Figure 6.7 Snapshots of hydropathicity for EAS in (A) Binding Motif 1 and (B) Binding Motif 2, as seen by the silica surface and (C) at the air-water interface from top view and (D) side view showing the interface boundary (air layer is above water molecules, water molecules below have been hidden for clarity). Blue and red colors represent hydrophobic and hydrophilic regions respectively.

Using pyMLP [391, 392], we have mapped the hydropathicity of the protein in both surface binding motifs (Figure 6.7) as well as at the air-water interface. As expected, the

surface-water adsorption motifs (Figure 6.7A, B) are both dominated by hydrophilic interactions, with binding motif 2 (Figure 6.7B) showing slightly increased hydrophobic interactions due to the aforementioned surface cavitation effects. Conversely, at the air-water interface (Figure 6.7C), we see a more dominant hydrophobic surface, particularly outside of the air-water interface. Furthermore, adsorption results in significant water loss, particularly around hydrophobic residues (Table 6.1), where on average at least one water molecule per residue was lost on adsorption to the air-water interface, behaviour not seen occurring at the surface-water interface. It is important to note that preferential bonding between silica and the charged groups of aspartic acid are likely to exclude water, and most likely the reason for the 5% difference. Also, for the large discrepancy in proline, there are only three proline residues in the studied area, and as seen in Appendices Figure A6.5, one of which is in the middle of three long hydrophobic side-chains, Leu34, Ile35 and Val37 extending out of the interface, and into the “air” environment, hence creating a significant loss in water.

Table 6.1 Average loss of contacts with water for residues in the region Gln20-Ile50 for systems that adsorbed at the air-water and surface-water interface (Binding Motif 1), compared to the bulk environment, over the last 10 ns of simulation. A contact was defined as a water atom coming within 3 Å of the amino acid group type defined by Livingstone and Barton [393]. A detailed plot can be found in Appendices Figure A6.5.

	Air-water	Surface-Water
Hydrophobic	34%	17%
Hydrophobic (long)	36%	16%
Polar	14%	14%
Proline	52%	20%
Aspartic Acid	24%	29%

The three-dimensional mean squared displacement (MSD) of water molecules at the surface-water interface and air-water interface with and without the presence of EAS have been compared to that of bulk water (Figure 6.8A). The curves are generated over a short-time domain (10 ps), with the gradient from a line of best fit plot proportional to the diffusion coefficient for the water molecules in the respective zones, similar to our previous work [364]. We observe a diffusion coefficient of 4.3×10^{-5} cm²/s for bulk water (Figure 6.8A),

which is slightly higher than the reported 4.0×10^{-5} cm²/s diffusion coefficient for TIP3P with Ewald summation [394]. As expected, the water at the surface-water interface (2.35×10^{-5} cm²/s) is significantly slower than bulk, due to stabilizing interactions with the silica surface. This is again reduced further when the protein is present (2.10×10^{-5} cm²/s), which shows that the protein does in fact trap water in the adsorption region, and limit the diffusion of water through aforementioned long polar and charged side-chain residues that are 5-6 Å from the surface, such as aspartic acid and serine. Conversely, at the air-water interface the diffusion is a factor of 10 faster without the protein, (1.15×10^{-4} cm²/s) slowing significantly in the presence of the protein (6.75×10^{-5} cm²/s). This behaviour is in turn replicated for the mobility of the protein itself, where the diffusion of the protein at the two interfaces can be seen in Figure 6.8B. At the surface-water interface the protein is practically immobile on the surface, with very little movement occurring once the protein is adsorbed (0.03, 0.01×10^{-5} cm²/s for Binding Motifs 1 and 2 respectively). Comparatively at the air-water interface the high water diffusion sweeps the protein along the interface quite quickly (3.94×10^{-5} cm²/s), suggesting that there may be different mechanisms involved for monolayer formation at the air-water and surface-water interface, due to the vastly different surface hydrophobicity and mobility of the protein. We believe that this provides further support to the theory that the Cys3-Cys4 loop has surfactant-like behaviour at the air-water interface, especially considering the significant effects it has on the water diffusion coefficient.

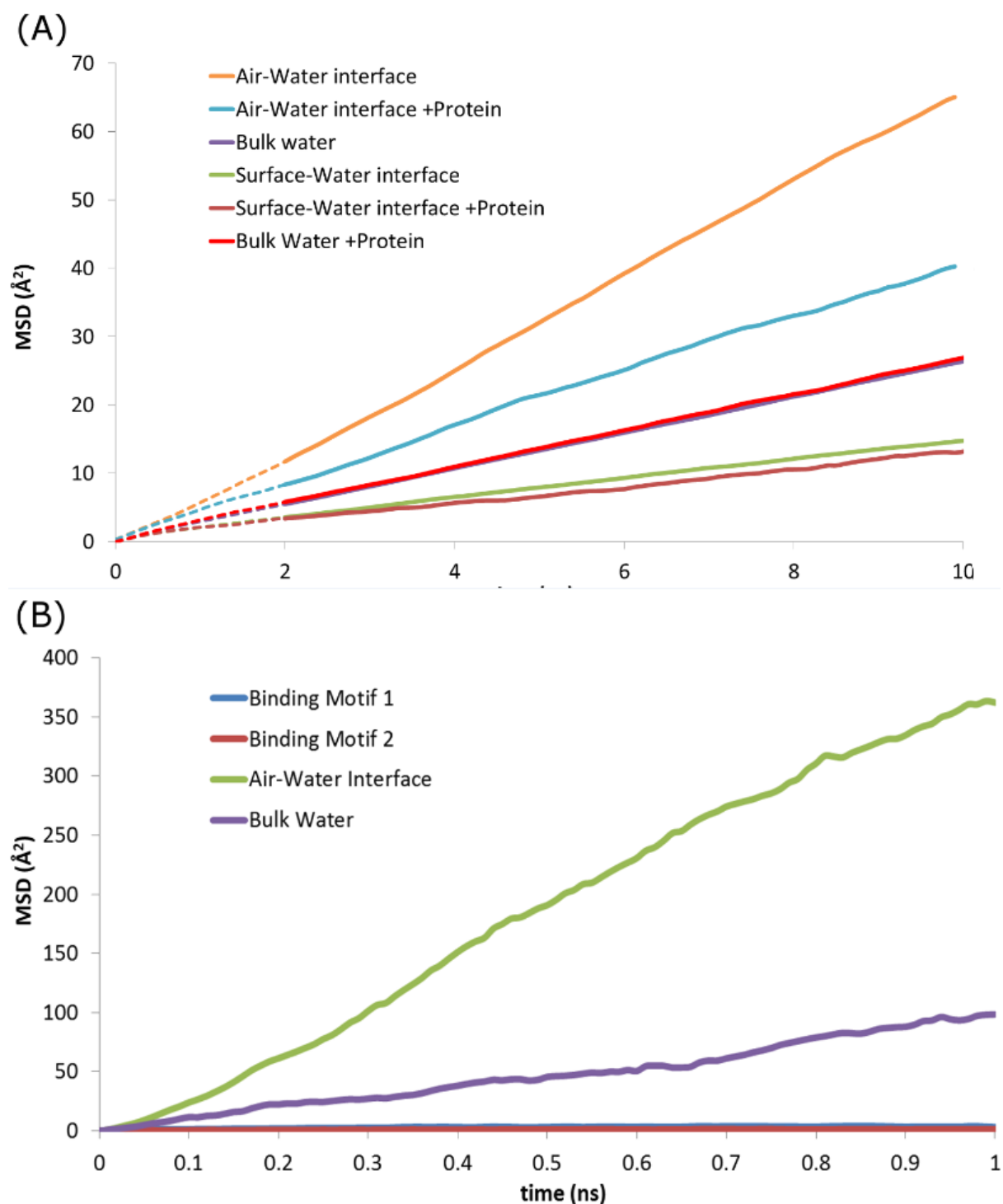


Figure 6.8 Mean squared displacement (MSD) plots of: (A) water molecules at the, air-water, bulk water and surface-water interface; both with and without the presence of EAS hydrophobin. (B) lateral MSD of the protein at the air-water interface, in bulk solution, and in both binding motifs at the surface-water interface.

These results demonstrate that the presence of water at the interface plays an important role in the mechanism of protein adsorption to the surface. Specifically, water mediates interactions between the surface hydroxyls and the protein by forming hydrogen

bond bridges between the hydroxyls and the polar residues with medium to long side chains like serine, asparagine and glutamine, or the negatively charged residues of aspartic and glutamic acids. Furthermore, it appears that the surface silanol layer does not provide sufficient hydration retention thus enabling some water-mediated contacts as the main water layer is displaced and residual water molecules are trapped. This stabilizes the adsorption by secondary bridging interactions in addition to direct protein-surface interactions. We believe this deficiency could be overcome through surface functionalisation by hydrophilic ligands that would be capable of maintaining a substantially thick and mobile hydration layer and prevent the protein from reaching the surface [95, 120-122].

6.5. Conclusion

In this work, we have shown two possible binding motifs for EAS hydrophobin at a hydrated silica surface during the early spontaneous adsorption events identified by MD simulations with atomic-level resolution. We found that for hydrophilic surfaces, the previously proposed aggregation state created by the unfolded Cys7-Cys8 loop is possible when hydrophobin adsorbs through residues 20-24 and 38-42 of the Cys3-Cys4 loop. It appears that there is a small energy barrier required to break a hydrogen bond formed between Ala41 and Ala77, which is necessary for the formation of the isolated β -sheet resulting from the unlocking of the Cys7-Cys8 loop. Furthermore, we have shown that the presence of areas void of water, due to roughness and hydroxyl spacing, allows the penetration of hydrophobic side chains, which bring the protein closer to the surface. Furthermore, there are significant interactions with the interfacial water layer which allow the formation of both intermittent and long-lasting interactions with this layer that seem to encourage rather than prevent the protein surface adhesion.

While this study does shed light on the monomeric hydrophobin behaviour at the surface water interface, the conformational sampling enabled by the brute force MD is far from comprehensive yet it remains a challenge for systems of such sizes at all-atom detail. In addition, there is significant information lacking to provide specific strategies for the development of anti-fouling coatings. In the next chapter, we will provide further investigation into the hydrophobin monolayer formation at various functionalised surfaces.

Chapter 7

7. Modelling Anti-Fouling Systems

7.1. Overview

In Chapter 5, we established a strong understanding of the interfacial behaviour of anti-fouling surfaces in water, comparing the hydration, heterogeneity, and chain dynamics of PEG and POX modified silica surfaces. Combining this knowledge with the behaviour of our contaminant, EAS hydrophobin, at the air-water and silica-water interfaces (Chapter 6), we look to elucidate whether entropic barriers associated with surface mobility or those from interfacial water have greater contributions to anti-fouling efficacy.

To do this, we have employed all-atom molecular dynamics to study initial stages of the spontaneous adsorption of monomeric EAS hydrophobin on PEG and POX functionalised silica surfaces. Due to the complexity of these interfaces, we have focussed on identifying general trends that can be attributed to the hydration and dynamics of the surface coatings detailed in Chapter 5. Whilst we were unable to identify any key interactions responsible for protein adsorption occurring, it appears that chains under the steric repulsion theory (Section 1.8.1) had a greater impact on delaying the initial adsorption of EAS, whilst hydration and hydrophobicity (Section 1.8.2) seemed to provide a more effective barrier for reducing the contact area.

7.2. Introduction

Over the last decade, significant research efforts have focussed on discovering anti-fouling surface coatings with good efficacy, robustness, and design simplicity. However, the

ability to design more effective anti-fouling coatings is limited by the paucity of fundamental knowledge on how these surfaces behave at a molecular level. To prevent the fouling of surfaces through protein adsorption, there are several approaches which can be separated into three main approaches, detailed earlier in this thesis, different surface chemistries (Section 1.6.1), surface roughness and morphology (Section 1.6.2), and a combination of both (Section 1.6.3). More recently, inspiration from plants like the lady's mantle leaf [395] has led to the implementation of coatings where common organic chain molecules are chemically grafted to surfaces, substantially reducing the amount of adsorbed protein compared to the base surface [138, 396]. Typical characteristics of these protein-resistant chains such as poly(ethylene glycol) (PEG) (Section 1.9.1) and poly(2-oxazoline) (POX) (Section 1.9.2), are their hydrophilic nature, the presence of hydrogen bond acceptors, no hydrogen bond donors, and charge neutrality [158, 369]. The origin of this resistance has been explained on the basis of hydration theory [148, 202, 397], steric repulsion [33, 34, 138] or as a combination of the two [159, 398], as detailed earlier in Section 1.8.

In Chapter 5, we have examined the conformity of existing theories that attempt to explain anti-fouling coating efficacy [33-35, 136-139, 157, 158]. We compared surfaces with high chain dynamics, relating to steric repulsion theories (Section 1.8.1) (PEG) to those with high hydration behaviour (Section 1.8.2) (POX), with results suggesting that current anti-fouling theories do not fully account for some of the more complicated atomistic detail of the traditional and novel chain functionalisation now being developed. We hypothesised that medium grafting density (2.2 chains/nm^2) PMeOx and PEtOx systems are leading candidates for high anti-fouling efficacy, as they combine atomic scale heterogeneity, and a hydration layer with almost twice the surface binding affinity to that of PEG. We believe that the hydrophobic exposure of PEG systems, particularly at medium and high grafting densities, is

likely to lead to the enhancement of protein adsorption, whilst low grafting density POX systems do not provide sufficient surface coverage.

To test these predictions, we have implemented all-atom MD simulations to investigate the adsorption of EAS Hydrophobin monomers to PEG and POX functionalised surfaces, and to further the fundamental understanding of interactions between a protein and functional coating, critical for the rational design of anti-fouling surfaces. In this chapter, we again use the Class I hydrophobin, EAS, as our contaminant model. Detailed background and information on EAS hydrophobin can be found in Section 1.4. In the previous chapter, we also identified two potential binding motifs (Figure 6.2) at the surface-water interface, and identified that roughness and hydrophobic exposure (in the form of hydroxyl spacing in silica), allows the penetration of hydrophobic side chains, which bring the protein closer to the surface, leading to enhanced protein adsorption. In this chapter we investigate if this behaviour is consistent even on functionalised surfaces, or if the added functionality is able to provide resistance/differences in adsorption behaviour.

7.3. Method

PEG and POX (PMeOx and PEtOx) surfaces. Both PEG and POX Systems were grafted in a manner compatible with grafting to and grafting from methods [365] at coverage densities of 1.4 and 2.2 chains/nm², corresponding to $\alpha = 0.32$ and 0.52, where α is the ratio of grafted chains to free silica surface hydroxyl groups.

The NMR solution structure of the class I hydrophobin EAS, determined by Kwan *et al.*, was obtained from the PDB structure 2FMC [76]. The protein was protonated in zwitterionic form and placed approximately 9 Å from the surface, in four different initial orientations rotated 90° about the y-axis, to allow the investigation of binding orientations in

spontaneous adsorption. The system was solvated using an explicit water layer of 80 Å thickness, with a 20 Å vacuum space above the water box added to create a pseudo air-water interface, and two counter-ions added to maintain system neutrality. Systems were first energy minimised using the conjugate gradient method. Following this, the water molecules were allowed to relax around the protein and surface by applying a short (2 ns) MD with the protein and surface constrained. Constraints were then removed and MD applied to the entire system for 200 ns to investigate the spontaneous initial adsorption events of the protein onto the silica surface. Five replicas were simulated for each orientation (except low PEG systems, where only 4 replicas were simulated) to accumulate statistics.

Simulation details

Simulations were performed using the LAMMPS [366] software with the CHARMM22 [246] force-field used for the protein, the CGENFF36 force-field used for the surface functionalisation, and the CHARMM-compatible Cruz-Chu [254] silica parameters. The TIP3P [367] water model was applied, with the SHAKE [267] algorithm employed to constrain water bond length and angle. For the evaluation of non-bonded interactions, a twin-range cutoff of 0.8 and 1 nm were used for van der Waals interactions, with a 1 nm cutoff for electrostatics and the PPPM solver used to calculate the long-range damping effect. The energy minimisations were carried out using the conjugate gradient method with a convergence criterion of 10^{-4} kcal/mol energy tolerance and 10^{-6} kcal/mol.Å force tolerance. MD was performed in the NVT ensemble using a timestep of 1 fs and a temperature of 298 K was maintained by a Nosé-Hoover thermostat [264] with a 0.1 ps coupling time.

7.4. Results and discussion

In Chapter 5, we examined the solvent behaviour of PEG and POX coatings, particularly focusing on the hydration and chain dynamics to check consistency or lack

thereof with current anti-fouling theories. We identified distinct differences in the interfaces presented by PEG and POX surfaces, with PEG coatings presenting a dynamic interface typical of anti-fouling surfaces described by steric repulsion theories (Section 1.8.1). POX coatings present a static interface with enhanced hydration behaviour (Section 1.8.2). In this chapter, we investigate the interaction of EAS hydrophobin with PEG and POX modified surfaces, to ascertain whether there is a relationship between PEG/POX responsive behaviour and anti-fouling efficacy.

Table 7.2 summarises results of the MD simulations (runs (R)) for each of the 6 systems at the completion of 200 ns of simulation. The non-interacting runs did not converge to the point where the protein diffused toward the surface-interface, in all these cases the protein had adsorbed at the air-water interface. As we have previously simulated EAS behaviour at the air-water interface (Chapter 6), the analysis in this chapter is based only on the “adsorbed runs” (ARs), the number of runs where the protein was in direct contact with the surface at termination of the run. Of these, runs with an average contact area greater than 750 \AA^2 over the last 50 ns have been labelled “AA”, and only those were used for adsorbed state analysis, as below this value the protein is in a metastable state. A disruption event “DE”, refers to events where the minimum of the protein comes within 0.5 \AA of the surface and then moves outside this region for more than 0.5 ns. To interpret this table, surfaces with showing better antifouling performance would have a low AA/AR ratio (i.e. proteins are adsorbing weakly rather than strongly) and a larger number of disruption events.

Table 7.2 Simulated system data summary: R = Total number of runs performed; NIR = non interacting runs; AR = adsorbed runs; AA = high contact area ARs used for adsorbed state analysis, DE = Number of disruption events. Low (L) and Medium (M) refer to the chain coverage density used (1.4 and 2.2 chains/nm²).

System	R	AR	AA	DE
PEG (L)	16	11	9	4.5
PEG (M)	20	20	20	2.3
PMeOx (L)	20	11	10	1.4
PMeOx (M)	20	20	16	1.9
PEtOx (L)	20	18	18	1.7
PEtOx (M)	20	20	16	3.2

The analysis performed here is split into two sections. First, we discuss the process of protein adsorption at the solid/liquid interface, comparing the ability of different surfaces to hinder initial protein adsorption, as well as the overall strength of adsorption (contact area) compared to previously investigated hydration and dynamic behaviour (Chapter 5). The final section of the results examines the adsorbed states of the protein at each of the solid/liquid interfaces compared to the previously observed behaviour of EAS hydrophobin at the air/water [77, 79, 376] and silica/water [368, 376] interfaces.

7.4.1. Initial adsorption process

As described in Chapter 5, there is only one structured persistent hydration layer at the surface-water interface that the protein must penetrate to contact the functional chains. This is due to the moderate packing density and flexibility of the chains. Furthermore, due to the thickness of the polymer layer, the protein is not able to form direct interactions with the substrate itself. Therefore, we have focussed our analysis on protein interactions with the hydration layer or the polymer chains.

Figure 7.9 shows the distance-time evolution for an exemplar adsorption trajectory of EAS at the low GD PEG/water interface, (An exemplar trajectory for each system is shown in Appendices Figure A7.1). EAS was initially started slightly within the cut-off distance from the surface to limit EAS diffusing to the air-water interface. It should also be noted that the chain max distance should only be used as a guide for all chains, especially PEG, as the chain length distributions identified previously (Figure 5.2) are very broad ($>10 \text{ \AA}$) at the grafting densities studied. We notice that the adsorption process is consistent across all systems, with the only differences being in the number of adsorption/contact events. Timing of events in the exemplar trajectory are used for the process description purpose and should not be considered as representative of average process time.

We observed a period of reversible engagement with the interface during the first ~ 20 ns (Figure 7.9). In this phase regions of the protein interact directly with the hydration layer above the interface, or come into direct contact with the polymer chains. At approximately 24 ns the protein becomes kinetically trapped at the interface, with minor fluctuations in the minimum protein height as the contact area between protein and surface increases. At approximately 26 ns, we see a small ($\sim 2 \text{ \AA}$) reduction in the protein minimum height, as the protein embeds into the polymer layer, where it remains stably adsorbed for the remainder of the run. The protein is able to penetrate into the polymer layer due to the lower grafting density of the polymer chains on amorphous silica substrate and associated reduced rigidity compared to the behaviour observed at typical SAMs [95, 122, 159]. Embedding of the protein into the body of the chains introduces an additional energy barrier which must be overcome in order for the protein to disengage with the interface.

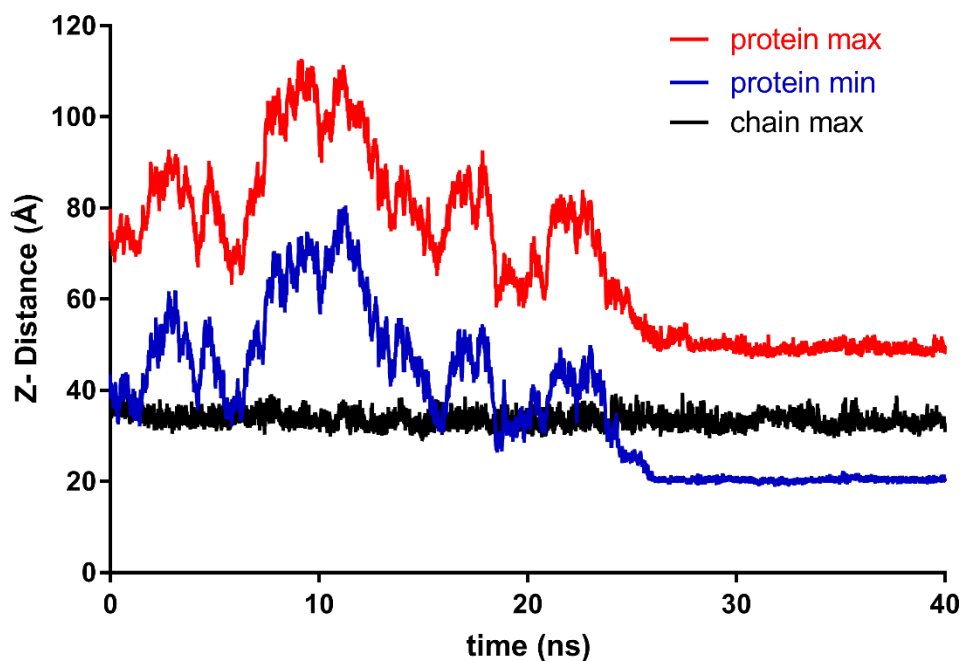


Figure 7.9 Exemplar temporal behaviour of the protein above low PEG chains (black); height of minimum of the protein (blue); and maximum (red).

Although the surfaces used in this study show significantly less ability to deter the protein than patterned systems used in a previous work [368], we notice that low GD PEG surfaces show the greatest ability to disrupt the initial adsorption (4.5 DE's), with medium PEtOx (3.2) and PEG (2.3) showing reasonable resistance. This suggests that the dynamic interface/steric repulsion behaviour provides a greater ability to prevent the formation of stable contact between the protein and the surface than the hydration and heterogeneity observed at the POX/water interfaces.

7.4.2. Adsorbed state analysis

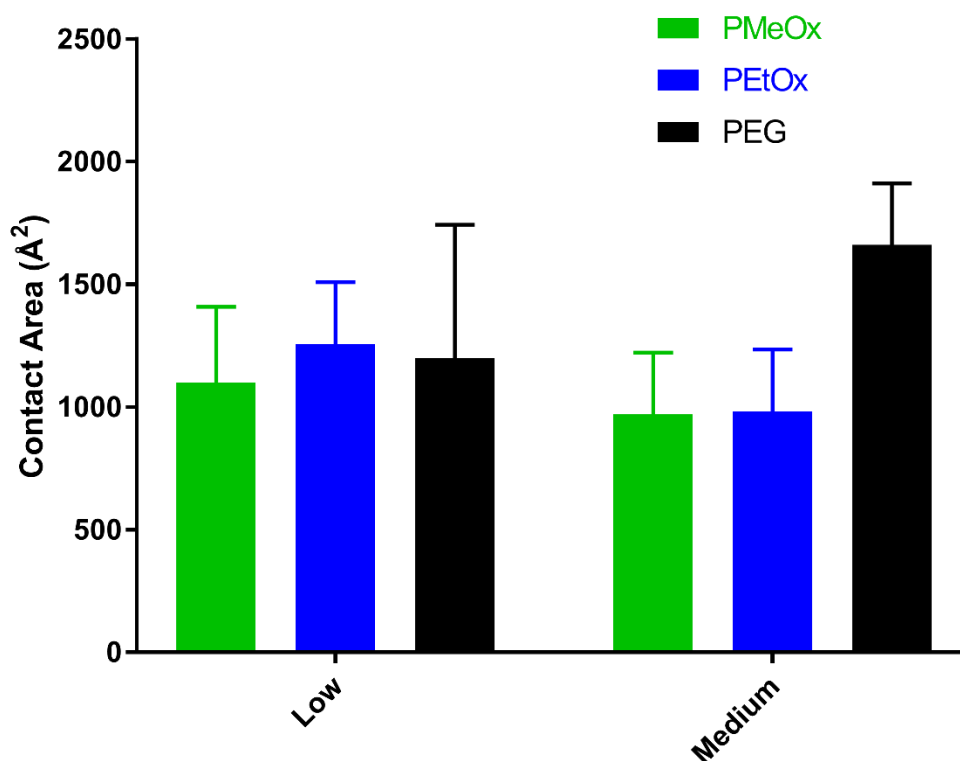


Figure 7.10 Average contact area of EAS at the solid/liquid interfaces of the adsorbed runs. The errors associated with the averages are the standard deviations across all such runs and do not consider fluctuations within individual runs.

To compare the strength of adsorption of EAS we use contact area as a metric, as it captures both the interaction strength between the protein and surface, as well as the displacement of water. As shown in Figure 7.10, we notice the contact area is generally lower for POX systems than PEG. In our simulations, low grafting density PMeOx (1099 \AA^2) chains perform slightly better than PEG (1199 \AA^2) and PEtOx (1256 \AA^2). However, there is no statistical difference between the 3 functional chains. Conversely, at medium grafting densities we see significant reduction from both PMeOx (969 \AA^2) and PEtOx (981 \AA^2) chains, whilst PEG (1661 \AA^2) sees enhanced strength of adsorption compared to the other surfaces.

This behaviour agrees with most of our predictions in the previous chapter, namely the low POX grafting systems do not provide sufficient surface coverage, and the flexibility of PEG terminal regions sees hydrophobic exposure for medium grafting PEG systems, resulting in reduced anti-fouling effectiveness. Interestingly, the slight increase in hydrophobicity and reduction in hydration retention of PEtOx is seen to have negligible effect at medium grafting densities. It should also be noted that whilst low grafting density PEG chains have an average contact area similar to that of POX chains, there is a significant larger standard deviation, likely attributed to the dynamic interface causing matches and mismatches in hydrophobicity and potential adsorption sites.

7.4.3. Chain dynamics

The sweeping mechanism proposed for long chains suggests that the dynamics of the chains at the interface can disrupt protein adsorption [136]. It was recently reported that increased dynamic behaviour of chains of varying length disrupts favourable short range interactions (hydrogen-bonds etc.) and improves anti-fouling efficacy [368]. Furthermore, a reduction in the chain mobility on contact with the protein suggests an entropic penalty working against protein adsorption [368]. In Chapter 5, we investigated the dynamics of chains in a solvent environment, noting significant differences in the dynamics of PEG and POX chains. We noted that PEG chains at low and medium grafting densities displayed almost indistinguishable RMSD profiles, due to surface interactions and the presence of a primer layer at low grafting densities, whilst PMeOx and PEtOx chains at low grafting density had a higher RMSD than those at medium grafting density. From these results, and under steric repulsion theories, we predicted that low grafting density POX would outperform medium grafting density POX, and medium grafting density PEG would outperform the lower grafting density PEG, due to the higher RMSD.

To the best of our knowledge, currently there is no method which can be easily implemented to calculate the loss of chain entropy upon protein adsorption. However, whilst the RMSD profile for chains in solvent give a semi-quantitative representation of chain dynamics, a reduction in the RMSD for chains in contact with the protein can be qualitatively used to describe the entropic penalty taken by the chains associated with protein adsorption. Figure 7.11 presents the RMSD profile for chains in solvent (as calculated in Chapter 5, Figure 5.5), as well as those in contact with EAS are shown. Despite having almost identical RMSD in a solvent environment, we see PEG chains at low grafting density providing significantly more entropic resistance to protein adsorption than those at medium grafting density, with a 40% and 25% reduction in RMSD respectively, suggesting that the primer layer presence, and conformational freedom attributed at the lower grafting density provide increased anti-fouling efficacy for PEG chains. A similar trend is noticed for POX systems, with PMeOx seeing 42% and 25%, and PEtOx 45% and 30% reductions for low and medium grafting density respectively. In Chapter 5 it was speculated that there was some optimal grafting density between 2.2 and 3 chains/nm² for the PEG system which would maximise the entropic penalty working against adsorption. Here the loss of chain dynamics is more significant at the lower grafting density. Considering the number of DE's and contact area for low and medium PEG systems, we believe it is more effective to have fewer chains with a higher reduction in RMSD than more chains with a moderate decrease in RMSD.

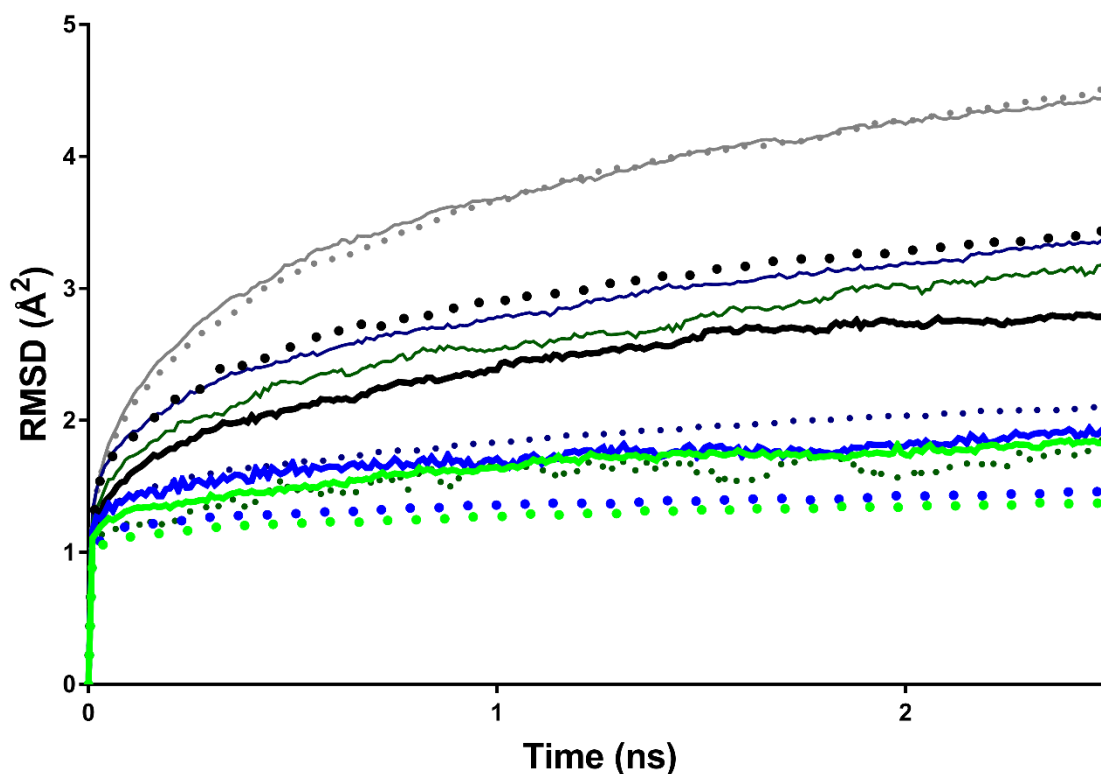


Figure 7.11 RMSD of chains for adsorbed runs for chains in contact (within 5\AA) with EAS. Colours: PMeOx (green), PETox (blue) and PEG (black), and the RMSD of chains in a solvent environment: PMeOx (dark green), PETox (dark blue) and PEG (grey) at low (solid) and medium (dotted) grafting densities.

However, when RMSD profiles are combined with the contact area plots (Figure 7.10), we notice that for PEG systems there is a relationship between the RMSD reduction and average contact area. Furthermore, we notice the entropic penalty associated with the sweeping mechanism of chains does not give a reliable indication of anti-fouling efficacy alone, as we see medium POX systems having the lowest average contact area for all systems studied. We believe that the difference in the trends of adsorption behaviour suggests two different mechanisms for anti-fouling are likely present, which we attribute to the heterogeneity and hydration behaviour of these coatings. Work by Sheikh *et al.* [146, 147] has linked the anti-fouling performance of surfaces to the ability of water to permeate the polymer layer. Their studies suggest that surfaces that allow greater hydration of the polymer layer should see increased anti-fouling efficacy. Furthermore, Whiteside's theories [157,

158], predicted that hydrophilic chains should be hydrogen bond acceptors rather than donors, and work by Kitano *et al.* [164-167] proposed that surfaces which are able to form strong interactions with interfacial water, whilst maintaining a disordered, bulk-like water layer, would provide limited entropic benefits for an approaching protein. Whilst we have not been able to determine which of these theories is most accurate, or to distinguish between them, we believe the hydration behaviour we observed in the simulations allows water molecules to compete with the protein for adsorption sites at the surface-water interface, thereby providing the additional entropic barrier responsible for minimising the protein contact area seen for medium POX systems in Figure 7.10.

7.4.4. Protein behaviour

The versatility of EAS to adsorb onto essentially any surface is likely due to its exposed surface consisting of hydrophobic and hydrophilic domains at a variety of length scales. A key region of this protein, the Cys3-Cys4 loop, portrays an inherently disordered conformation and high flexibility to both prevent aggregation in bulk phase [77], and at the air/water interface. It displays surfactant-like behaviour [77] and potentially stabilises adsorption [376], most likely due to the presence of a mixture of hydrophobic and hydrophilic residues capable of interacting with non-homogeneous interfaces. In other work [104, 114], amphiphilic domains at the amino acid length scale have been shown to aid protein adsorption to the surface of tightly packed hydrophobic/hydrophilic domain separated SAM surfaces. In addition, the overall surface of EAS has been shown to have large hydrophobic and hydrophilic domains [399]. Another key region on this protein is the Cys7-Cys8 loop. This loop plays a pivotal role in the mechanism for monolayer formation important for biofouling. It has been shown to adopt a beta barrel secondary structure positioned at opposite sides of the adsorbed protein to enable association with the Cys7-Cys8 loop of other monomers, thereby enabling fibril propagation [80]. An important aspect of the

anti-fouling capacity of these ligands is the capacity to limit and disrupt the interaction of the Cys7-Cys8 loop with the surface.

With this behaviour in mind, we have plotted the average contact probability for EAS residues with the functional chains for all systems (Figure 7.12). For most systems, we see a profile very typical of EAS adsorption at the surface/water interface, as detailed on silica (Chapter 6) and other work [368], with adsorption is predominantly occurring via contact between the Cys3-Cys4 loop and surface, consistent with the Binding Motif I identified in chapter 6 (Figure 6.2). Whilst we do see some adsorption profiles similar to Binding Motif II, there is a clear dominance for adsorption through the Cys3-Cys4 loop, likely attributed to the need for the flexibility and heterogeneity to neutralise the added surface functionality.

At low grafting density, there is little difference between the adsorption profiles, except that PEtOx has a greater portion of the Cys3-Cys4 loop in contact with the surface than other systems. At medium grafting densities, however, we notice significant differences in the adsorbed conformation. For PEG surfaces, there is increased contact for all four Cys loops. This is not surprising given its significantly larger contact area compared with other systems. However, the overall dominance of the Cys3-Cys4 loop suggests that the flexibility of this region provides a natural defence mechanism able to negate the sweeping motion functionality. Conversely, for POX systems at medium grafting density, especially PMeOx, we see a small increase in contact probability for the Cys7-Cys8 loop, and a significant decrease in all other peaks. As mentioned earlier, the capacity of anti-fouling chains to prevent this type of adsorption behaviour could potentially interfere with monolayer formation as amyloidogenic region is less accessible.

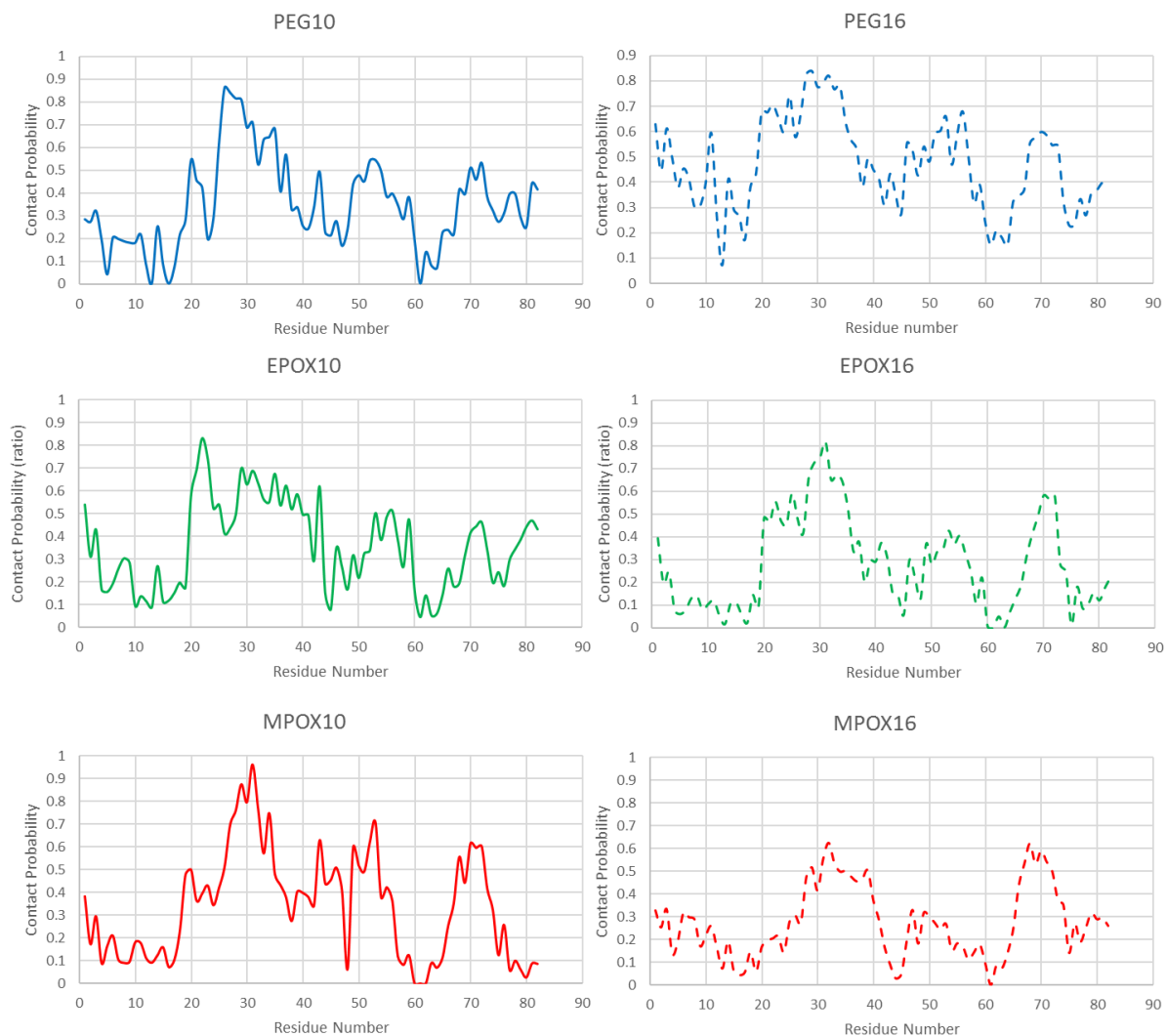


Figure 7.12 Probability for residues of EAS coming in contact with PEG/POX surfaces.

7.5. Conclusions

In this work we have employed all-atom MD simulations to examine the adsorption process and early phase of the adsorbed behaviour for EAS hydrophobin at the interface between short functional chains tethered to an amorphous silica surface and water. Three different functional chains, PMeOx, PEtOx and PEG, were grafted to silica at low (1.37 chains/nm²) and medium (2.19 chains/nm²) grafting densities. We have explored the two

predominant anti-fouling theories, steric repulsion and hydration theories, to gain a fundamental understanding of anti-fouling coatings, and to design principles for producing anti biofouling surfaces.

These results confirmed some predictions that were based on the solvent phase behaviour of these systems (Chapter 5), with medium PMeOx and PEtOx systems showing a strong ability to reduce contact area of the protein. We believe that this is because they combine atomic scale heterogeneity, and a hydration layer that is able to prevent the protein from forming a large contact area with the coating. We correctly predicted that the medium grafting density PEG system would have the least effective anti-fouling efficacy, which we reason is likely to be due to hydrophobic exposure, and the inherent flexibility of EAS' Cys3-Cys4 loop. However, we incorrectly predicted the ability of low PEG systems to heavily disturb and delay the adsorption of proteins.

Whilst we were unable to identify any key interactions responsible for protein adsorption occurring, it appears that chains under the steric repulsion (PEG) theory had a greater impact on delaying the initial adsorption of EAS, whilst hydration and hydrophobicity (POX) seemed to provide a more effective barrier for reducing the contact area. It would be interesting to investigate surface coatings that are capable of providing both these functionalities, and the effect this may have on protein adsorption.

Conclusions and Future Work

8. Conclusions

Responsive surfaces have been suggested to enhance anti-fouling performance and longevity of materials in many applications from industrial coatings to tissue engineering and drug delivery. However, in order to tailor surfaces for specific applications the underlying molecular mechanism that enables a functionalised surface to change properties in response to an external trigger must be understood. Atomistic simulations provide a useful tool to design more effective anti-fouling coatings, providing insight to the fundamental knowledge on how these surfaces behave at a molecular level.

Initially, we investigated the hydration-induced response of PEGylated substrates that include soft, organic polyester and a hard, inorganic silica surfaces. We showed that PEG chains grafted onto the hard silica substrates exhibit a dehydration induced collapse that is far more pronounced compared to chains grafted onto the soft polyester surface, especially at low grafting densities. We conclude that soft substrates may be detrimental for the efficient response of the functionalised surfaces to changes in hydration.

In a comparison of PEG and POX functionalised silica surfaces, we show that PEG systems exhibit greater chain dynamics, whilst POX systems show superior hydrophobicity and hydration behaviour. The observed structure-property relations for the PEG and POX modified surfaces provide an improved molecular understanding of the effects of molecular features on anti-fouling properties, and highlight the importance of entropic barriers associated with surface ligand mobility and interfacial water structure and dynamics for anti-fouling efficacy.

We successfully modelled the interaction of EAS with unmodified, and PEG/POX modified silica surfaces. On unmodified silica surfaces we were able to identify two possible binding motifs, and several key interactions that appeared key for adsorption at the surface-water interface. However, upon adsorption of EAS hydrophobin at PEG and POX functionalised surfaces, we were unable to identify any key interactions responsible for protein adsorption occurring. Whilst we did see some adsorption profiles similar to Binding Motif II, we noticed a clear dominance for adsorption through the Cys3-Cys4 loop, likely attributed to the need for the flexibility and heterogeneity to neutralise the added surface functionality.

Finally, we have explored the two predominant anti-fouling theories, steric repulsion and hydration theories, to gain a fundamental understanding of anti-fouling coatings, and to design principles for producing anti biofouling surfaces. From our simulations, it appears that chains under the steric repulsion theory had a greater impact on delaying the initial adsorption of EAS, whilst hydration and hydrophobicity seemed to provide a more effective barrier for reducing the contact area.

9. Future Work

We have shown that functionalised surfaces with chains presenting under steric repulsion theory have a greater impact on delaying the initial adsorption of protein contaminants, whilst hydration and hydrophobicity seemed to provide a more effective barrier for reducing the strength of adsorption. However, from our simulations it is apparent that individually, these surfaces are not able to fully deter protein adsorption. It would be interesting to investigate surface coatings that are capable of providing both these functionalities, and the effect this may have on protein adsorption.

One method of achieving this is through more advanced chains, like polyelectrolytic chains, as mentioned in Section 1.9.3. PEI's present significantly enhanced hydration properties than POX, and also have potential for high chain dynamics too. However, as mentioned earlier in this thesis, the computational power required to simulate the quantum region severely limits the overall system size. Although QM/MM could allow a small surface to be modelled, we believe the current computational power is not sufficient to accommodate simulations including the surface, protein and explicit water.

Another method is to look at varying degrees of chemical heterogeneity, dynamics and roughness, by functionalising substrates with alternating hydrophobic/hydrophilic chains. In recent work not included in this thesis [368], we have begun to explore these effects by investigating the effect such alternating ligands have on interfacial water, the adsorption process and conformational rearrangements of EAS hydrophobin.

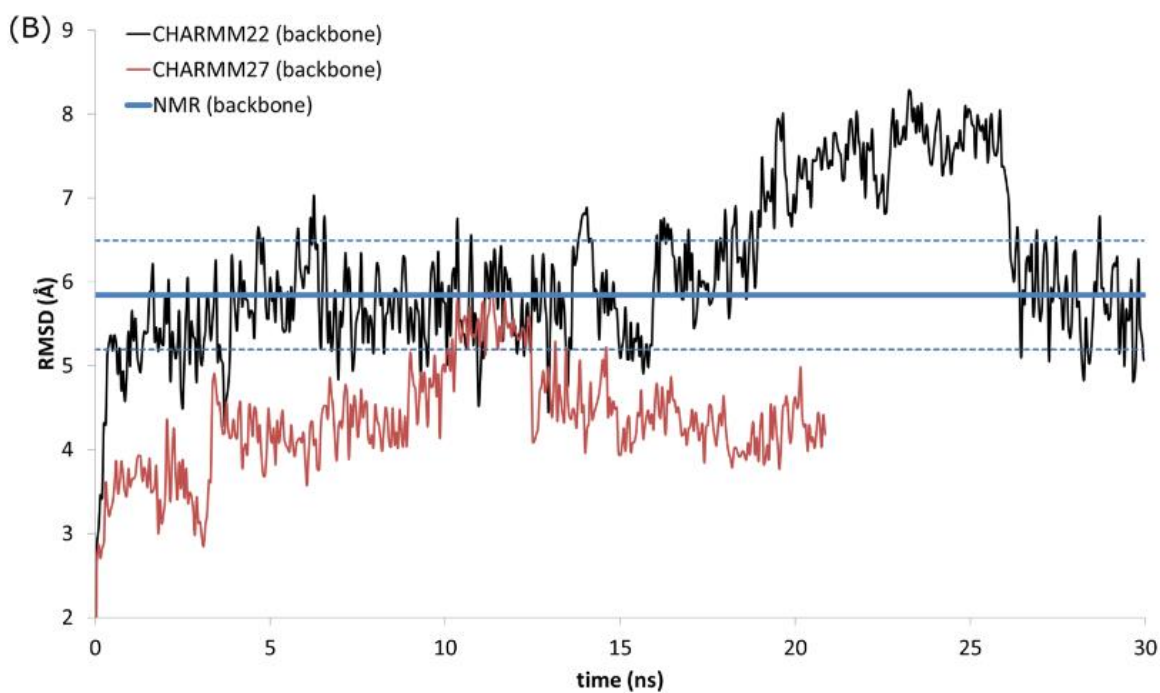
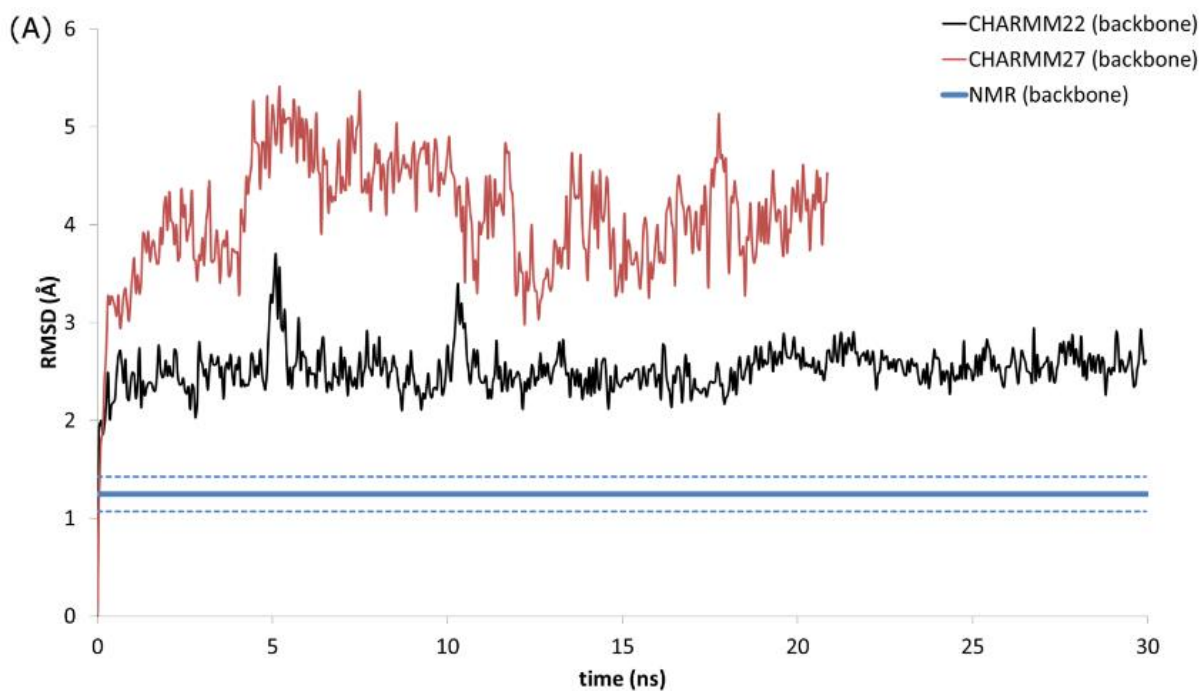
It should also be noted that in order to fully be able to understand and design more effective anti-fouling coatings, a greater understanding of the biofouling process is still needed. Focusing specifically on EAS and other hydrophobins, although suggestions on the monolayer formation structure have been suggested [80], the method by which these

monolayers form is still not yet known. Whilst being able to deter/delay the adsorption of monomers, or force them to adsorb in unfavourable conformations seems like an effective strategy, we do not fully know if this will achieve the desired effect. We believe that synergy between experimental characterisation and theoretical calculations will help design more effective antifouling coating strategies and technologies.

Appendices

The RMSD plots (Appendices Figure A6.1) show that the CHARMM22 force-field is a much better representation of the solution structure than the CHARMM27 force-field. The rigid regions of the protein (Appendices Figure A6.1A) have a much lower RMSD using CHARMM22 than CHARMM27, showing a better representation of the NMR structure. Conversely, for the Cys3-Cys4 loop we see much higher RMSD in CHARMM22 than CHARMM27, however as this region is highly flexible and mobile, as well as intrinsically disordered, the CHARMM22 force-field is again more suitable.

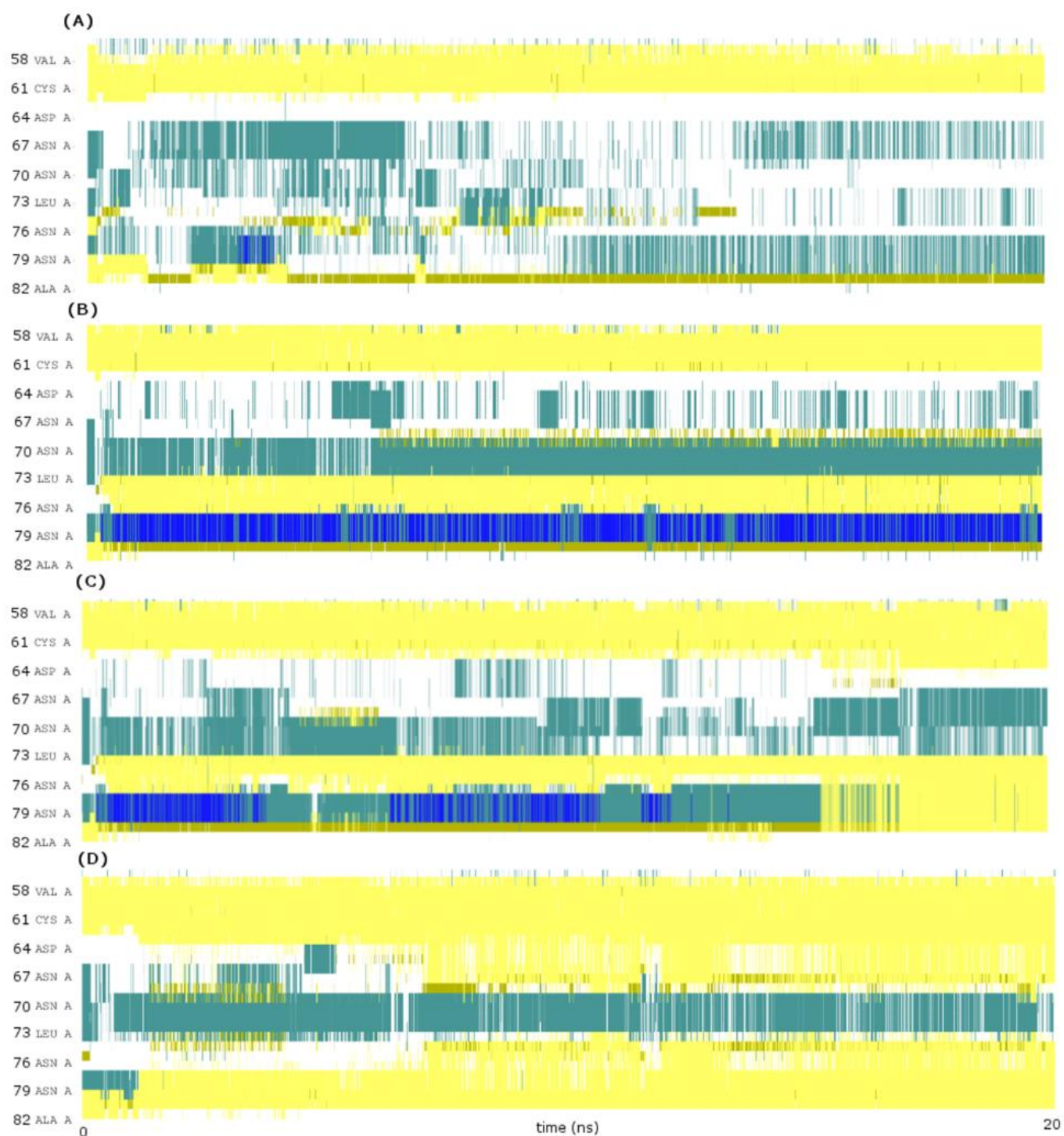
When looking at the secondary structure reproduction for CHARMM22 (Appendices Figure A6.2B), we see slight diminishing in the anti-parallel β -sheets of the core region (residues 43-47, 52-54, 58-62, 79-82). However, we do see the formation of an anti-parallel β -sheet in residues 73-76 as the Cys7-Cys8 loop remains folded to the β -core. For the CHARMM27 (Appendices Figure A6.2C) system we see much better retention of core and turn regions; however, as the Cys7-Cys8 loop spontaneously unfolds in solution we see full loss of β -sheet secondary structure for this loop. We also see small segments occasionally forming a 3_{10} -helix in residues 67-69.



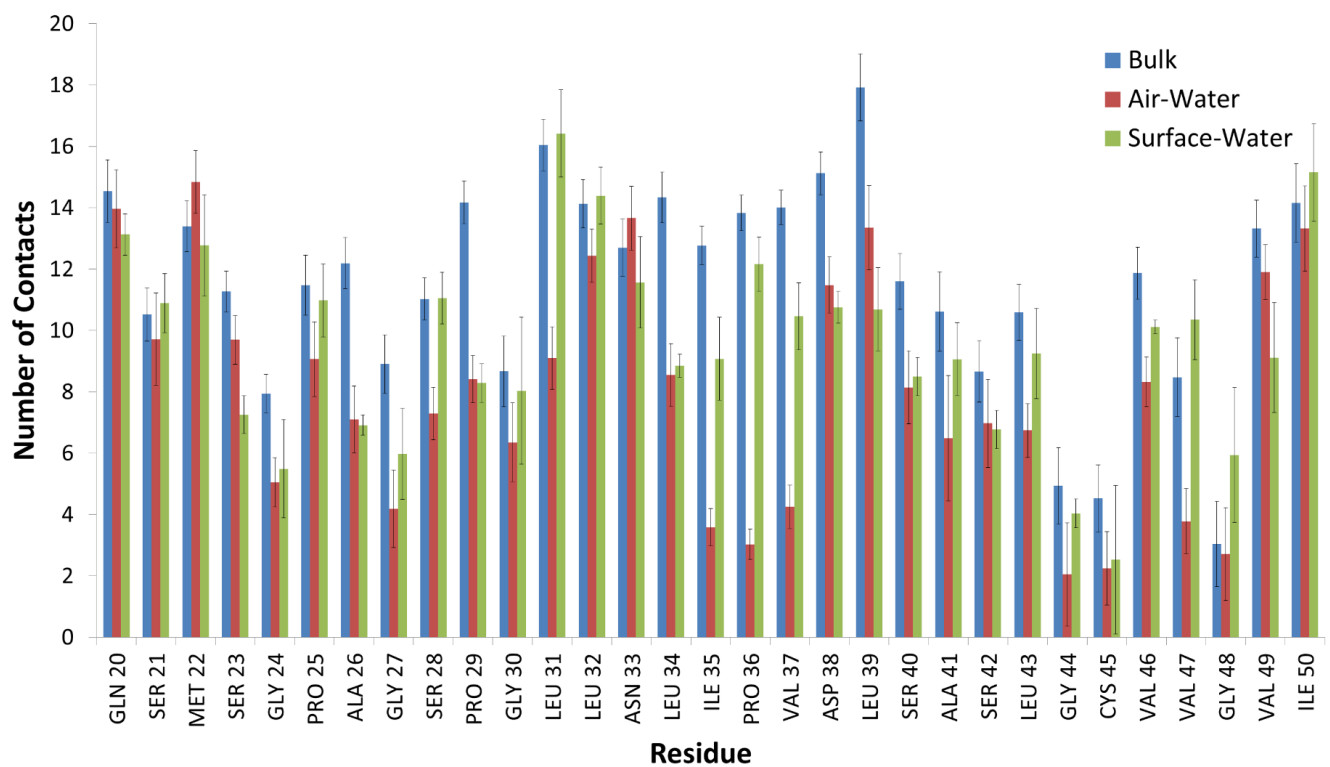
Appendices Figure A6.1 - RMSD plots for NMR structures (blue), CHARMM22 (black) and CHARMM27 (red) of (A) protein and not Cys3-Cys4 loop; and (B) Cys3-Cys4 loop only. Systems are compared to the lowest energy NMR structure from Kwan *et al.* 2006. Dotted blue lines represent the standard deviation for the 20 NMR structures.



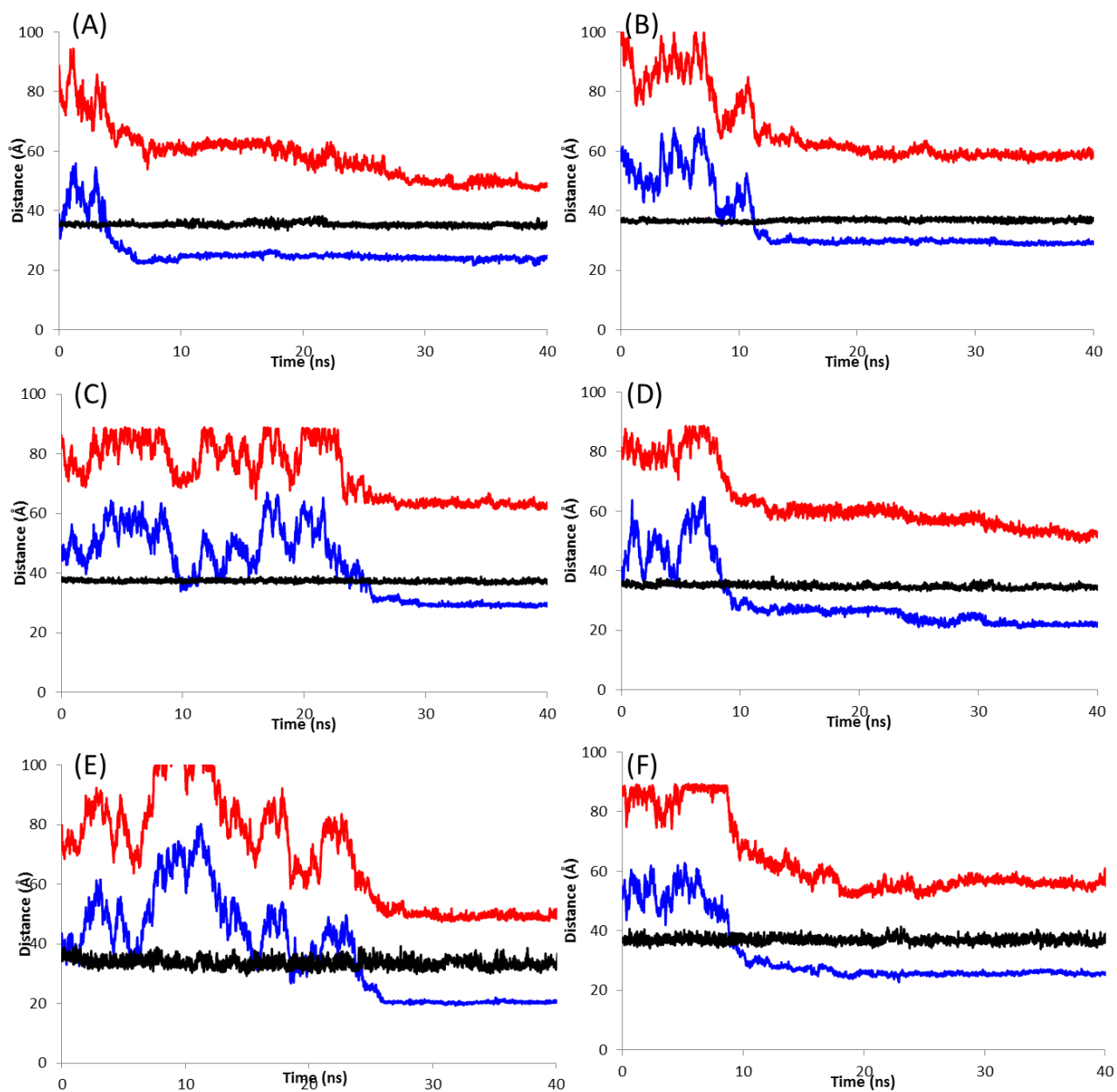
Appendices Figure A6.2 - Timeline graphs showing secondary structure of (A) 20 lowest energy configurations from NMR (PDB ID 2FMC, Kwan *et al.* 2006) (B) Secondary structure fluctuations for EAS in bulk solution using CHARMM22 (C) Secondary structure fluctuations for EAS in bulk solution using CHARMM27. Green color represents a turn structure, blue a 3_{10} -helix, yellow a parallel/anti-parallel β -sheet and gold an isolated β -sheet.



Appendices Figure A6.3 - Timeline graph of secondary structure for Cys7-Cys8 loop regions of (A) Binding Motif 2 and the three different systems in Binding Motif 1 (B-D). For Binding Motif 1, (B), (C), and (D) correspond to the black, green, and red simulation runs in Figure 2 and Figure 3 of the main text. Green colors represent a turn structure, blue a 3_{10} -helix, yellow a parallel/anti-parallel β -sheet and gold an isolated β -sheet.



Appendices Figure A6.4 - Average number of contacts with water for residues in the Cys3-Cys4 loop in bulk solution, and again at the air-water and surface-water interface over the last 10 ns of simulation. A contact was defined as a water atom coming within 3Å of the specified residue.



Appendices Figure A7.1 - Exemplar temporal behaviour of the protein above PMeOx low (A), medium (B), PEtOx low (C), medium (D) and PEG low (E) and medium (F). Colours: polymer maximum height (black); height of minimum of the protein (blue); and maximum (red).

References

1. Thevenot, P., W. Hu, and L. Tang, *Surface Chemistry influence implant biocompatibility*. Current Topics in Medicinal Chemistry, 2008. **8**(4): p. 270-280.
2. Lynch, I., A. Salvati, and K.A. Dawson, *Protein-nanoparticle interactions: What does the cell see?* Nature Nanotechnology, 2009. **4**(9): p. 546-7.
3. Shemetov, A.A., I. Nabiev, and A. Sukhanova, *Molecular interaction of proteins and peptides with nanoparticles*. ACS Nano, 2012. **6**(6): p. 4585-602.
4. Callow, J.A. and M.E. Callow, *Trends in the development of environmentally friendly fouling-resistant marine coatings*. Nat Commun, 2011. **2**: p. 244.
5. Banerjee, I., R.C. Pangule, and R.S. Kane, *Antifouling coatings: recent developments in the design of surfaces that prevent fouling by proteins, bacteria, and marine organisms*. Advanced Materials (Weinheim, Germany), 2011. **23**(6): p. 690-718.
6. Vroman, L., *Effect of Adsorbed Proteins on the Wettability of Hydrophilic and Hydrophobic Solids*. Nature, 1962. **196**(4853): p. 476-477.
7. Boks, N.P., et al., *Forces involved in bacterial adhesion to hydrophilic and hydrophobic surfaces*. Microbiology, 2008. **154**(Pt 10): p. 3122-33.
8. Gray, J.J., *The interaction of proteins with solid surfaces*. Current Opinion in Structural Biology, 2004. **14**(1): p. 110-5.
9. Argyris, D., P.D. Ashby, and A. Striolo, *Structure and Orientation of Interfacial Water Determine Atomic Force Microscopy Results: Insights from Molecular Dynamics Simulations*. ACS Nano, 2011. **5**(3): p. 2215-2223.
10. Argyris, D., et al., *Molecular Dynamics Studies of Interfacial Water at the Alumina Surface*. The Journal of Physical Chemistry C, 2011. **115**(5): p. 2038-2046.
11. Baudin, M. and K. Hermansson, *Metal oxide surface dynamics from molecular dynamics simulations: the alpha-Al₂O₃(0001) surface*. Surface Science, 2001. **474**(1-3): p. 107-113.
12. Winkler, A., et al., *Structure and diffusion in amorphous aluminum silicate: a molecular dynamics computer simulation*. Journal of Chemical Physics, 2004. **120**(1): p. 384-93.
13. Hass, K.C., et al., *The Chemistry of Water on Alumina Surfaces: Reaction Dynamics from First Principles*. Science, 1998(282).
14. Gutiérrez, G. and B. Johansson, *Molecular dynamics study of structural properties of amorphous Al₂O₃*. Physical Review B, 2002. **65**(10).
15. Naicker, P.K., et al., *Characterization of titanium dioxide nanoparticles using molecular dynamics simulations*. Journal of Physical Chemistry B, 2005. **109**(32): p. 15243-9.
16. Koparde, V.N. and P.T. Cummings, *Molecular Dynamics Study of Water Adsorption on TiO₂ Nanoparticles*. Journal of Physical Chemistry C, 2007. **111**(19): p. 6920-6926.
17. Matsui, M. and M. Akaogi, *Molecular Dynamics Simulation of the Structural and Physical Properties of the Four Polymorphs of TiO₂*. Molecular Simulation, 1991. **6**(4-6): p. 239-244.
18. Ogata, S., et al., *Variable-charge interatomic potentials for molecular-dynamics simulations of TiO₂*. Journal of Applied Physics, 1999. **86**(6): p. 3036.
19. Langel, W. and L. Menken, *Simulation of the interface between titanium oxide and amino acids in solution by first principles MD*. Surface Science, 2003. **538**(1-2): p. 1-9.

20. Kornherr, A., et al., *Multilayer adsorption of water at a rutile TiO₂(110) surface: towards a realistic modeling by molecular dynamics*. Journal of Chemical Physics, 2004. **121**(8): p. 3722-6.
21. Teppen, B.J., et al., *Molecular dynamics modeling of clay minerals .1. Gibbsite, kaolinite, pyrophyllite, and beidellite*. Journal of Physical Chemistry B, 1997. **101**(9): p. 1579-1587.
22. Teppen, B.J., et al., *Molecular dynamics simulations of sorption of organic compounds at the clay mineral aqueous solution interface*. Journal of Computational Chemistry, 1998. **19**(2): p. 144-153.
23. Yu, C.H., et al., *Molecular dynamics simulations of the adsorption of proteins on clay mineral surfaces*. Journal of Molecular Structure, 2000. **556**(1-3): p. 95-103.
24. Tunega, D., et al., *Ab initio molecular dynamics study of adsorption sites on the (001) surfaces of 1 : 1 dioctahedral clay minerals*. Journal of Physical Chemistry B, 2002. **106**(44): p. 11515-11525.
25. Zeng, Q.H., et al., *Molecular dynamics simulation of organic-inorganic nanocomposites: Layering behavior and interlayer structure of organoclays*. Chemistry of Materials, 2003. **15**(25): p. 4732-4738.
26. Cygan, R.T., J.-J. Liang, and A.G. Kalinichev, *Molecular Models of Hydroxide, Oxyhydroxide, and Clay Phases and the Development of a General Force Field*. The Journal of Physical Chemistry B, 2004. **108**(4): p. 1255-1266.
27. McCoustra, M.R., *Water at interfaces*. Physical Chemistry Chemical Physics, 2008. **10**(32): p. 4676-7.
28. Sodeifian, G., H.R. Nikooamal, and A.A. Yousefi, *Molecular dynamics study of epoxy/clay nanocomposites: rheology and molecular confinement*. Journal of Polymer Research, 2012. **19**(6).
29. Chen, Y., et al., *Mechanical characterization of interfaces in epoxy-clay nanocomposites by molecular simulations*. Polymer, 2013. **54**(2): p. 766-773.
30. Rimola, A., et al., *Silica surface features and their role in the adsorption of biomolecules: computational modeling and experiments*. Chem Rev, 2013. **113**(6): p. 4216-313.
31. Kasemo, B., *Biological surface science*. Surface Science, 2002. **500**(1-3): p. 656-677.
32. McPherson, T., et al., *Prevention of Protein Adsorption by Tethered Poly(ethylene oxide) Layers: Experiments and Single-Chain Mean-Field Analysis*. Langmuir, 1998. **14**(1): p. 176-186.
33. Szleifer, I., *Protein adsorption on tethered polymer layers: effect of polymer chain architecture and composition*. Physica A: Statistical Mechanics and its Applications, 1997. **244**(1-4): p. 370-388.
34. Szleifer, I., *Protein Adsorption on Surfaces with Grafted Polymers*. Biophysical Journal, 1997. **72**(2): p. 595-612.
35. Szleifer, I., *Polymers and proteins: interactions at interfaces*. Current Opinion in Solid State and Materials Science, 1997. **2**(3): p. 337-344.
36. Morriss-Andrews, A. and J.E. Shea, *Computational studies of protein aggregation: methods and applications*. Annual Review of Physical Chemistry, 2015. **66**: p. 643-66.
37. Yebra, D.M., S. Kiil, and K. Dam-Johansen, *Antifouling technology—past, present and future steps towards efficient and environmentally friendly antifouling coatings*. Progress in Organic Coatings, 2004. **50**(2): p. 75-104.
38. Campoccia, D., L. Montanaro, and C.R. Arciola, *A review of the biomaterials technologies for infection-resistant surfaces*. Biomaterials, 2013. **34**(34): p. 8533-54.

39. Desrousseaux, C., et al., *Modification of the surfaces of medical devices to prevent microbial adhesion and biofilm formation*. Journal of Hospital Infection, 2013. **85**(2): p. 87-93.
40. Harding, J.L. and M.M. Reynolds, *Combating medical device fouling*. Trends in Biotechnology, 2014. **32**(3): p. 140-6.
41. Díaz, C., et al., *Nano/microscale order affects the early stages of biofilm formation on metal surfaces*. Langmuir, 2007. **23**(22): p. 11206-11210.
42. Hasan, J., R.J. Crawford, and E.P. Ivanova, *Antibacterial surfaces: the quest for a new generation of biomaterials*. Trends in Biotechnology, 2013. **31**(5): p. 295-304.
43. Flemming, H.-C., *Microbial biofouling: Unsolved problems, insufficient approaches, and possible solutions*, in *Biofilm highlights*. 2011, Springer. p. 81-109.
44. Kamino, K., *Mini-review: barnacle adhesives and adhesion*. Biofouling, 2013. **29**(6): p. 735-49.
45. Bixler, G.D. and B. Bhushan, *Biofouling: lessons from nature*. Philos Trans A Math Phys Eng Sci, 2012. **370**(1967): p. 2381-417.
46. Magin, C.M., S.P. Cooper, and A.B. Brennan, *Non-toxic antifouling strategies*. Materials Today, 2010. **13**(4): p. 36-44.
47. Ostuni, E., et al., *A Survey of Structure–Property Relationships of Surfaces that Resist the Adsorption of Protein*. Langmuir, 2001. **17**(18): p. 5605-5620.
48. Wells-Bennik, M.H., et al., *Bacterial Spores in Food: Survival, Emergence, and Outgrowth*. Annu Rev Food Sci Technol, 2016. **7**: p. 457-82.
49. O'Toole, G., H.B. Kaplan, and R. Kolter, *Biofilm formation as microbial development*. Annual Review of Microbiology, 2000. **54**: p. 49-79.
50. Bergkvist, M., J. Carlsson, and S. Oscarsson, *Surface-dependent conformations of human plasma fibronectin adsorbed to silica, mica, and hydrophobic surfaces, studied with use of Atomic Force Microscopy*. J Biomed Mater Res A, 2003. **64**(2): p. 349-56.
51. Wösten, H.A., *Hydrophobins: multipurpose proteins*. Annual Reviews in Microbiology, 2001. **55**(1): p. 625-646.
52. Rabe, M., D. Verdes, and S. Seeger, *Understanding protein adsorption phenomena at solid surfaces*. Advances in Colloid and Interface Science, 2011. **162**(1-2): p. 87-106.
53. Norde, W., *My voyage of discovery to proteins in flatland ...and beyond*. Colloids Surf B Biointerfaces, 2008. **61**(1): p. 1-9.
54. Paslay, L.C., et al., *Kinetics and control of self-assembly of ABH1 hydrophobin from the edible white button mushroom*. Biomacromolecules, 2013. **14**(7): p. 2283-93.
55. Stewart, P.S. and M.J. Franklin, *Physiological heterogeneity in biofilms*. Nature Reviews Microbiology, 2008. **6**(3): p. 199-210.
56. Townsin, R.L., *The ship hull fouling penalty*. Biofouling, 2003. **19 Suppl**: p. 9-15.
57. Hallegraeff, G.M., *A review of harmful algal blooms and their apparent global increase**. Phycologia, 1993. **32**(2): p. 79-99.
58. De Groot, P.W., et al., *The Agaricus bisporus hypA gene encodes a hydrophobin and specifically accumulates in peel tissue of mushroom caps during fruit body development*. Journal of Molecular Biology, 1996. **257**(5): p. 1008-18.
59. Kazmierczak, P., et al., *A Hydrophobin of the chestnut blight fungus, Cryphonectria parasitica, is required for stromal pustule eruption*. Eukaryotic Cell, 2005. **4**(5): p. 931-6.
60. Scherrer, S., et al., *Interfacial self-assembly of fungal hydrophobins of the lichen-forming ascomycetes Xanthoria parietina and X. ectaneoides*. Fungal Genetics and Biology, 2000. **30**(1): p. 81-93.

61. Talbot, N.J., et al., *MPG1 Encodes a Fungal Hydrophobin Involved in Surface Interactions during Infection-Related Development of Magnaporthe grisea*. Plant Cell, 1996. **8**(6): p. 985-999.
62. Bruns, S., et al., *Production of extracellular traps against Aspergillus fumigatus in vitro and in infected lung tissue is dependent on invading neutrophils and influenced by hydrophobin RodA*. PLoS Pathogens, 2010. **6**(4): p. e1000873.
63. Aïmanianda, V., et al., *Surface hydrophobin prevents immune recognition of airborne fungal spores*. Nature, 2009. **460**(7259): p. 1117-21.
64. Dagenais, T.R., et al., *Aspergillus fumigatus LaeA-mediated phagocytosis is associated with a decreased hydrophobin layer*. Infection and Immunity, 2010. **78**(2): p. 823-9.
65. Hohl, T.M., et al., *Aspergillus fumigatus triggers inflammatory responses by stage-specific beta-glucan display*. PLoS Pathogens, 2005. **1**(3): p. e30.
66. Linder, M.B., et al., *Hydrophobins: the protein-amphiphiles of filamentous fungi*. FEMS Microbiology Reviews, 2005. **29**(5): p. 877-896.
67. Wösten, H.A.B., et al., *How a fungus escapes the water to grow into the air*. Current Biology, 1999. **9**(2): p. 85-88.
68. Wösten, H.A.B. and M.L. de Vocht, *Hydrophobins, the fungal coat unravelled*. Biochimica et Biophysica Acta (BBA) - Reviews on Biomembranes, 2000. **1469**(2): p. 79-86.
69. Linder, M.B., *Hydrophobins: Proteins that self assemble at interfaces*. Current Opinion in Colloid & Interface Science, 2009. **14**(5): p. 356-363.
70. Lo, V.C., et al., *Fungal Hydrophobin Proteins Produce Self-Assembling Protein Films with Diverse Structure and Chemical Stability*. Nanomaterials, 2014. **4**(3): p. 827-843.
71. Wösten, H.A. and M.L. de Vocht, *Hydrophobins, the fungal coat unravelled*. Biochimica et Biophysica Acta (BBA)-Reviews on Biomembranes, 2000. **1469**(2): p. 79-86.
72. Bayry, J., et al., *Hydrophobins--unique fungal proteins*. PLoS Pathogens, 2012. **8**(5): p. e1002700.
73. Lugones, L.G., et al., *An abundant hydrophobin (ABH1) forms hydrophobic rodlet layers in Agaricus bisporus fruiting bodies*. Microbiology, 1996. **142**(5): p. 1321-1329.
74. Paananen, A., et al., *Structural hierarchy in molecular films of two class II hydrophobins*. Biochemistry, 2003. **42**(18): p. 5253-5258.
75. de Vocht, M.L., et al., *Structural Characterization of the Hydrophobin SC3, as a Monomer and after Self-Assembly at Hydrophobic/Hydrophilic Interfaces*. Biophysical Journal, 1998. **74**(4): p. 2059-2068.
76. Kwan, A.H.Y., et al., *Structural basis for rodlet assembly in fungal hydrophobins*. Proceedings of the National Academy of Sciences, 2006. **103**(10): p. 3621-3626.
77. De Simone, A., et al., *Intrinsic disorder modulates protein self-assembly and aggregation*. Proceedings of the National Academy of Sciences, 2012. **109**(18): p. 6951-6956.
78. Mackay, J.P., et al., *The hydrophobin EAS is largely unstructured in solution and functions by forming amyloid-like structures*. Structure, 2001. **9**(2): p. 83-91.
79. Kwan, A.H., et al., *The Cys3-Cys4 loop of the hydrophobin EAS is not required for rodlet formation and surface activity*. Journal of Molecular Biology, 2008. **382**(3): p. 708-20.

80. Macindoe, I., et al., *Self-assembly of functional, amphipathic amyloid monolayers by the fungal hydrophobin EAS*. Proceedings of the National Academy of Sciences of the United States of America, 2012. **109**(14): p. E804-11.
81. Chambers, L.D., et al., *Modern approaches to marine antifouling coatings*. Surface and Coatings Technology, 2006. **201**(6): p. 3642-3652.
82. Champ, M.A. *The status of the treaty to ban TBT in marine antifouling paints and alternatives*. in *Proceedings of the 24th UJNR (US/Japan) Marine Facilities Panel Meeting, Hawaii*. 2001.
83. Champ, M.A., *A review of organotin regulatory strategies, pending actions, related costs and benefits*. Science of the Total Environment, 2000. **258**(1-2): p. 21-71.
84. Evans, S.M., T. Leksono, and P.D. McKinnell, *Tributyltin pollution: A diminishing problem following legislation limiting the use of TBT-based anti-fouling paints*. Marine Pollution Bulletin, 1995. **30**(1): p. 14-21.
85. Denis, F.A., et al., *Protein Adsorption on Model Surfaces with Controlled Nanotopography and Chemistry*. Langmuir, 2002. **18**(3): p. 819-828.
86. Mitik-Dineva, N., et al., *Adhesion of Bacteria*. Wiley Encyclopedia of Biomedical Engineering, 2006.
87. Ulman, A., *Formation and Structure of Self-Assembled Monolayers*. Chemical Reviews, 1996. **96**(4): p. 1533-1554.
88. Love, J.C., et al., *Self-assembled monolayers of thiolates on metals as a form of nanotechnology*. Chem Rev, 2005. **105**(4): p. 1103-69.
89. Krishnan, S., C.J. Weinman, and C.K. Ober, *Advances in polymers for anti-biofouling surfaces*. Journal of Materials Chemistry, 2008. **18**(29): p. 3405-3413.
90. Umoren, S.A. and M.M. Solomon, *Recent Developments on the Use of Polymers as Corrosion Inhibitors - A Review*. The Open Materials Science Journal, 2014. **8**(1): p. 39-54.
91. Bagwe, R.P., L.R. Hilliard, and W. Tan, *Surface modification of silica nanoparticles to reduce aggregation and nonspecific binding*. Langmuir, 2006. **22**(9): p. 4357-62.
92. Price, P.M., J.H. Clark, and D.J. Macquarrie, *Modified silicas for clean technology*. Journal of the Chemical Society-Dalton Transactions, 2000. **2**: p. 101-110.
93. Patel, A.J., et al., *Sitting at the edge: How biomolecules use hydrophobicity to tune their interactions and function*. The Journal of Physical Chemistry B, 2012. **116**(8): p. 2498-2503.
94. Roach, P., D. Farrar, and C.C. Perry, *Interpretation of protein adsorption: surface-induced conformational changes*. Journal of the American Chemical Society, 2005. **127**(22): p. 8168-73.
95. Chen, S., et al., *Surface hydration: Principles and applications toward low-fouling/nonfouling biomaterials*. Polymer, 2010. **51**(23): p. 5283-5293.
96. Yiapanis, G., et al., *Effect of surface composition and atomic roughness on interfacial adhesion between polyester and amorphous carbon*. The Journal of Physical Chemistry C, 2007. **111**(7): p. 3000-3009.
97. Schwierz, N., et al., *On the relationship between peptide adsorption resistance and surface contact angle: a combined experimental and simulation single-molecule study*. Journal of the American Chemical Society, 2012. **134**(48): p. 19628-19638.
98. Bazaka, K., R.J. Crawford, and E.P. Ivanova, *Do bacteria differentiate between degrees of nanoscale surface roughness?* Biotechnology Journal, 2011. **6**(9): p. 1103-14.
99. Martinez, E., et al., *Effects of artificial micro- and nano-structured surfaces on cell behaviour*. Annals of Anatomy, 2009. **191**(1): p. 126-35.

100. Lord, M.S., M. Foss, and F. Besenbacher, *Influence of nanoscale surface topography on protein adsorption and cellular response*. Nano Today, 2010. **5**(1): p. 66-78.
101. Crawford, R.J., et al., *Surface topographical factors influencing bacterial attachment*. Advances in Colloid and Interface Science, 2012. **179-182**: p. 142-9.
102. Schumacher, J.F., et al., *Engineered antifouling microtopographies - effect of feature size, geometry, and roughness on settlement of zoospores of the green alga Ulva*. Biofouling, 2007. **23**(1-2): p. 55-62.
103. Lau, K.H., et al., *Modulation of protein-surface interactions on nanopatterned polymer films*. Biomacromolecules, 2009. **10**(5): p. 1061-6.
104. Hung, A., et al., *Ordering surfaces on the nanoscale: implications for protein adsorption*. Journal of the American Chemical Society, 2011. **133**(5): p. 1438-50.
105. Mitragotri, S. and J. Lahann, *Physical approaches to biomaterial design*. Nature Materials, 2009. **8**(1): p. 15-23.
106. Jackson, A.M., J.W. Myerson, and F. Stellacci, *Spontaneous assembly of subnanometre-ordered domains in the ligand shell of monolayer-protected nanoparticles*. Nature Materials, 2004. **3**(5): p. 330-6.
107. Mager, M.D., V. LaPointe, and M.M. Stevens, *Exploring and exploiting chemistry at the cell surface*. Nat Chem, 2011. **3**(8): p. 582-9.
108. Zhao, C., et al., *Functional polymer thin films designed for antifouling materials and biosensors*. Chemical Papers, 2012. **66**(5).
109. Charnley, M., M. Textor, and C. Acikgoz, *Designed polymer structures with antifouling–antimicrobial properties*. Reactive and Functional Polymers, 2011. **71**(3): p. 329-334.
110. Shen, L. and J. Zhu, *Heterogeneous surfaces to repel proteins*. Advances in Colloid and Interface Science, 2016. **228**: p. 40-54.
111. Glotzer, S.C. and M.J. Solomon, *Anisotropy of building blocks and their assembly into complex structures*. Nature Materials, 2007. **6**(8): p. 557-62.
112. Kuna, J.J., et al., *The effect of nanometre-scale structure on interfacial energy*. Nature Materials, 2009. **8**(10): p. 837-42.
113. Jackson, A.M., et al., *From homoligand- to mixed-ligand- monolayer-protected metal nanoparticles: a scanning tunneling microscopy investigation*. Journal of the American Chemical Society, 2006. **128**(34): p. 11135-49.
114. Hung, A., et al., *Amphiphilic amino acids: a key to adsorbing proteins to nanopatterned surfaces?* Chemical Science, 2013. **4**(3): p. 928-937.
115. Leng, C., et al., *Molecular level studies on interfacial hydration of zwitterionic and other antifouling polymers in situ*. Acta Biomater, 2016. **40**: p. 6-15.
116. Notman, R. and T.R. Walsh, *Molecular dynamics studies of the interactions of water and amino acid analogues with quartz surfaces*. Langmuir, 2009. **25**(3): p. 1638-44.
117. Schneider, J. and L.C. Ciacchi, *Specific material recognition by small peptides mediated by the interfacial solvent structure*. Journal of the American Chemical Society, 2012. **134**(4): p. 2407-13.
118. Penna, M.J., M. Mijajlovic, and M.J. Biggs, *Molecular-level understanding of protein adsorption at the interface between water and a strongly interacting uncharged solid surface*. Journal of the American Chemical Society, 2014. **136**(14): p. 5323-5331.
119. Kim, J. and P.S. Cremer, *Elucidating changes in interfacial water structure upon protein adsorption*. ChemPhysChem, 2001. **2**(8-9): p. 543-546.
120. Leung, B.O., et al., *Role of interfacial water on protein adsorption at cross-linked polyethylene oxide interfaces*. Langmuir, 2012. **28**(13): p. 5724-5728.
121. Yiapanis, G., et al., *Nanoscale wetting and fouling resistance of functionalized surfaces: a computational approach*. Langmuir, 2014. **30**(35): p. 10617-25.

122. Zheng, J., et al., *Strong repulsive forces between protein and oligo (ethylene glycol) self-assembled monolayers: a molecular simulation study*. *Biophysical Journal*, 2005. **89**(1): p. 158-66.
123. Argyris, D., et al., *Molecular Structure and Dynamics in Thin Water Films at the Silica and Graphite Surfaces*. *The Journal of Physical Chemistry C*, 2008. **112**(35): p. 13587-13599.
124. Argyris, D., D.R. Cole, and A. Striolo, *Dynamic Behavior of Interfacial Water at the Silica Surface*. *The Journal of Physical Chemistry C*, 2009. **113**(45): p. 19591-19600.
125. Argyris, D., D.R. Cole, and A. Striolo, *Ion-specific effects under confinement: the role of interfacial water*. *ACS Nano*, 2010. **4**(4): p. 2035-42.
126. Argyris, D., D.R. Cole, and A. Striolo, *Hydration structure on crystalline silica substrates*. *Langmuir*, 2009. **25**(14): p. 8025-35.
127. Ho, T.A., et al., *Aqueous NaCl and CsCl solutions confined in crystalline slit-shaped silica nanopores of varying degree of protonation*. *Langmuir*, 2012. **28**(2): p. 1256-66.
128. Granick, S. and S.C. Bae, *Chemistry. A curious antipathy for water*. *Science*, 2008. **322**(5907): p. 1477-8.
129. Poynor, A., et al., *How water meets a hydrophobic surface*. *Physical Review Letters*, 2006. **97**(26): p. 266101.
130. Zhang, X., Y. Zhu, and S. Granick, *Hydrophobicity at a Janus interface*. *Science*, 2002. **295**(5555): p. 663-6.
131. Zhu, Y. and S. Granick, *Viscosity of interfacial water*. *Physical Review Letters*, 2001. **87**(9): p. 096104.
132. Luzinov, I., S. Minko, and V.V. Tsukruk, *Adaptive and responsive surfaces through controlled reorganization of interfacial polymer layers*. *Progress in Polymer Science*, 2004. **29**(7): p. 635-698.
133. Aumsuwan, N., S. Heinhorst, and M.W. Urban, *Antibacterial Surfaces on Expanded Polytetrafluoroethylene; Penicillin Attachment*. *Biomacromolecules*, 2007. **8**(2): p. 713-718.
134. Aumsuwan, N., et al., *Attachment of Ampicillin to Expanded Poly(tetrafluoroethylene): Surface Reactions Leading to Inhibition of Microbial Growth*. *Biomacromolecules*, 2008. **9**(7): p. 1712-1718.
135. Lee, J., H. Lee, and J. Andrade, *Blood compatibility of polyethylene oxide surfaces*. *Progress in Polymer Science*, 1995. **20**(6): p. 1043-1079.
136. Andrade, J.D. and V. Hlady, *Protein adsorption and materials biocompatibility: A tutorial review and suggested hypotheses*. 1986. **79**: p. 1-63.
137. Nagaoka, S., et al., *Interaction Between Blood Components and Hydrogels With Poly(Oxyethylene) Chains*. 1984: p. 361-374.
138. Jeon, S.I., et al., *Protein—surface interactions in the presence of polyethylene oxide*. *Journal of Colloid and Interface Science*, 1991. **142**(1): p. 149-158.
139. Jeon, S.I. and J.D. Andrade, *Protein—surface interactions in the presence of polyethylene oxide*. *Journal of Colloid and Interface Science*, 1991. **142**(1): p. 159-166.
140. Kingshott, P., H. Thissen, and H.J. Griesser, *Effects of cloud-point grafting, chain length, and density of PEG layers on competitive adsorption of ocular proteins*. *Biomaterials*, 2002. **23**(9): p. 2043-2056.
141. Desai, N.P. and J.A. Hubbell, *Biological responses to polyethylene oxide modified polyethylene terephthalate surfaces*. *Journal of Biomedical Materials Research*, 1991. **25**(7): p. 829-43.

142. Desai, N.P. and J.A. Hubbell, *Solution technique to incorporate polyethylene oxide and other water-soluble polymers into surfaces of polymeric biomaterials*. Biomaterials, 1991. **12**(2): p. 144-153.
143. Gombotz, W.R., et al., *Protein adsorption to poly(ethylene oxide) surfaces*. Journal of Biomedical Materials Research, 1991. **25**(12): p. 1547-62.
144. Prime, K. and G. Whitesides, *Self-assembled organic monolayers: model systems for studying adsorption of proteins at surfaces*. Science, 1991. **252**(5009): p. 1164-1167.
145. Prime, K.L. and G.M. Whitesides, *Adsorption of proteins onto surfaces containing end-attached oligo(ethylene oxide): a model system using self-assembled monolayers*. Journal of the American Chemical Society, 1993. **115**(23): p. 10714-10721.
146. Sheikh, S., et al., *On the hydration of subnanometric antifouling organosilane adlayers: a molecular dynamics simulation*. Journal of Colloid and Interface Science, 2015. **437**: p. 197-204.
147. Sheikh, S., et al., *Single ether group in a glycol-based ultra-thin layer prevents surface fouling from undiluted serum*. Chem Commun (Camb), 2012. **48**(9): p. 1305-7.
148. Harder, P., et al., *Molecular Conformation in Oligo(ethylene glycol)-Terminated Self-Assembled Monolayers on Gold and Silver Surfaces Determines Their Ability To Resist Protein Adsorption*. The Journal of Physical Chemistry B, 1998. **102**(2): p. 426-436.
149. Kreuzer, H.J., R.L.C. Wang, and M. Grunze, *Effect of stretching on the molecular conformation of oligo (ethylene oxide): a theoretical study*. New Journal of Physics, 1999. **1**(1): p. 21.
150. Wang, R.L.C., H.J. Kreuzer, and M. Grunze, *Molecular Conformation and Solvation of Oligo(ethylene glycol)-Terminated Self-Assembled Monolayers and Their Resistance to Protein Adsorption*. The Journal of Physical Chemistry B, 1997. **101**(47): p. 9767-9773.
151. Pertsin, A.J. and M. Grunze, *Computer Simulation of Water near the Surface of Oligo(ethylene glycol)-Terminated Alkanethiol Self-Assembled Monolayers†*. Langmuir, 2000. **16**(23): p. 8829-8841.
152. Pertsin, A.J., T. Hayashi, and M. Grunze, *Grand Canonical Monte Carlo Simulations of the Hydration Interaction between Oligo(ethylene glycol)-Terminated Alkanethiol Self-Assembled Monolayers*. The Journal of Physical Chemistry B, 2002. **106**(47): p. 12274-12281.
153. Unsworth, L.D., H. Sheardown, and J.L. Brash, *Protein resistance of surfaces prepared by sorption of end-thiolated poly(ethylene glycol) to gold: effect of surface chain density*. Langmuir, 2005. **21**(3): p. 1036-41.
154. Unsworth, L.D., H. Sheardown, and J.L. Brash, *Protein-resistant poly(ethylene oxide)-grafted surfaces: chain density-dependent multiple mechanisms of action*. Langmuir, 2008. **24**(5): p. 1924-9.
155. Unsworth, L.D., et al., *In situ neutron reflectometry investigation of gold-chemisorbed PEO layers of varying chain density: relationship of layer structure to protein resistance*. Journal of Colloid and Interface Science, 2006. **296**(2): p. 520-6.
156. Besseling, N.A.M., *Theory of Hydration Forces between Surfaces*. Langmuir, 1997. **13**(7): p. 2113-2122.
157. Sigal, G.B., M. Mrksich, and G.M. Whitesides, *Effect of Surface Wettability on the Adsorption of Proteins and Detergents*. Journal of the American Chemical Society, 1998. **120**(14): p. 3464-3473.

158. Ostuni, E., et al., *Self-Assembled Monolayers That Resist the Adsorption of Proteins and the Adhesion of Bacterial and Mammalian Cells*. Langmuir, 2001. **17**(20): p. 6336-6343.
159. Li, L., et al., *Protein adsorption on oligo(ethylene glycol)-terminated alkanethiolate self-assembled monolayers: The molecular basis for nonfouling behavior*. Journal of Physical Chemistry B, 2005. **109**(7): p. 2934-41.
160. Cao, X., et al., *Resistance of polysaccharide coatings to proteins, hematopoietic cells, and marine organisms*. Biomacromolecules, 2009. **10**(4): p. 907-15.
161. Mohan, T., et al., *Antifouling coating of cellulose acetate thin films with polysaccharide multilayers*. Carbohydrate Polymers, 2015. **116**: p. 149-58.
162. Cao, B., et al., *Zwitteration of dextran: a facile route to integrate antifouling, switchability and optical transparency into natural polymers*. Chem Commun (Camb), 2014. **50**(24): p. 3234-7.
163. Österberg, E., et al., *Comparison of polysaccharide and poly(ethylene glycol) coatings for reduction of protein adsorption on polystyrene surfaces*. Colloids and Surfaces A: Physicochemical and Engineering Aspects, 1993. **77**(2): p. 159-169.
164. Kitano, H., et al., *Hydrogen-Bonded Network Structure of Water in Aqueous Solution of Sulfobetaine Polymers†*. The Journal of Physical Chemistry B, 2002. **106**(43): p. 11391-11396.
165. Kitano, H., et al., *Structure of water incorporated in sulfobetaine polymer films as studied by ATR-FTIR*. Macromolecular Bioscience, 2005. **5**(4): p. 314-21.
166. Kitano, H., et al., *Raman Spectroscopic Study on the Structure of Water in Aqueous Polyelectrolyte Solutions†*. The Journal of Physical Chemistry B, 2000. **104**(47): p. 11425-11429.
167. Kondo, T., et al., *Structure of water at zwitterionic copolymer film-liquid water interfaces as examined by the sum frequency generation method*. Colloids Surf B Biointerfaces, 2014. **113**: p. 361-7.
168. Rechendorff, K., et al., *Enhancement of protein adsorption induced by surface roughness*. Langmuir, 2006. **22**(26): p. 10885-8.
169. Scopelliti, P.E., et al., *The effect of surface nanometre-scale morphology on protein adsorption*. PLoS One, 2010. **5**(7): p. e11862.
170. Hasan, J., et al., *Selective bactericidal activity of nanopatterned superhydrophobic cicada *Psaltoda claripennis* wing surfaces*. Applied Microbiology and Biotechnology, 2013. **97**(20): p. 9257-62.
171. Ivanova, E.P., et al., *Bactericidal activity of black silicon*. Nat Commun, 2013. **4**: p. 2838.
172. Ivanova, E.P., et al., *Natural bactericidal surfaces: mechanical rupture of *Pseudomonas aeruginosa* cells by cicada wings*. Small, 2012. **8**(16): p. 2489-94.
173. Pogodin, S., et al., *Biophysical model of bacterial cell interactions with nanopatterned cicada wing surfaces*. Biophysical Journal, 2013. **104**(4): p. 835-40.
174. Bellion, M., et al., *Protein adsorption on tailored substrates: long-range forces and conformational changes*. Journal of Physics: Condensed Matter, 2008. **20**(40): p. 404226.
175. Kim, M., et al., *From Self-Assembled Monolayers to Coatings: Advances in the Synthesis and Nanobio Applications of Polymer Brushes*. Polymers, 2015. **7**(7): p. 1346-1378.
176. Wang, H., et al., *Evaluation of photochemically immobilized poly(2-ethyl-2-oxazoline) thin films as protein-resistant surfaces*. ACS Applied Materials & Interfaces, 2011. **3**(9): p. 3463-71.

177. Clare, A.S., et al., *Molecular approaches to nontoxic antifouling*. Invertebrate Reproduction & Development, 1992. **22**(1-3): p. 67-76.
178. Hasan, A. and L.M. Pandey, *Review: Polymers, Surface-Modified Polymers, and Self Assembled Monolayers as Surface-Modifying Agents for Biomaterials*. Polymer-Plastics Technology and Engineering, 2015. **54**(13): p. 1358-1378.
179. Kirschner, C.M. and A.B. Brennan, *Bio-Inspired Antifouling Strategies*. Annual Review of Materials Research, 2012. **42**(1): p. 211-229.
180. Salta, M., et al., *Designing biomimetic antifouling surfaces*. Philos Trans A Math Phys Eng Sci, 2010. **368**(1929): p. 4729-54.
181. Sheparovych, R., M. Motornov, and S. Minko, *Adapting Low-Adhesive Thin Films from Mixed Polymer Brushes*. Langmuir, 2008. **24**(24): p. 13828-13832.
182. Sheparovych, R., M. Motornov, and S. Minko, *Low Adhesive Surfaces that Adapt to Changing Environments*. Advanced Materials, 2009. **21**(18): p. 1840-1844.
183. Fan, X., et al., *Biomimetic Anchor for Surface-Initiated Polymerization from Metal Substrates*. Journal of the American Chemical Society, 2005. **127**(45): p. 15843-15847.
184. Fan, X., L. Lin, and P.B. Messersmith, *Cell Fouling Resistance of Polymer Brushes Grafted from Ti Substrates by Surface-Initiated Polymerization: Effect of Ethylene Glycol Side Chain Length*. Biomacromolecules, 2006. **7**(8): p. 2443-2448.
185. Jo, S. and K. Park, *Surface modification using silanated poly(ethylene glycol)s*. Biomaterials, 2000. **21**(6): p. 605-616.
186. Richard, S., et al., *Optimization of pegylated iron oxide nanoplateforms for antibody coupling and bio-targeting*. J. Mater. Chem. B, 2017. **5**(16): p. 2896-2907.
187. Bedrov, D. and G.D. Smith, *Molecular dynamics simulation study of the structure of poly (ethylene oxide) brushes on nonpolar surfaces in aqueous solution*. Langmuir, 2006. **22**(14): p. 6189-6194.
188. Sofia, S.J., V. Premnath, and E.W. Merrill, *Poly (ethylene oxide) grafted to silicon surfaces: grafting density and protein adsorption*. Macromolecules, 1998. **31**(15): p. 5059-5070.
189. Efremova, N., S. Sheth, and D. Leckband, *Protein-induced changes in poly (ethylene glycol) brushes: molecular weight and temperature dependence*. Langmuir, 2001. **17**(24): p. 7628-7636.
190. Roosjen, A., et al., *Microbial adhesion to poly (ethylene oxide) brushes: influence of polymer chain length and temperature*. Langmuir, 2004. **20**(25): p. 10949-10955.
191. Lee, H., *Molecular Dynamics Studies of PEGylated Single-Walled Carbon Nanotubes: The Effect of PEG Size and Grafting Density*. The Journal of Physical Chemistry C, 2013. **117**(49): p. 26334-26341.
192. Benková, Z. and M.N.D.S. Cordeiro, *Molecular Dynamics Study of Water Interacting with Siloxane Surface Modified by Poly(ethylene oxide) Chains*. The Journal of Physical Chemistry C, 2011. **115**(38): p. 18740-18751.
193. Benková, Z. and M.N. D. S. Cordeiro, *Molecular Dynamics Study of Poly(Ethylene Oxide) Chains Densely Grafted on Siloxane Surface in Dry Conditions*. The Journal of Physical Chemistry C, 2012. **116**(5): p. 3576-3584.
194. Benková, Z., B. Szefczyk, and M.N.I. D. S. Cordeiro, *Molecular Dynamics Study of Hydrated Poly(ethylene oxide) Chains Grafted on Siloxane Surface*. Macromolecules, 2011. **44**(9): p. 3639-3648.
195. Ley, K.J., et al., *Effect of substrate on the responsive behaviour of functionalised surfaces: insights from molecular simulation*. Molecular Simulation, 2015. **42**(6-7): p. 563-572.

196. Oelmeier, S.A., F. Dimer, and J. Hubbuch, *Molecular dynamics simulations on aqueous two-phase systems - Single PEG-molecules in solution*. BMC Biophys, 2012. **5**: p. 14.
197. Li, E., Z. Du, and S. Yuan, *Properties of a water layer on hydrophilic and hydrophobic self-assembled monolayer surfaces: A molecular dynamics study*. Science China Chemistry, 2013. **56**(6): p. 773-781.
198. Rosso, M., et al., *Protein-repellent silicon nitride surfaces: UV-induced formation of oligoethylene oxide monolayers*. ACS Applied Materials & Interfaces, 2011. **3**(3): p. 697-704.
199. Hayashi, T. and M. Hara, *Nonfouling self-assembled monolayers: mechanisms underlying protein and cell resistance*. Current Physical Chemistry, 2011. **1**(2): p. 90-98.
200. Ng, C.C.A., et al., *Antifouling behaviour of silicon surfaces modified with self-assembled monolayers containing both ethylene glycol and charged moieties*. Surface Science, 2010. **604**(17-18): p. 1388-1394.
201. Blaszykowski, C., S. Sheikh, and M. Thompson, *Surface chemistry to minimize fouling from blood-based fluids*. Chemical Society Reviews, 2012. **41**(17): p. 5599-612.
202. Pawlowska, N.M., et al., *Probing the hydration of ultrathin antifouling organosilane adlayers using neutron reflectometry*. Langmuir, 2014. **30**(5): p. 1199-203.
203. Kobayashi, M., et al., *Wettability and antifouling behavior on the surfaces of superhydrophilic polymer brushes*. Langmuir, 2012. **28**(18): p. 7212-7222.
204. Herrwerth, S., et al., *Factors that determine the protein resistance of oligoether self-assembled monolayers --internal hydrophilicity, terminal hydrophilicity, and lateral packing density*. Journal of the American Chemical Society, 2003. **125**(31): p. 9359-66.
205. Feldman, K., et al., *Probing Resistance to Protein Adsorption of Oligo(ethylene glycol)-Terminated Self-Assembled Monolayers by Scanning Force Microscopy*. Journal of the American Chemical Society, 1999. **121**(43): p. 10134-10141.
206. Chen, S. and S. Jiang, *An New Avenue to Nonfouling Materials*. Advanced Materials, 2008. **20**(2): p. 335-338.
207. Singh, C., et al., *Entropy-mediated patterning of surfactant-coated nanoparticles and surfaces*. Physical Review Letters, 2007. **99**(22): p. 226106.
208. Singh, C., et al., *Striped nanowires and nanorods from mixed SAMS*. Nanoscale, 2011. **3**(8): p. 3244-50.
209. Fukuma, T., M.J. Higgins, and S.P. Jarvis, *Direct imaging of individual intrinsic hydration layers on lipid bilayers at Angstrom resolution*. Biophysical Journal, 2007. **92**(10): p. 3603-9.
210. Fukuma, T., M.J. Higgins, and S.P. Jarvis, *Direct imaging of lipid-ion network formation under physiological conditions by frequency modulation atomic force microscopy*. Physical Review Letters, 2007. **98**(10): p. 106101.
211. Kroning, A., et al., *Probing carbonyl-water hydrogen-bond interactions in thin polyoxazoline brushes*. Biointerphases, 2016. **11**(1): p. 019005.
212. Pidhatika, B., et al., *Comparative stability studies of poly(2-methyl-2-oxazoline) and poly(ethylene glycol) brush coatings*. Biointerphases, 2012. **7**(1-4): p. 1-15.
213. Konradi, R., C. Acikgoz, and M. Textor, *Polyoxazolines for nonfouling surface coatings--a direct comparison to the gold standard PEG*. Macromolecular Rapid Communications, 2012. **33**(19): p. 1663-76.

214. Zalipsky, S., et al., *Evaluation of blood clearance rates and biodistribution of poly(2-oxazoline)-grafted liposomes*. Journal of Pharmaceutical Sciences, 1996. **85**(2): p. 133-7.
215. Woodle, M.C., C.M. Engbers, and S. Zalipsky, *New Amphipatic Polymer-Lipid Conjugates Forming Long-Circulating Reticuloendothelial System-Evading Liposomes*. Bioconjugate Chemistry, 1994. **5**(6): p. 493-496.
216. Goddard, P., et al., *Soluble Polymeric Carriers for Drug Delivery--Part 4: Tissue Autoradiography, and Whole-Body Tissue Distribution in Mice, of N-(2-Hydroxypropyl)Methacrylamide Copolymers Following Intravenous Administration*. Journal of Bioactive and Compatible Polymers, 1991. **6**(1): p. 4-24.
217. Kronek, J., et al., *In vitro bio-immunological and cytotoxicity studies of poly(2-oxazolines)*. J Mater Sci Mater Med, 2011. **22**(7): p. 1725-34.
218. Luxenhofer, R., et al., *Structure-property relationship in cytotoxicity and cell uptake of poly(2-oxazoline) amphiphiles*. Journal of Controlled Release, 2011. **153**(1): p. 73-82.
219. Pan, C., et al., *Dopamine-assisted immobilization of partially hydrolyzed poly(2-methyl-2-oxazoline) for antifouling and biocompatible coating*. Journal of Materials Science, 2015.
220. He, T., et al., *Efficient and robust coatings using poly(2-methyl-2-oxazoline) and its copolymers for marine and bacterial fouling prevention*. Journal of Polymer Science Part A: Polymer Chemistry, 2015: p. n/a-n/a.
221. de la Rosa, V.R., *Poly(2-oxazoline)s as materials for biomedical applications*. J Mater Sci Mater Med, 2014. **25**(5): p. 1211-25.
222. Hoogenboom, R., *Poly(2-oxazoline)s: a polymer class with numerous potential applications*. Angew Chem Int Ed Engl, 2009. **48**(43): p. 7978-94.
223. Chang, B.-J., et al., *Surface-attached polymer monolayers for the control of endothelial cell adhesion*. Colloids and Surfaces A: Physicochemical and Engineering Aspects, 2002. **198-200**: p. 519-526.
224. Bissadi, G. and R. Weberskirch, *Efficient synthesis of polyoxazoline-silica hybrid nanoparticles by using the "grafting-onto" approach*. Polym. Chem., 2016. **7**(6): p. 1271-1280.
225. Konradi, R., et al., *Poly-2-methyl-2-oxazoline: a peptide-like polymer for protein-repellent surfaces*. Langmuir, 2008. **24**(3): p. 613-6.
226. Macgregor-Ramiasa, M.N., A.A. Cavallaro, and K. Vasilev, *Properties and reactivity of polyoxazoline plasma polymer films*. J. Mater. Chem. B, 2015. **3**(30): p. 6327-6337.
227. Ramiasa, M.N., et al., *Plasma polymerised polyoxazoline thin films for biomedical applications*. Chem Commun (Camb), 2015. **51**(20): p. 4279-82.
228. Zhang, N., et al., *Tailored poly(2-oxazoline) polymer brushes to control protein adsorption and cell adhesion*. Macromolecular Bioscience, 2012. **12**(7): p. 926-36.
229. Sedlacek, O., et al., *Poly(2-oxazoline)s--are they more advantageous for biomedical applications than other polymers?* Macromolecular Rapid Communications, 2012. **33**(19): p. 1648-62.
230. Viegas, T.X., et al., *Polyoxazoline: chemistry, properties, and applications in drug delivery*. Bioconjugate Chemistry, 2011. **22**(5): p. 976-86.
231. Sharma, S., R.W. Johnson, and T.A. Desai, *Evaluation of the Stability of Nonfouling Ultrathin Poly(ethylene glycol) Films for Silicon-Based Microdevices*. Langmuir, 2004. **20**(2): p. 348-356.
232. Branch, D., *Long-term stability of grafted polyethylene glycol surfaces for use with microstamped substrates in neuronal cell culture*. Biomaterials, 2001. **22**(10): p. 1035-1047.

233. Zhang, F., et al., *Modification of Si(100) surface by the grafting of poly(ethylene glycol) for reduction in protein adsorption and platelet adhesion*. Journal of Biomedical Materials Research, 2001. **56**(3): p. 324-332.
234. Kuang, J. and P.B. Messersmith, *Universal surface-initiated polymerization of antifouling zwitterionic brushes using a mussel-mimetic peptide initiator*. Langmuir, 2012. **28**(18): p. 7258-66.
235. Schlenoff, J.B., *Zwitteration: coating surfaces with zwitterionic functionality to reduce nonspecific adsorption*. Langmuir, 2014. **30**(32): p. 9625-36.
236. Wu, J., et al., *Investigation of the hydration of nonfouling material poly(sulfobetaine methacrylate) by low-field nuclear magnetic resonance*. Langmuir, 2012. **28**(19): p. 7436-41.
237. Murphy, E.F., et al., *The Reduced Adsorption of Proteins at the Phosphoryl Choline Incorporated Polymer–Water Interface*. Langmuir, 1999. **15**(4): p. 1313-1322.
238. Schlenoff, J.B., A.H. Rmaile, and C.B. Bucur, *Hydration contributions to association in polyelectrolyte multilayers and complexes: visualizing hydrophobicity*. Journal of the American Chemical Society, 2008. **130**(41): p. 13589-97.
239. Shao, Q., et al., *Difference in hydration between carboxybetaine and sulfobetaine*. Journal of Physical Chemistry B, 2010. **114**(49): p. 16625-31.
240. He, Y., et al., *Molecular simulation studies of protein interactions with zwitterionic phosphorylcholine self-assembled monolayers in the presence of water*. Langmuir, 2008. **24**(18): p. 10358-10364.
241. Shinoda, W., R. DeVane, and M.L. Klein, *Zwitterionic lipid assemblies: molecular dynamics studies of monolayers, bilayers, and vesicles using a new coarse grain force field*. Journal of Physical Chemistry B, 2010. **114**(20): p. 6836-49.
242. Butenuth, A., et al., *Ab initio derived force-field parameters for molecular dynamics simulations of deprotonated amorphous-SiO₂/water interfaces*. Physica Status Solidi B-Basic Solid State Physics, 2012. **249**(2): p. 292-305.
243. Charchar, P., et al., *Understanding and Designing the Gold-Bio Interface: Insights from Simulations*. Small, 2016. **12**(18): p. 2395-418.
244. Marrink, S.J. and D.P. Tieleman, *Perspective on the Martini model*. Chemical Society Reviews, 2013. **42**(16): p. 6801-22.
245. Cornell, W.D., et al., *A Second Generation Force Field for the Simulation of Proteins, Nucleic Acids, and Organic Molecules*. Journal of the American Chemical Society, 1995. **117**(19): p. 5179-5197.
246. MacKerell, A.D., et al., *All-atom empirical potential for molecular modeling and dynamics studies of proteins*. The Journal of Physical Chemistry B, 1998. **102**(18): p. 3586-3616.
247. Jorgensen, W.L., D.S. Maxwell, and J. Tirado-Rives, *Development and Testing of the OPLS All-Atom Force Field on Conformational Energetics and Properties of Organic Liquids*. Journal of the American Chemical Society, 1996. **118**(45): p. 11225-11236.
248. Oostenbrink, C., et al., *A biomolecular force field based on the free enthalpy of hydration and solvation: the GROMOS force-field parameter sets 53A5 and 53A6*. Journal of Computational Chemistry, 2004. **25**(13): p. 1656-76.
249. Mu, D.S. Kosov, and G. Stock, *Conformational Dynamics of Trialanine in Water. 2. Comparison of AMBER, CHARMM, GROMOS, and OPLS Force Fields to NMR and Infrared Experiments*. The Journal of Physical Chemistry B, 2003. **107**(21): p. 5064-5073.
250. Hu, H., M. Elstner, and J. Hermans, *Comparison of a QM/MM force field and molecular mechanics force fields in simulations of alanine and glycine "dipeptides"*

- (Ace-Ala-Nme and Ace-Gly-Nme) in water in relation to the problem of modeling the unfolded peptide backbone in solution. *Proteins*, 2003. **50**(3): p. 451-63.
251. Smith, P.E., *The alanine dipeptide free energy surface in solution*. *The Journal of Chemical Physics*, 1999. **111**(12): p. 5568-5579.
 252. Snyder, J.A., et al., *Development of a tuned interfacial force field parameter set for the simulation of protein adsorption to silica glass*. *Biointerphases*, 2012. **7**(1-4): p. 56.
 253. Sun, H., *COMPASS: An ab Initio Force-Field Optimized for Condensed-Phase Applications Overview with Details on Alkane and Benzene Compounds*. *The Journal of Physical Chemistry B*, 1998. **102**(38): p. 7338-7364.
 254. Cruz-Chu, E.R., A. Aksimentiev, and K. Schulten, *Water-silica force field for simulating nanodevices*. *Journal of Physical Chemistry B*, 2006. **110**(43): p. 21497-508.
 255. Vanommeslaeghe, K., et al., *CHARMM general force field: A force field for drug-like molecules compatible with the CHARMM all-atom additive biological force fields*. *Journal of Computational Chemistry*, 2010. **31**(4): p. 671-90.
 256. Jensen, F., *Introduction to Computational Chemistry*. 2007, Denmark: John Wiley & Sons.
 257. Leach, A.R., *Molecular modelling: principles and applications*. 2001: Pearson Education.
 258. Polak, E. and G. Ribiere, *Note sur la convergence de méthodes de directions conjuguées*. *Revue française d'informatique et de recherche opérationnelle, série rouge*, 1969. **3**(1): p. 35-43.
 259. Swope, W.C., et al., *A computer simulation method for the calculation of equilibrium constants for the formation of physical clusters of molecules: Application to small water clusters*. *The Journal of Chemical Physics*, 1982. **76**(1): p. 637-649.
 260. Verlet, L., *Computer "Experiments" on Classical Fluids. I. Thermodynamical Properties of Lennard-Jones Molecules*. *Physical Review*, 1967. **159**(1): p. 98-103.
 261. Karasawa, N. and W.A. Goddard, *Acceleration of convergence for lattice sums*. *The Journal of Physical Chemistry*, 1989. **93**(21): p. 7320-7327.
 262. Hockney, R.W. and J.W. Eastwood, *Computer simulation using particles*. 1988, Bristol: CRC Press.
 263. Pollock, E.L. and J. Glosli, *Comments on P3M, FMM, and the Ewald method for large periodic Coulombic systems*. *Computer Physics Communications*, 1996. **95**(2-3): p. 93-110.
 264. Nosé, S., *A unified formulation of the constant temperature molecular dynamics methods*. *The Journal of Chemical Physics*, 1984. **81**(1): p. 511-519.
 265. Hoover, W.G., *Canonical dynamics: Equilibrium phase-space distributions*. *Physical Review A*, 1985. **31**(3): p. 1695-1697.
 266. Andersen, H.C., *Molecular dynamics simulations at constant pressure and/or temperature*. *The Journal of Chemical Physics*, 1980. **72**(4): p. 2384-2393.
 267. Ryckaert, J.-P., G. Ciccotti, and H.J. Berendsen, *Numerical integration of the cartesian equations of motion of a system with constraints: molecular dynamics of n-alkanes*. *Journal of Computational Physics*, 1977. **23**(3): p. 327-341.
 268. Liu, P., et al., *Replica exchange with solute tempering: a method for sampling biological systems in explicit water*. *Proceedings of the National Academy of Sciences of the United States of America*, 2005. **102**(39): p. 13749-54.
 269. Sugita, Y. and Y. Okamoto, *Replica-exchange molecular dynamics method for protein folding*. *Chemical Physics Letters*, 1999. **314**(1-2): p. 141-151.

270. Torrie, G.M. and J.P. Valleau, *Nonphysical sampling distributions in Monte Carlo free-energy estimation: Umbrella sampling*. Journal of Computational Physics, 1977. **23**(2): p. 187-199.
271. Bernardi, R.C., M.C. Melo, and K. Schulten, *Enhanced sampling techniques in molecular dynamics simulations of biological systems*. Biochimica et Biophysica Acta, 2015. **1850**(5): p. 872-7.
272. Latour, R.A., *Molecular simulation of protein-surface interactions: Benefits, problems, solutions, and future directions (Review)*. Biointerphases, 2008. **3**(3): p. FC2-FC12.
273. Latour, R.A., *Perspectives on the simulation of protein-surface interactions using empirical force field methods*. Colloids Surf B Biointerfaces, 2014. **124**: p. 25-37.
274. Cohavi, O., et al., *Protein-surface interactions: challenging experiments and computations*. Journal of Molecular Recognition, 2010. **23**(3): p. 259-62.
275. Mahmoudi, M., et al., *Protein-nanoparticle interactions: opportunities and challenges*. Chem Rev, 2011. **111**(9): p. 5610-37.
276. Szott, L.M. and T.A. Horbett, *Protein interactions with surfaces: Computational approaches and repellency*. Current Opinion in Chemical Biology, 2011. **15**(5): p. 683-9.
277. Wang, Q., et al., *Computer simulation of biomolecule-biomaterial interactions at surfaces and interfaces*. Biomed Mater, 2015. **10**(3): p. 032001.
278. Ozboyaci, M., et al., *Modeling and simulation of protein-surface interactions: achievements and challenges*. Quarterly Reviews of Biophysics, 2016. **49**: p. e4.
279. Makarucha, A.J., N. Todorova, and I. Yarovsky, *Nanomaterials in biological environment: a review of computer modelling studies*. European Biophysics Journal, 2011. **40**(2): p. 103-15.
280. Yarovsky, I., *Atomistic simulation of interfaces in materials: Theory and applications*. Australian Journal of Physics, 1997. **50**(2): p. 407-424.
281. Yarovsky, I. and E. Evans, *Computer simulation of structure and properties of crosslinked polymers: application to epoxy resins*. Polymer, 2002. **43**(3): p. 963-969.
282. Wu, C. and W. Xu, *Atomistic molecular modelling of crosslinked epoxy resin*. Polymer, 2006. **47**(16): p. 6004-6009.
283. Wu, C. and W. Xu, *Atomistic molecular simulations of structure and dynamics of crosslinked epoxy resin*. Polymer, 2007. **48**(19): p. 5802-5812.
284. Fan, H.B. and M.M.F. Yuen, *Material properties of the cross-linked epoxy resin compound predicted by molecular dynamics simulation*. Polymer, 2007. **48**(7): p. 2174-2178.
285. Muller-Plathe, F., *Coarse-graining in polymer simulation: from the atomistic to the mesoscopic scale and back*. ChemPhysChem, 2002. **3**(9): p. 755-69.
286. Morita, H., et al., *Study of the glass transition temperature of polymer surface by coarse-grained molecular dynamics simulation*. Macromolecules, 2006. **39**(18): p. 6233-6237.
287. Henry, D.J., E. Evans, and I. Yarovsky, *Classical molecular dynamics study of [60]fullerene interactions with silica and polyester surfaces*. Journal of Physical Chemistry B, 2006. **110**(32): p. 15963-72.
288. Henry, D.J., et al., *Theoretical study of adhesion between graphite, polyester and silica surfaces*. Molecular Simulation, 2005. **31**(6-7): p. 449-455.
289. Henry, D.J., et al., *Adhesion between graphite and modified polyester surfaces: A theoretical study*. Journal of Physical Chemistry B, 2005. **109**(36): p. 17224-17231.

290. Yiapanis, G., et al., *Effect of aging on interfacial adhesion between polyester and carbon-based particles: A classical molecular dynamics study*. Journal of Physical Chemistry C, 2007. **111**(17): p. 6465-6472.
291. Yiapanis, G., et al., *Molecular Dynamics Study of Polyester Surfaces and Fullerene Particles in Aqueous Environment*. Journal of Physical Chemistry C, 2008. **112**(46): p. 18141-18149.
292. Yiapanis, G., et al., *Simulations of Nanoindentation of Polymer Surfaces: Effects of Surface Cross-Linking on Adhesion and Hardness*. Journal of Physical Chemistry C, 2010. **114**(1): p. 478-486.
293. Schoch, P.K. and J. Genzer, *Adsorption of "soft" spherical particles onto sinusoidally-corrugated substrates*. Soft Matter, 2014. **10**(38): p. 7452-8.
294. Lichter, J.A., et al., *Substrata mechanical stiffness can regulate adhesion of viable bacteria*. Biomacromolecules, 2008. **9**(6): p. 1571-8.
295. Wei, T., M.A. Carignano, and I. Szleifer, *Lysozyme adsorption on polyethylene surfaces: why are long simulations needed?* Langmuir, 2011. **27**(19): p. 12074-81.
296. Wei, T., M.A. Carignano, and I. Szleifer, *Molecular dynamics simulation of lysozyme adsorption/desorption on hydrophobic surfaces*. Journal of Physical Chemistry B, 2012. **116**(34): p. 10189-94.
297. Li, Y., et al., *Challenges in Multiscale Modeling of Polymer Dynamics*. Polymers, 2013. **5**(2): p. 751-832.
298. Feuston, B.P. and S.H. Garofalini, *Topological and Bonding Defects in Vitreous Silica Surfaces*. Journal of Chemical Physics, 1989. **91**(1): p. 564-570.
299. Feuston, B.P. and S.H. Garofalini, *Water-Induced Relaxation of the Vitreous Silica Surface*. Journal of Applied Physics, 1990. **68**(9): p. 4830-4836.
300. Ewing, C.S., et al., *Accurate amorphous silica surface models from first-principles thermodynamics of surface dehydroxylation*. Langmuir, 2014. **30**(18): p. 5133-41.
301. Fuerstenau, D.W. and Pradip, *Zeta potentials in the flotation of oxide and silicate minerals*. Advances in Colloid and Interface Science, 2005. **114-115**: p. 9-26.
302. Zhang, H., et al., *The water-amorphous silica interface: analysis of the Stern layer and surface conduction*. Journal of Chemical Physics, 2011. **134**(2): p. 024705.
303. Hassanali, A.A., et al., *The Dissociated Amorphous Silica Surface: Model Development and Evaluation*. Journal of Chemical Theory and Computation, 2010. **6**(11): p. 3456-3471.
304. Piana, S., et al., *Water dispersion interactions strongly influence simulated structural properties of disordered protein States*. Journal of Physical Chemistry B, 2015. **119**(16): p. 5113-23.
305. Izadi, S., R. Anandakrishnan, and A.V. Onufriev, *Building Water Models: A Different Approach*. J Phys Chem Lett, 2014. **5**(21): p. 3863-3871.
306. Best, R.B. and J. Mittal, *Protein simulations with an optimized water model: cooperative helix formation and temperature-induced unfolded state collapse*. Journal of Physical Chemistry B, 2010. **114**(46): p. 14916-23.
307. Lopes, P.E., et al., *Development of an empirical force field for silica. Application to the quartz-water interface*. Journal of Physical Chemistry B, 2006. **110**(6): p. 2782-92.
308. Skelton, A.A., et al., *Simulations of the Quartz(10 $\bar{1}$)/Water Interface: A Comparison of Classical Force Fields, Ab Initio Molecular Dynamics, and X-ray Reflectivity Experiments*. The Journal of Physical Chemistry C, 2011. **115**(5): p. 2076-2088.
309. Du, Z. and N.H. de Leeuw, *Molecular dynamics simulations of hydration, dissolution and nucleation processes at the alpha-quartz (0001) surface in liquid water*. Dalton Transactions, 2006(22): p. 2623-34.

310. Ostroverkhov, V., G.A. Waychunas, and Y.R. Shen, *Vibrational spectra of water at water/ α -quartz (0001) interface*. Chemical Physics Letters, 2004. **386**(1-3): p. 144-148.
311. Zhuravlev, L.T., *Concentration of Hydroxyl-Groups on the Surface of Amorphous Silicas*. Langmuir, 1987. **3**(3): p. 316-318.
312. Zhuravlev, L.T., *The surface chemistry of amorphous silica. Zhuravlev model*. Colloids and Surfaces a-Physicochemical and Engineering Aspects, 2000. **173**(1-3): p. 1-38.
313. Gaigeot, M.P., M. Sprik, and M. Sulpizi, *Oxide/water interfaces: how the surface chemistry modifies interfacial water properties*. J Phys Condens Matter, 2012. **24**(12): p. 124106.
314. Sulpizi, M., M.-P. Gaigeot, and M. Sprik, *The Silica–Water Interface: How the Silanols Determine the Surface Acidity and Modulate the Water Properties*. Journal of Chemical Theory and Computation, 2012. **8**(3): p. 1037-1047.
315. Cimas, A., et al., *The amorphous silica-liquid water interface studied by ab initio molecular dynamics (AIMD): local organization in global disorder*. J Phys Condens Matter, 2014. **26**(24): p. 244106.
316. Beck, D.A. and V. Daggett, *Methods for molecular dynamics simulations of protein folding/unfolding in solution*. Methods, 2004. **34**(1): p. 112-20.
317. Hofinger, S., B. Almeida, and U.H. Hansmann, *Parallel tempering molecular dynamics folding simulation of a signal peptide in explicit water*. Proteins, 2007. **68**(3): p. 662-9.
318. Schaeffer, R.D., A. Fersht, and V. Daggett, *Combining experiment and simulation in protein folding: closing the gap for small model systems*. Current Opinion in Structural Biology, 2008. **18**(1): p. 4-9.
319. Ehrlich, L.P., M. Nilges, and R.C. Wade, *The impact of protein flexibility on protein-protein docking*. Proteins, 2005. **58**(1): p. 126-33.
320. Wang, W., et al., *Biomolecular simulations: recent developments in force fields, simulations of enzyme catalysis, protein-ligand, protein-protein, and protein-nucleic acid noncovalent interactions*. Annual Review of Biophysics and Biomolecular Structure, 2001. **30**: p. 211-43.
321. Bond, P.J. and M.S. Sansom, *Insertion and assembly of membrane proteins via simulation*. Journal of the American Chemical Society, 2006. **128**(8): p. 2697-704.
322. Efremov, R.G., et al., *A Solvent Model for Simulations of Peptides in Bilayers. II. Membrane-Spanning α -Helices*. Biophysical Journal, 1999. **76**(5): p. 2460-2471.
323. Biswas, P.K., et al., *Simulation of multiphase systems utilizing independent force fields to control intraphase and interphase behavior*. Journal of Computational Chemistry, 2012. **33**(16): p. 1458-66.
324. Abramyan, T.M., et al., *Parameterization of an interfacial force field for accurate representation of peptide adsorption free energy on high-density polyethylene*. Biointerphases, 2015. **10**(2): p. 021002.
325. Heinz, H., et al., *Thermodynamically consistent force fields for the assembly of inorganic, organic, and biological nanostructures: the INTERFACE force field*. Langmuir, 2013. **29**(6): p. 1754-65.
326. Penna, M.J., et al., *Molecular-level understanding of the adsorption mechanism of a graphite-binding peptide at the water/graphite interface*. Soft Matter, 2015. **11**(26): p. 5192-203.
327. Xie, Y., J. Zhou, and S. Jiang, *Parallel tempering Monte Carlo simulations of lysozyme orientation on charged surfaces*. Journal of Chemical Physics, 2010. **132**(6): p. 065101.

328. Hildebrand, N., et al., *Adsorption Orientation and Binding Motifs of Lysozyme and Chymotrypsin on Amorphous Silica*. The Journal of Physical Chemistry C, 2015. **119**(13): p. 7295-7307.
329. Kubiak, K. and P.A. Mulheran, *Molecular dynamics simulations of hen egg white lysozyme adsorption at a charged solid surface*. Journal of Physical Chemistry B, 2009. **113**(36): p. 12189-200.
330. Wei, T., et al., *Self-Assembled Monolayers of an Azobenzene Derivative on Silica and Their Interactions with Lysozyme*. Langmuir, 2015. **31**(50): p. 13543-52.
331. Hower, J.C., et al., *Understanding the nonfouling mechanism of surfaces through molecular simulations of sugar-based self-assembled monolayers*. Journal of Chemical Physics, 2006. **125**(21): p. 214704.
332. Jamadagni, S.N., R. Godawat, and S. Garde, *How surface wettability affects the binding, folding, and dynamics of hydrophobic polymers at interfaces*. Langmuir, 2009. **25**(22): p. 13092-9.
333. Tosaka, R., et al., *Adsorption mechanism of ribosomal protein L2 onto a silica surface: a molecular dynamics simulation study*. Langmuir, 2010. **26**(12): p. 9950-5.
334. Benavidez, T.E., et al., *Adsorption of soft and hard proteins onto OTCEs under the influence of an external electric field*. Langmuir, 2015. **31**(8): p. 2455-62.
335. Mereghetti, P. and R.C. Wade, *Diffusion of hydrophobin proteins in solution and interactions with a graphite surface*. BMC Biophys, 2011. **4**: p. 9.
336. Liu, Y., et al., *Adsorption behavior of hydrophobin proteins on polydimethylsiloxane substrates*. Journal of Physical Chemistry B, 2012. **116**(40): p. 12227-34.
337. Yarovsky, I., M.L. Aguilar, and M.T.W. Hearn, *Influence of the Chain-Length and Surface-Density on the Conformation and Mobility of N-Alkyl Ligands Chemically Immobilized onto a Silica Surface*. Analytical Chemistry, 1995. **67**(13): p. 2145-2153.
338. Harris, J.M., K. Lim, and J.N. Herron, *Poly(Ethylene Glycol) Chemistry: Biotechnical and Biomedical Applications*, ed. J.M. Harris. 1992, New York: Springer Science & Business Media.
339. Loh, X.J., et al., *Controlled drug release from biodegradable thermoresponsive physical hydrogel nanofibers*. Journal of Controlled Release, 2010. **143**(2): p. 175-182.
340. Alcantar, N.A., E.S. Aydil, and J.N. Israelachvili, *Polyethylene glycol-coated biocompatible surfaces*. Journal of Biomedical Materials Research, 2000. **51**(3): p. 343-351.
341. Li, Z., et al., *Mesoporous silica nanoparticles in biomedical applications*. Chemical Society Reviews, 2012. **41**(7): p. 2590-2605.
342. Zhongmin, O., et al., *Functional single-walled carbon nanotubes based on an integrin $\alpha v \beta 3$ monoclonal antibody for highly efficient cancer cell targeting*. Nanotechnology, 2009. **20**(10): p. 105102.
343. Chee Leng, L., et al., *Delivery of paclitaxel by physically loading onto poly(ethylene glycol) (PEG)-graftcarbon nanotubes for potent cancer therapeutics*. Nanotechnology, 2010. **21**(6): p. 065101.
344. Dessy, A., et al., *Dead Sea Minerals loaded polymeric nanoparticles*. Colloids and Surfaces B: Biointerfaces, 2011. **87**(2): p. 236-242.
345. Wu, J. and S. Chen, *Investigation of the hydration of nonfouling material poly(ethylene glycol) by low-field nuclear magnetic resonance*. Langmuir, 2012. **28**(4): p. 2137-44.
346. Oesterhelt, F., M. Rief, and H. Gaub, *Single molecule force spectroscopy by AFM indicates helical structure of poly(ethylene-glycol) in water*. New Journal of Physics, 1999. **1**(1): p. 6.

347. Braithwaite, G.J.C., A. Howe, and P.F. Luckham, *Interactions between Poly(ethylene oxide) Layers Adsorbed to Glass Surfaces Probed by Using a Modified Atomic Force Microscope*. *Langmuir*, 1996. **12**(17): p. 4224-4237.
348. Heymann, B. and H. Grubmüller, *Elastic properties of poly(ethylene-glycol) studied by molecular dynamics stretching simulations*. *Chemical Physics Letters*, 1999. **307**(5–6): p. 425-432.
349. Smith, G.D., D. Bedrov, and O. Borodin, *Conformations and Chain Dimensions of Poly(ethylene oxide) in Aqueous Solution: A Molecular Dynamics Simulation Study*. *Journal of the American Chemical Society*, 2000. **122**(39): p. 9548-9549.
350. Tasaki, K., *Poly(oxyethylene)–Water Interactions: A Molecular Dynamics Study*. *Journal of the American Chemical Society*, 1996. **118**(35): p. 8459-8469.
351. Lee, H., et al., *Molecular Dynamics Studies of Polyethylene Oxide and Polyethylene Glycol: Hydrodynamic Radius and Shape Anisotropy*. *Biophysical Journal*, 2008. **95**(4): p. 1590-1599.
352. Koenig, S.P., et al., *Ultrastrong adhesion of graphene membranes*. *Nature Nanotechnology*, 2011. **6**(9): p. 543-6.
353. Compton, O.C., et al., *Tuning the Mechanical Properties of Graphene Oxide Paper and Its Associated Polymer Nanocomposites by Controlling Cooperative Intersheet Hydrogen Bonding*. *ACS Nano*, 2011. **6**(3): p. 2008-2019.
354. Kang, J.-H., K.-S. Kim, and K.-W. Kim, *Prediction of surface and adhesion energies of nanoimprint lithography materials and anti-sticking layers by molecular dynamics simulation*. *Applied Surface Science*, 2012. **258**(14): p. 5438-5442.
355. Viola Kusminskiy, S., et al., *Pinning of a two-dimensional membrane on top of a patterned substrate: The case of graphene*. *Physical Review B*, 2011. **83**(16): p. 165405.
356. Lee, M., et al., *Chemical modification of nylon 6 and polyester fabrics by ozone-gas treatment*. *Journal of Applied Polymer Science*, 2006. **100**(2): p. 1344-1348.
357. Rigby, D., H. Sun, and B.E. Eichinger, *Computer simulations of poly(ethylene oxide): force field, pvt diagram and cyclization behaviour*. *Polymer International*, 1997. **44**(3): p. 311-330.
358. Liu, G., et al., *Study of the kinetics of the pancake-to-brush transition of poly(*N*-isopropylacrylamide) chains*. *Journal of Physical Chemistry B*, 2005. **109**(47): p. 22603-7.
359. Advincula, R.C., et al., *Polymer Brushes: Synthesis, Characterization, Applications*. 2004, Federal Republic of Germany Weinheim: Wiley-VCH. 483.
360. Saeki, S., et al., *Upper and lower critical solution temperatures in poly (ethylene glycol) solutions*. *Polymer*, 1976. **17**(8): p. 685-689.
361. Weber, C., R. Hoogenboom, and U.S. Schubert, *Temperature responsive biocompatible polymers based on poly(ethylene oxide) and poly(2-oxazoline)s*. *Progress in Polymer Science*, 2012. **37**(5): p. 686-714.
362. Yiapanis, G., et al., *Effect of substrate on the mechanical response and adhesion of PEGylated surfaces: insights from all-atom simulations*. *Langmuir*, 2012. **28**(50): p. 17263-72.
363. Shaw, L.A., et al., *Surface crosslinking effects on contamination resistance of functionalised polymers*. *Soft Matter*, 2013. **9**(6): p. 1798-1806.
364. Yiapanis, G., et al., *Molecular mechanism of stabilization of thin films for improved water evaporation protection*. *Langmuir*, 2013. **29**(47): p. 14451-14459.
365. Tauhardt, L., et al., *Poly(2-oxazoline) functionalized surfaces: from modification to application*. *Chemical Society Reviews*, 2013. **42**(20): p. 7998-8011.

366. Plimpton, S., *Fast parallel algorithms for short-range molecular dynamics*. Journal of Computational Physics, 1995. **117**(1): p. 1-19.
367. Jorgensen, W.L., et al., *Comparison of simple potential functions for simulating liquid water*. The Journal of Chemical Physics, 1983. **79**(2): p. 926-935.
368. Penna, M., et al., *Surface heterogeneity: a friend or foe of protein adsorption - insights from theoretical simulations*. Faraday Discussions, 2016. **191**: p. 435-464.
369. Wei, Q., et al., *Protein interactions with polymer coatings and biomaterials*. Angew Chem Int Ed Engl, 2014. **53**(31): p. 8004-31.
370. Ostuni, E., et al., *Adsorption of Proteins to Hydrophobic Sites on Mixed Self-Assembled Monolayers†*. Langmuir, 2003. **19**(5): p. 1861-1872.
371. Finlay, J.A., et al., *Settlement of Ulva zoospores on patterned fluorinated and PEGylated monolayer surfaces*. Langmuir, 2008. **24**(2): p. 503-10.
372. Penna, M., et al., *Surface heterogeneity: a friend or foe of protein adsorption - insights from theoretical simulations*. Faraday Discuss, 2016.
373. Striolo, A., et al., *Applications: general discussion*. Faraday Discussions, 2016. **191**: p. 565-595.
374. Ye, H., et al., *Superior Antifouling Performance of a Zwitterionic Peptide Compared to an Amphiphilic, Non-Ionic Peptide*. ACS Applied Materials & Interfaces, 2015. **7**(40): p. 22448-57.
375. Cheng, G., et al., *Inhibition of bacterial adhesion and biofilm formation on zwitterionic surfaces*. Biomaterials, 2007. **28**(29): p. 4192-4199.
376. Ley, K., et al., *Surface-water Interface Induces Conformational Changes Critical for Protein Adsorption: Implications for Monolayer Formation of EAS Hydrophobin*. Front Mol Biosci, 2015. **2**: p. 64.
377. Schultz, M.P., et al., *Economic impact of biofouling on a naval surface ship*. Biofouling, 2011. **27**(1): p. 87-98.
378. Prentice, T., R. Beaglehole, and A. Irwin, *The World Health Report, 2004: Changing History*. 2004: World Health Organization.
379. Mittelman, M.W., *Adhesion to biomaterials*. Bacterial adhesion: molecular and ecological diversity. 1996, New York: Wiley-Liss, Inc. 89-127.
380. Dill, K.A. and J.L. MacCallum, *The protein-folding problem, 50 years on*. Science, 2012. **338**(6110): p. 1042-1046.
381. Karplus, M. and R. Lavery, *Significance of Molecular Dynamics Simulations for Life Sciences*. Israel Journal of Chemistry, 2014. **54**(8-9): p. 1042-1051.
382. Meredith, J.C., *Advances in combinatorial and high-throughput screening of biofunctional polymers for gene delivery, tissue engineering and anti-fouling coatings*. Journal of Materials Chemistry, 2009. **19**(1): p. 34.
383. Faver, J.C., W. Yang, and K.M. Merz Jr, *The Effects of computational modeling errors on the estimation of statistical mechanical variables*. Journal of Chemical Theory and Computation, 2012. **8**(10): p. 3769-3776.
384. Mobley, D.L., *Let's get honest about sampling*. Journal of Computer-Aided Molecular Design, 2012. **26**(1): p. 93-95.
385. Jimenez, M., et al. *Antifouling stainless steel surface: competition between roughness and surface energy*. in *Materials Science Forum*. 2012. Trans Tech Publ.
386. Puddu, V. and C.C. Perry, *Interactions at the silica-peptide interface: the influence of particle size and surface functionality*. Langmuir, 2014. **30**(1): p. 227-33.
387. Treuel, L. and G.U. Nienhaus, *Toward a molecular understanding of nanoparticle-protein interactions*. Biophysical Reviews, 2012. **4**(2): p. 137-147.
388. Buck, M., et al., *Importance of the CMAP correction to the CHARMM22 protein force field: dynamics of hen lysozyme*. Biophysical Journal, 2006. **90**(4): p. L36-L38.

389. Oren, E.E., et al., *Probing the molecular mechanisms of quartz-binding peptides*. Langmuir, 2010. **26**(13): p. 11003-9.
390. Raschke, T.M., *Water structure and interactions with protein surfaces*. Current Opinion in Structural Biology, 2006. **16**(2): p. 152-159.
391. Broto, P., G. Moreau, and C. Vandycke, *Molecular structures: perception, autocorrelation descriptor and sar studies: system of atomic contributions for the calculation of the n-octanol/water partition coefficients*. European Journal of Medicinal Chemistry, 1984. **19**(1): p. 71-78.
392. Laguerre, M., et al., *MLPP: A Program for the Calculation of Molecular Lipophilicity Potential in Proteins*. Pharmacy and Pharmacology Communications, 1997. **3**(5-6): p. 217-222.
393. Livingstone, C.D. and G.J. Barton, *Protein sequence alignments: a strategy for the hierarchical analysis of residue conservation*. Comput Appl Biosci, 1993. **9**(6): p. 745-56.
394. Price, D.J. and C.L. Brooks III, *A modified TIP3P water potential for simulation with Ewald summation*. The Journal of Chemical Physics, 2004. **121**(20): p. 10096-10103.
395. Otten, A. and S. Herminghaus, *How plants keep dry: A physicist's point of view*. Langmuir, 2004. **20**(6): p. 2405-2408.
396. Lee, J.H., J. Kopecek, and J.D. Andrade, *Protein-resistant surfaces prepared by PEO-containing block copolymer surfactants*. Journal of Biomedical Materials Research, 1989. **23**(3): p. 351-68.
397. Wang, R., et al., Nature, 1997. **388**(6641): p. 431-432.
398. Pasche, S., et al., *Relationship between Interfacial Forces Measured by Colloid-Probe Atomic Force Microscopy and Protein Resistance of Poly(ethylene glycol)-Grafted Poly(l-lysine) Adlayers on Niobia Surfaces*. Langmuir, 2005. **21**(14): p. 6508-6520.
399. Sunde, M., et al., *Structural analysis of hydrophobins*. Micron, 2008. **39**(7): p. 773-84.